# Synaptic Integration and its Control in Neocortical Pyramidal Cells

Thesis by Jan Öjvind Bernander

In Partial Fulfillment of the Requirements

for the Degree of

Doctor of Philosophy

California Institute of Technology

Pasadena, California

1993

(Defended May 20, 1993)

# Acknowledgements

Thanks to my advisor Christof Koch, without whom none of this work would have come about. His constant enthusiasm has spurred on my work and fostered a spirit of camaraderie in the research group. Despite a back-breaking work load, he has always been available to provide guidance through difficult turns.

Rodney Douglas has been a fantastic collaborator. Never afraid of rolling up his shirt sleeves and getting down and dirty with the nitty-gritty details, he has been invaluable in developing cell models and formulating problems.

I am also in debt to my candidacy and thesis committees. John Allman, Al Barr, Jim Bower, Gilles Laurent, Henry Lester, Mark Konishi, and David Van Essen all have provided useful feedback and comments.

Thanks to Michael Hines for providing me with the NEURON simulator and for rapid-fire responses to any simulation problems. Thanks to Tom Tromey for writing the graphics utility **tndp** and to Dave Flowers for maintaining it.

Thanks to everybody in the Koch lab and fellow CNS students-in-arms for moral support and a fun time. Special thanks to Hsiaolan Hsu, Bartlett Mel, Adam Strassberg, Humbert Suarez, Marius Usher, Anthony Zador, and Haiyun Zhang for useful scientific discussions. Thanks to Kjell Post, Denise Simon, and Jonas Sjöberg for

megabytes of electronic epistles. Thanks to Jack Hwang for food and wine, Belinda Reser for spice, Ernie for burritos, and Bruno Olshausen for sharing freeze-dried calories during 10,000 foot adventures.

Finally, the greatest thanks of all go to my parents, my grandmother, and my brother Michael for their unconditional love and constant support, and for teaching me what is truly important in life.

Support for this research has been provided by the Office of Naval Research, the National Science Foundation, and the National Institute of Mental Health.

# Abstract

The main goal of this thesis is to investigate the input/output relationship of single regular-firing neocortical pyramidal neurons and how this relationship can be controlled by external inputs. The thesis can be divided into three main parts. First, a detailed single cell model was developed, based on the morphology of reconstructed cells and experimental values for membrane conductances and synaptic input distributions. This model was used for the following investigations.

Second, the spatio-temporal integration of single and multiple inputs was studied. Several measures for the efficacy and time delay of single synapses were defined and shown to vary dramatically. For example, a somatic synapse was only 2.2 times stronger than a very distal synapse using the *charge attenuation* measure, but more than 450 times stronger in the *voltage attenuation* measure. The effect that temporal synchronicity of multiple inputs had on firing rate was shown to vary with the number of inputs: for just-threshold input rates, synchronicity increased firing rate; for large inputs, high synchronicity strongly reduced firing rate, due to inputs being "wasted" during the refractory period.

Third, a subset of the inputs were considered to constitute a control signal, and their effect on other inputs was studied for three cases. The first case considers the

level of synaptic background activity to be a control signal; since each synapse is a small conductance change, and not a voltage-independent current source, the sum total of all "background" synapses will constitute the lion's share of the membrane conductance. The background firing rate, $f_b$, will therefore determine the electrotonic structure of the cell. For $f_b$ in the range of 0–10 $Hz$, a more than 10-fold decrease was seen in both input resistance (50.4–5.1 M$\Omega$) and membrane time constant (33.7–1.6 $msec$). Electrotonic length and resting potential were similarly affected. The second case treats input to the apical trunk as the control signal; when this input was weak and excitatory, the more distal input to the apical tuft could be facilitated, but when this input was strong or combined with inhibition, more distal input were reduced. The third case involves distributing two types of active conductances throughout the apical dendrites. The activation curves of these conductances were "designed" to ensure that the current delivered to the soma was linear in the input rate and amplified, since a passive tree strongly attenuates large apical inputs. The linearization was implemented with a persistent potassium conductance in the superficial layer I–III and the amplification with a persistent calcium conductance in the apical trunk (layer IV). The amplification gain could be set arbitrarily by modulating the channel density of either the potassium or calcium conductance.

# Contents

# List of Tables

# Chapter 1

# Introduction

*Since it is the* understanding *that sets man above the rest of sensible beings, and gives him all the advantage and dominion which he has over them, it is certainly a subject, even for its nobleness, worth our labour to inquire into.*

– John Locke, *An Essay Concerning Human Understanding*

## 1.1 Single neurons: A perspective

According to the *neuron doctrine*, nerve cells constitute the basic building blocks of brains [Ramon ỳ Cajal, 1909]. Despite a century of research, this building block is not fully understood. This thesis combines analytic and simulation techniques to investigate the integration of synaptic input and how this integration can be controlled.

Neurons are complex devices. In the era of electronics, neurons have often been compared to switching elements, transistors, and logic gates. However, it has become increasingly clear that the dendritic morphology and a spate of channel types

[McCormick, 1990] allow for more sophisticated computations than those electronic devices. While it is true that networks of simplistic neurons can show interesting behavior [Hopfield, 1982], models of direction selectivity and pattern recognition often depend crucially on the details of the neuron model [Borg-Graham and Grzywacz, 1992, Mel, 1992].

This very complexity of single neurons has made the investigation technically difficult. The assault proceeds along several lines of attack: anatomists stain cells to reveal their morphologies and interconnections; physiologists record the electrical behavior in response to natural or artificial stimuli; biophysicists measure the properties of membrane channels and their interactions via membrane potential and ionic concentrations. A fourth approach, espoused in this thesis, involves analysis and simulation of theoretical cell models.

Cell models range from simple to very detailed. Examples of simple models used in this thesis are the integrate-and-fire family of models which integrate charge onto a single capacitor [Knight, 1972; chapter 4], and equivalent cylinder models that collapse an entire dendritic tree into a single cable [Rall, 1969; chapter 5]. The advantage of simple models is that they often allow for an analytic treatment that can explain a phenomenon in terms of one or two variables. More detailed models have become commonplace as the price of CPU seconds have steadily decreased over the last few decades. These models take into account the full morphology of dendritic trees [for instance, Koch et al., 1982] and the technique of *compartmental modeling* is now widely used: the dendritic tree is mapped onto a network of resistors and capacitors and the circuit equations subsequently solved [for instance, Segev et al., 1989]. This thesis centers around such a detailed compartmental cell model that complements the simpler models. It is used when simpler models do not suffice because the complex morphology is crucial to the problem under investigation and preclude an analytic treatment (chapters 3 and 6). It is also used to demonstrate that simplifications are

frequently valid and to identify finer details that are not captured by the simpler models.

## 1.2 The dynamic neuron

It is a central tenet of this thesis that neurons are not static, but dynamic devices, the properties of which may change on a sub-second time-scale.

The (non-linear) transfer function depends in a complex way on the morphology of the cell, the pattern of synaptic input in space and time, and the properties of intrinsic membrane conductances:

$$f_{out} = fnc\ [t, x_i, G_{max,j}],$$

where $x_i$ are synaptic inputs and $G_{max,j}$ are the amplitudes of intrinsic membrane conductances that may depend on time, voltage, and ionic concentration. In this thesis, a subset of inputs or intrinsic conductances will be conceptually separated from the rest and treated as control signals:

$$f'_{out} = fnc\ [t, x_i, G_{max,j} \mid x_i^{control}, G_{max,j}^{control}].$$

This allows us to treat the transfer function, $f'_{out}$, as a dynamic entity, the exact form of which can be set by the control signals, $x_i^{control}$ and $G_{max,j}^{control}$. In this formalism, basic spatio-temporal integration parameters, such as input resistance, time constant, and electrotonic distance, can be controlled (chapters 3 and 5), receptive fields and tuning curves can be varied (chapters 3 and 5), and the dendritic tree can be broken down into separate units, the contributions of which can be gated selectively (chapter 6).

It is easy to envision highly specific control signals that target a small number of inputs with high selectivity. Such schemes would put high demands on the precision

of wiring and run the risk of non-robustness. We therefore focus on widely distributed control signals that terminate throughout the dendritic tree or over large chunks of membrane. Examples of synaptic control signals, $x_i^{control}$, are the average background activity of all synapses (chapters 3 and 5) and layer IV input to the apical trunk (chapter 6). The key fact underlying this work is that *synapses are conductance changes* and not current sources. In most previous analyses of the cable equation, the current source approximation is used [for instance, Rinzel and Rall, 1974]. This approximation is based on the assumptions that the conductance of a single synapse is small compared to the local input conductance. Then the local voltage change will be small compared to the driving force and the approximation is valid. Multiple synaptic inputs will hence add linearly. However, when $g_{syn}$ is on the same order as, or larger than, the local input conductance, the approximation is no longer valid. The synapse will give a significant contribution to the membrane conductance, *changing the electrotonic structure of the cell.* It will be shown that quite low levels of network activity can have a dramatic impact on spatio-temporal integration.

Neuromodular control signals, $G_{max,j}^{control}$, can vary the density of calcium channels in the apical trunk and potassium channels in the superficial layers I–III (chapter 6). The problem addressed in that chapter is that the axial resistance of the apical trunk severely limits the amount of current that superficial input can deliver to the cell body. This is in contrast to experimental evidence that synaptic input to layer I can drive pyramidal cells in the deep layers more than 1 $mm$ away. We introduce the technique of deriving "optimal" activation curves for putative dendritic conductances that will amplify the apical signal. By modulating the density of these conductances, the gain can be set arbitrarily, connecting and disconnecting the apical tuft in a graded manner.

## 1.3 Organization of this thesis

This thesis is organized in seven chapters. Chapters 2 through 6 are based on material previously published or in preparation [Bernander et al., 1991, Bernander et al., 1992, Bernander et al., 1993b, Bernander et al., 1993c, Bernander et al., 1993a]. They have been partially rewritten and reorganized to avoid excessive repetitions.

Chapter 1 gives a brief introduction and defines terms and conventions used throughout the thesis. Chapter 2 gives a detailed description of two model cells, motivates parameter choices, compares to experimental recordings, and gives several examples of the basic model at work. The results presented in the following four chapters are largely based on this model. Chapters 3 and 4 investigate the spatio-temporal integration of synaptic input. Chapter 3 concentrates on the efficacy and delay of single synapses, while Chapter 4 studies the effect of synchronization of large numbers of inputs on output firing rate. Chapters 5 and 6 investigate various schemes by which synaptic integration can be modulated and controlled by external inputs. Chapter 5 demonstrates the impact of background activity level on input resistance and time constant, while Chapter 6 describes how the apical tuft can be treated as a separate integrative unit, the contribution of which can be reduced, amplified, and linearized. Chapter 7 summarizes the contribution of the research presented here. Each chapter will begin with a review of previous work and define goals.

Part of the work was done in collaboration with Drs. Rodney Douglas (chapters 2, 5, 6), Kevan Martin (chapter 5), and Marius Usher (chapter 4).

## 1.4 Glossary, notation, definitions, and conventions

Tables 1.1 and 1.2 summarize terms and definitions that are used throughout this thesis.

Membrane potential is measured with the extracellular medium defined as 0 $mV$. The resting potential, $V_{rest}$, is therefore negative. Values of membrane potential are ordered with the minus sign in mind, e.g., -75 < -65, as opposed to a small minority of authors who use the opposite inequality.

Units are usually not the standard SI units, but are prefixed. For example, membrane resistance, $R_m$, is given in units of $\Omega cm^2$ rather than $\Omega m^2$. While this has the disadvantage of making formulas and simulations error-prone by lack of internal consistency, it conforms with conventions in the literature and is the standard of simulation packages such as NEURON and GENESIS.

| | |
|---|---|
| AMPA | amino-3-hydroxy-5-methyl-4-isoxazolepropionic acid<br>agonist of the non-NMDA subtypes of excitatory synapse |
| CNQX | 6-cyano-7-nitro-quinoxaline-2,3-dione<br>antagonist of the non-NMDA receptor |
| NMDA | N-methyl-D-aspartate<br>agonist of the NMDA subtype of excitatory synapse |
| AP5 | 2-amino-phosphovaleric acid<br>antagonist of the NMDA receptor |
| GABA | $\gamma$-amino-butyric acid<br>inhibitory neurotransmitter |
| TTX | tetrodotoxin<br>blocks sodium conductances, found in fish ovaries, e.g., puffer fish |
| TEA | tetra-ethyl-ammonium<br>blocks potassium conductances |
| 4-AP | 4-aminopyridine<br>blocks certain types of potassium conductances |
| BAPTA | 1,2-bis(o-aminophenoxy)ethane-N-N-N'-N'-tetra-acetic acid<br>chelates calcium |
| EGTA | ethylene bis-($\beta$-aminoethyl ether)-N,N'-tetra-acetic acid<br>chelates calcium |

Table 1.1: Commonly used acronyms.

| Symbol | Units | Comment |
|---|---|---|
| $V_m$ | $mV$ | Membrane potential |
| $V_{rest}$ | $mV$ | $V_m$ at rest |
| $E_{rev}$ | $mV$ | Reversal potential |
| $V_t$ | $mV$ | Threshold for action potential generation |
| $dV$ | $mV$ | Amplitude of single EPSP |
| $C_m$ | $\mu F/cm^2$ | Membrane capacitance |
| $C$ | $nF$ | Absolute capacitance |
| $R_m$ | $\Omega cm^2$ | Passive membrane resistance |
| $R_{m,eff}$ | $\Omega cm^2$ | Effective $R_m$, including synaptic input |
| $R_i$ | $\Omega cm$ | Intracellular resistivity |
| $R_{in}$ | $M\Omega$ | Input resistance |
| $K_{ii}$ | $M\Omega$ | Local $R_{in}$ at location $i$ |
| $K_{ij} = K_{ji}$ | $M\Omega$ | Transfer resistance between locations $i$ and $j$ |
| $A_V = K_{is}/K_{ii}$ | | Voltage attenuation |
| $A_Q = K_{ss}/K_{is}$ | | Charge attenuation |
| $\tau_m$ | $msec$ | Membrane time constant |
| $\Delta T$ | $msec$ | Desynchronization interval |
| $T_{spike}$, ISI | $msec$ | Inter-spike interval |
| $T_{rp}$ | $msec$ | Refractory period |
| $N$ | | Number of input events |
| $N_{sp}$ | | Number of output spikes |
| $g_{syn}$ | $nS$ | Synaptic conductance |
| $G$ | $nS$ | Absolute passive conductance |
| $G_{max}$ | $mS/cm^2$ | Maxium active conductance |
| $G_{syn}$ | $nS \cdot sec$ | Time integral of $g_{syn}$ |
| $l$ | $\mu m$ | Length |
| $d$ | $\mu m$ | Diameter |
| $\lambda = \sqrt{\frac{d \cdot R_m}{4 \cdot R_i}}$ | $\mu m$ | Length constant, |
| $L = l/\lambda$ | | Electrotonic length |

Table 1.2: Notation and definitions used throughout this thesis.

# Chapter 2

# Model Description

## 2.1 Introduction

This chapter gives a detailed description of a computer model of two cortical pyramidal neurons. The model was developed in collaboration with Rodney Douglas and is used throughout this thesis and other publications [Bernander et al., 1991, Bernander et al., 1993c, Bernander et al., 1993a]. It has been used, sometimes in modified form, by other investigators [Softky and Koch, 1992, Mel, 1992, Softky and Koch, 1993, Softky, 1993].

Morphologies were derived from careful microanatomical reconstructions carried out in Rodney Douglas' lab. In this thesis we refer to the "standard" model, which explicitly models all branches of the dendritic tree. The standard model incorporates eight active conductances in the soma and three types of synaptic inputs; the dendritic tree is passive and the axon is ignored. Variations on the standard model include the removal of active somatic conductances, addition of dendritic active conductances, and the addition of a fourth type of synapse, the NMDA synapse.

Simpler models are sometimes used to allow for an analytic treatment or to demon-

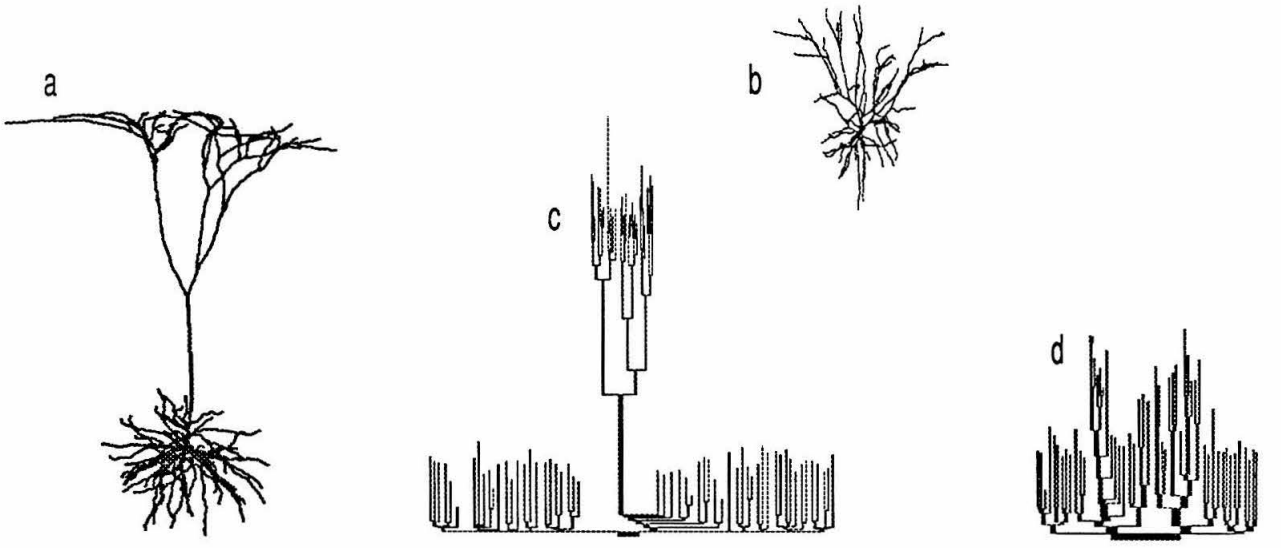


Figure 2.1: Morphologies of the two cells used in simulations. **(a)** Layer V cell. **(b)** Layer II/III cell. **(c),(d)** Scholl diagrams of the same cells as in (a) and (b). Diameters and lengths have different scales.

---

strate that a phenomenon is independent of the detailed morphology. These models will be described separately in the chapters where they are put to use. Such simplified models include variations on the integrate-and-fire model, single cables with uniform membrane resistance, and a single compartment with the same set of active conductances as the standard model. The standard model has been implemented in the compartmental simulator NEURON, which was graciously made available to us by Hines [Hines, 1989].

Section 2.2 summarizes the model and is intended as a quick reference guide. Section 2.3 gives a detailed discussion of the choice of parameters. Section 2.4 demonstrates the model at work with several examples, compares it to experimental data, and discusses issues of robustness.

## 2.2 Model summary

This section summarizes the model. It is intended to be a review and quick reference rather than an in-depth discussion. In the following sections we will justify parameter choices and give examples of the model at work.

### 2.2.1 Morphology

The morphologies were derived from typical layer V and layer II/III pyramidal cells in area V1. The cells were filled with HRP during *in vivo* experiments in the anesthetized, adult cat [Douglas et al., 1991]. The 3-D coordinates and diameters of the dendritic trees were measured by a computer-assisted method and each branch was replaced by a single equivalent cylinder. The resulting morphologies have been used in several previous simulations studies [Koch et al., 1990, Bernander et al., 1991, Lytton and Sejnowski, 1991, Mel, 1992, Softky and Koch, 1992, Bush and Sejnowski, 1992, Softky and Koch, 1993, Softky, 1993]. Fig. 2.1(a,b) show 2-D projections of the cells and fig. 2.1(c,d) show Scholl diagrams, with lengths and diameters preserved. The layer V cell, upon which most simulations were performed, has a total of 163 branches, with the most distal tip at a distance of 1387 $\mu m$ from the soma (see Fig. 6.1 for a close-up). The soma is small, making up only 2% of the total membrane area. The basal dendrites, including layer V obliques off the apical trunk, account for approximately 60% of the membrane area. The apical trunk and apical tuft account for the remainder. Branches were further subdivided into several compartments, depending on the local effective membrane resistance $R_{m,eff}$ (see below). The axon (diameter $d = 1\ \mu m$) was not included in the model since its effect on the integrative properties of the cell was small. The small diameter of the axon ensures that it will provide a negligible passive load. Further, simulations indicate that the effect of active axonal conductances can be mimicked by increasing the channel density of the corresponding

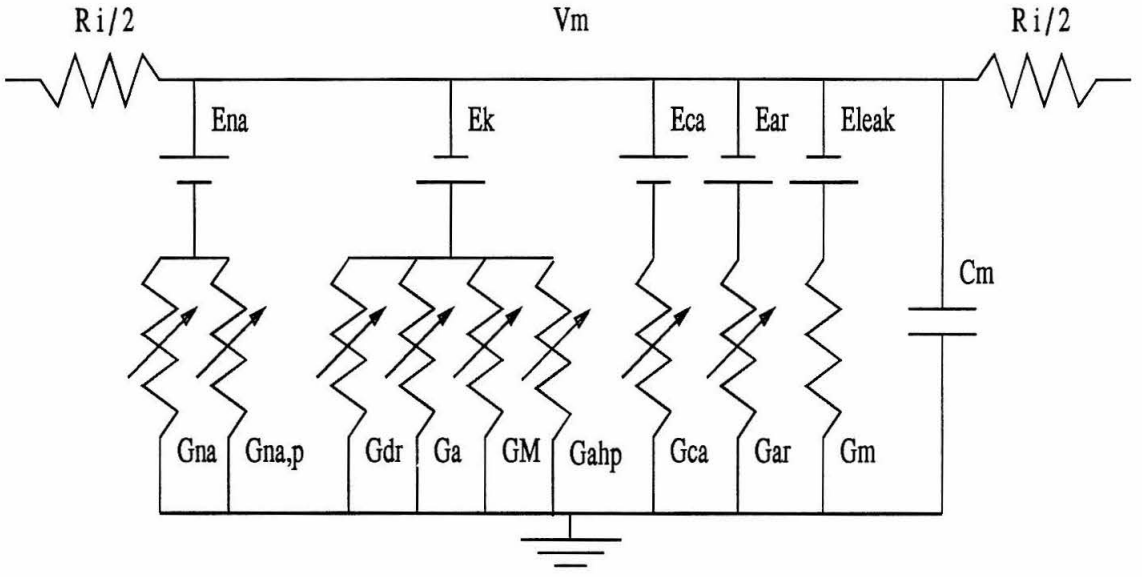


Figure 2.2: Compartment used in simulations, representing the soma. In addition to passive components ($R_m$, $R_i$, and $C_m$), this compartment has eight active conductances. Synapses are not shown, but also are modeled with a battery in series with a conductance. Dendrites typically contained no active conductances.

---

somatic conductances. A decomposition of the layer V cell by cortical layer is given in Table 2.1. Membrane area, total dendritic length, and other morphological data is given in Table 2.4.

### 2.2.2 Compartmental modeling

To simulate the neurons we used a compartmental model as described in [Segev et al., 1989]. Each branch was represented by at least one compartment, but often five or ten compartments would be used per branch, ensuring that no compartment was longer than 0.1 $\lambda$ (length constant). Each compartment has a minimum of three resistances (representing axial and membrane resistance) and one capacitance (see

| | Layer I | Layer II | Layer III | Layer IV | Layer V | Soma |
|---|---|---|---|---|---|---|
| Number branches | 50 | 6 | 4 | 1 | 102 | 1 |
| Area ($\mu m^2$) | 7073 | 2460 | 4773 | 5700 | 34378 | 1233 |
| Length ($\mu m$) | 5142 | 689 | 918 | 409 | 10976 | 23 |
| Number excitatory synapses | 576 | 200 | 389 | 463 | 2362 | 9 |
| Number $GABA_A$ synapses | 0 | 0 | 0 | 12 | 427 | 61 |
| Number $GABA_B$ synapses | 13 | 5 | 9 | 33 | 427 | 13 |

Table 2.1: Morphological comparison of different regions of a layer V pyramidal neuron. Layer IV is identical to the apical trunk. Layer V includes apical obliques and all other processes that are proximal to the apical trunk except the soma. The six regions exactly cover the neuron with no overlap.

---

Fig. 2.2). Active conductances and synapses are modeled with a time and voltage dependent conductance in series with a battery representing the reversal potential.

### 2.2.3 Passive membrane properties

The axial resistance $R_i$ was 200 $\Omega cm$ and the specific membrane capacitance $C_m$ was 1 $\mu F/cm^2$.

The passive leak current was defined by the membrane resistance, $R_m$, which was set to 100 k$\Omega cm^2$, throughout the cell ($G_m$ in Fig. 2.2). The reversal potential of this passive current was -66 $mV$.

### 2.2.4 Active membrane conductances

The following eight conductances were restricted to the soma: two sodium conductances, $G_{Na}$ and $G_{Na,p}$, one calcium conductance, $G_{Ca}$, four potassium conductances, $G_{DR}$, $G_{AHP}$, $G_A$, and $G_M$, and a mixed potassium/sodium conductance, $G_{AR}$. One of the potassium conductances, $G_{AHP}$, was calcium dependent.

We used a Hodgkin-Huxley-like formalism with the simplifying assumption that

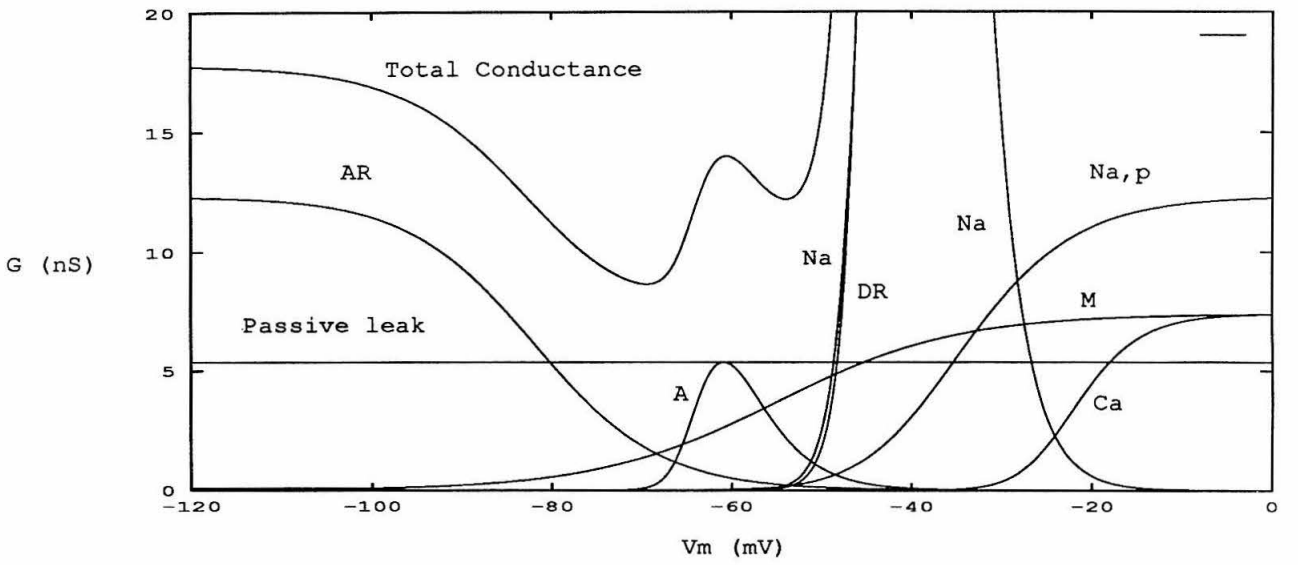


Figure 2.3: Steady state activation curves for seven active conductances for the layer V pyramid, whose somatic area was 1233 $\mu m^2$. The graph shows absolute conductance. Since $G_{AHP}$ is independent of voltage, it is not included in this graph. $G_m$ (from $R_m$) is summed over the whole neuron, while the active conductances only exist in the soma. $G_{Na}$ and $G_{DR}$ attain very large values above threshold (truncated in graph). Their maximum steady state conductances are 100 nS and 1480 nS, respectively.

---

the particle time constants did not depend on voltage[1]. The active currents had the following form:

$$I_x = G_{max,x} \cdot f_{active,x} \cdot (V - E_{rev,x}),$$

where $x$ stands for one of the eight conductances (e.g., $G_{Na}$), $f_{active}$ is the fraction of channels that are open, and $E_{rev}$ is the reversal potential of the ionic species.

$f_{active}$ has the form $f_{active} = m^a h^b$, where the so-called *gating particles* $m$ and $h$ obey first-order dynamic equations:

[1]See section 2.3.4 for a discussion of this assumption.

$$\frac{dm}{dt} = \frac{m_{ss} - m}{\tau}.$$

The steady state values $m_{ss}$ and $h_{ss}$ are sigmoids of the form

$$m_{ss} = \frac{1}{1 + e^{(V_{1/2} - V)/K}}.$$

where $V_{1/2}$ is the half-activation voltage, and the slope factor $K$ gives the steepness of the sigmoid, such that a small $K$ implies a steep curve. The parameters for the conductances are listed in Table 2.2. Where two values are given, the first refers to the $m$ (activation) particle and the second to the $h$ (inactivation) particle.

The steady state activation curves are shown in Fig. 2.3.

### Special case: Anomalous rectifier $G_{AR}$

The anomalous rectifier has no activation particle, but two inactivation particles with different time constants:

$$f_{active,AR} = 0.8 \cdot h_1 + 0.2 \cdot h_2,$$

$$\frac{dh_1}{dt} = \frac{h_{ss,1} - h_1}{40},$$

$$\frac{dh_2}{dt} = \frac{h_{ss,2} - h_2}{300}.$$

### Special case: Calcium dependent conductance $G_{AHP}$

Calcium enters the cell when $G_{Ca}$ is active and is removed through various mechanisms (buffering, sequestering, and pumping). This is modeled with a leaky integrator:

$$\frac{d[\mathrm{Ca}^{2+}]}{dt} = \alpha G_{Ca} - \frac{[\mathrm{Ca}^{2+}]}{\tau_{Ca\ decay}},$$

| | $G_{Na}$ | $G_{DR}$ | $G_{Ca}$ | $G_{Na,p}$ | $G_{AHP}$ | $G_A$ | $G_M$ | $G_{AR}$ | $G_m$ |
|---|---|---|---|---|---|---|---|---|---|
| Ion | $Na^+$ | $K^+$ | $Ca^{2+}$ | $Na^+$ | $K^+$ | $K^+$ | $K^+$ | $K^+/Na^+$ | - |
| $f_{active}$ | $m^2h$ | $m^2$ | $m^2$ | $m^2$ | $m^2$ | $m^2h$ | $m$ | $0.8h_1 + 0.2h_2$ | - |
| $V_{1/2}$ (mV) | -40/-45 | -40 | -25 | -40 | - | -65/-60 | -55 | -82/-82 | - |
| $K$ | 3/-3 | 3 | 4 | 7 | - | 2/-4 | 10 | -7/-7 | - |
| $\tau$ (ms) | .05/.5 | 2 | 2 | 2 | 2 | 20/100 | 20 | 40/300 | - |
| $E_{rev}$ | 50 | -95 | 115 | 50 | -95 | -95 | -95 | -50 | -66 |
| $G_{max}$, P5$_{(mS/cm^2)}$ | 200 | 120 | 0.6 | 1 | 45 | 1 | 0.6 | 1 | 1 |
| $G_{max}$, P2$_{(mS/cm^2)}$ | 120 | 72 | 0.2 | 1 | 45 | 1 | 0.6 | 1 | - |

Table 2.2: Parameters for one passive and eight active conductances. Where two values are given, the first refers to the m (activation) particle, or, in the case of $G_{AR}$, the first inactivation particle, $h_1$, and the second to the h (inactivation) particle.

---

where $\alpha = 10^{10}$ M/C and $\tau_{Ca\ decay} = 50ms$. The constant $\alpha$ depends on the volume in which the incoming calcium ions reside. Due to the slow pace of calcium diffusion within a cell, this volume is taken to be a thin shell just below the cell membrane. The effective shell thickness corresponding to the value of $\alpha$ that was chosen is 0.43 $\mu m$. Diffusion is not explicitly modeled.

The steady state value of $G_{AHP}$, in our model, does not depend on voltage but on calcium concentration, $[Ca^{2+}]$ as follows:

$$m_{ss} = \frac{[Ca^{2+}]}{[Ca^{2+}] + 0.00004}$$

This is a sigmoidal function with half-activation occurring at $[Ca^{2+}] = 40\mu$M.

### Special case: $G_A$ de-inactivation

$G_A$ activates and inactivates slowly during depolarization, but de-inactivates rapidly upon hyperpolarization. Since no other time constants are voltage dependent in this model, we chose to model this fact by de-inactivating instantly upon spiking, i.e., $h = 1$, if $V > 0$.

### 2.2.5 Synaptic input

The cell receives 5000 synapses of four different types. Of these, 80% are excitatory, each activating either an AMPA conductance alone or in conjunction with a voltage dependent NMDA conductance, 10% are inhibitory $GABA_A$, and 10% are inhibitory $GABA_B$ synapses.

#### Time course of conductance change

Synaptic inputs were modeled with a conductance directly onto the soma or dendrite. The current flow through the synapse is given by:

$$I(t) = G(V,t) \cdot (V(t) - E_{rev}).$$

For the non-NMDA types, the conductance was shaped like an alpha function:

$$G(t) = \frac{G_{syn}e}{t_{peak}} \cdot t\, e^{-\frac{t}{t_{peak}}}.$$

The function peaks at $G_{syn}$ for $t = t_{peak}$.

The NMDA synapse depends not only on time but also on voltage:

$$G(V,t) = 1.05 \cdot G_{syn} \cdot \frac{e^{-t/\tau_1} - e^{-t/\tau_2}}{1 + \eta \cdot [Mg^{2+}] \cdot e^{-\gamma V}},$$

where $\tau_1 = 80\ msec$, $\tau_2 = 0.67\ msec$, $\eta = 0.33\ mM^{-1}$, $[Mg^{2+}] = 1\ mM$, $\gamma = 0.06\ mV^{-1}$. The voltage- and time-dependences are separable.

The time courses for the four synapses are graphed in Fig. 2.4(a). The voltage dependence of the NMDA synapse is graphed in Fig. 2.4(b).

#### Distribution of synapses across the cell

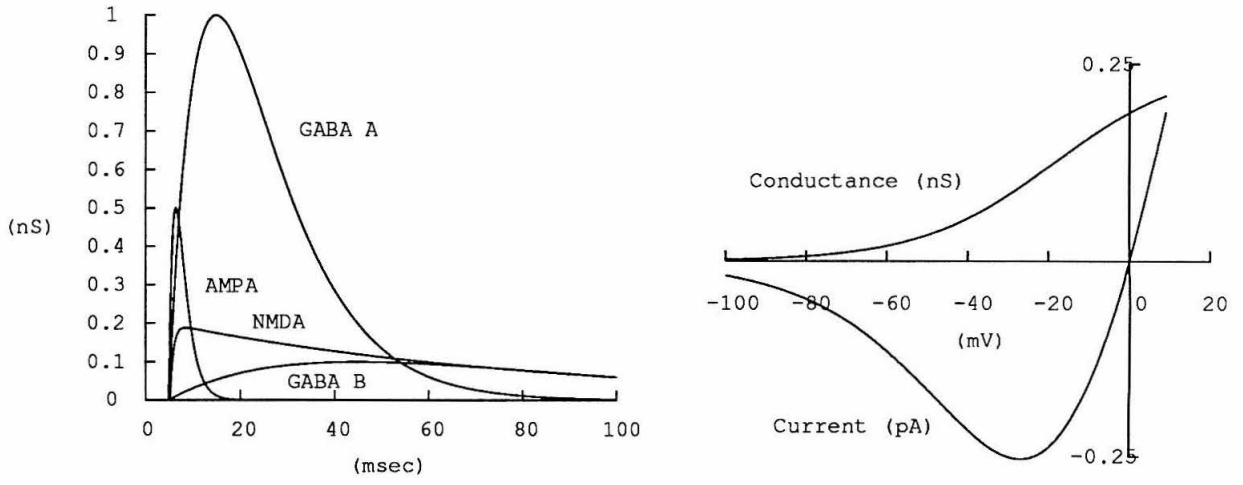


Figure 2.4: **(a)** Time courses of four types of synaptic conductances. Three of the conductances are alpha functions: AMPA excitatory (fast), $GABA_A$ (medium), and $GABA_B$ (slow). The fourth one is the NMDA conductance, which is voltage dependent, and is shown for large $V_m$ (no $Mg^{2+}$ block). **(b)** Voltage dependence of the peak NMDA conductance. Both the absolute conductance and the I-V relationship, $I = G(V - E_{rev})$, are shown.

The synapses are not distributed uniformly across the cell membrane; rather the synapse density varies with distance from the soma. For excitatory inputs, the number of synapses per unit area as a function of distance was modeled as a hyperbolic tangent:

$$D(l) \propto \frac{1}{2} + \frac{1}{2} \cdot \tanh \frac{l - 40}{22.73}, \tag{2.1}$$

where $l$ is the distance to the soma in $\mu m$. This function ranges between 0 and 1. Its midpoint is at $l = 40$ $\mu m$, and it takes on the values 0.1 and 0.9 at $l = 15$ and $l = 65$ $\mu m$, respectively.

For inhibitory inputs we chose the gamma distribution to model the number of synapses as a function of distance from the soma. The gamma distribution has the form:

$$D_{\alpha,l_{peak}}(l) = \frac{l^{\alpha-1}\, e^{-l\nu}}{\nu^{-\alpha}\, \Gamma(\alpha)}, \quad \nu = \frac{\alpha - 1}{l_{peak}}.$$

$\alpha$ determines the sharpness of the distribution, which peaks at $l_{peak}$, except when $\alpha = 1$, in which case the distribution reduces to a decaying exponential. For $GABA_A$ we used $\alpha = 1$. For $GABA_B$ we used $\alpha = 2$. This distribution would rapidly approach zero, so in order to have some $GABA_B$ synapses distally, we added a constant term to this function, so that $D_{\alpha,l_{peak}}(\infty) = \frac{1}{10} \cdot D_{\alpha,l_{peak}}(l_{peak})$, or in other words, the peak is ten times larger than the asymptote.

The values for all parameters are listed in Table 2.3, and the three distributions are graphed in Fig. 2.5.

### Time-averaging of synaptic inputs

To simulate all 5,000 synapses individually slows the simulations by about an order of magnitude and introduces noise. Therefore, it was often convenient to adjust

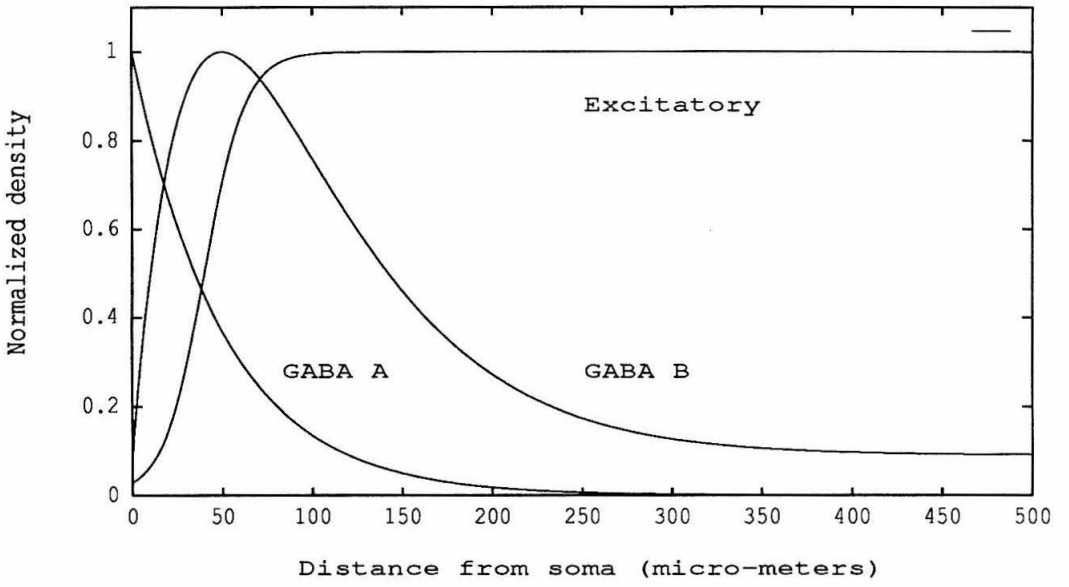


Figure 2.5: Distribution of synapses. The graphs show the (normalized) number of synapses per area of membrane, as a function of distance from the soma.

---

the passive leak in each segment to incorporate the average input to that segment. The following formulas were used to obtain the equivalent conductance and reversal potential:

$$G_{\text{m,eff}} = G_m + G_e + G_{ia} + G_{ib},$$

$$E_{eff} = \frac{G_m E_{leak} + G_e E_{rev,e} + G_{ia} E_{rev,ia} + G_{ib} E_{rev,ib}}{G_{\text{m,eff}}},$$

where $G_x$ are the average conductances, integrated from the time courses above. This yields for the non-NMDA synapses:

$$G_x = [\text{synapse density}] G_{syn} t_{peak} e f, \tag{2.2}$$

| | Number | $G_{syn}$ $(nS)$ | $t_{peak}, \tau_{1,2}$ $(msec)$ | $E_{rev}$ $(msec)$ | $\alpha$ | $l_{peak}$ $(\mu m)$ |
|---|---|---|---|---|---|---|
| Excitatory, AMPA | 4000 | 0.5/0.25 | 1.5 | 0 | - | - |
| Excitatory, NMDA | 4000 | 0.5/0.25 | 40/0.33 | 0 | - | - |
| Inhibitory, $GABA_A$ | 500 | 1.0 | 10 | -70 | 1 | 50 |
| Inhibitory, $GABA_B$ | 500 | 0.1 | 40 | -95 | 2 | 50 |

Table 2.3: Form and distribution of synapses. For AMPA and NMDA synapses, two values are given for $G_{syn}$. The larger value is used when only one type of synapse was present and the smaller value, when the synapses were co-activated.

---

where $f$ is the average presynaptic input frequency. The time-averaged NMDA synapse yields a voltage dependent conductance:

$$G_{ave}(V) = [\text{synapse density}]1.05 \cdot G_{syn} \cdot f \cdot \frac{\tau_1 - \tau_2}{1 + \eta \cdot [Mg^{2+}] \cdot e^{-\gamma V}} \qquad (2.3)$$

Note that each compartment will have different $G_{\text{m,eff}}$ and $E_{eff}$ because of the non-uniform distribution of synapses. For 1 Hz background input, $R_{\text{m,eff}} = \frac{1}{G_{\text{m,eff}}}$ varied between 6 k$\Omega cm^2$ and 35 k$\Omega cm^2$ and $E_{eff}$ between -71 and -30 mV.

This approximation obviates the need to average over many voltage traces and simplifies the investigation of certain properties of the cell, such as $R_{in}$, $\tau_m$, attenuation factors, and post-synaptic potentials, and also was used for generating discharge curves. The only time we saw a clear difference from this simplification was at very low (threshold) firing frequencies (e.g., spontaneous activity), when the simplified version exhibited a more regular firing pattern and occasionally fewer spikes.

### Adjusting for spines

As we saw previously, the total area for P5 is approximately 54,000 $\mu m^2$. This ignores spines. If we assume that each one of the 4000 excitatory synapses ends on a spine

of area 1 $\mu m^2$ this adds another 4,000 $\mu m^2$, or about 7.5%.

Stratford et al. [Stratford et al., 1989] show how the spine membrane can be absorbed into the dendrites, by adjusting their lengths and diameters, while preserving the total area, input resistance, axial resistance and electrotonic length. They used the following transformation:

$$F = \frac{Area_{dendrite} + Area_{spines}}{Area_{dendrite}},$$

$$l_{new} = l_{old} \cdot F^{\frac{2}{3}},$$

$$diam_{new} = diam_{old} \cdot F^{\frac{1}{3}}.$$

For the layer V cell in our simulations, F is approximately 1.075, and hence length and diameter would be adjusted by 5% and 2.5% respectively, less than the estimated measurement error. These small adjustments have little impact on the qualitative behavior of the cell, but were still included in the model.

### 2.2.6 Computer simulations

Simulations were performed on SPARC 2 and SPARC 10 workstations, manufactured by Sun Microsystems, with the simulator NEURON, developed by Mike Hines [Hines, 1989]. The simulator uses an implicit Euler integration scheme that is first order in time, second order in space, and stable under all conditions. Compartment size was chosen so as to ensure that no compartment had an electrotonic length larger than 0.1 $\lambda$ (space constant). The time step $dt$ was made small enough to ensure convergence. This often required a time step as small as 10–20 $\mu sec$, though for certain steady state properties, such as $R_{in}$, the stability of the integration scheme allowed

for arbitrarily large time steps. A typical 1 *sec* simulation with $dt = 20$ $\mu sec$ and 400 compartments took about 6 minutes on a SPARC 10 workstation. For a discussion of compartmental modeling, see, e.g., Segev et al. [Segev et al., 1989].

## 2.3 Discussion of parameter choices

### 2.3.1 Morphology

Two cells in striate cortex were filled with HRP during *in vivo* experiments in anesthetized adult cats [Douglas et al., 1991]. See Fig. 2.1. One cell was a layer V pyramidal cell and the other cell was a layer II/III spiny stellate cell with two apical dendrites, a subtype referred to as a modified superficial pyramid [O'Leary, 1941, Larkman, 1991a]. The 3-D coordinates and diameters of the dendritic tree were measured by a computer-assisted method, and each branch was replaced by a single equivalent cylinder.

How typical are these two neurons on which we perform most of our simulations? Larkman [Larkman, 1991a] has studied 39 HRP-injected pyramids from rat visual cortex using a light microscope. He catalogued a long series of morphological data for these neurons, and in Table 2.4 we compare his findings to our two neurons. Larkman divided the neurons into three classes, and in the table we give the average for these classes, without weighing them according to the number of cells from each class. Sometimes only a single neuron was shown from each class, in which case we use that value without knowing if it was an "average" cell.

Comparing our cells with Larkman's, we find in general that our cells are larger, branch more profusely, and have fewer spines. The membrane area for the layer II/III cell is about average for the whole population, but large for a layer II/III cell (average area 12,700 $\mu m^2$). The layer V cell is twice as large as Larkman's thick

| | Larkman [Larkman, 1991a] | Layer V | Layer II/III |
|---|---|---|---|
| Number basal dendrites | 4.8 (3–9) | 10 | 2 |
| Number apical dendrites | 1 | 1 | 2 |
| Number basal tips | 30 | 45 | 18 |
| Path length to basal tips ($\mu m$) | 161 | 227 | 182 |
| Terminal branch diameter, basal ($\mu m$) | 0.7 | 0.87 | 0.56 |
| Terminal branch diameter, apical ($\mu m$) | 0.45 | 0.37 | 0.54 |
| Total dendritic length ($mm$) | 7.1 | 17.7 | 8.3 |
| Total membrane area ($\mu m^2$) | 18,400 | 53,600 | 19,700 |
| Number of spines per neuron | 10,500 | 4,000 | 2,000 |

Table 2.4: Morphological comparison of simulated neurons to a study by Larkman [Larkman, 1991a]. Values are averages, except for ranges which are given in parentheses.

layer V cells (average area 26,200 $\mu m^2$). The same thing holds for total dendritic lengths. Furthermore, the number of basal dendrites is ten for our layer V cell, while Larkman finds none with more than nine among 39 cells. Similarly, the number of basal tips is 50–80% higher, and the average path length (distance from soma) to basal tips is 40–60% higher. The diameters of terminal branches are fairly close. There is some variation, but Larkman points out that the measured diameters for small-diameter branches are quite error-prone. Note that Larkman made no correction for tissue shrinkage or "wiggles," which may underestimate the dendritic lengths by 20% [Desmond and Levy, 1982]. See section 2.3.5 (*Spine size and numbers*) for a discussion of the discrepancy in spine numbers.

Larkman points out that most of the branching of basal dendrites occurs close to the soma and that the terminal segments account for most of the dendritic membrane. This is true of our neurons as well.

The neurons had axons of approximately 1 $\mu m$ diameter. The effect of these axons was ignored. The first reason for ignoring the axon was that we were only interested

in the behavior of the dendrites and the soma, which is where synaptic integration takes place. We consider the axon merely to be an output medium that connects to other cells, and it was not the subject of this study.

However, because the axon is electrically coupled to the soma, it does have an effect on it. The input resistance is decreased by 2.5% if an axon is added to a passive cell, assuming a uniform $R_m$ of 10 k$\Omega cm^2$. During action potentials, the addition of an (active) axon will increase the spiking frequency in a way very similar to what is obtained if we increase $G_{max,NA}$ and $G_{max,DR}$ in an axon-less soma. These effects of the axon thus can be absorbed easily into the soma itself. A recent review paper on model development also argues that the axon can be ignored [Rall et al., 1992].

When modeling realistic neurons, it is common to collapse the dendritic tree into one or a few compartments to make computations tractable [Stratford et al., 1989, Wilson and Bower, 1989, Bush and Sejnowski, 1992]. While this simplification saves simulation time, it is likely to be inadequate when studying the properties of single neurons. Dendritic trees will shape the profile of EPSPs and delay and attenuate them to a degree dependent on the exact location of the synapse. Due to the high input resistance of many dendrites, it has been predicted that local processing may occur, such as saturation and clustering [Mel, 1992]. A model like ours is ideally suited to study these effects.

### 2.3.2 Passive membrane properties – $R_m$, $C_m$, $R_i$

MEMBRANE CAPACITANCE, $C_m$

The generally accepted value for $C_m$ is close to 1 $\mu F/cm^2$ [Jack et al., 1975, Kuffler et al., 1984, Kandel and Schwartz, 1985, Shelton, 1985]. For a pure lipid bi-

layer $C_m$ has been measured to 0.8 $\mu F/cm^2$ [Hille, 1984].

Major et al. [Major et al., 1990] compare experimental impulse responses to those of a model and find the best fits for $C_m$ to be 0.6–0.7 $\mu F/cm^2$. However, morphological measurement errors are possible and to correct for tissue shrinkage and spine area is an error-prone procedure. Segev et al. [Segev et al., 1992] in similar simulations find a $C_m$ of 1.64 $\mu F/cm^2$ to give the best fit.

## AXIAL RESISTANCE, $R_i$

$R_i$ has traditionally been assumed to be in the range 50–100 $\Omega cm$ [Koch et al., 1982, Wilson and Bower, 1989, Zador et al., 1990, Koch et al., 1990, Lytton and Sejnowski, 1991]. The resistance of sea water is 20 $\Omega cm$, mammalian saline is 60 $\Omega cm$, and frog's Ringer's solution is 80 $\Omega cm$ [Hille, 1984]. This would be expected to set a lower bound on the true value of $R_i$ [Borg-Graham, 1987], since the cytoplasm contains many structures in addition to electrolyte, such as the cytoskeleton and various organelles. In Aplysia, Carpenter et al. reported an axoplasmic $R_i$ equal that of sea water (20 $\Omega cm$) and a cytoplasmic $R_i$ — measured at the soma — of 200 $\Omega cm$ [Carpenter et al., 1971]. However, recent evidence suggests that the figure for central neurons should be significantly larger. Shelton [Shelton, 1985] estimates $R_i$ = 225 $\Omega cm$. He uses computer simulations of a reconstructed cerebellar Purkinje cell to find good fits for current clamps, pulse attenuation and input resistance. Using smaller values for $R_i$ does not give accurate fits. Similarly, Stratford et al. [Stratford et al., 1989] estimate $R_i$ = 286–378 $\Omega cm$ for neocortical pyramids and Segev et al. [Segev et al., 1992] find a value of 250 $\Omega cm$ for cerebellar Purkinje cells. We set the value of $R_i$ to 200 $\Omega cm$.

## MEMBRANE RESISTANCE, $R_m$ and $R_m$

$R_m$ is defined as the non-synaptic, non-voltage-dependent resistance of a piece of membrane. The passive conductance that is left when all active conductances have been blocked is often referred to as the membrane leak conductance, $G_m = 1/R_m$. The molecular correlate of this leak conductance is not precisely known. In saline solutions a pure phospholipid bilayer has a very high resistance, up to $10^{15}$ $\Omega cm^2$ [Hille, 1984] and oxidized cholesterol membranes measure $10^8$ $\Omega cm^2$ [Ehrenstein et al., 1970]. The much lower values recorded for $R_m$ in neurons could be due to imperfect blockade, electrode leak, or some voltage-independent "leak" channel.

The evidence for "leak" channels is scant. Patch-clamp studies of frog sympathetic neurons reveal a nearly-ohmic (linear) region between -70 and -110 mV [Jones, 1989]. The underlying current is insensitive to blockers that block other known currents of the cell. A large fraction is carried by $K^+$ and reverses at -65 mV (after adjusting for a 10 mV contribution from the electrogenic $Na^+/K^+$ pump). Muscarine evokes a slow EPSP in hippocampal CA1 pyramidal cells [Cole and Nicoll, 1984]. This EPSP appears to be due to the blockade of non-voltage-dependent $K^+$ channels that carry a significant current at rest [Madison et al., 1987].

Because $R_m$ cannot be measured directly, most reports discuss the experimentally attainable $R_{in}$ and $\tau_m$. For a single passive compartment (electrically compact cell), both $R_{in}$ and $\tau_m$ are directly proportional to $R_m$. For extended neurons this is not always the case for $R_{in}$, since electrotonically distant conductances contribute less to $R_{in}$ than proximal ones [Koch et al., 1990]. In our model of a passive layer V neuron with $R_m$=100 k$\Omega cm^2$ (a fairly compact neuron), 93% of the total conductance was visible[2]. This fraction dropped to 72% for $R_m$=10 k$\Omega cm^2$ and 37% for $R_m$=1 k$\Omega cm^2$.

[2]The measure of visibility used here was $\Gamma = \frac{G_{in}}{G_{tot}}$, where $G_{in}$ was the input conductance seen at the soma and $G_{tot}$ was the total membrane conductance, summed over the whole neuron. In the limiting case of a length constant of 0 $\lambda$, this ratio is 1.

$R_{in}$ and $\tau_m$ are good indicators of $R_m$, and the discussion below of $R_{in}$ and $\tau_m$ thus bears on this section.

Recent reports suggest that $R_m$ is high. Major et al. [Major et al., 1990] estimate $R_m$ to 100–600 k$\Omega cm^2$ by fitting experimental recordings to a computer model of a hippocampal pyramid. Shelton [Shelton, 1985] uses a computer model of a cerebellar Purkinje cell and estimates the dendritic $R_m$ to be 46 k$\Omega cm^2$. Segev et al. [Segev et al., 1992] find that $R_m$ = 110 k$\Omega cm^2$ gives the best fit. These reports are in contrast to previous estimates that give much lower values for $R_m$. Several reports on cat motoneurons give values in the range 0.5–4 k$\Omega cm^2$ [Barrett and Crill, 1974]. Consequently, most simulations of neurons in the past use $R_m$=2–20 k$\Omega cm^2$ [Koch et al., 1982, Yamada et al., 1989, Wilson and Bower, 1989, Koch et al., 1990, Traub et al., 1991, Lytton and Sejnowski, 1991]. As will be discussed in detail in chapter 5, the *effective* membrane resistance, $G_{\mathrm{m,eff}}$, may have a large synaptic contribution in addition to the non-synaptic $G_m$.

We used a reversal potential of -66 mV, which was the measured resting potential *in vivo*. At $f_b = 0.5\ Hz$, the simulated neuron had a resting potential of -65 mV.

## INPUT RESISTANCE, $R_{in}$

As discussed above, $R_{in}$ is not an independent parameter that we set in our simulations. It depends on the value of $R_m$ and the morphology of the neuron. For a passive neuron, $R_{in}$ always increases with $R_m$. Recent patch-clamp studies (where we reduce the risk of introducing a somatic shunt due to impalement) show very large values for $R_{in}$. For example, Andersen et al. [Andersen et al., 1990] find values of 500–1000 $M\Omega$ for hippocampal CA1 pyramids and 700–2000 $M\Omega$ for dentate granule cells. In another study, Spruston and Johnston [Spruston and Johnston, 1992] using perforated patch-clamps, find $R_{in}$ ranging from 100–450 M$\Omega$. These values are three

to ten times larger than the values found in three other studies that used intracellular electrodes. Note that active conductances were not blocked. When applying $Cs^+$ (a $K^+$ current blocker) to the bath and clamping the potential to other values, $R_{in}$ could increase by up to 100%.

In our model, the layer V cell had an input resistance of 53 M$\Omega$ when there was no synaptic activity. When all active conductances were blocked, $R_{in}$ increased to 190 M$\Omega$. When synapses were activated at a very low "background" rate of 0.5 $Hz$, $R_{in}$ decreased to 20 M$\Omega$. In the layer II cell, these values were 80, 500, and 49 M$\Omega$, respectively.

TIME CONSTANT, $\tau_m$

The time constant $\tau_m$ of a cell is also indicative of $R_m$. For a passive cell with uniform $R_m$, $R_m = \tau_m / C_m$. For $\tau_m = 100$ $msec$, this gives $R_m = 100$ k$\Omega cm^2$.

Anderson et al. found time constants ranging from 50–140 $msec$ in the Hippocampus [Andersen et al., 1990]. Spruston and Johnston found time constants in the range of 28–66 $msec$ when active conductances were not blocked. These values are two to four times larger than three other studies using intracellular electrodes. When using $Cs^+$ to block some conductances and depolarizing the membrane, time constants as large as 155 $msec$ were recorded.

### 2.3.3 Active membrane conductances: Dendrites

So far the only voltage dependent conductance that we have put in the dendrites is NMDA. This is partly to simplify and speed up simulations and partly because it is difficult to find good estimates for parameters associated with other active conductances. There is, however, much recent evidence for active conductances in dendrites of central

neurons. Pockberger recorded directly from the dendrites of rat neocortical pyramids [Pockberger, 1991]. At distances of more than 300 $\mu m$ from the soma, dendrites displayed fast spikes followed by slow afterdepolarizations, presumably mediated by a low-threshold $Ca^{2+}$-conductance. Amitai et al. [Amitai et al., 1993] record very similar potentials and conclude from a simulation study that the early fast spike is likely a passive artifact of a somatic spike, while the slow afterdepolarization probably is due to dendritic calcium channels, since it is TTX-resistant and resembles confirmed $Ca^{2+}$ spikes in hippocampus and cerebellum. Thomson et al. [Thomson et al., 1988] compared the decay of EPSPs to that of injected current pulses. In several cases the EPSP decay would be much slower, indicating active channels in the dendrites. Williams and Johnston [Williams and Johnston, 1991] similarly compared EPSPs to injected currents shaped like alpha functions. The EPSPs decayed much more slowly (up to 135 $msec$) and showed a strong voltage dependence, while the alpha currents showed faster decay and little voltage dependence. They conjecture that this is due to dendritic calcium or sodium channels, since potassium currents should be blocked by intracellular cesium, and APV, an NMDA blocker, had little effect. The issue of active dendritic conductances will be further discussed in chapter 6.

Simulations suggest that many dendrites are electrotonically compact in the absence of background firing, especially basal dendrites and proximal apical dendrites [Shelton, 1985, Bush and Sejnowski, 1992, confirmed in our simulations]. Compactness implies that the voltage attenuation from the soma to the dendrites is small and that most of the charge injected into a dendrite will reach the soma. However, the voltage attenuation *from* the dendrite *to* the soma can often be large, due to high dendritic input resistance, $R_{in,dend}$ [Zador et al., 1991, e.g.]. Large depolarizations can therefore be highly localized [Rinzel and Rall, 1974]. These local changes in membrane potential can support interesting non-linear computations, such as sublinear addition (OR-like saturation) for a passive dendrite, superlinear (AND-like) summation for an

active dendrite [Mel, 1992, Bush and Sejnowski, 1992], and even an XOR-like non-monotonic dependence of output frequency on input strength [Zador et al., 1992].

### 2.3.4 Active membrane conductances: Soma

Our model uses eight active conductances restricted to the soma. All eight somatic conductances have been observed in pyramidal cells [Stafstrom et al., 1985, Spain et al., 1987, Schwindt et al., 1988, Spain et al., 1991, McCormick, 1992, Schwindt et al., 1992]. Unfortunately, there is little detailed information about exact channel kinetics (steady state activation and time constant), density, and distribution throughout the cell. Parameters for the kinetics were based on data for neocortical cells when possible, but data from other cells (hippocampal and sympathetic ganglial) was also used. These parameters, as well as channel densities, were modified to produce desired behavior as will be discussed below for each channel separately. This is the approach taken by other investigators as well [Lytton and Sejnowski, 1991, Bhalla and Bower, 1993, De Schutter and Bower, 1993].

In general, we use voltage-independent time constants, and the steady state activation[3] is of the form:

$$m_{ss} = \frac{1}{1 + e^{(V_{1/2} - V)/K}}.$$

VOLTAGE-INDEPENDENCE OF TIME CONSTANTS

[3] A note on fitting data with sigmoids: Instead of using a single particle, $m$, a higher power is often used, usually $m^2$. $m$ and $m^2$ have very similar forms. In fact, if $G(V)$ is fit by a single $m$ with half-activation $V_{1/2}$ and slope factor $K$, it also can be fit by $m^2$ with half-activation $V_{1/2} + K \cdot \ln(\sqrt{2}-1) \cong V_{1/2} - 0.88 \cdot K$ and slope factor $2 \cdot (\sqrt{2}-1) \cdot \sqrt{2} \cdot K \cong 1.172 \cdot K$, conserving the half-activation voltage and slope at that point.

We have chosen to model the time constants as being independent of voltage. This has the advantage of simplifying fine-tuning of the conductance parameters. In addition very little data exists on the voltage dependence of the time constant; $G_{AR}$, which is the best described conductance for neocortical neurons, turns out to have practically voltage-independent time constants! Similarly, the activation and inactivation time constants of a transient potassium channel in Betz cells showed no voltage dependence in the voltage ranges studied [Spain et al., 1991]. The same held true for an A-like conductance in hippocampal and spinal neurons [Segal et al., 1984].

## TEMPERATURE DEPENDENCE

While the steady state activation and inactivation curves show little temperature dependence, time constants often do. The time course speeds up with a factor $Q_{10}$ for every 10°C. Even though $Q_{10}$ has been shown to vary, it often is close to 3 [Hodgkin and Huxley, 1952, Borg-Graham, 1987], which is the value we have used below, whenever an experiment was not carried out at 37°C.

## ARE REVERSAL POTENTIALS CONSTANT?

The reversal potential for a channel that is permeable to a single ionic species, $X$, can be calculated from the Nernst equation:

$$E_{rev} = \frac{RT}{zF} \ln \frac{[X]_o}{[X]_i},$$

which generalizes to the Goldman-Hodgkin-Katz equation for multiple ions (here: potassium, sodium, and chloride):

$$E_{rev} = \frac{RT}{F} \ln \frac{p_K[K^+]_o + p_{Na}[Na^+]_o + p_{Cl}[Cl^-]_i}{p_K[K^+]_i + p_{Na}[Na^+]_i + p_{Cl}[Cl^-]_o},$$

where $p_K$, $p_{Na}$, and $p_{Cl}$ are the permeabilities of the three ions. The reversal potential depends on both intra- and extra-cellular ion concentrations and will change due to current flow and ion accumulation. Most obvious is the case of intracellular calcium, the concentration of which may transiently change over two orders of magnitude and cause a 50 $mV$ reduction in driving potential [Yamada et al., 1989]. Also, potassium ions may accumulate transiently in the extracellular space, leading to changes in $E_K$ of 5–10 $mV$ during action potentials.

Since these changes will be very brief, we chose to ignore them for simplicity. The main effect of ignoring this temporary shift in $E_{rev}$ during action potentials will be that the delayed rectifier, $G_{DR}$, and the calcium conductance, $G_{Ca}$, will deliver somewhat more current. Since the magnitudes of both these conductances have been set somewhat arbitrarily with the goal of obtaining realistic action potentials and spike frequency adaptation, there is no need for second-order adjustments.

Extracellular current flow can be important under special circumstances. Synchronized activity has been detected in hippocampal slices where all synaptic transmission was blocked. Traub et al. [Traub et al., 1985] have shown how this coupling can be generated via extracellular field potentials. However, extracellular currents are unlikely to have a qualitative effect on most simulations.

### Detailed kinetics

SODIUM: Transient, $G_{Na}$

This conductance underlies the regenerative phase of action potentials. The pa-

rameters were modified from Frankenhaeuser and Huxley (FH) [1964], so as to yield action potentials with a threshold of approximately -50 $mV$ and a width at half amplitude of about 1 $msec$ [Hirsch and Gilbert, 1991].

While the $Q_{10}$-adjusted FH $m$ and $h$ particles had time constants in the ranges 0.0–0.2 $msec$ and 0.0–0.8 $msec$, respectively, we chose 0.05 and 0.5 $msec$. The steady state curves were made steeper by changing $K$ from 10 and -4.5 $mV$ to 3 and -3 $mV$, yielding a sharper threshold. The midpoints were shifted from -36 and -63 $mV$ to -40 and -45 $mV$. An example of an action potential is given in Fig. 2.6(a).

SODIUM: Persistent, $G_{Na,p}$

We used two activation particles, $m^2$, but no inactivation particle. $m$ had $V_{1/2}$ = -40 $mV$, $K$ = 7 $mV$, and $G_{max}$ = 1 $mS/cm^2$. Half-activation for $m^2$ was hence -34 $mV$. The time constant was 2 $msec$. The parameters are based on two studies of the persistent sodium conductance.

French et al. [French et al., 1990] studied slices and dissociated CA1 pyramids from rat and guinea-pig hippocampus. They found a TTX-sensitive, cadmium-insensitive current that partially inactivated (by 40%) very slowly. They found a $K$ ranging from 5 to 9 $mV$ and a $V_{1/2}$ close to -50 $mV$. Our value for $K$ is in the middle of the range found, while our $V_{1/2}$ is 15 $mV$ higher. The absolute conductance average 7.8 nS in slice and 4.4 nS in dissociated cells. Since dissociated cells lose most of their non-somatic membrane (average total area was 940 $\mu m$), this suggests that most of the conductance is concentrated at or proximal to the soma. 7.8 nS would translate to a density of 0.64 $mS/cm^2$ for our layer V cell.

Stafstrom et al. [Stafstrom et al., 1985] studied layer V pyramids in slices of cat sensorimotor cortex. They found a persistent sodium current, but did not measure detailed kinetics. They did find, however, that full activation was achieved within 2–

4 $msec$ at 37° $C$. With a time constant of 2 $msec$ in our model, we get 86% activation in 4 $msec$.

CALCIUM: High-threshold, L-type, $G_{Ca}$

The calcium conductance in our model carries very little current when the cell is not spiking. In cat sensorimotor cortex it is also apparently small; calcium spikes could be evoked ony after blockade of $Na^+$ spikes, $G_{Na,p}$, and $K^+$ conductances [Stafstrom et al., 1985]. Its main function is to introduce calcium into the cytoplasm, which in turn activates a $Ca^{2+}$ dependent $K^+$ conductance, $G_{AHP}$. Other purported roles for calcium include burst generation [Johnston et al., 1980, Brown and Griffith, 1983, Baxter and Byrne, 1991, McCormick et al., 1992], control of transmitter release [Smith and Augustine, 1988], long-term plasticity [Zador et al., 1990, Turner et al., 1982], muscle contraction and regulation of the metabolic state of neurons via second-messengers [Rasmussen, 1986].

Fisher et al. [Fisher et al., 1990] studied CA1 and CA3 pyramids in slices of guinea-pig hippocampus, using patch-clamp electrodes. They found three calcium channels which they call small-, medium-, and large-conductance channels. They point out that they resemble in their characteristics the T-, N-, and L-type of conductances described in cultured chick sensory neurons [Fox et al., 1987]. They found half-activation values of approximately -18, -2, and 17 $mV$. Because of the ionic composition of the bathing solutions, these values are expected to shift by 10–20 $mV$ to the left (in the hyperpolarizing direction) during more physiological conditions. They also found slope factors $K$ ranging from 4.3 to 7.2, from 6.3 to 7.7, and 4.7 $mV$, respectively. The three conductances showed fast, variable, and no inactivation, respectively.

Our $Ca^{2+}$ current most resembles the third of these current, the L-type, or large-

conductance, current with a high threshold and no inactivation.

Since the main motivation for introducing $G_{Ca}$ is to cause the cell to adapt, there was no need to explicitly model diffusion, buffering, sequestering and pumping. Instead we lumped all these mechanisms into a leaky integrator that was confined to the soma only. If $G_{Ca}$ were present in the dendrites, diffusion might, under certain circumstances, become important. The time constant was set to yield adaptation within about 50 *msec*.

POTASSIUM: Delayed rectifier, $G_{DR}$

This conductance underlies the repolarization phase of action potentials. The parameters were modified from Frankenhaeuser and Huxley [1964] (FH), who studied toad myelinated fiber in *Xenopus Laevis*.

While the $Q_{10}$-adjusted FH $n$ particle had time constants in the range 0.0–0.5 *msec*, we chose 2 *msec*. The steady state curve was made steeper by changing $K$ from 8 $mV$ to 3 $mV$. The midpoint was kept at -40 $mV$.

POTASSIUM: Slowly activating and inactivating, A-type, $G_A$

The $A$ current was first described in Onchidium [Hagiwara et al., 1961], but two $A$-like currents have been reported in cat sensorimotor cortex [Spain et al., 1991].

The $A$ conductance in our model activates slowly ($\tau = 20$ *msec*) and inactivates even more slowly ($\tau = 100$ *msec*). For just-threshold currents, it will thus delay spike generation. In this way the neuron can be made to fire at very low output frequencies [Connor and Stevens, 1971]. Norepinephrine has been shown to reduce this current [McCormick, 1990].

Segal and Barker [Segal and Barker, 1984] studied rat hippocampal neurons in

culture. They describe an A-like current that reaches its peak in 3–6 *msec* (1–2 *msec* with $Q_{10}$ adjustment) and inactivates with a time constant of 20–24 *msec* (4–8 *msec* with $Q_{10}$ adjustment). It de-inactivates rapidly upon hyperpolarization. Half-activation was at approximately -30 $mV$ and half-inactivation at about -70 $mV$. In visual cortex there is evidence of a considerably slower $G_A$. In response to depolarizing current steps, these cells often show a sag and a subsequent recovery from sag, consistent with a slow $G_A$ (unpublished observations).

POTASSIUM: Slowly activating, M-type, $G_M$

The $M$ conductance we used is a modified version of that described for bullfrog sympathetic ganglion cells [Yamada et al., 1989]. The midpoint was shifted from -35 to -55 $mV$, and for the time constant, the $Q_{10}$-adjusted value over the normal range of operation, 20 *msec*, was used.

The $M$ conductance activates slowly during depolarization, providing negative feedback to keep $V_m$ closer to $V_{rest}$. Since it activates slowly it can contribute to spike frequency adaptation. The $M$ current gets its name from muscarine, since $G_M$ is reduced by activation of muscarinic cholinergic receptors [McCormick, 1990].

POTASSIUM: Calcium dependent, $G_{AHP}$

Neocortical pyramids usually show one of two distinct responses to current steps [McCormick et al., 1985]. *Regular-firing* cells initially fire at a high frequency, but then adapt and settle down at a much lower firing frequency, 10-20% of the initial frequency *in vitro* [Mason and Larkman, 1990] and approximately 40% *in vivo* [Anderson et al., 1993b]. Adaptation is complete within approximately 50 *msec* [Stafstrom et al., 1984, McCormick et al., 1985, Bush, 1989, Connors and Gutnick, 1990]. *Burst-*

*firing* cells respond with repetitive bursts of two to five spikes, sometimes changing to single-spiking after a few bursts [Connors and Gutnick, 1990]. Burst-firing cells can in some cases be converted to regular-firing cells by depolarization of the membrane in the thalamus and hyperpolarization in neocortex [McCormick et al., 1985, Baxter and Byrne, 1991]. In neocortex, a $Ca^{2+}$ dependent $K^+$ current in conjunction with a slow sodium current underlies bursting behavior [Baxter and Byrne, 1991]. Also, the $Ca^{2+}$ chelator BAPTA abolished a $Ca^{2+}$-dependent hyperpolarization in cat neocortex [Schwindt et al., 1992b]. $G_{AHP}$ is reduced by application of acetylcholine [McCormick, 1992].

The role of $G_{AHP}$ in our model, in conjunction with $G_{Ca}$, is to cause the cell to adapt. An example of an adapting spike train is shown in Fig. 2.6(b). $G_{AHP}$ has been shown to be influenced by several putative neurotransmitters, among them norepinephrine, acetylcholine, serotonin, and histamine [McCormick, 1990]. These neurotransmitters could control adaptation rate.

We model adaptation using a calcium dependent potassium conductance. The time it takes for the cell to adapt completely is approximately equal to the time constant of decay of internal calcium. The time constant of decay is 50 $msec$.

Lancaster et al. [Lancaster et al., 1991] studied hippocampal pyramids in culture with patch-clamp electrodes. They found two $Ca^{2+}$ dependent $K^+$ currents. One had a relatively small single-channel conductance (19 $pS$), showed some rectification on the single-channel level, was insensitive to sub-millimolar concentrations of TEA, had closed-times ranging from 0.5 to 5 $msec$, and did not inactivate. The second had a large single-channel conductance (220 $pS$), opened only at depolarized potentials, and was sensitive to TEA.

$G_{AHP}$ in our model resembles the first, small-conductance current, in that it is fast (depends on $[Ca]_i$ only and not on time), has no voltage dependence, and does not inactivate. We chose $G_{max}$ for $G_{AHP}$ and $G_{Ca}$ as well as the shell thickness $\alpha$ to yield

appropriate spike frequency adaptation. Even though 2 $Ca^{2+}$-dependent $K^+$-channels have been reported in neocortex [Schwindt et al., 1992a], only one was modeled, since one is sufficient to achieve spike-frequency adaptation.

MIXED: Anomalous rectifier, $G_{AR}$

While most conductances activate upon *de*polarization, several studies have found activation upon *hyper*polarization in many types of cells, including hippocampus and neocortex [Purpura et al., 1968, Spain et al., 1987]. This phenomenon has been called anomalous rectification, and when the reversal potential is positive to the resting potential, the voltage response to a current step will often display an overshoot and "sag."

Spain et al. [Spain et al., 1987] studied brain slices from cat sensorimotor cortex. They found such an anomalous rectifier with a reversal potential of -50 $mV$ (the channel was permeable to $Na^+$ and $K^+$, but not $Cl^-$). Half-inactivation was at -82 $mV$ and the slope factor, $K$, was -7. The conductance displayed two time constants, 40 and 300 $msec$, that showed no measurable dependence on voltage in the range -60 to -110 $mV$. These are the values we use in our simulation. For $G_{max}$ we chose a value of 1 $mS/cm^2$. This gives a 13–25% sag at $f_b = 0.5\ Hz$ and 15–22% at $f_b = 0\ Hz$. This is consistent with what has been observed in neocortical pyramids. For example, Mason and Larkman [Mason and Larkman, 1990] find sags from 0% to over 25%.

A similar current has been described for cultured hippocampal neurons [Segal and Barker, 1984], with the same midpoint, but different reversal potential (-75 – -80 $mV$). The $Q_{10}$-adjusted decay time was 30–80 $msec$.

Postulated roles for $G_{AR}$ include keeping the resting potential closer to threshold, pace-maker generation [DiFrancesco, 1987], rhythmic burst-firing in thalamic relay cells [Baxter and Byrne, 1991, McCormick et al., 1992], oscillations in stellate cells in

entorhinal cortex [Baxter and Byrne, 1991] as well as contributing towards spike repolarization, spike adaptation and afterhyperpolarization wave forms [Spain et al., 1987]. Similar currents have been found and given interesting names, such as $I_Q$ for queer, $I_h$ for hyperpolarization-activated, and $I_f$ for funny [McCormick, 1990].

Another role for $G_{AR}$ has been suggested by Wilson [Wilson, 1992]. Due to saturation effects in passive dendrites, EPSPs add *sub*-linearly, i.e., the first EPSP reduces the driving force for subsequent EPSPs. However, if $G_{AR}$ (with $E_{AR} < V_{rest}$) is present in the dendrite, this picture will change. As the first EPSP will cause $V_m$ to increase, the $G_{AR}$ conductance will decrease and shunt less of the synaptic current. Thus, while the driving force for the excitatory synapse decreases, $R_{in}$ may increase. The addition of EPSPs will be less sub-linear or even *super*-linear.

### 2.3.5 Synaptic input - time course, distribution, and spines

#### Excitatory AMPA (non-NMDA) input

The AMPA synapses in our model peak at $t_{peak} = 1.5\ msec$, have a peak conductance of $G_{syn} = 0.5\ nS$ and reverse at $V_m = 0\ mV$.

TIME COURSE

The synaptic conductance change is modeled with an alpha function:

$$G(t) = \frac{G_{syn}e}{t_{peak}} \cdot t\ e^{-\frac{t}{t_{peak}}}.$$

Williams and Johnston [1991] found that they could fit alpha functions very closely to recorded synaptic currents from proximal synapses.

$t_{peak}$ denotes the time-to-peak (or 0-100% rise time). The 10-90% rise time, $T_{10-90}$,

which is often the measured quantity, will be $0.57 \cdot t_{peak}$ or $t_{peak} = 1.75 \cdot T_{10-90}$. Hence $t_{peak}$ is nearly double the rise time.

Experimental data derive either from voltage-clamp experiments, in which case *currents* (EPSCs) are measured, or from non-clamped intracellular recordings, in which case *potentials* (EPSPs) are measured. These waveforms will differ.

For an *isopotential cell*, the EPSC waveform will exactly follow the conductance change, and hence it is straightforward to find $t_{peak}$ and check how well the data is fit by an alpha function. The EPSP waveform will lag the conductance change.

When the cell is *non-isopotential*, effective space-clamp is not possible, and distant synapses will give rise to EPSCs time courses that are slower than at source. We simulated excitatory synapses with $t_{peak} = 1.5\ msec$ at $f_b = 0$ and found EPSC $T_{10-90}$ of 0.85, 1.8, and 11.1 for inputs to the soma, halfway out on a basal dendrite and far out on a distal apical dendrite, respectively. Decay times were 1.7, 1.9, and 20 msec. Thus, for the soma, $G(t)$ is followed quite well. But for basal input there is some slowing of the rise time, while for the apical input the slowing is large.

Studying EPSPs, instead, the slowing is even more marked. Rise times ($T_{10-90}$) are 2.4, 4.1, and 21.7 msec, and decay times are approximately 30 $msec$ for all (due to the active currents, it is difficult to fit exponentials to the decay), and the membrane time constant will dominate instead of the synaptic time constant. Note, however, that with a lower $R_m$, and hence a lower $\tau_m$, the EPSP rise time will follow $G(t)$ much more closely. For example, at $f_b = 5\ Hz$ the EPSP rise time for a somatic synapse will be 1.5 $msec$.

The simulation studies are in good agreement with experimental data. Thomson et al. [Thomson et al., 1988] studied EPSPs in slices of rat cingulate and sensorimotor cortex. They found $T_{10-90}$ in the range of 1–5 $msec$. Since any distortion in an EPSP is likely to slow down the time course [Williams and Johnston, 1991], the lower end of this range (1 $msec$) should be considered. If the EPSP closely followed $G(t)$, we

find a $T_{10-90}$ close to 1 $msec$ and hence a $Tpeak$ of 2 $msec$. The time constants of these cells were quite small (7 $msec$ average) and thus the EPSP should be at most a factor 2 slower, yielding a $t_{peak} \geq 1$ $msec$.

Williams and Johnston [Williams and Johnston, 1991] studied EPSCs in slices of rat hippocampal CA3 pyramids. They found a similar range of $T_{10-90}$ of 1–3 $msec$ for mossy fiber input (which terminate proximal to the soma; the more distal commissural/associational inputs ranged from 2–5 $msec$). This gives a $t_{peak}$ of just under 2 $msec$.

Mason et al. [Mason et al., 1991] studied EPSPs in slices of rat visual cortex. They found $T_{10-90}$ ranging from 0.5–3 $msec$. Using 0.5 $msec$ rise times gives the fastest estimate so far, suggesting $t_{peak} \leq 1$ $msec$. However, only 3 out of 44 EPSPs showed $T_{10-90} < 0.8$.

In short, estimates range from less than 1 $msec$ to 2 $msec$, and so for the simulations 1.5 $msec$ was chosen.

## MAXIMUM SYNAPTIC CONDUCTANCE

We used a $G_{syn}$ of 0.5 $nS$. This produced EPSPs of amplitudes 0.1–0.3 $mV$ for proximal inputs, for $f_b$ ranging from 0 to 5 $Hz$.

Thomson et al. [Thomson et al., 1988] found EPSP amplitudes in the range of 0.08–2.3 $mV$, with an average of 0.4 $mV$ at $V_m = -70$ $mV$. The amplitudes did not seem to correlate with distance from the soma, as discerned from shape indices. Note that while these EPSPs arise from a single presynaptic cell, there may be more than one contact made. Hence the amplitude per synapse may be smaller than 0.4 $mV$.

Mason et al. [Mason et al., 1991] found EPSP amplitudes in a similar range of 0.05–2.08 $mV$ with a mean of 0.55 $mV$ at $V_m = -74$ $mV$. Larkman et al. [1990] found quantal EPSPs in rat hippocampal slice in the range of 0.075–0.18 $mV$.

The total charge injected by a somatic synapse at rest in the absence of synaptic background activity is 140 $fC$. Since the cell is quite compact under these circumstances, the charge injected by an *average* synapse will on the order of 100–120 $fC$, as measured by a somatic voltage clamp. In hippocampal slice, Bekkers and Stevens [1989] record "minis" with an average of about 120 $fC$ (estimated from their Fig. 3a), in very close agreement to our model.

## REVERSAL POTENTIAL

Williams and Johnston [Williams and Johnston, 1991] measured $E_{rev} = -2.8\ mV$ in hippocampal CA3 neurons. Several other studies [Finkel and Redman, 1983, Jahr and Stevens, 1987, Yakel et al., 1988] measured approximately 0 $mV$ in motoneurons and hippocampal cells.

## INPUT DISTRIBUTION

The density of spines is much reduced over the first 50–75 $\mu m$ of neocortical dendrites [Cauller and Connors, 1992]. We use an excitatory input distribution where the surface density of synapses varies as a tanh function of the distance from the soma. The midpoint is at $l$=40 $\mu m$, and the densities are 10% and 90% of maximum at $l$=15 and $l$=65 $\mu m$, respectively.

Larkman [Larkman, 1991b] found that proximal non-terminal branch segments have very few spines, while the long, terminal basal branches have a high density of spines. The terminal basal branches of our layer V pyramidal neuron start on average 41 $\mu m$ from the soma, and for the layer II/III pyramid, they start at 49 $\mu m$. Our distribution puts few spines on the intermediate segments, and an almost uniform distribution on the terminal segments. This almost uniform distribution is different

from the peaked distribution found in Larkman's study. The proximal end of terminal segments will have a density that is approximately 70% of the peak value. The peak occurs at approximately 40% of the distance from the proximal end. From there on the density decreases to about 55% at the tip of the dendrite. This distribution is somewhat tilted towards the proximal end, with a center-of-mass 42% of the distance from the proximal end (our calculations, using data from [Larkman, 1991b, figure 4C]).

## SPINE SIZE AND NUMBERS

For the two neurons, 4000 and 2000 excitatory inputs are simulated, respectively. We chose not to model spines explicitly for the following reasons. First, our own and other studies suggest that the voltage attenuation across the spine neck is less than 20% [Segev et al., 1992]. From the point of view of the dendritic voltage, a synaptic conductance change, $G_{syn}$, on a spine can be mimicked by $G'_{syn} = \frac{G_{syn}}{1+G_{syn} \cdot R_{neck}}$. We now believe that $G_{neck} = \frac{1}{R_{neck}} \gg G_{syn}$. Thus $G'_{syn} \cong G_{syn}$ within a few percent [Koch et al., 1992]. Second, the added membrane area is not very large. A spiny stellate cell from the same sample of neurons that ours were taken from was analyzed for spine size. Average spine area was 0.95 $\mu m^2$ [Anderson et al., 1993b], which would add less than 8% to the membrane area.

Other estimates of spine sizes vary. Holmes and Woody [Holmes and Woody, 1989] modeled Betz cells (motor cortex pyramids) in cat. Their model, based on several anatomical studies, used spine areas in the range 1.3–2.3 $\mu m^2$. In other parts of the brain, spine areas have been estimated to 1.5 $\mu m^2$ (neostriatum), 1 $\mu m^2$ [Coss, 1985, fish tectum] and 4.4 $\mu m^2$ [Woolf et al., 1991, mouse olfactory bulb]. Hippocampal spines have been modeled using a total area of 0.8 $\mu m^2$ [Zador et al., 1990].

Larkman [Larkman, 1991b] has estimated the number of spines on rat pyramids,

by counting the spines on some of the branches, correcting for obscured spines, and then extrapolating to the remaining branches. He finds a spine density of 0.5–0.6 spines/$\mu m^2$. However, we have found that there are marked difference in spine counts over various dendritic regions [Anderson et al., 1993a]. Using 0.5 and extrapolating to our two neurons, we would get 26,800 and 9,850 spines – many more than we use. Since Larkman did not correct for tissue shrinkage or "wiggle" factor, this number can be reduced by 20%. On the other hand, 15–50% of the excitatory inputs are not made onto spines but directly onto the dendritic shaft [Peters, 1987, Anderson et al., 1993b], which could more than cancel this correction factor. Other studies give similar spine counts for layer II/III neurons in rat: 9,000–10,300 [Thomas et al., 1980], 10,350–11,950 [Warren and Bedi, 1982], 10,350–15,320 [Warren and K.S., 1984], 7,590–11,070 [Bhide and Bedi, 1984], and 9,500 [Turner and Greenough, 1985].

Why do we count fewer spines? First, we used adult cats, while Larkman uses young rats. There may be a difference between species and with age. Absolute synaptic numbers come into play when we study effects of spontaneous background activity. The combined strength will depend on $f \cdot G_{syn} \cdot t_{peak} \cdot n$, where $n$ is the number of inputs. If $n$ has been underestimated, background effects will thus be even stronger than predicted. Also, we don't know what fraction of all the visible spines actually host active synapses. If this fraction is considerably less than 1, a smaller $n$ is appropriate.

### Excitatory NMDA input

Most parameters, including the waveform, were taken from the model by Zador et al. [Zador et al., 1990], who in turn based their model on unpublished data by Nobre, Xiang and Brown, as well as Stevens. The physiological concentration of $Mg^{2+}$ is approximately 1 $mM$ [Mayer and Westbrook, 1987, Jahr and Stevens, 1990].

The value for the maximum excitatory conductance was chosen so that when half of the AMPA synapses were replaced by the same number of NMDA synapses, the somatic depolarization was similar. The distribution of NMDA synapses was assumed to be identical to that of AMPA synapses.

### Inhibitory $GABA_A$ input

The $GABA_A$ synapses in our model peak at $t_{peak} = 10\ msec$, $G_{syn} = 1\ nS$ and reverse at $V_m = -70\ mV$.

Data for the time course of $GABA_A$ synapses is best described in hippocampus. There is much less data for neocortex, but a slower time course is suggested.

Rat CA1 neurons *in vitro* display a bicuculline-sensitive IPSP that peaks on average 17.4 *msec* after electrical stimulation of the stratum radiatum [LaCaille, 1991]. This includes a usually mono-synaptic delay of a few *msec* and the lag between peak conductance and peak PSP, as discussed above for AMPA excitatory synapses. This suggests a $t_{peak}$ of approximately 10 *msec*.

Electrical stimulation of neocortical afferents produce an IPSP in layer V/VI that peaks within 20-40 *msec* [Douglas and Martin, 1991]. Due to latencies and circuit effects, this is likely to be considerably slower than the underlying synaptic conductance change.

Studies of hippocampal cells suggest faster time courses. Fast IPSPs in guinea-pig CA3 pyramids have $t_{peak}$ ranging from 3 to 20 *msec* [Miles and Wong, 1984].

Faster still are IPSCs in hippocampal granule cells with rise times of about 1 *msec* [Busch and Sakmann, 1990, Edwards et al., 1990]. However, the decay is much slower and can be fit with 2 exponentials having time constants of 2 *msec* and 55–66 *msec*, giving a much larger time integral than an alpha function with $t_{peak} = 1\ msec$.

The reversal potential for the $GABA_A$ conductance has been estimated in the range -70 to -80 mV. Rat CA1 neurons *in vitro* display a bicuculline-sensitive IPSP

that reverses at $V_m = -73\ mV$ [LaCaille, 1991]. In guinea-pig CA3 pyramids *in vitro*, a fast picrotoxin-sensitive IPSP reverses between -73 and -80 $mV$ [Miles and Wong, 1984].

Estimates of the peak synaptic conductance vary considerably. Kriegstein and LoTorco [Kriegstein and LoTorco, 1990] made whole-cell and outside-out patch recordings from pyramidal cells in slices of rat neocortex. They found the average value for $G_{syn}$ for inhibitory synapses to be 0.457 nS. This is approximately half of the value we use.

A study of quantal IPSCs in hippocampus [Edwards et al., 1990] found quantal conductances of 0.4–1 $nS$, assuming a reversal potential of -70 $mV$.

Another study of unitary IPSPs in guinea-pig CA3 pyramids gives a much larger value of 6.7 $nS$ [Miles and Wong, 1984]. Note that even though the IPSPs were most likely due to input from a single pre-synaptic neuron, several synaptic contacts may have been made.

Activating all $GABA_A$ synapses at $G_{syn}$ causes a conductance increase of 350 $nS$. This provides an upper limit; indeed, electrical stimulation of afferent fibers evoked an early IPSP with a maximal 5–20 $nS$ conductance.

Inhibitory synapses can be found throughout the dendritic tree, but the highest densities are found at or close to the soma [Douglas and Martin, 1990]. $GABA_A$ receptors are mainly found close to the soma, while $GABA_B$ receptors are found more distally.

### Inhibitory $GABA_B$ input

The $GABA_B$ synapses in our model peak at $t_{peak} = 40\ msec$, $G_{syn} = 0.1\ nS$ and reverse at $V_m = -95\ mV$.

Focal application of the $GABA_B$-agonist baclofen induced an IPSP in neocortical pyramids that peaked after approximately 30 $msec$ [Connors et al., 1988].

Electrical stimulation of neocortical afferents produce a late IPSP in layer II/III that peaks within 80-140 *msec* [Douglas and Martin, 1991]. Due to latencies and circuit effects, this is likely to be considerably slower than the underlying synaptic conductance change. Nevertheless, the duration of the conductance change must be a factor 10-100 times greater than that of the AMPA conductance change.

In hippocampus, rat CA1 neurons *in vitro* display a phaclofen-sensitive IPSP that peaks on average 130.6 *msec* after electrical stimulation of the stratum radiatum [LaCaille, 1991].

The reversal potential appears to be in the range expected for a $K^+$ conductance. In neocortical pyramids, baclofen induced an IPSP that reversed at -90 mV [Connors et al., 1988]. In hippocampus, rat CA1 neurons *in vitro* displayed a phaclofen-sensitive IPSP that reversed at $V_m = -108\ mV$ [LaCaille, 1991].

A peak conductance of 0.1 nS was chosen. Saturating doses of baclofen induced a total conductance change of 12 $nS$ in rat layer II/III pyramids [Connors et al., 1988], while electrical stimulation of afferent fibers evoked a late IPSP with a maximal 5–20 $nS$ conductance. Activating all $GABA_B$ synapses in our layer II/III simulation yields 40 $nS$. This is more than twice as much, while our membrane area is only 55% larger than the average rat layer II/III pyramid [Larkman et al., 1990]. This is in reasonable agreement if we take into account that neither baclofen nor electrical stimulation is likely to achieve 100% activation of synapses.

For a discussion of the input distribution, see section above on $GABA_A$.

## 2.4 Model performance

How good is the model? In one sense, it can be claimed that the model is not good at all. Due to tissue shrinkage and measurement errors, morphological data for dendritic lengths and diameters may well be off by 20% [Desmond and Levy, 1982].

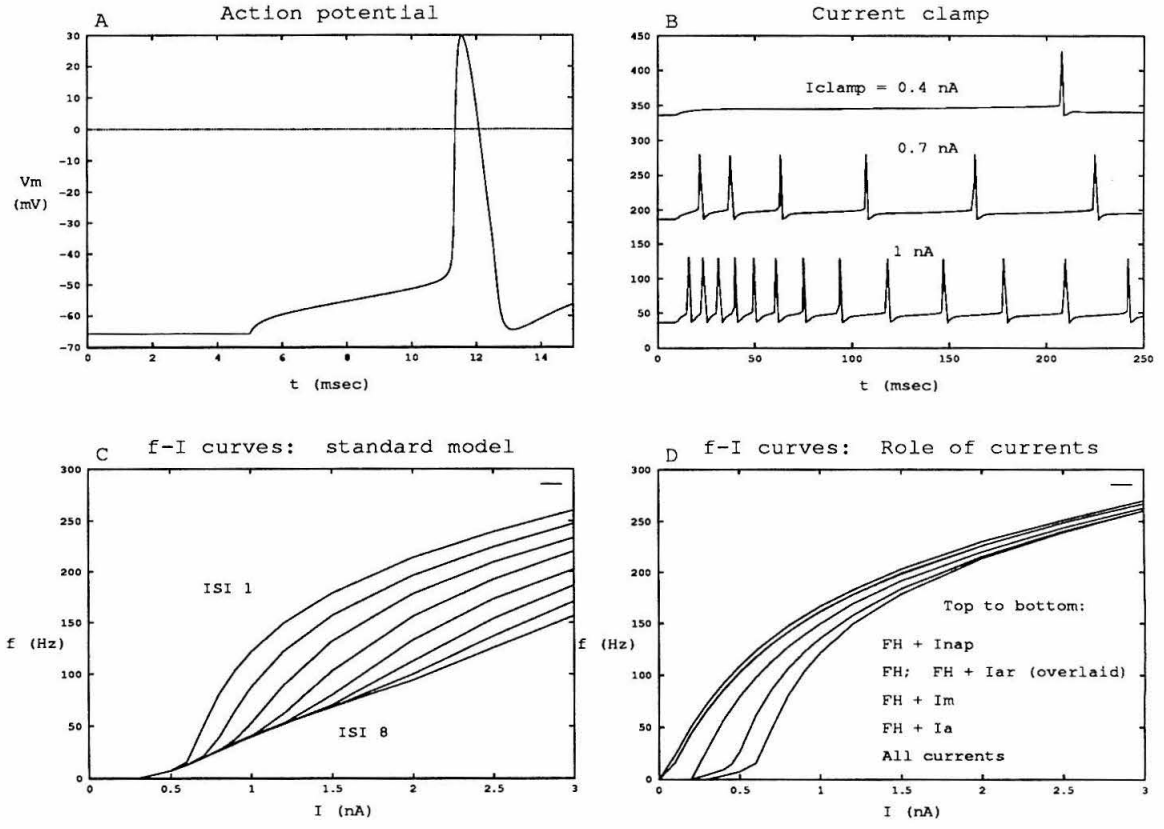


Figure 2.6: Action potential generation and discharge (f-I) curves. **(a)** Single action potential in response to a 1 $nA$ current clamp (at $t = 5$ $msec$). The width at half height is 0.9 $msec$. **(b)** Adapting trains of action potentials in response to current clamp of varying amplitude, as indicated in the figure. The adaptation is due to the $Ca^{2+}$ dependent $K^+$ conductance $G_{AHP}$. Adaptation is complete after about 50 $msec$ and the adapted frequency is about 30% of the initial frequency. **(c,d)** Starting at rest, current steps of various magnitudes were injected at the soma and the time of action potentials recorded. Instantaneous frequency is plotted. In (c) the full model was used. Leftmost curve corresponds to the first ISI (inter-spike interval) and the rightmost to the eighth ISI. In (d) only the first ISI is plotted and for each curve we used the two spike currents (FH) – $G_{Na}$ and $G_{DR}$ – either in isolation or together with one more current as indicated in the figure.

Estimates of basic passive parameters such as $R_m$ and $R_i$ vary by more than a factor 2, and the same holds for the time course and amplitude of synaptic conductance changes. Similarly, parameters for active conductances are not well known for cortical pyramidal cells, and so channel parameters from other cells were modified.

On the other hand, the model reproduces many aspects of neuronal behavior, such as realistic spikes and (adapting) spike trains, f-I curves, EPSPs, sag, input resistance, time constant, and resting potential (with and without background noise). There is a risk, of course, that another set of parameters would have produced identical results in all those cases, but something completely different for the predictions made in the remaining chapters of this thesis, and that some heretofore ignored characteristic of pyramidal cells will turn out to be crucial for the neuronal transfer function. This risk unfortunately is inherent in all simulations studies.

Nevertheless, weak spots often can be identified (such as the lack of active conductances in the dendrites). In each chapter, these weak spots are addressed, often by exploratory simulations of possible effects. The robustness of the model to changes in parameter values will be important for two reasons. First, if such robustness is evidenced, any predictions drawn from the model will be backed up more forcefully. Second, robustness is important for the credibility of any proposed neuronal mechanism, since cell-to-cell variability is often large, even within a given cell class.

Modeling choices were justified in detail in the previous section. In this section a few more examples will be given of the basic performance of the model as well as a discussion of the robustness to variations in model parameters.

### 2.4.1 Action potentials and discharge (f-I) curves

In response to current clamps larger than 0.3 $nA$ (rheobase), the cell fires repetitive action potentials. Action potentials in the model are of a highly stereotyped

form with little variation from spike to spike. One action potential is depicted in Fig. 2.6(a). The amplitude is about 80 $mV$ and the width at half-amplitude is 0.9 $msec$. For comparison, the average amplitude given in four studies of neocortical pyramidal cells *in vivo* and *in vitro* is 82 $mV$ while spike widths vary from 0.4 to 1.5 $msec$ [Bindman and Prince, 1983, Spain et al., 1990, Hirsch and Gilbert, 1991, Pockberger, 1991, Spain et al., 1991].

Fig. 2.6(b) shows the response on a longer time scale. The cell can be made to spike at arbitrarily low frequencies, but does not adapt in that regime (top trace) For larger currents the output spike rate adapts a factor 2–3 within about 50 $msec$. This is in accordance with experimental data, as discussed in section 2.3.4.

The discharge curves (or f-I curves) were also computed (Fig. 2.6(c)). The output frequency is plotted against the magnitude of a sustained current step applied at the soma (Fig. 2.6(c)). The frequency was computed from the inverse of the inter-spike interval (ISI), i.e., the time interval between two consecutive spikes. Since the spike rate adapts, a family of curves is obtained, one for each ISI. The curves show an initial, linear part that is shallow, known as the primary slope. It is followed by a steeper portion known as the secondary slope. Qualitatively, these curves are very similar to those obtained from real neurons [Douglas and Martin, 1990, e.g.]. The f-I curve in the *adapted* cell is almost linear with a slope of $\approx 60Hz/nA$. The average slope in one study on cat V1 was $\approx 90Hz/nA$, somewhat larger than the model. Note however that the layer V cell is one of the largest cells in neocortex; the slope is expected to increase with input capacitance, $C_{in}$.

The discharge curves also demonstrate the impact of individual active conductances (Fig. 2.6(d)). When only $G_{Na}$ and $G_{DR}$ are present (second from top), the cell starts spiking for very small input currents, approximately 0.1 $nA$. Since adaptation only occurs when both $G_{Ca}$ and $G_{AHP}$ are present, only the first ISI needs to be graphed. There is no primary slope. Note that arbitrarily low spike rates can

be obtained, as opposed to what is seen in the squid giant axon, even though low rates are only to be found in a narrow range of clamp currents. Adding $G_{AR}$ causes almost no shift in the curve. This is partly due to the very slow inactivation of this current (40–300 $msec$), and partly because of the low half-activation voltage (-82 mV) which leads to 92% inactivation at rest. $G_{Na,p}$ (top curve) provides a general weak excitation, while $G_M$ (third curve from top) causes a somewhat stronger inhibition. The $A$ current (second from bottom), however, not only provides inhibition, but also expresses the primary slope, which allows the neuron to spike at low rate over a much wider range of input currents. Finally, for comparison, the first ISI curve from Fig. 2.6(c) has been included (bottom curve).

### 2.4.2 Time-averaging of synaptic inputs

In most of our simulations, the effect of synaptic input is time-averaged. The validity of this procedure can be assessed by the results shown in Figs. 2.7. If the time-course of all synapses activated by the spontaneous background activity is explicitly included into NEURON, the membrane potential has the jagged appearance seen in Fig. 2.7A. The somatic voltage swings approximately 3–4 $mV$, in close agreement with intracellular recordings [Douglas et al., 1991]. The somatic voltage has a mean value (averaged over 20 $sec$) of $-65.17$ $mV$ with a variance of 0.6 mV (lower solid line in Fig. 2.7A). This noise makes it difficult to study single EPSPs and small voltage steps, as well as the precise timing between spikes, necessitating averaging over multiple simulations. In addition, the explicit incorporation of 5,000 synapses slows down each simulation considerably. To speed up simulations 10- to 1000-fold, the synaptic conductances were time-averaged, as described above in section 2.2. When the individual transient synaptic inputs are replaced by their total time-averaged synaptic input (described in Section 2.2.5), the membrane potential stabilizes at $-65.04$ $mV$

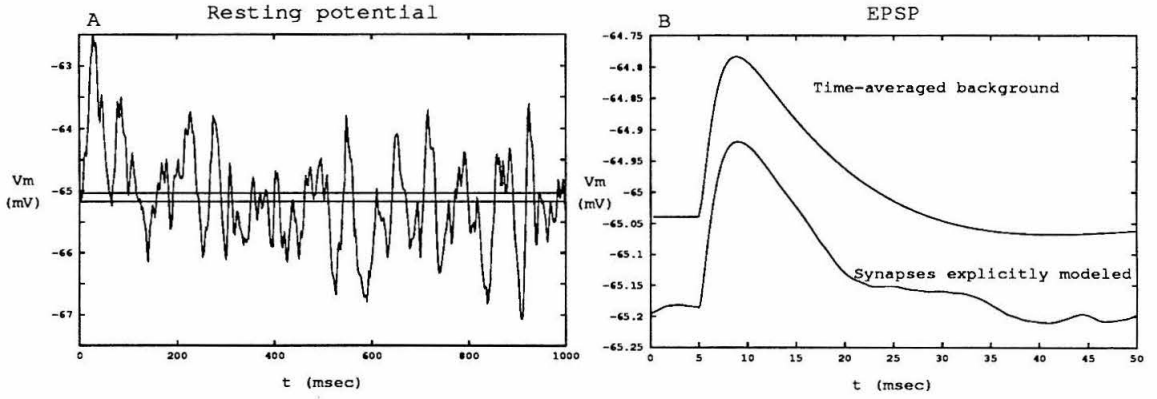


Figure 2.7: Time-averaging of synaptic inputs. **(a)** Cell at rest. All 5,000 synapses were explicitly simulated (jagged trace) and the average of that trace computed (lower flat line). For comparison, the potential that results time-averaging the synaptic conductances is shown (upper flat line). **(b)** EPSP. Again, all 5,000 synapses were explicitly simulated. On top of this background, a single somatic excitatory synapse was activated. The simulation was repeated 400 times and the traces averaged (lower trace). For comparison, the EPSP during time-averaging of synaptic input is also shown (upper trace).

(for a 0.5 $Hz$ background activity; upper line). The membrane potential is 0.13 $mV$ lower in the non-averaged case, due to saturation effects that arise when synaptic conductances occasionally occur together in space and time.

A second demonstration of the validity of time-averaging synapses in a passive dendritic tree is given in Fig. 2.7(b). One somatic synapse was activated every 50 $msec$ for a period of 20 $sec$ and the resulting traces were averaged, as is commonly done under experimental conditions. When all synapses are explicitly modeled, the trace is shifted by $\approx 0.15\ mV$, but otherwise strongly resembles the top trace. Since the signal-to-noise ratio (SNR) is very low for a single EPSP, as many as 400 traces were needed. Note, however, that the SNR improves approximately quadratically with signal amplitude, so that a compound EPSP of ten somatic synapses would have required a much smaller number of traces.

### 2.4.3 Robustness

In cerebellar Purkinje cells, a segregation of different active conductances between proximal and distal regions has been inferred [Llinás and Sugimori, 1980a, Llinás and Sugimori, 1989b]. However, it is unlikely that proximal channels are confined strictly to the soma, without diffusing into neighboring dendritic membrane at all. We tested whether such diffusion of $G_{Na}$ and $G_{DR}$ had any impact on action potential profiles. The channels were spread over all first- and second-order branches, increasing the active membrane area by a factor 6. If the channel *density* were reduced by six, keeping the total number of channels constant, spike amplitude was reduced by 10 $mV$. If the number of channels were increased by 50%, however, the original amplitude was restored. This example demonstrates that the model's sensitivity to the exact distribution of proximal conductances is small.

Another way to assess the model's robustness to parameter changes is to randomly

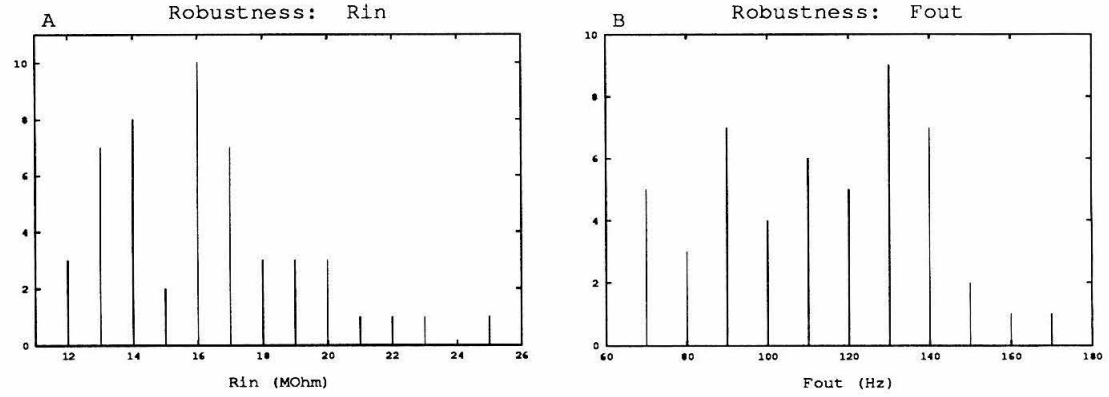


Figure 2.8: Robustness to variations in model parameters. The following parameters were all scaled randomly by up to 20%: $G_{max}$ for each active conductance, $R_m$ for each compartment, length $l$ and diameter $d$ (same scaling for all compartments). Histograms of 50 trials were collected. **(a)** Histogram for $R_{in}$. Average = 17.1 MΩvs. 16.5 MΩin the standard model; S.D. = 1.63 MΩ. **(b)** Histogram for $f_{out}$ in response to a 1 $nA$ current clamp. Average = 120 $Hz$ vs. 118 $Hz$ in the standard model; S.D. = 19.4 $Hz$. Only the first ISI was computed.

vary $G_{max}$ for all non-synaptic conductances as well as the length and diameter of all branches. These parameters were randomly perturbed by $\pm 20\%$ and a total of 50 simulations were run. The resulting $R_{in}$ and $f_{out}$ (first ISI only) were computed and histogramed in Fig. 2.8. The standard deviation of $R_{in}$ and $f_{out}$ were only 10–20% of the average value.

The sensitivity to variations in synaptic conductances, timing of input, and density of active *dendritic* channels will be the subject of chapters 4, 5, and 6.

# Chapter 3

# Efficacy, Delay, and Integration of Synaptic Input

## 3.1 Introduction

The first part of this chapter aspires to answer the question "how efficacious are synapses at different locations, and how large are dendritic delays?" This question has been asked by a large number of researchers in the past [Rinzel and Rall, 1974; Stratford et al., 1989; Williams and Johnston, 1991; Zador et al., 1991; Bush and Sejnowski, 1992; Cauller and Connors, 1992]. Therefore, in addition to cataloguing the range of efficacies and delays for different sites and studying their variation under different circumstances, we will focus on the *definitions* of efficacy and delay. Most studies use a single definition of efficacy, e.g., peak amplitude or the time-integral of the EPSP, with a few exceptions where multiple definitions are used [Koch et al., 1982, Cauller and Connors, 1992]. In this chapter, nine measures of efficacy and four measures of dendritic delay of single synaptic inputs will be defined and their various merits compared. Commonly used measures will be shown to differ

dramatically in the values they assign to a given synapse; for example, the voltage attenuation may vary 500-fold across the dendritic tree, while the time-integral of the somatic EPSP will vary only 4-fold. The computed time-delays can be used to create a direction-selective response.

The second part studies the interactions of large numbers of inputs. During massive conductance changes, distal conductances will be less "visible," giving rise to several phenomena. Combined with the asymmetric distribution of inhibitory (more proximal) and excitatory (more distal) inputs, this will make inhibition more effective as network activity increases. The problem of visibility is a well-known electrophysiological problem during imperfect space clamping [Rall and Segev, 1985]. It has previously been given a quantitative treatment for single synaptic inputs [Koch et al., 1990], while this chapter focuses on massive synaptic input. One previous study has acknowledged the importance of the more distal location of excitatory inputs *vs.* the more proximal location of inhibitory inputs [Abbott, 1991]. That study used a single-cable model of neurons and investigated the firing-rate problem. Below, we will use the full model and show the impact of input asymmetry to resting potential, negative feedback control of output firing rate, and receptive field size control. The full neuron model is also compared to a Hopfield neuron.

The interaction between large numbers of inputs will be further studied in chapter 4 with regard to temporal synchronicity of inputs, and in chapter 5 in the context of background firing rate.

## 3.2 Single inputs

Synaptic input will be investigated in two different cells and under different conditions. These conditions include the absence or presence of NMDA and different degrees of membrane leak. The membrane leak will be expressed in terms of background activity,

$f_b$. A background activity of $f_b$=0.5 $Hz$ is the standard model, $f_b$=0 $Hz$ corresponds to a slice preparation (very large $R_m$), and $f_b$=5 $Hz$ corresponds to a small $R_m$. The background firing rate maps onto the effective membrane resistance, $R_{\mathrm{m,eff}}$, as described above in section 2.2.5; chapter 5 is devoted to the impact of background activity on integration properties. For the purposes of this chapter, $f_b$ will only signify the degree of "leakiness" of the membrane.

### 3.2.1 Synaptic waveforms

Fig. 3.1 gives several examples of EPSPs. Each graph shows the response to a somatic, a basal and an apical synapse. In (a) the background frequency is 0 $Hz$, in (b) 0.5 $Hz$ (standard model), and in (c) 5 $Hz$. As the background frequency increases, both input resistance and time constant decrease. This results in a reduced amplitude and faster time course of the EPSP. The amplitude of somatic inputs is reduced by less than a factor 2, but apical inputs are reduced more than 100-fold (compare (a) and (c)).

Fig. 3.2 compares the local response of basal dendrites to the somatic response. Basal dendrites branch repeatedly within the first 50 $\mu m$ from the soma (preterminal branches) and end in long unbranched terminal branches, 150–200 $\mu m$ in length [Larkman, 1991a, our observations]. In 3.2(a) the synapse was placed at a pre-terminal branch, within 50 $\mu m$ from the soma. The local response is about 75% larger than the somatic response. For the center of the terminal branch (Fig. 3.2(b) — note different scale on $y$ axis), the local response is 9 mV or about 40 times larger than the somatic response (that is to say, the voltage attenuation, defined below, is 0.025). For apical dendrites the local response can be over 15 mV.

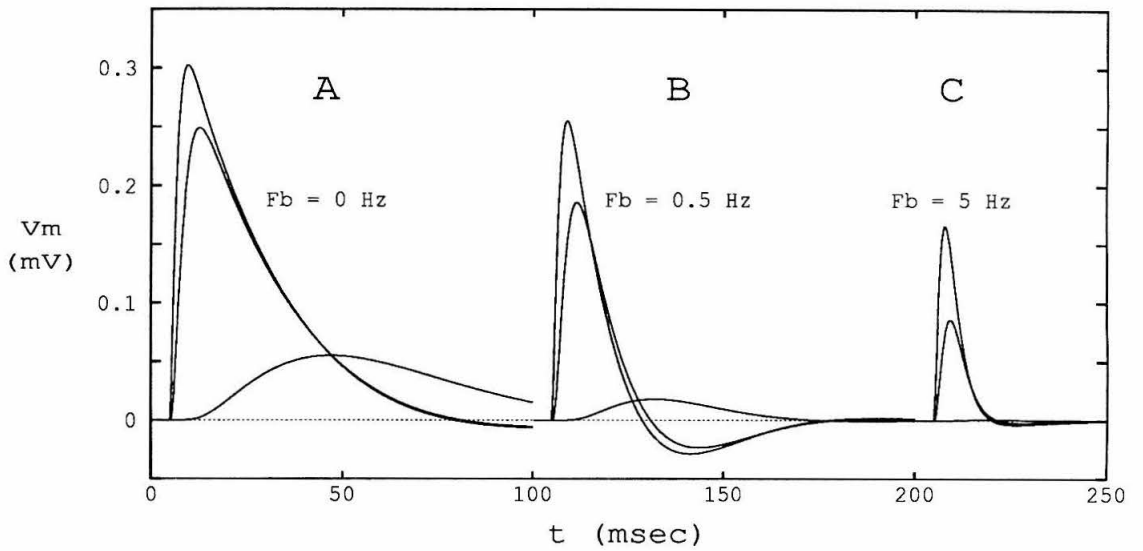


Figure 3.1: Somatic EPSP for three different input sites at three different background firing rates, $f_b$. Top trace, somatic input; middle trace, basal input; bottom trace, apical input. Membrane voltage is offset from resting potential which varies with $f_b$. The amplitude of the apical trace for $f_b = 5\ Hz$ is too low to be discerned.

### 3.2.2 Efficacy of inputs

In artificial neural network models, the definition of synaptic efficacy is straightforward: it is the weight $w$ used to produce a weighted sum of inputs, before applying a sigmoid activation function. In the linear case, $f_{out} = \sigma(\Sigma_i w_i x_i)$, where $x_i$ are the inputs and $\sigma$ is some sigmoid function.

For biological neurons, the notion of efficacy is more complicated. EPSPs from distal synapses undergo dispersion as they travel down the dendritic tree towards the soma, becoming broader and smaller in amplitude. The contribution of an input does not only affect $f_{out}$ at a single point in time, but is associated with a dendritic delay, followed by an approximately exponential decay, characterized by $\tau_m$. Due to high input resistance, the local response can be large in distal dendrites (10-15 mV) and so initiate non-linear events locally, while contributing little to the somatic potential. In addition, multiple inputs often summate non-linearly. As demonstrated below, the common measures of synaptic efficacy differ dramatically in their evaluation of distal synapses.

#### Definition of 9 efficacy measures

Fig. 3.3 summarizes the measures we have defined. They fall into two classes. The first seven measures are strength measures and are normalized with respect to somatic synapses, i.e., somatic synapses have an efficacy of 1 while all other synapses have an efficacy smaller than 1. The last two measures are distance measures, indicating the electrotonic distance from the soma. While a strength measure is largest at the soma, a distance measure is zero at the soma and positive for all other locations. A strength measure, $E^s$, can be converted into a distance measure, $E^d$, by the transform $E^d = -\ln(E^s)$ and *vice versa*.

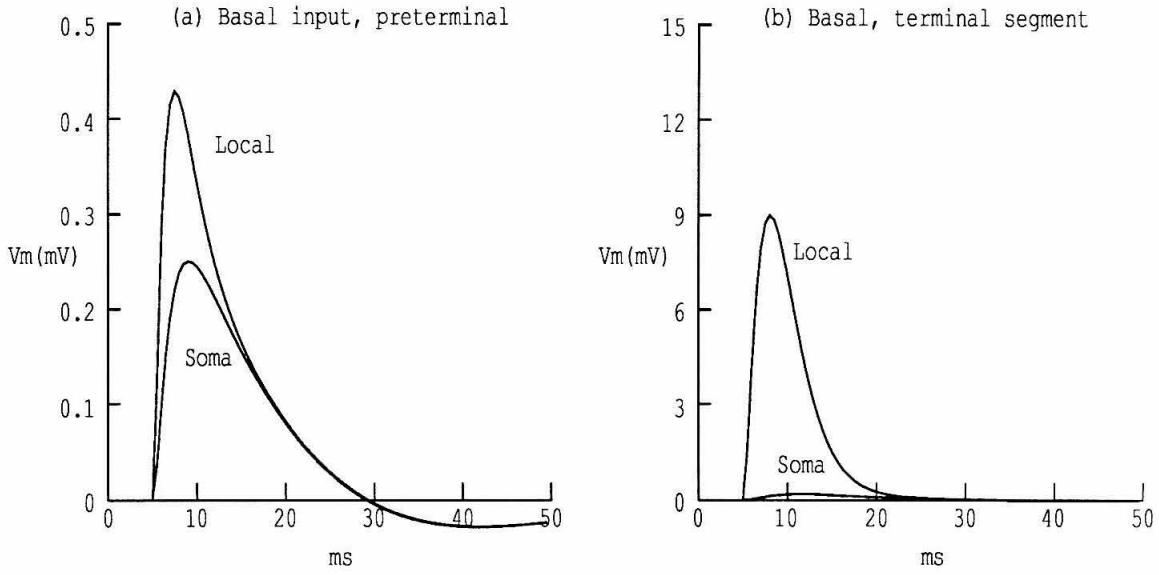


Figure 3.2: Comparison of local and somatic response. Upper trace is the local EPSP at the site of injection, while the lower trace is the somatic EPSP. **(a)** Synapse at a pre-terminal basal branch. **(b)** Synapse at the center of a terminal basal branch. Graphs have different scales on the y axes.

---

**Peak somatic depolarization:** $V_{peak}$. EPSP amplitude has the obvious advantage that it is easy to measure experimentally [Thomson et al., 1988, Andersen et al., 1990, Larkman et al., 1990, Mason et al., 1991]. The soma is the site of most successful electrode penetrations. It is also immediately adjacent to the axon hillock, where the action potential is initiated, and so the EPSP amplitude determines the minimum number of inputs required to raise membrane potential from rest to threshold. In the standard model, $V_{peak}$ varied from 18 to 250 $\mu V$.

**Steady state voltage attenuation:** $A_V$. We define the voltage attenuation as $A_V = \frac{\Delta V_{soma}}{\Delta V_{syn}}$, where $\Delta V_{soma}$ is the steady state change in somatic potential in response to $\Delta V_{syn}$, a voltage step at the synaptic site. This measure can be expressed in terms of input and transfer impedances as $A_V = \frac{K_{is}}{K_{ii}}$, where $K_{is}$ is the transfer

impedance from the synapse to the soma, and $K_{ii}$ is the input impedance at the synapse. This measure has been used in simulation studies of retinal ganglion cells and neocortical pyramids [Koch et al., 1982, Cauller and Connors, 1992]. Note that the definition used here implies that $0 < A_V \leq 1$. Note that synapses which have different input impedances may inject approximately the same total charge but cause very different local depolarization and hence be assigned different values of $A_V$. In the standard model, $A_V$ varied from 0.002 to 1.

**Transient voltage attenuation:** $A_{V,t}$. This is similar to $A_V$, but instead of a steady state voltage, a transient synaptic conductance change is used and the ratio of peak amplitudes, somatic to local, are calculated. Thus if the EPSP amplitude is attenuated by a factor 100 from the input site to the soma, the voltage attenuation, $A_V$, is 0.01. In the standard model, $A_{V,t}$ varied from 0.001 to 1.

**Time integral of somatic EPSP:** *Area*. Although the amplitude of a distal synapse will attenuate, the waveform will broaden and the effect on the soma will linger for a longer time than for a proximal synapse. During prolonged stimulation, an EPSP will have a similar effect if its amplitude is halved while its time course is slowed by a factor two. In fact, it can be shown that for a linear cell, the EPSP area is directly proportional to the amount of charge that reaches the soma. The area measure has been used in simulations of neocortical pyramids [Stratford et al., 1989, Cauller and Connors, 1992]. It is also straightforward to measure EPSP area experimentally. The cell model displays a certain amount of "ringing" (undershoot, followed by overshot) and only the area up to the first zero crossing was used. In the standard model, *Area* varied from 0.59 to 2.83 $msec \cdot mV$.

**Charge attenuation:** $A_Q$. Charge attenuation measures how much of the injected charge will reach the soma: $A_Q = \frac{\Delta Q_{soma}}{\Delta Q_{syn}}$ [Koch et al., 1982, Cauller and Connors, 1992]. In terms of impedances we have: $A_Q = \frac{K_{is}}{K_{ss}}$. It can be shown that this is true regardless of the time-course of charge injection [Koch et al., 1982]. The

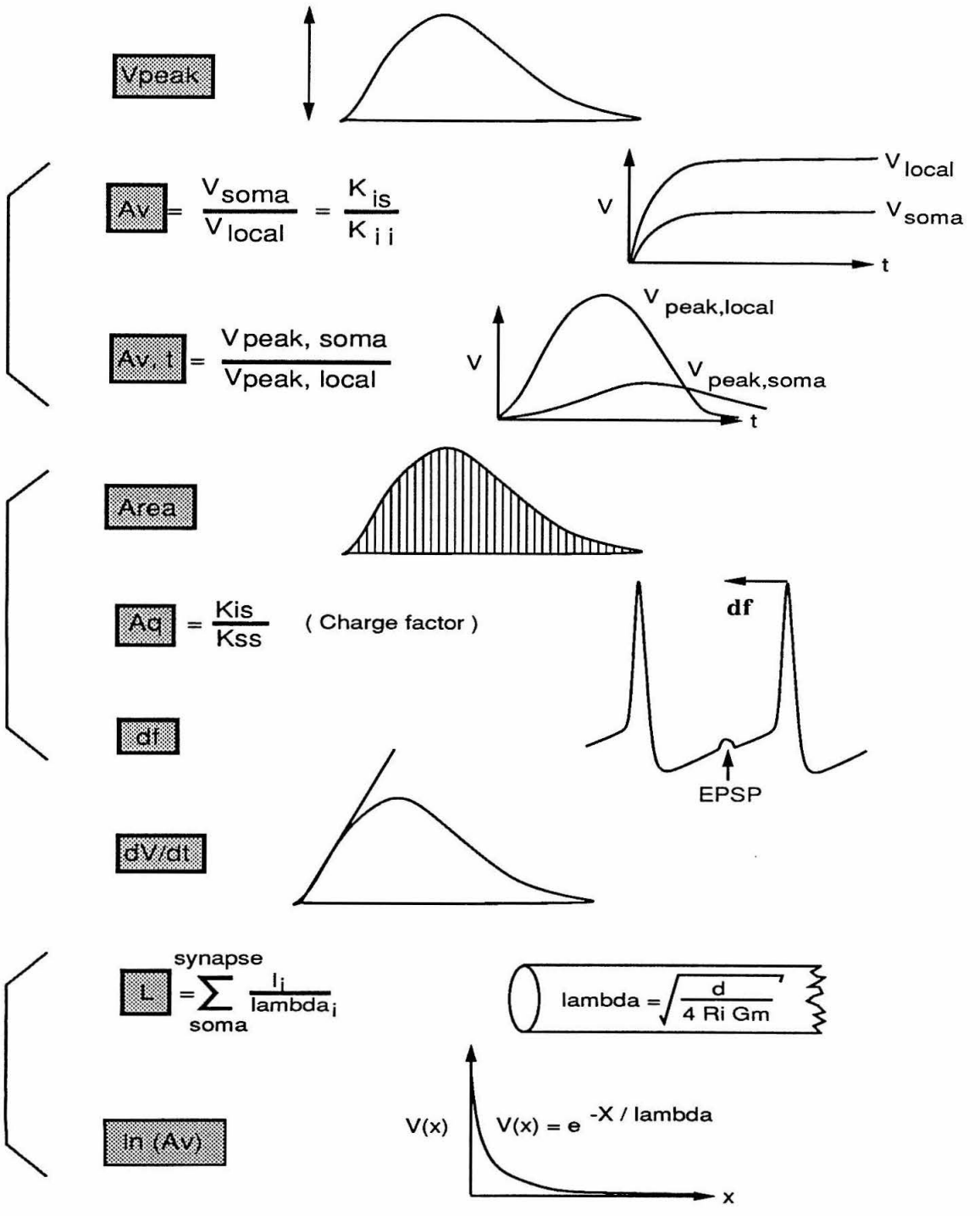


Figure 3.3: Definition of 9 efficacy measures. See section 3.2.2 for details. Similar measures have been grouped with right brackets.

charge attenuation is limited just like the voltage attenuation: $0 < A_Q \leq 1$. In the standard model, $A_Q$ varied from 0.46 to 1.

**Change in output frequency:** $df$. This is a functional measure that tells us what the incremental effect of a synapse is upon the firing rate of the neuron. We have defined it as follows: inject a bias current into the soma so that the cell spikes at approximately $10Hz$; activate the synapse under study every 10 $msec$ and record the percent change in frequency of the first interstimulus interval after activation. The reason for repeated activation is that the change in frequency due to a single activation depends strongly on the exact time of activation: the increase in firing frequency is much larger if the synapse is activated shortly before the second spike than just after the first spike. By repeatedly stimulating the same synapse, we average over a range of activation times. Further, since EPSPs from distal synapses have a larger propagation delay than proximal synapses, the ideal time for activation varies. The exact values for the parameters (input and output frequencies) was an arbitrary choice. In the standard model, $df$ varied from 1.42 to 6.33 $Hz$.

**Slope of somatic EPSP:** $dV/dt$. The maximum slope of the rising phase of the EPSP is often taken as a measure of efficacy [Kauer et al., 1988, e.g.], since it is straightforward to record experimentally. In the standard model, $dV/dt$ varied from 1.3 to 137 $mV/sec$.

**Electrotonic distance:** $L$. The length constant of a cable segment is $\lambda = \sqrt{\frac{d \cdot R_m}{4 \cdot R_i}}$ and its electrotonic length is $L_i = l_i/\lambda = l_i \cdot \sqrt{\frac{4 \cdot R_i}{d \cdot R_m}}$, where $l_i$ is its physical length. By summing up the individual $L_i$ on the path from the soma to the synaptic site, we arrive at $L = \Sigma_i L_i$ [Bernander et al., 1991]. In the standard model, $L$ varied from 0 to 1.7 $\lambda$.

**Negative logarithm of steady state voltage attenuation:** $-\ln(A_V)$. For an infinite unbranched cable of uniform diameter and membrane resistance, $R_m$, the length constant, $\lambda$, is the distance over which the steady state membrane potential

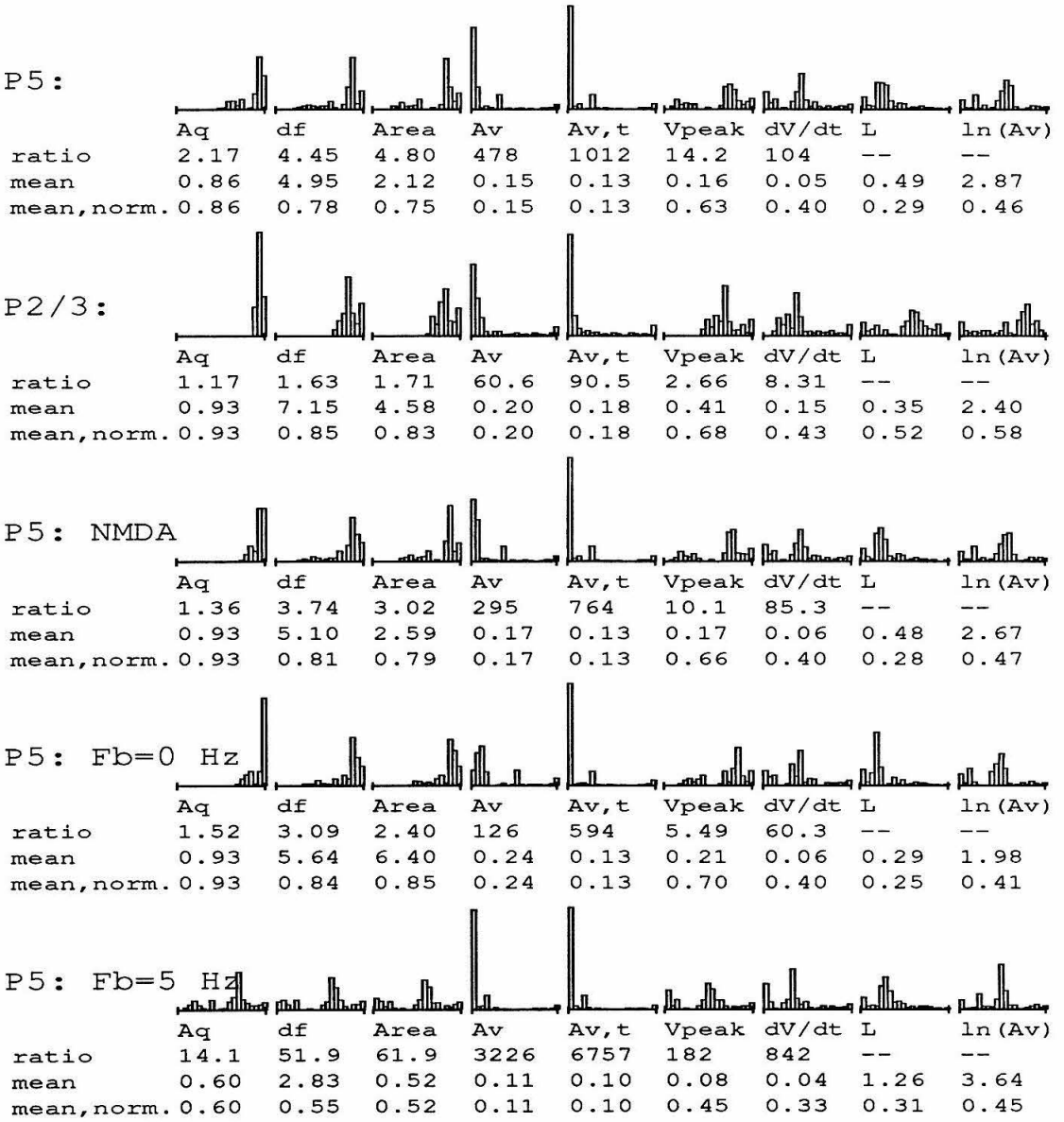


| | Aq | df | Area | Av | Av,t | Vpeak | dV/dt | L | ln(Av) |
|---|---|---|---|---|---|---|---|---|---|
| **P5:** | | | | | | | | | |
| ratio | 2.17 | 4.45 | 4.80 | 478 | 1012 | 14.2 | 104 | -- | -- |
| mean | 0.86 | 4.95 | 2.12 | 0.15 | 0.13 | 0.16 | 0.05 | 0.49 | 2.87 |
| mean,norm. | 0.86 | 0.78 | 0.75 | 0.15 | 0.13 | 0.63 | 0.40 | 0.29 | 0.46 |
| **P2/3:** | | | | | | | | | |
| ratio | 1.17 | 1.63 | 1.71 | 60.6 | 90.5 | 2.66 | 8.31 | -- | -- |
| mean | 0.93 | 7.15 | 4.58 | 0.20 | 0.18 | 0.41 | 0.15 | 0.35 | 2.40 |
| mean,norm. | 0.93 | 0.85 | 0.83 | 0.20 | 0.18 | 0.68 | 0.43 | 0.52 | 0.58 |
| **P5: NMDA** | | | | | | | | | |
| ratio | 1.36 | 3.74 | 3.02 | 295 | 764 | 10.1 | 85.3 | -- | -- |
| mean | 0.93 | 5.10 | 2.59 | 0.17 | 0.13 | 0.17 | 0.06 | 0.48 | 2.67 |
| mean,norm. | 0.93 | 0.81 | 0.79 | 0.17 | 0.13 | 0.66 | 0.40 | 0.28 | 0.47 |
| **P5: Fb=0 Hz** | | | | | | | | | |
| ratio | 1.52 | 3.09 | 2.40 | 126 | 594 | 5.49 | 60.3 | -- | -- |
| mean | 0.93 | 5.64 | 6.40 | 0.24 | 0.13 | 0.21 | 0.06 | 0.29 | 1.98 |
| mean,norm. | 0.93 | 0.84 | 0.85 | 0.24 | 0.13 | 0.70 | 0.40 | 0.25 | 0.41 |
| **P5: Fb=5 Hz** | | | | | | | | | |
| ratio | 14.1 | 51.9 | 61.9 | 3226 | 6757 | 182 | 842 | -- | -- |
| mean | 0.60 | 2.83 | 0.52 | 0.11 | 0.10 | 0.08 | 0.04 | 1.26 | 3.64 |
| mean,norm. | 0.60 | 0.55 | 0.52 | 0.11 | 0.10 | 0.45 | 0.33 | 0.31 | 0.45 |

Figure 3.4: Efficacy histograms for all cell locations. The $x$ axis shows the efficacy and the $y$ axis, the number of data points. "Ratio" refers to the ratio of the strongest to the weakest synapse. "Mean" is the average strength. Units are mV ($V_{peak}$), mV·$msec$ (Area), mV/$msec$ (dV/dt), $\lambda$ (L), percent (df), and unitless ($A_Q$, $A_v$, $A_{v,t}$, and -ln($A_v$)). For "normalized mean" the measure has been normalized so that the largest value is 1. The scale for the abscissa is from 0 to 1 for the first 7 histograms in each row, and from 0 to the largest value for the last 2 histograms. Top to bottom: **(a)** Standard model ($f_b$=0.5 $Hz$, no NMDA synapses). **(b)** Layer 2/3 cell, standard model. **(c)** Mixed AMPA and NMDA. **(d)** AMPA, $f_b$=0 $Hz$. **(e)** AMPA, $f_b$=5 $Hz$.

decays by a factor $e$. In other words, $V(x) = V_0 \cdot e^{-x/\lambda}$. By solving for $x$ we find $-\ln \frac{V(x)}{V_0} = x/\lambda = L$ [Zador et al., 1991]. Thus, $L = -\ln A_V$ and so this measure and the previous measure should be identical. For a branched cable structure this is not the case. In the standard model, $-\ln(A_V)$ varied from 0 to 6.17. Similarly, one can define the measure $-\ln(A_Q)$, which is also identical for an infinite cable, but which will differ for our model cells.

### Comparison of efficacy measures

The results are summarized in Fig. 3.4.

A synapse was placed at the center of each dendritic branch and the efficacy measured according to all nine measures. Since only one synapse was placed at each branch regardless of its size, data points were binned multiple times in proportion to branch area. The resulting histograms thus show the efficacy distribution assuming a uniform density throughout the dendritic tree and soma.

Three numbers are printed below each histogram. "Ratio" refers to the ratio of the largest to the smallest value. "Mean" refers simply to the average value and "normalized mean" to the average after all synapses have been normalized to give the strength of 1 for a somatic synapse. The weakest synapse will therefore have a normalized strength $1/ratio$. The mean is useful to compare the same measure for the five different cases (rows), while the normalized mean compares different measures for the same case (row). If two measures have similar ratios and the histograms look alike, the two measures are approximately equivalent.[1]

Some of the measures group together, giving similar results in most cases. Below,

[1] While it is theoretically possible that synapse A is stronger than synapse B using one measure, while A is weaker than B using another measure, this is almost never the case. When plotting a correlogram, that is a scatter diagram of synapse with the two measures used as coordinates, the points normally line up close to a straight line with correlation coefficients greater than 0.9. (Correlograms not shown.)

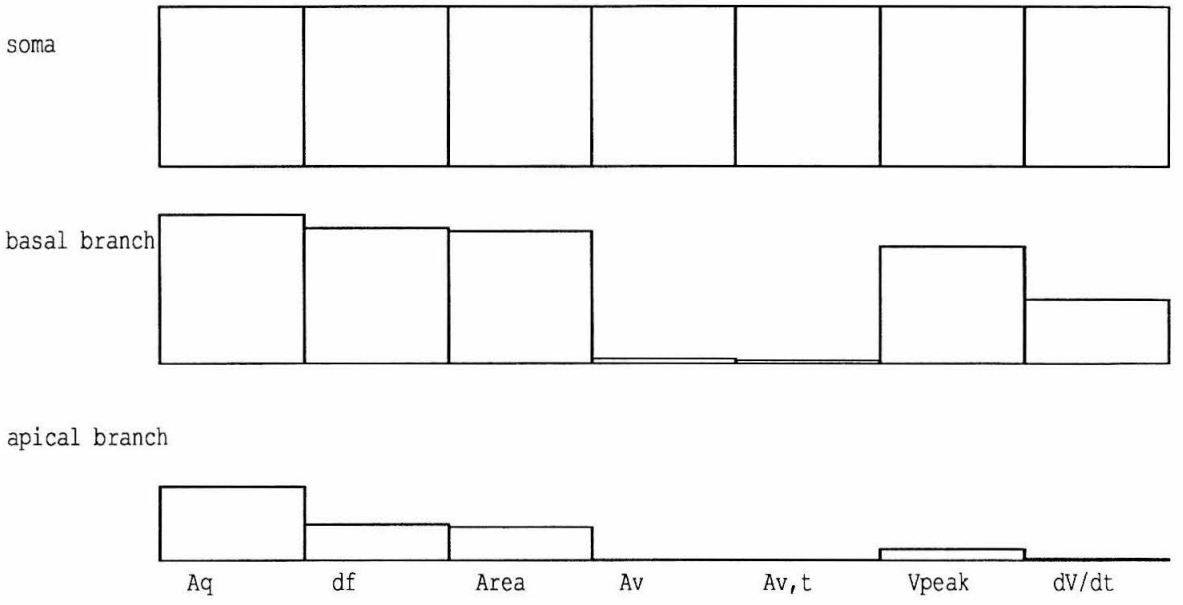


Figure 3.5: Comparison of 7 strength (non-distance) measures for three locations. The locations are (1) at the soma, (2) at the center of a terminal basal branch, and (3) at the center of a terminal apical branch. The height of the bars correspond to efficacy, and all synapses are normalized to give an efficacy of 1 at the soma.

---

these measures will be discussed together.

**$A_Q$-like measures: $A_Q$, *df*, and *Area*.** $A_Q$ is the fraction of injected charge that reaches the soma. The time-integral of the somatic EPSP is proportional to the total charge reaching the soma. Therefore, if the synapses were current inputs, $A_Q$ and *Area* would assign the same (normalized) efficacy to every synapse. However, since synapses are conductance changes, they will inject less charge if the membrane is depolarized. Distal dendrites are indeed more depolarized due to the asymmetric distribution of inputs. In addition, the higher input resistance of distal dendrites will cause a larger local depolarization, further reducing the driving force. Thus, while a

distal synapse may deliver half of its injected charge to the soma, only half the total charge is injected, giving it only one quarter the strength as measured by *df* and *Area*. As the histograms demonstrate, the *Area* measure assigns a smaller efficacy to distal synapses than the $A_Q$ measure does. For the standard cell the difference is only about a factor 2, but during intense stimulation ($f_b = 5\ Hz$, more strongly marked saturation) the difference increases to a factor 4. *df*, on the other hand, correlates very strongly with *Area*. This is to be expected since *Area* corresponds to the total charge delivered to the soma. This charge is available for bringing the cell to threshold faster and thus increasing the firing rate. Since *df* is a functional measure correlating very closely with *Area*, these two measures are the most appropriate for prolonged, unsynchronized inputs. $A_Q$ is not only impractical to measure, but also fails to capture saturation effects, though it still provides a decent approximation in many situations. In all cases, the average synapse is assigned a value larger than 0.5 for all three measures.

**$A_V$-like measures:** $A_V$, $A_{V,t}$. These two measures assign very small efficacies to most synapses, and so the histograms are strongly skewed to the left. On average, the efficacy is never larger than 0.25. Several effects conspire to cause the very small $A_V$ for distal synapses. Due to dispersion, the somatic amplitude will decrease dramatically (see discussion of $V_{peak}$ below) and the concomitant widening of the EPSP is ignored. Further, the local input resistance is often 10-20 times larger in a thin dendrite than at the soma, giving a large local boost in potential. Thus these two measures are not of much use. At best, a very small $A_V$ indicates a large local input resistance which may enhance local, non-linear effects, especially in the presence of active conductances. This can be seen when comparing the AMPA with the NMDA case (rows 1 and 3): the ratios are smaller in the NMDA case, indicating that distal synapses get an extra boost. Only in an infinite, unbranched cable will $A_V$ equal $A_Q$. In a branched structure the two measures differ dramatically.

**EPSP amplitude:** $V_{peak}$. As mentioned previously, $V_{peak}$ is a useful measure when the input is synchronized, since the cell will spike only if it reaches threshold. Since the dispersion of distal synapses is not taken into account, a much larger spread in assigned efficacies is seen than for the $A_Q$-like measures, though not as large as for $A_V$ and $A_{V,t}$. $V_{peak}$ is not found to correlate well with any other measure.

**Slope:** $dV/dt$. This measure, which is popular because it is straightforward to measure for large EPSPs, does not correlate well with any other measure. It tends to underestimate the strength of distal synapses even more than $V_{peak}$ does, since a reduced amplitude is often accompanied by a slower time course. Since distal synapses have very small slopes, they may in fact be difficult to detect experimentally. The measure may still be useful when measuring *change* in efficacy of the *same* synapse, as is often done in LTP studies [Kauer et al., 1988].

**Distance measures:** $L$ **and** $-ln(A_V)$. These two measures differ from the previous ones in that they measure the "electrical distance" from the soma. Proximal synapses thus have smaller values than distal ones, and the distance of a somatic location is zero. As can be seen in the figure, they have little in common. The shapes of the histograms differ strongly and the means are off by a factor 3–7. The $L$ measure gives smaller values than the $-ln(A_V)$ measure since it simply adds up the electrotonic lengths of individual branches, ignoring a sub-tree at every branch point. These sub-trees provide considerable loads, draining away much of the charge. As was noted above, $A_V$ does not equal $A_Q$ in a branched structure. Neither does $e^L$ (not shown), and $L$ can therefore not be considered a useful measure.

Fig. 3.5 compares the 7 non-distance measures for three locations. The three locations are the soma, the center of a basal terminal dendrite and the center of an apical terminal dendrite. Normalized measures are graphed, and thus they all give an efficacy of 1 at the soma. The $A_V$-like measures decrease the fastest with distance from the soma, $dV/dt$ and $V_{peak}$ decrease at an intermediate rate, and the $A_Q$-like

measures decrease only by a factor 2–4.

Comparison of the 5 different cases (rows in Fig. 3.4) shows that the average efficacies drop when $f_b$ is increased. This is due to a decrease in input resistance and time constant. Comparison of the layer 5 cell with the layer 2/3 cell shows that the second "hump" that often appears for the former cell often is absent for the latter. The second hump represents the apical tree which is much more distant than the basal tree. Even though the layer 2/3 cell actually has two apical trees, these are much shorter, only about twice as long as the basal trees. Finally, the effect of NMDA is to boost distal synapses. The large local input resistance of distal synapses increases the local voltage and activates the voltage-dependent NMDA synapses. Hence, using the *Area* measure, the most distal synapse is only one third as efficacious as one at the soma, as opposed to one fifth in the AMPA case.

In response to the question "how strong is synapse A" or "how much stronger is synapse A than synapse B," the $A_Q$-like measures are the most useful ones for studying prolonged input, especially *Area* and $df$, while $V_{peak}$ is the most relevant measure for highly synchronized input. Note, however, that if we only ask "is synapse A stronger than synapse B," then almost any measure will do, because it rarely happens that $A$ is stronger than $B$ in one measure while $B$ is stronger than $A$ in another. Further, if we only ask the question "did the efficacy of synapse $A$ change over time," then any strength (non-distance) measure will be useful.

### 3.2.3 Delay of inputs

Experimentally, the most common form of measured delay is latency. This delay is from stimulation of a presynaptic cell to the onset of the somatic EPSP. The latency typically involves propagation delays down one or several axons as well as diffusion of transmitter across the synaptic cleft. The resultant EPSPs are usually the compound

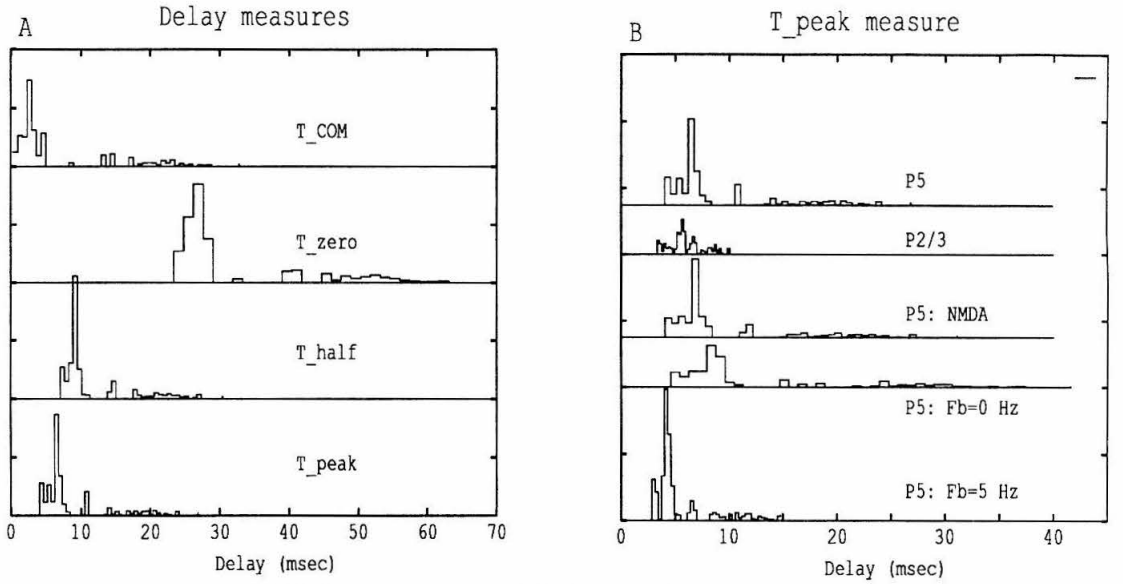


Figure 3.6: Histograms of delay measures. **(a)** Three different measures described in text. The standard model of the layer 5 cell was used. **(b)** Only the delay measure $T_{peak}$ was used for five different cases.

of different synapses at several locations on the cell.

Since this paper focuses on single cells, we will only study dendritic delays. We define the dendritic delay as the time from onset of conductance change to one of the following:

- $T_{peak}$, the peak of the somatic EPSP.
- $T_{half}$, the time at which the time-integral of the somatic EPSP has reached half its maximum value.
- $T_{zero}$, the time at which the time-integral of the somatic EPSP has reached its maximum value. This is the time when the EPSP undershoots the resting potential.
- $T_{COM}$, the centroid or center-of-mass (COM) of the somatic EPSP: $\frac{\int t \cdot v(t) dt}{\int v(t) dt}$ [Agmon-Snir and Segev, 1992].

$T_{peak}$ is a useful measure for highly synchronized input. This measure can be useful for wiring up a direction-selective cell, as discussed below in section 3.3.2. $T_{half}$ is the time at which the synapses has had, in a sense, half its total effect on the soma. This will yield a larger value than $T_{peak}$, since EPSPs are typically not symmetric, but skewed to the left. $T_{zero}$ marks the time when the EPSP is "over." Since EPSPs often have long tails and, for a passive neuron, may never cross the resting potential, $T_{zero}$ is not a very practical measure, but was included for completeness. Due to asymmetry, $T_{zero}$ will be more than twice as large as either $T_{peak}$ or $T_{half}$.

Similarly to the case of efficacy measures, synapses were placed on every branch, and the measured delays were binned multiple times to correct for branch area. The resulting histograms are shown in Fig. 3.6. In (a) the four measures are compared for the standard model. The histograms have very similar forms, but are scaled on the time axis. The means for $T_{peak}$, $T_{half}$, $T_{zero}$, and $T_{COM}$ are 9.9, 13.0, 34.5, and

8.9 *msec*, respectively. For the $T_{peak}$ measure, about three quarters of the synapses are clumped below 10 msec, corresponding to basal and proximal apical synapses. The remaining one quarter are spread between 12 and 25 msec, corresponding to the apical tuft. $T_{COM}$ is almost identical to the "total delay" as defined by Agmon-Snir and Segev [Agmon-Snir and Segev, 1992]. Using the centroid as the "time of occurrence" of a signal leads to a series of theorems and useful properties for passive trees. For example, the propagation delay between two points is independent of the waveform and is equal in the two directions. However, it turns out not to be very useful in our model where active currents are present. While $T_{COM}$ for distal synapses are 3–4 *msec* larger than $T_{peak}$, $T_{COM}$ can be less than 1 *msec* for proximal synapses. This is because the undershoot of the EPSP is significant and weighted strongly in the integral $\int t \cdot v(t)dt$. As a result the average $T_{COM}$ is *smaller* than the average $T_{peak}$, which would not be the case in a passive cell and could possibly become negative.

The $T_{peak}$ measure was studied for the same five cases as were the efficacy measures. Delays for the much smaller layer 2/3 cell were all below 10 msec with a mean of 5.8 msec. Substituting NMDA for half of the synapses resulted in slightly larger delays, with the mean increasing from 9.9 to 10.8 msec. Changing the background frequency stretched the histograms in expected directions. For $f_b$=0 $Hz$, the time constant increased and the mean was 14.1 msec. For $f_b$=5 $Hz$, the time constant decreased and the mean was 6.3 msec.

To conclude, $T_{peak}$ and $T_{half}$ are both useful measures, while $T_{zero}$ may be impossible to measure and $T_{COM}$ breaks down if non-linear conductances are present in high densities.

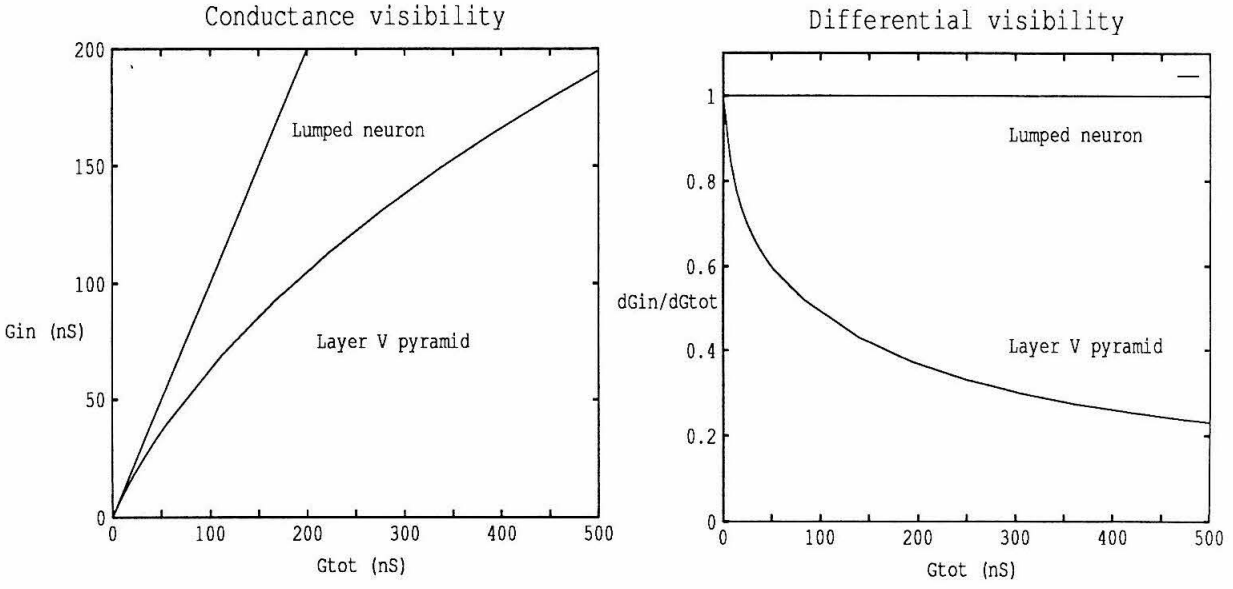


Figure 3.7: Visibility of membrane conductance for a passive neuron. $G_{in}$ is the input resistance measured at the soma. The top curve is for a lumped neuron, modeled with a single compartment. The bottom curve is for the layer 5 cell. $G_{tot}$ is the total parallel conductance, summed over the entire neuron. **(a)** $G_{in}$ increases sublinearly with $G_{tot}$. **(b)** $\frac{dG_{in}}{dG_{tot}}$ is the derivative of the curve in (a). $G_{tot}$ = 5.6, 56, and 560 nS correspond to $R_m$ = 100, 10, and 1 k$\Omega cm^2$, respectively.

## 3.3 Interaction between multiple inputs

So far we have only been concerned with the effect of single synapses. The only facet of multi-synapse interactions explored was the impact of background frequency, which reduces the efficacy of distal synapses more than proximal ones.

In this section we will investigate several forms of synaptic interactions. The emphasis will be on how distal inputs are partially "screened" by proximal inputs and how this selects for inhibition (which is more proximal than excitation) during massive inputs. We will also investigate the importance of the temporal sequence of activation of large number of inputs.

### 3.3.1 Conductance screening

A classical problem in experimental neurophysiology is the imperfect space clamp [Rall and Segev, 1985]. While neuronal membrane in close proximity to the clamp electrode will follow the command potential well, electrically distant sites will not. Thus, if there is a change in conductance, $\Delta G$, at a distant location, a smaller value, $\Delta G^*$, will be "visible" from the soma, when measured with current or voltage steps. Visibility, $\Gamma$, is defined as the fraction of $\Delta G$ that can be measured:

$$\Gamma = \frac{\Delta G^*}{\Delta G}.$$

For small conductance changes in an infinite cable, the visibility $\Gamma$ falls off approximately exponentially with a space constant of $\frac{\lambda}{2}$ [Koch et al., 1990] [2]:

$$\Gamma = e^{\frac{-2x}{\lambda}}.$$

The visibility $\Gamma$ is the fraction of the conductance change that is measured at the recording site. Obviously the visibility must decay, since an infinite cable has a finite input resistance, while the total parallel conductance is infinite.

#### Visibility of uniform membrane conductance

To demonstrate this effect we simulated the layer 5 cell with uniform $R_m = \frac{1}{G_m}$ and no active conductances. Fig. 3.7(a) graphs input conductance, $G_{in}$, versus the total membrane conductance, $G_{tot} = Area/R_m$. If a single compartment is used to model the cell (lumped neuron), then $G_{in}$ is identical to $G_{tot}$ (top curve). However, when simulating the dendritic morphology, the measured $G_{in}$ can be considerably

[2] The factor 2 arises from the fact that the injected current must propagate from the electrode site to the synapse and then back again.

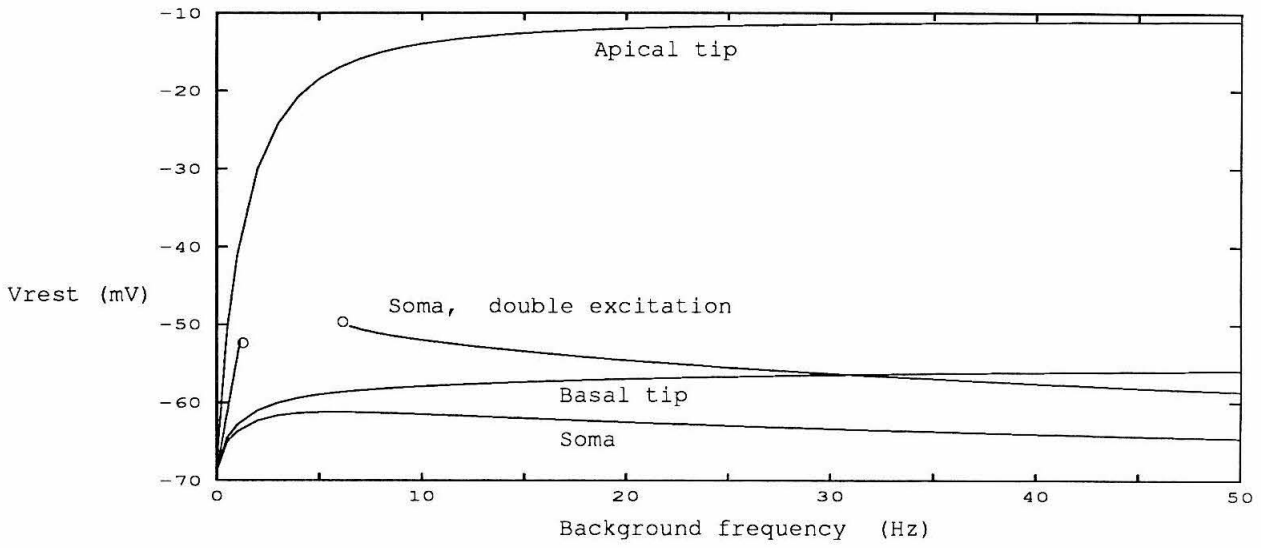


Figure 3.8: Inhibition screening out excitation: Resting potential at three locations as a function of background activity. The more distal the location, the more excitation dominates over inhibition. The broken curve represents the somatic resting potential when the excitatory synapses were driven at twice the frequency of inhibitory synapses (marked on the $x$ axis); between 1.1 and 6 $Hz$ the cell spikes and hence the resting potential is undefined.

---

smaller than $G_{tot}$. The visibility, now defined not for a single synapse as an average over the total cell conductance, $\Gamma = \frac{G_{in}}{G_{tot}}$, can be used to quantify this effect. For Rm=100k$\Omega cm^2$, $\Gamma$ is 0.93, suggesting a fairly compact neuron. As $R_m$ increases to 10k$\Omega cm^2$, $\Gamma$ falls to 0.71, and for $R_m$=1k$\Omega cm^2$ $\Gamma$=0.37. Fig. 3.7(b) graphs the derivative of the curve in (a). The $y$ axis tells how much of an *additional* conductance change will be visible. For the same $R_m$ quoted above, this differential visibility is 88%, 58%, and 22%. In this simplified and reduced model, the most obvious manifestation of the interaction of multiple inputs is conductance screening.

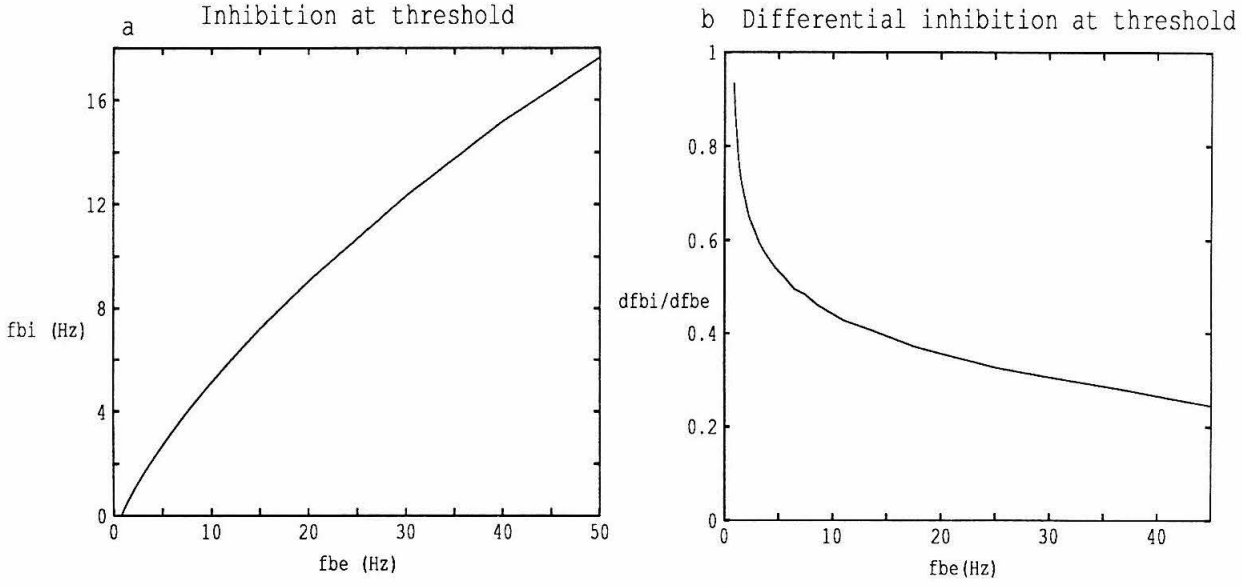


Figure 3.9: Inhibition screening out excitation: balance between excitation and inhibition at threshold. $f_{b,e}$ and $f_{b,i}$ refer to the frequency at excitatory and inhibitory synapses respectively; $f_{b,i}$ lumps both $GABA_A$ and $GABA_B$. **(a)** Inhibitory background frequency needed to keep neuron just below threshold as a function of excitatory background frequency. **(b)** Derivative of graph in (a). The derivative corresponds to the amount of additional inhibition needed to counteract one additional $Hz$ of excitation.

---

### Resting potential

Inhibitory synapses are more proximal than excitatory ones on average [Holmes and Woody, 1989, White, 1989, Douglas and Martin, 1990, Larkman, 1991b]. Since proximal conductances are more visible than distal ones, we expect inhibitory synapses to be more effective than excitatory ones. Specifically, the balance will shift in favor of inhibition during massive stimulation when the effective $R_m$ decreases.

We activated all synapses at background frequencies, $f_b$, from 0 to 50 $Hz$ and recorded the potential at the soma, at a basal tip, and at an apical tip. For 0 $Hz$ background the cell is compact and almost isopotential at -67 – -68 mV. The resting

potential is a compromise between the reversal potential of the uniformly distributed passive leak current, -66 mV, and partially activated currents in the soma (mainly potassium at -95 mV and anomalous rectifier at -50 mV). As the background frequency increases, the total synaptic conductance will dominate over the leak and the somatic active currents. For low $f_b$, when the cell is still fairly compact, the high reversal potential of excitatory synapses will pull up the resting potential. For larger $f_b$ the more distal excitation is screened out by more proximal inhibition and so the somatic potential is pulled down again. Note that the potential at more distal locations stays high because excitation dominates locally. The asymptote for somatic potential was -71 mV. The broken curve represents the case when the excitatory synapses were activated at twice the inhibitory frequency. In the interval 1.1–6 $Hz$ the cell fired repetitively, creating a "window of firing," where the resting potential was undefined.

The results are in qualitative agreement with experimental data. *In vivo* recordings show somatic resting potentials between -40 and -60 mV [Holmes and Woody, 1989, Douglas et al., 1991, Pockberger, 1991] except in one study where it was -81 $mV$ [Bindman et al., 1988], while *in vitro* recordings (no synaptic background activity) give lower values, ranging between -65 and -85 mV [Bindman et al., 1988, Thomson et al., 1988, Mason and Larkman, 1990, Spain et al., 1990, Mason et al., 1991, Spain et al., 1991, Cauller and Connors, 1992]. The larger depolarization in the dendrites also has some support. While it is technically difficult to record in dendrites, except for the apical trunk [Wong et al., 1979, Woody et al., 1988, Pockberger, 1991, Amitai et al., 1993], Ferster deduced this result [Ferster and Jagadeesh, 1992]. He recorded compound EPSPs from the soma and found that the amplitude decreased by a factor five during visual stimulation. The most likely explanation for this is a reduced driving force, as the dendritic potential approaches the reversal potential of the excitatory synapses.

### Balance of inhibition and excitation at firing threshold

One obvious role for inhibition is to keep a neuron from firing. The question therefore arises of how much inhibition is needed to keep the neuron just below threshold, for a given amount of excitation.

We stimulated the cell with different background frequencies. Initially, the excitatory and inhibitory frequencies, $f_{b,e}$ and $f_{b,i}$[3], were set to the same value. Next, $f_{b,i}$ was slowly decreased until the cell fired. The $f_{b,i}$ at which this occurred was recorded.

The result is shown in Fig. 3.9(a). At an $f_{b,e}$ of 5 $Hz$, 2.7 $Hz$ of inhibition is needed, or 54%. At an $f_{b,e}$ of 50 $Hz$, 17.6 $Hz$ of inhibition is needed, or 35%. We see that, in a relative sense, inhibition becomes more powerful for large inputs. In Fig. 3.9(b) the derivative of the curve in (a) is graphed. The derivative gives the *additional* inhibition needed to counteract an additional Hertz of excitation. This curve gives a more dramatic demonstration of the asymmetry between the distributions: over the graphed range this amount decreases from 0.94 $Hz$ to 0.24 $Hz$ — a factor 4.

We thus conclude that the asymmetric input distributions serve to provide a form of negative feedback, keeping the cell from firing out of control. The same conclusion was reached by Abbott [Abbott, 1991] who solved the cable equations analytically for a simpler model constisting of a soma and a single cable. Note that for an unstructured, compact ("single-compartment") neuron, the curve in Fig. 3.9(a) would be linear.

### Comparison to Hopfield neuron

A pressing question for researchers studying artificial neural networks is how well a "Hopfield" neuron approximates a biological cell. A Hopfield neuron sums its inputs linearly and computes a continuous output $f_{out}$, which can be thought of as

[3] $f_{b,i}$ refers to the input frequency at both $GABA_A$ and $GABA_B$ synapses.

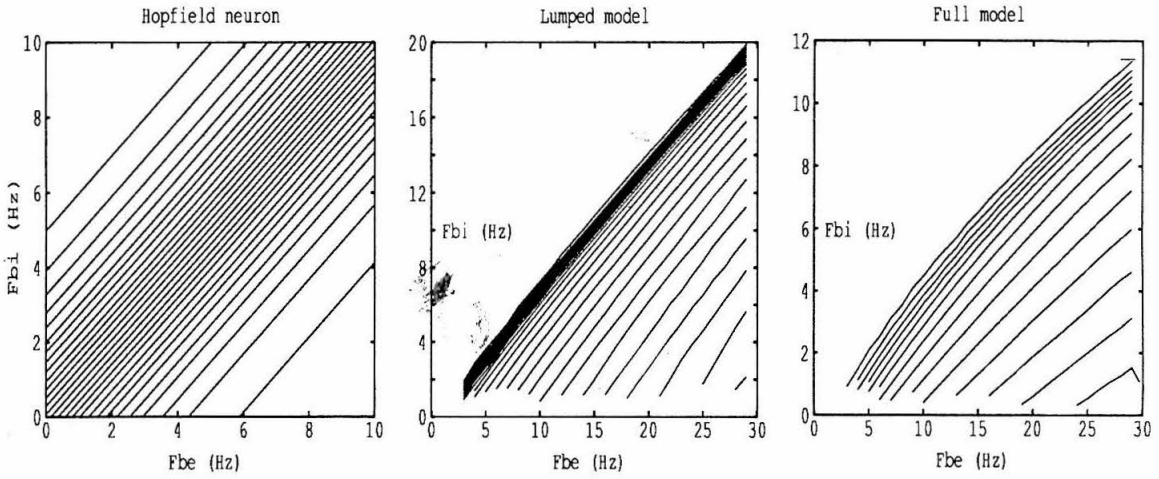


Figure 3.10: Inhibition screening out excitation: $f_{in}$–$f_{out}$ curve. 2-dimensional contour plots of $f_{out}$ as a function of inhibition and excitation as independent variables ($f_{b,e}$ and $f_{b,i}$). The output firing rate is zero in the top left corner, but increases sigmoidally along the diagonal towards the bottom right corner; a diagonal cut would thus reveal a sigmoid. **(a)** Hopfield neuron. **(b)** Layer 5 pyramid, lumped. **(c)** Layer 5 pyramid, full dendritic tree. For (b) and (c) the spacing between contours is 20 $Hz$. Note that the contours in (c) are non-parallel due to screening of excitation.

"instantaneous" frequency:

$$f_{out} = \sigma(w_i \cdot f_i + w_e \cdot f_e),$$

where $\sigma$ is some sigmoid function, usually bound between 0 and 1 [Hopfield, 1984, Rumelhart and McClelland, 1986]. $w_e > 0$ and $w_i < 0$ are the weights for the excitatory and inhibitory inputs, $f_e$ and $f_i$.

A Hopfield neuron lacks features such as dispersion, dendritic delays, adaptation, and fractionation of the dendritic trees into subunits [Koch et al., 1982]. We are left with the sigmoid and the linear sum of inputs.

As we showed in the previous chapter (Fig. 2.6), $f_{out}$ is a sigmoid in input current over the normal range of operation[4].

But just how linear is the sum? A contour plot of $f_{out}$ as a 2-dimensional function of $f_{b,e}$ and $f_{b,i}$ is shown for a Hopfield neuron in Fig. 3.10(a). A diagonal cut from the upper left corner (small $f_{out}$) to the lower right corner (large $f_{out}$) yields a sigmoid. Linearity is revealed in the fact that all contours are straight and parallel, so that $w_i \cdot f_i + w_e \cdot f_e$ is constant along straight lines.

Fig. 3.10(b) shows the contour plot for a single-compartment model of the layer 5 cell. Even though a diagonal cut still yields a sigmoid, it is asymmetric: for $f_i > f_e$ the cell doesn't spike at all. The contours are almost parallel, reflecting quasi-linear summation of inhibition and excitation over the range studied. The wiggles seen especially for small $f_{out}$ arise from grid sampling.

Fig. 3.10(c) shows the contour plot for the full model of the layer 5 cell. The contours are much less parallel, reflecting the non-linear summation discussed in previous sections. Note also that $f_{out}$ is lower for a given input, which is a consequence

[4]For very large inputs the spiking mechanism becomes dysfunctional and the membrane potential "locks up" at some intermediate value between the action potential peak and the resting potential.

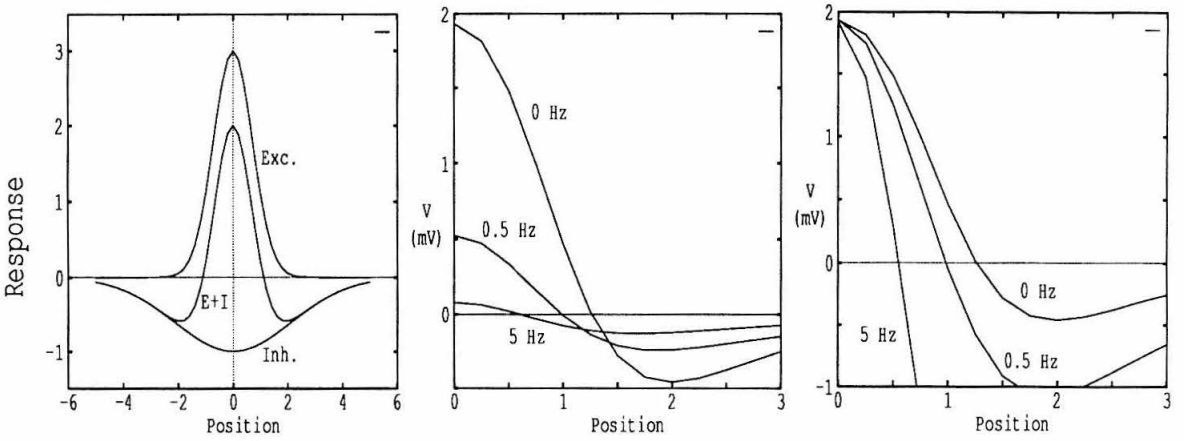


Figure 3.11: Control of receptive field profile. **(a)** A "Mexican hat" (Difference of Gaussians) receptive field is constructed using two Gaussians with amplitudes 3 and 1 and a $\sigma$ of 1 and 3. **(b)** Receptive fields when the background frequency varied from 0 to 5 $Hz$. Total excitatory conductance peaked at $\overline{g_e} = 1.1\ nS$, and the inhibitory conductance peaked at $\overline{g_i} = 1.46\ nS$. **(c)** Same as (b), except that the conductances were increased to $\overline{g_e} = 4.8$ and $\overline{g_i} = 6.4\ nS$ for $f_b = 0.5\ Hz$ and to $\overline{g_e} = 60$ and $\overline{g_i} = 80\ nS$ for $f_b = 5\ Hz$. The ratio of excitatory to inhibitory conductance stayed the same.

---

of the low visibility of distal excitatory conductance inputs.

### Control of receptive field size

As will be demonstrated in chapter 5, the background activity $f_b$ can change the tuning curve of the neuron for synchronization sensitivity. Here we will briefly study how the width of a "Mexican hat" receptive field can change with background activity, as a result of the different input distributions of excitation and inhibition. This dynamic change in receptive field size has been postulated by theories for visual attention [Olshausen et al., 1992] and has been measured experimentally [Pettet and Gilbert, 1992] (see below).

Fig. 3.11(a) shows how a Mexican hat receptive field can be constructed using a

narrow Gaussian of large amplitude for excitatory input and a wide, shallow Gaussian for inhibitory input. The $y$ axis, labeled "response" in the graph, was taken to be a conductance change, spread out across the cell according to the input distributions described in section 2, with a ratio of $\overline{g_i}/\overline{g_e} = 4/3$. In other words, the cell receives conductance inputs that are a function of the position $x$ of the stimulus:

$$g_e(x) = \overline{g_e} \cdot e^{-\frac{1}{2}\frac{x^2}{\sigma_e^2}}.$$

$$g_i(x) = \overline{g_i} \cdot e^{-\frac{1}{2}\frac{x^2}{\sigma_i^2}}.$$

The inhibitory conductance was split evenly between $GABA_A$ and $GABA_B$. Since excitatory inputs are more distal, their efficacy will decrease faster with $f_b$ than will the efficacy of inhibitory inputs. Thus the positive part of the Mexican hat will drop faster than the negative part, resulting in a smaller and narrower ON-center "bump."

The somatic voltage response (from rest) is graphed in Fig. 3.11(b). The conductance inputs, $g_e$ and $g_i$, were held constant as the background activity, $f_b$, was increased from 0 to 0.5 to 5 $Hz$. Since the input resistance decreases, the total response decreases, but the width of the receptive field, as measured by the intersection with the $x$ axis, decreases by more than a factor two.

In Fig. 3.11(c) the conductance input was changed from trial to trial to normalize for input resistance, keeping the ratio $g_i/g_e$ constant. The narrowing of the receptive field shows up more clearly. The positive central region decreases by a factor 2.45. For a 2-dimensional receptive field, this corresponds to a factor $(2.45)^2 = 6$.

There is much evidence that the response of neurons is influenced by stimuli lying outside the classical receptive field (RF) [Nelson and Frost, 1985, Allman et al., 1985, Gulyas et al., 1987]. Pettet and Gilbert demonstrate how the RF of neurons in cat V1 will expand in area by about a factor 5 when an artificial scotoma covers the RF

[Pettet and Gilbert, 1992]. The scotoma is simply a blank spot in the visual field while the surround is stimulated. Upon stimulation of the RF, it will collapse to its original size. Assuming that the neuron receives a lower level of synaptic activity during the scotoma, our model is consistent with the results.[5]

This form of receptive field size control has been proposed for a model of visual attention in which retinal information is shifted and rescaled as it is routed to higher cortical areas [Olshausen et al., 1992, Olshausen et al., 1993]. At this higher level of representation, all objects are centered and appear at the same size, allowing position- and scale-invariant pattern matching. The number of templates that needs to be stored is thus dramatically reduced. We have shown that a very simple control signal, diffuse input, can accomplish the scaling, but not the shifting, of the receptive field. Using a more elaborate wiring scheme that controls inhibition and excitation separately could result in more precise control and eliminate the effect that the smaller receptive field is less sensitive to inputs.

### 3.3.2 Sequencing of excitatory input

As shown in Fig. 3.1 the EPSP from a somatic excitatory synapse has an amplitude of approximately 0.25 mV. Since the action potential threshold is approximately 16 mV above the resting potential, we expect that a minimum of 60–70 somatic synapses are necessary to bring the cell to fire[6]. A larger number is required if the synapses are spread out in space (across the dendritic tree) or time (desynchronized, see chapter 4).

For a small or moderate number of synapses, the peak somatic response is larger if inputs are synchronized. This will be further discussed in chapter 4. Fig. 3.12 (bottom trace) shows the response to 100 synapses, distributed at 20 locations and

[5]Note however, that in the absence of stimuli outside the scotoma, no expansion occurs.
[6]The exact number turns out to be 66 for the standard model.

activated in a random sequence over a time interval $T$. For a moderate spread in time of 20 $msec$ ($\approx \tau_m$) the response is 5–6 mV, but then drops rapidly as the input is more desynchronized.

The time-to-peak delays, $T_{peak}$, of these synapses varied from 3.8 to 22.7 $msec$. If stimulated in sequences, so that the individual EPSPs peak at the same time, a larger response is obtained (Fig. 3.12 (top trace)). The curve peaks close to the calculated optimal delay of $T = 22.7 - 3.8 = 18.9$ $msec$ and then drops slowly, not dipping below 5 mV until $T = 65$ $msec$. In the null direction (middle trace) the response is initially smaller than for random input, but for $T > 20$ $msec$ it is larger. This may at first seem surprising, but can be understood as follows: Of the 20 locations, 13 are in the apical tree. These synapses are considerably weaker (in the $V_{peak}$ measure) than the basal synapses. Activation in the null direction will activate the stronger basal synapses during a small part of $T$, while for random activation these basal synapses are spread out over the full time interval. Comparing the preferred and null direction, we notice that the response in the preferred direction is only about 40% larger. This is consistent with intracellular sub-threshold recordings that show a remarkably small difference between the two directions [Douglas et al., 1991].

## 3.4 Conclusions

In this chapter we have investigated the efficacies and delays of single synapses as well as integration of large numbers of synapses under different conditions.

A comparison of nine measures of efficacy showed that commonly used measures differ dramatically in the relative values they assign to different synaptic locations. The $A_Q$-like measures ($A_Q$, $Area$, and $df$) have the smallest spread across the dendritic tree (2–4 for the layer 5 cell and less than a factor 2 for the smaller layer 2/3 cell). These measures are also the most relevant for sustained input. $V_{peak}$ has a considerably

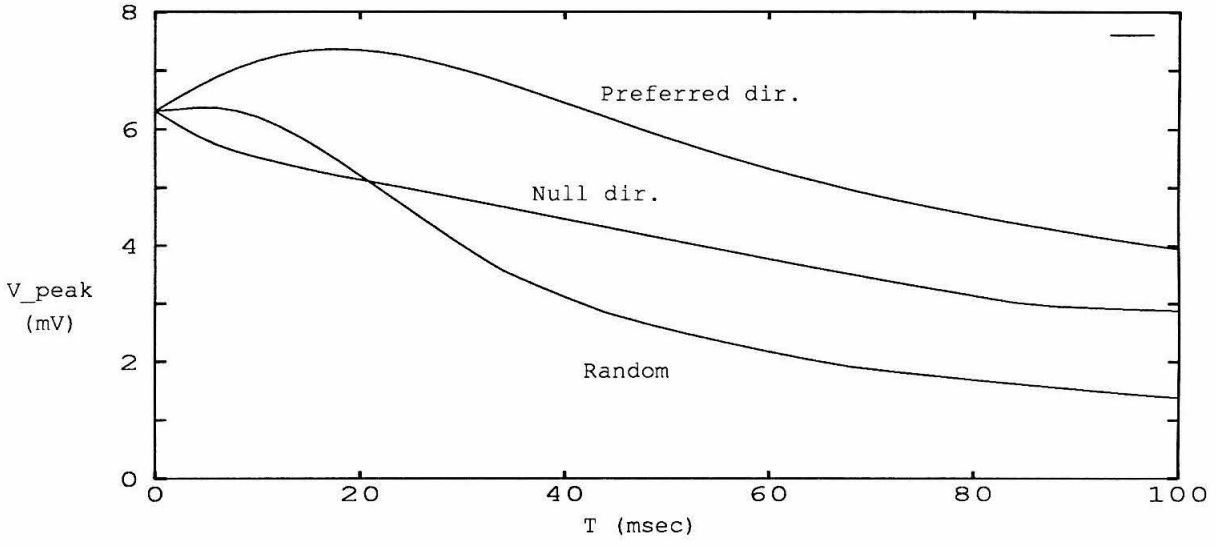


Figure 3.12: Sequenced excitatory input. 100 AMPA synapses were distributed at 20 locations. They were activated during a time interval $T$ ($x$ axis), either sequentially in the preferred direction (top), sequentially in the null direction (middle), or randomly (bottom). $V_{peak}$ ($y$ axis) is the maximum somatic deflection from $V_{rest}$.

larger spread, but is still a useful measure for transient or synchronized inputs. The rising slope, $dV/dt$, has a larger spread still. While not very meaningful for comparing the efficacies of *different* synapses, it can be used for measuring changes in efficacy for a single synapse. The $A_V$-like measures strongly underestimate distal synapses.

Four measures of dendritic delay were compared. Two intuitively useful measures, $T_{peak}$ and $T_{half}$, assigned similar values to synapses. Delays ranged approximately from 5 to 30 $msec$ for the layer 5 cell and from 4 to 10 $msec$ for the layer 2/3 cell. The centroid measure, $T_{COM}$, is not very meaningful in the presence of phenomenological inductances (undershoot in EPSPs), yielding delays as small as 1 $msec$. However, $T_{COM}$ has been shown to be analytically tractable for passive trees, possessing such useful properties as symmetry and additivity [Agmon-Snir and Segev, 1992].

Both efficacies and delays will be reduced in the presence of large synaptic background activity. This is due to changes in input resistance and time constant, as will be discussed in chapter 5.

During massive synaptic input, distal conductance change will be only partially visible [Koch et al., 1990]. Since inhibitory synapses are on average located closer to the soma than excitatory synapses, inhibition will gain in relative strength during strong stimulation. This effect can be useful in keeping the network from locking up at high firing rates [Abbott, 1991] in addition to other mechanisms such as spike rate adaptation of excitatory cells [McCormick et al., 1985, Mason and Larkman, 1990, Anderson et al., 1993b] and negative adaptation of inhibitory cells (output frequency increases with time) [McCormick et al., 1985]. It also provides for a possible mechanism of receptive field size control, by reducing the excitatory center ON-field.

A direction-sensitive cell was simulated by stimulating 100 synapses sequentially according to the calculated delay $T_{peak}$. The sensitivity was not very strong, giving only a 40% larger response in the preferred direction.

Integration of massive synaptic input will be further discussed in chapters 4 and 5.

# Chapter 4

# Synchronization

## 4.1 Introduction

It has long been postulated that the synchronous firing activity of cortical neurons is a crucial stage underlying perception. The psychologist Milner [1974] first proposed that neurons responding to a "figure" fire synchronously in time, while neurons responding to another figure or to the "ground" fire randomly: the "primitive unity of a figure" would be defined at the neuronal level by synchronized firing activity. Several years later, von der Malsburg formulated his influential *correlation theory* of brain function on the basis of the importance of synchronized activity and demonstrated how this theory could be used to temporally segregate patterns [von der Malsburg and Schneider, 1986]. Using computer simulations, they showed that from an initially totally interconnected set of tonotopic neurons, two distinct groups of neurons—corresponding to two distinct voices—arise. The mechanism of this segmentation is the temporal synchronization of simultaneously active cells using a fast Hebbian synaptic modulation mechanism. This idea has been extended by Crick and Koch [Crick and Koch, 1990, Crick and Koch, 1992], who postulated that

synchronized and oscillatory firing activity in a subset of cortical neurons constitutes the neuronal correlate of visual attention and awareness.

Electrophysiologists have studied the synchronized electrical activity among two or more simultaneously recorded neurons in the cortex of cats and monkeys [for instance, Ts'o et al., 1986, Aertsen et al., 1989, Nelson et al., 1992, Kreiter and Singer, 1992]. In some of these studies, cross-correlation among two cortical cells reveals a central peak with a width of less than 1 *msec*. Further, Gray et al. [Gray et al., 1989] showed that the oscillatory responses of cells can become temporally *synchronized* in a stimulus dependent manner. In the cat, the oscillations can be phase-locked with a phase-shift of $\pm 3$ *msec* around the origin at distances up to 7 *mm* [Engel et al., 1992].

The principal idea underlying theoretical studies is the belief that synchronized neuronal firing in large populations of pyramidal cells causes a higher firing rate in postsynaptic target cells (after suitably accounting for axonal and synaptic delays). This, in fact, is already inherent in the McCullough and Pitts neuron: if one such binary "unit" has a threshold of two, the simultaneous activity of two presynaptic neurons is required to bring the unit above threshold [McCullough and Pitts, 1943]. However, it has rarely been asked to what extent more realistic and biophysically plausible models of neurons prefer synchronized to desynchronized, excitatory synaptic input. Are there physiologically meaningful conditions under which temporally synchronized input leads to less effective postsynaptic firing than less synchronized activity? This is the question we address here, and we find that under many conditions synchronized firing is *not* good for the cell in terms of generating the largest number of spikes. The principal—and most limiting—assumption we make here is that the dendritic tree of cells is passive and does not contain special, fast voltage-dependent nonlinearities, which are limited to the cell body.

To our knowledge, only a single paper has investigated the possible "negative" effect of synaptic synchrony on postsynaptic firing frequency [Murthy and Fetz, 1993].

Their numerical study varies the fraction of cells, $r$, that are perfectly synchronized among each other, concluding that synchronization only increases the postsynaptic firing frequency under certain conditions. In our more general investigation, we use both an analytically treatable neuron model (from the family of integrate-and-fire models) as well as computer simulations of the detailed model described in chapter 2 to investigate the effect of single-shot and repetitive synaptic input at various synchronization levels. Our main finding is that if the number of inputs, $N$, is much larger than the minimum number of inputs needed to reach threshold, $N_t$, then it is better to desynchronize the input temporally over some non-zero interval $T$. The simplified intergrate-and-fire models demonstrate that this effect can be explained by a combination of the membrane leak, $G$, which favors small $T$, and the refractory period, $T_{rp}$, which favors large $T$.

The degree of synaptic correlation in the input varies in accordance with two independent factors: the temporal spread of synchronization, $T$, referred to as the *desynchronization interval* and the fraction of neurons that are synchronized, $r$. As we shall see, these two factors affect the postsynaptic firing frequency in different ways. In the first two sections of this chapter, we will investigate the effect of the desynchronization interval on the firing rate, assuming that $N$ synapses are each activated only once, under two extreme assumptions: **i.**) the input is Poisson distributed throughout $T$ with on average $N$ synaptic inputs and **ii.**) the input is constant, approximating the situation of regular input activity every $T/N$ *msec*. In the section 4.4, we will deal with the added complication arising from repetitive synaptic input.

## 4.2 Synchronicity in integrate-and-fire models

We will first consider different variants of the *integrate-and-fire* (I&F) model neuron [Knight, 1972; Fig. 4.1], under the assumption that $N$ synapses are activated only

once (*single-shot* case).

In its simplest version, discrete synaptic inputs arriving at times $t_i$ place an identical charge $Q_0$ onto a capacitance $C$, charging up the membrane potential across the capacitance by $\Delta V = Q_0/C$. When the voltage reaches a fixed threshold value, $V_t$, a point-like pulse is generated and the potential $V(t)$ is reset to 0. Two important modifications to this model include a membrane leak conductance $G$ and an absolute refractory period $T_{rp}$. The *leaky* or *forgetful* integrate-and-fire model has finite memory: since the membrane potential decays exponentially between synaptic inputs (with time-constant $\tau_m = C/G$), events that occurred in the past are less effective than more recent ones. The effect of $T_{rp}$ is to hold the potential $V(t)$ to 0 for the duration $T_{rp}$ after the model has generated a spike, rendering all synaptic inputs ineffective during this time. The main virtue of this family of models is their simplicity, allowing us to study some of their properties analytically.

### 4.2.1 Regular synaptic input

For "regular" synaptic input we assume that the synaptic input arrives at a constant rate $\lambda = N/T$; in other words during the interval $T$, $N$ synaptic inputs arrive in a regular manner, spaced $T/N$ *msec* apart. Let $T_{spike}$ be the time required to charge up the membrane from rest ($V = 0$) to $V_t$. The total number of output spikes, $N_{sp}$, generated during this interval $T$ will be the largest integer $n$ for which

$$n \cdot T_{spike} + (n-1) \cdot T_{rp} \; < \; T, \tag{4.1}$$

that is

$$N_{sp} = Floor \; [\frac{T + T_{rp}}{T_{spike} + T_{rp}}], \tag{4.2}$$

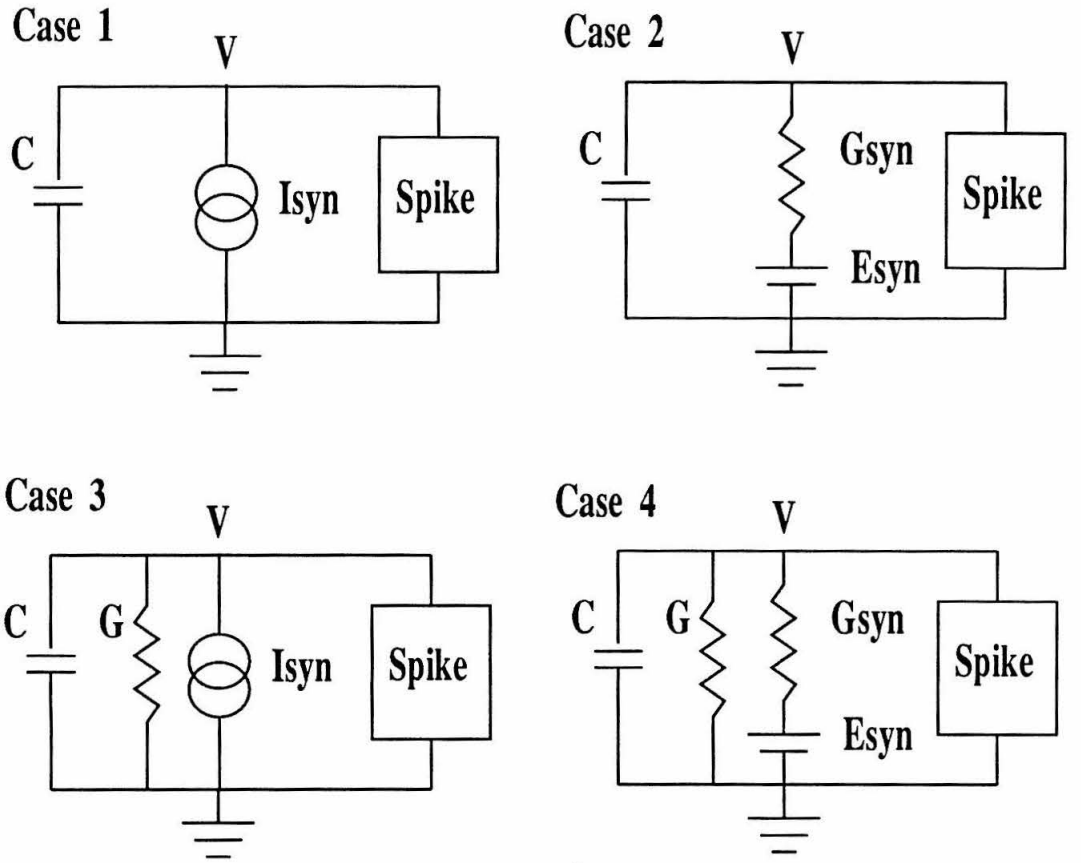


Figure 4.1: Four versions of the integrate-and-fire model. The model includes an optional membrane leak $G$ (cases 3 and 4). Synaptic input can be either modeled as a current source $I_{syn}$ (cases 1 and 3) or as a conductance change, $G_{syn}$ (cases 2 and 4). The spike mechanism resets the potential $V$ to 0 $mV$ and includes a refractory period, $T_{rp}$, during which $V$ is clamped to 0 $mV$; $T_{rp}$ may be set to 0 $msec$.

| Case | Model | Synaptic Input | $T_{spike}$ |
|---|---|---|---|
| 1 | I&F | Current $I_0 = C\lambda\Delta V$ | $\frac{N_t}{\lambda}$ |
| 2 | I&F | Conductance | $-\frac{C}{\lambda G_{syn}} \ln(1 - \frac{V_t}{E_{syn}})$ |
| 3 | leaky I&F | Current $I_0 = C\lambda\Delta V$ | $-\tau_m \ln(1 - \frac{N_t}{\tau_m \lambda})$ |
| 4 | leaky I&F | Conductance | $-\frac{C}{G+\lambda G_{syn}} \ln(1 - \frac{V_t G}{\lambda E_{syn} G_{syn}} - \frac{V_t}{E_{syn}})$ |

Table 4.1: Analytic expressions for the time $T_{spike}$ required for constant synaptic input arriving at rate $\lambda = N/T$ to reach threshold, assuming a continuous approximation of the discrete input. See appendix A for derivation.

---

where $Floor[x]$ is the largest integer smaller than or equal to $x$. For an analytical treatment it is more convenient to use a continuous approximation without the $Floor[]$ function:

$$N_{sp} = \frac{T + T_{rp}}{T_{spike} + T_{rp}}. \tag{4.3}$$

The only quantity that needs to be evaluated in eq. (4.3) is $T_{spike}$. Case 1 is an integrate-and-fire model with a constant rate $\lambda = N/T$ of identical synaptic input pulses, each one dumping the charge $Q_0 = C\Delta V$ onto the capacitance. This is equivalent to injecting the constant current $I_0 = C\lambda\Delta V$ onto the capacitance. In the third case, the same current $I_0$ is injected into the *leaky* integrate-and-fire model. In the other two cases, the input is treated as conductance input $G_{syn} > 0\ nS \cdot sec$ in series with a synaptic battery $E_{syn} = 70\ mV$, for the standard (case 2) or for the leaky I&F model (case 4). This is equivalent to a single effective conductance of value $\lambda G_{syn}$ that is activated during the interval $T$.

We first derive an analytic expression for $T_{spike}$ in the fourth and most general case (see Table 4.1). $T_{spike}$ is the time it takes for a constant conductance input, $\lambda G_{syn}$, to charge the membrane from 0 to $V_t$ in the leaky integrate-and-fire model (case 4 in Table 4.1). The input is approximated by a constant synaptic conductance increase in series with a synaptic battery $E_{syn}$ (here, $E_{syn}G_{syn} = C\Delta V$). Replacing

the two parallel conductances $G$ and $\lambda G_{syn}$ with a single equivalent conductance $G' = G + \lambda G_{syn}$ and replacing the battery $E_{syn}$ with $E' = E_{syn}\lambda G_{syn}/G'$, we arrive at a first-order, ordinary differential equation:

$$C \cdot \frac{\Delta V}{dt} + (V - E') \cdot G' = 0.$$

Solving this and setting $V$ to $V_t$ and $t = T_{spike}$ leads to

$$T_{spike} = \frac{C}{G'} \cdot \ln\,(1 - \frac{V_t}{E'}),$$

which can be rewritten as

$$T_{spike} = -\frac{C}{G + \lambda G_{syn}} \ln(1 - \frac{V_t G}{\lambda E_{syn} G_{syn}} - \frac{V_t}{E_{syn}}).$$

The expression for current inputs (case 3) can be obtained as a limiting case by setting $I_0 = \lambda \cdot C \cdot \Delta V = \lambda \cdot E_{syn} \cdot G_{syn}$ and letting $G_{syn} \rightarrow 0$ and $E_{syn} \rightarrow \infty$, keeping $G_{syn} \cdot E_{syn}$ constant. $T_{spike}$ for the nonleaky I&F model (cases 1 and 2) can be simply obtained by setting the membrane leak $G$ to 0 (and exploiting $\ln(1 + dx) = dx$ for small values of $dx$). While conductance inputs are more relevant to the physiological situation where massive synaptic input fires the pyramidal cell at high rates (see chapter 5), further analysis is simplified if current inputs are used.

We evaluated eq. 4.3 for the case of conductance inputs to the I&F model with $N = 1,000$ inputs and either no or a fixed refractory period ($T_{rp} = 2\ msec$; see Fig. 4.2) and used values for $G, C, T_{rp}$ and $N_t$ that mimic the values observed in cortical pyramidal cells (see below).

For the standard integrator (with $T_{rp} = 0$ and $G = 0$; top curve), the number of output spikes, $N_{sp}$, is independent of $T$. In fact, $N_{sp}$ is always independent of the arrival times of the input, but only depends on the total number of inputs: $N_{sp} =$

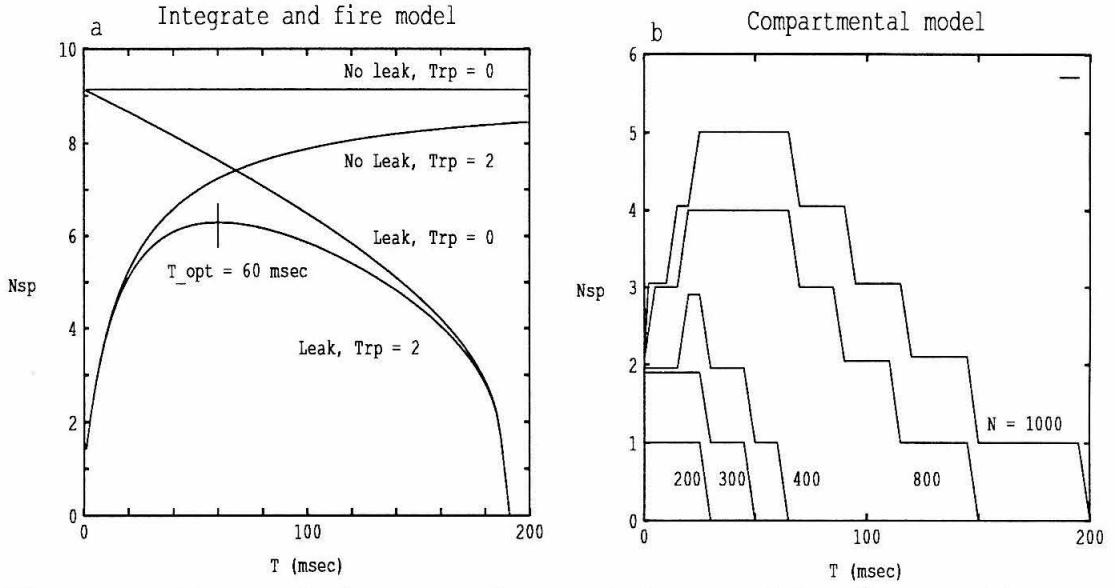


Figure 4.2: Temporal dispersion of synaptic input and its effect on firing rate for different single cell models. A fixed number of identical excitatory inputs $N$ is evenly distributed along the interval $T$ and the number of output spikes $N_{sp}$ is computed as a function of $T$. **(a)** Leaky integrate-and-fire model with $N = 1,000$ conductance inputs. The leak conductance $G$ is either 0 or 58.8 $nS$, and the refractory period $T_{rp}$ is either 0 or 2 $msec$. The membrane leakage "pulls down" the right end of the curve, while the refractory period pulls down the left end of the curve. $\Delta V = 0.25, V_t = 15\ mV, \tau_m = 17\ msec$ and $N_t = 60$. These parameters are similar to those of the detailed model. The optimal value of $T$, $T_{opt}$, is marked on the bottom curve. **(b)** Compartmental model of layer V pyramidal cell. $N$ = 200–1,000 excitatory, fast AMPA synapses were distributed throughout the cell. $N_t = 66$ synchronized *somatic* synaptic input are required to trigger one action potential. For $N = 1,000$ the I&F model with refractory period and conductance inputs is in good qualitative agreement with the compartmental model. The principal result of our study is that for $N >> N_t$, synchronization of synaptic input causes the cell to fire fewer spikes than if the synaptic input is temporally dispersed (i.e., the optimal $T > 0$).

$N/N_t$ for the I&F model with an infinite memory. When a membrane leak $G$ is introduced, the number of output spikes decreases with $T$ because earlier inputs leak away with a time constant $\tau_m \approx C/G$. This is at the heart of the traditional argument for the advantage of synchronizing synaptic input in terms of eliciting the maximum number of postsynaptic spikes: *temporal dispersion of synaptic input reduce their effectiveness* [e.g., Abeles, 1982]. However, when a refractory period, $T_{rp}$ is introduced into the leaky I&F neuron (lower curve in Fig. 4.2a), the initial part of the curve is "pulled down," so that for small desynchronization intervals $T$, $N_{sp}$ will *increase* with $T$. The reason for this "overcrowding" effect is that synaptic input in excess of $N_t$ will be "wasted." Synaptic inputs arriving during the refractory period do not contribute to the excitability of the cell. Thus, for $N > N_t$, desynchronized synaptic input increases the spiking rate, or, *high synchronicity of massive synaptic input reduces firing rate.* The optimal $T$ is a compromise between the effects of $G$ and $T_{rp}$ and is about 60 $msec$ for $N = 1,000$ as shown in Fig. 4.2.

Substituting current inputs for conductance inputs had only a minor effect on the I&F models. If the parameters were adjusted to give similar values of $N_{sp}$ for small $T$, then current inputs give slightly larger values for large $T$ (graphs not shown).

It is conceivable that the peaked form of $N_{sp}$ could be due to synaptic saturation. Rather than inputs being "wasted" during the refractory period, an increased resting potential would reduce the driving force $E_{rev} - V(t)$ for the excitatory synapses. Such saturation effects only exist if the synaptic input is treated as a conductance change and could, in principle, reduce $N_{sp}$ for high input rates $\lambda = N/T$ and small values of $T$. However, $dN_{sp}/dT < 0$ for case 4 with $T_{rp} = 0$ $msec$, independent of $E_{syn}$, and therefore no peak can occur (see monotonically decreasing curve in Fig 4.2a).

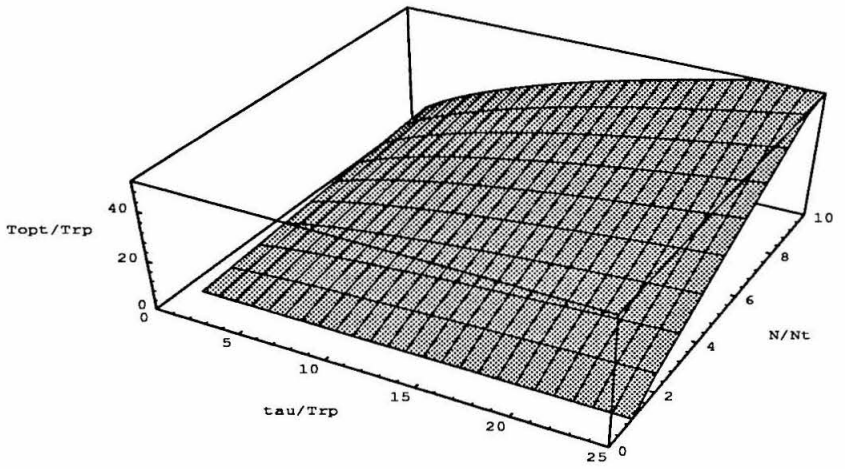


Figure 4.3: The optimal value of $T$, $T_{opt}$, in units of $T_{opt}/T_{rp}$, in the leaky integrate-and-fire model for current input as a function of the normalized number of inputs $N/N_t$ and normalized time-constant $\tau_m/T_{rp}$. $T_{opt}$ is almost linear in $N$ for $N >> N_t = 60$; e.g., if the number of inputs $N$ doubles, they should be spread out over twice as long an interval $T$ as before in order to maximize firing frequency.

### 4.2.2 Optimal desynchronization interval

How does $T_{opt}$, the optimal value of $T$, that is the desynchronization interval at which $N_{sp}$ is maximized, depend on the various parameters? To find $T_{opt}$, we compute $dN_{sp}/dT$ for the leaky I&F model with current inputs and set this derivative to zero. For current inputs, the number of output spikes is

$$N_{sp}(T) = \frac{T + T_{rp}}{T_{rp} - \tau_m log(1 - \frac{N_t T}{\tau_m N})}. \tag{4.4}$$

If we define the dimensionless variables $a_1 = N/N_t$, $a_2 = \tau_m/T_{rp}$, and $y = N_t T/(N\tau_m)$, take the derivative of eq. (6) and set the resulting expression to zero, we obtain

$$\frac{y + \frac{1}{a_1 a_2}}{1 - y} = \frac{1}{a_2} - \log(1 - y) \tag{4.5}$$

Note that $y$ depends only on the two dimensionless quantities $a_1$ and $a_2$. No closed-form expression exists for the solution of $y(a_1, a_2)$, which was therefore solved numerically. The numerically obtained value of $T_{opt}$ is shown in Fig. 4.3. Note that all three axes are in dimensionless variables: $T_{opt}/T_{rp}$, $\tau_m/T_{rp}$, and $N/N_t$.

As can be seen, $T$ is almost exactly linear in $N/N_t$, except for values of $N/N_t$ in the neighborhood of 1. This is not too surprising, since at high input rates $T_{opt}$ becomes much larger than $\tau_m$ and a dynamic steady state condition prevails during most of the single-shot. It can also be seen when $y(a_1, a_2)$ is graphed (not shown): $y$ is almost independent of $a_1$ except for small values of $a_1$. In other words, for $N >> N_t$ there exists an optimal input rate $f_{in} = N/T$. For our parameter values in the leaky I&F model, this rate is approximately 10 inputs/$msec$. If $f_{in}$ is increased above this 10 $kHz$ rate, the refractory period will reduce $N_{sp}$, while if $f_{in}$ is decreased below 10 $kHz$, the membrane leak causes a reduction in $N_{sp}$.

$T_{opt}$ increases with $\tau_m = C/G$ but not in a linear fashion due to the opposing

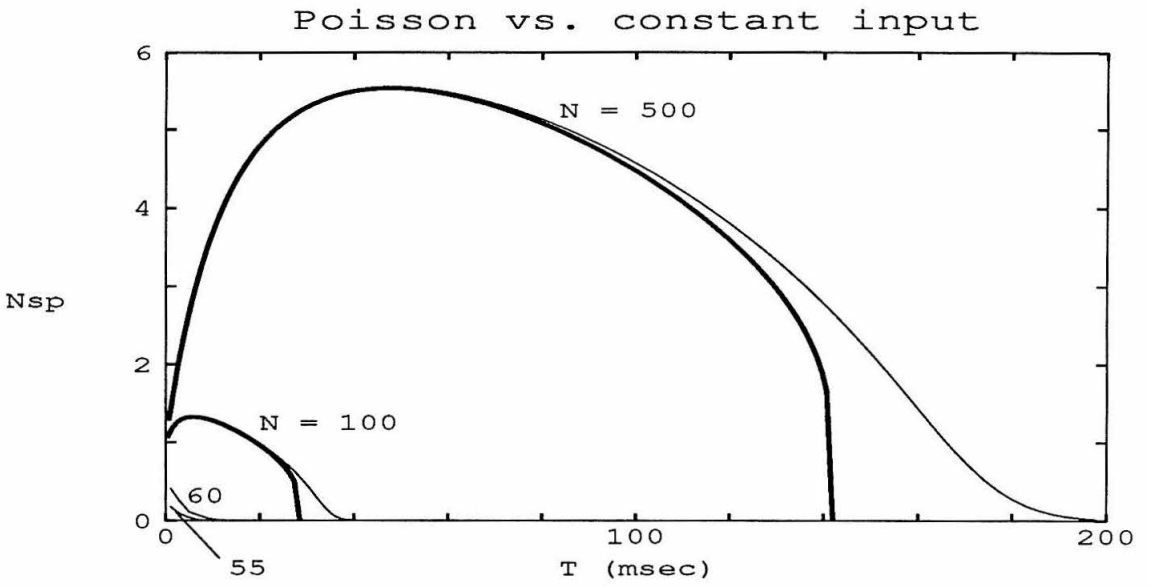


Figure 4.4: Number of output spikes for Poisson distributed (thin lines) and for constant synaptic input (thick lines) for the leaky integrate-and-fire model with current input (see case 3 in Table 4.1) as a function of the desynchronization interval $T$. The different curves are for different values of $N$, i.e., the average number of synaptic inputs arriving during the interval $T$. For $N < N_t = 60$ or for $T > T_{cut-off}$, fluctuations in the random input can always push the potential above threshold, while the model ceases to respond to constant input. For $T < T_{cut-off}$ and $N > N_t$, i.e., for large input rates $\lambda = N/T$, the two models agree closely. For $N \leq N_t$, the analytical approximation deviates significantly from the numerical one due to truncation error, and only the latter is shown for $N = 55$ and 60.

---

effects of $T_{rp}$ (favoring larger values of $T_{opt}$) and $G$ (favoring smaller values).

### 4.2.3 Synchronicity for Poisson-distributed input

Up to now we considered synaptic input to arrive at a constant rate. Let us now analyze the more realistic situation of Poisson distributed current inputs with a mean rate $\lambda = N/T$ to the leaky integrate-and-fire model over a fixed temporal interval of duration $T$. Intuition has it that if the stimulation is intense, driving $V$ towards

$V_t$ much faster than $\tau_m$, the fine structure of the input should not matter, only its average rate. However, if the stimulation is less intense so that $V$ approaches $V_t$ very slowly, then the random fluctuations of a Poisson process may matter. In the extreme case where the asymptote for $V$ is below threshold, regular input will never cause the neuron to spike, while Poisson fluctuations will effect occasional spikes.

An analytic expression for $T_{spike}$ was obtained by M. Usher [Bernander et al., 1993c] and $N_{sp}$ was obtained using eq. (4.3. for large $N$ of 100 and 500. For small $N$ (55 and 60) the continuous approximation formula, eq. (4.3, breaks down, and instead simulations were used to compute the curves. The resulting $N_{sp}$ as a function of $T$ are graphed in Fig. 4.4 together with the curves for regular (constant) input. We can see two important differences at the two extremes of the axes. One difference is when, on average, less than $N_t$ inputs are present. For constant synaptic input, no spikes are generated for $N < N_t = 60$ and $N_{sp} \neq 0$ only for $T = 0$ at $N = 60$. However, for Poisson distributed input, there always exists a non-zero probability that stochastic fluctuations in the input will carry the potential above threshold. Likewise, Poisson input can in principle, for large values of T, always exceed the threshold $N_t$, while this is not possible for regularly timed input (where the cutoff value of T is given by $T_{cut-off} = \tau_m N/N_t$), resulting in a "tail" for large values of $T$. For all other values of $T < T_{cut-off}$ and $N > N_t$, the constant synaptic input closely approximates Poisson distributed input. In other words, for large enough values of the synaptic input rate $\lambda = N/T$, Poisson input can be approximated by constant input (case 3 in Table 4.1).

## 4.3 Synchronicity in a detailed model of a pyramidal cell

To what extent are our results due to the very simple neuronal model we have been using? After all, I&F neurons have a fixed threshold, no dendritic tree, no voltage- and time-dependent conductances and no synaptic dynamics.

We simulated the detailed compartmental model of the layer V pyramidal cell.

A simulation was run on the full model for $N = 200$ to $1,000$ fast, excitatory, voltage-independent AMPA synapses distributed throughout the dendritic arbor in accordance with the known anatomical distribution (Fig. 4.2b). For $N = 1,000$ the same basic effect is observed as in the leaky I&F model with refractory period. In the case of total synchronization, $T = 0$, only two spikes are produced due to overcrowding. A maximum of 5 spikes is obtained for $T = 25 - 65$ $msec$ and the response decreases to 0 spikes for $T = 200$ $msec$. When $N$ is reduced to 300 synapses or less, the peak in $N_{sp}$ disappears. Note, however, that now $N_{sp}$ is essentially flat around the origin, implying that the cell is not highly tuned to small $T$ (for the $\tau_m = 17$ $msec$ used here).

To assess to what extent this behavior is due to the fact that synaptic input increases the membrane conductance—rather than injecting a current into the cell—we approximated this condition by reducing the synaptic conductance change $G_{max}$ for each synapse by a factor 10, while increasing the driving force $E_{rev} - V$ by a factor 10. This removed any saturation in the dendritic tree, and thus more current was injected during stimulation (curves not shown). The main difference was that a few more spikes was obtained at every $T$, while the $N_{sp}$ still peaked for approximately the same values of $T$.

Substituting NMDA synapses for half of the AMPA synapses had the effect of

broadening the peak, as well as making it less pronounced. This can be explained by the much slower time course of the NMDA synapses ($\tau_{m_{decay}} = 40\ msec$), which is conceptually similar to desynchronizing the much faster AMPA synapses. No obvious cooperative effects were seen due to the negative input conductance of the NMDA synapses.

## 4.4 Correlated synaptic input

In the previous sections, we assumed that $N$ independent synapses were each activated only once (*single-shot case*). However, synaptic input is repetitive (cells fire more than once) and can be correlated. How are our previous results affected by such correlated activity? The degree of correlation in the input may vary in accordance with two factors: the temporal spread of synchronization ($T$ as expressed by the width of the cross-covariance function between input neurons), and the fraction of neurons, $r$, that are synchronized. By varying each of the factors independently, one can interpolate between a fully synchronized and a fully desynchronized input.

If each of the $N$ input neurons is firing with a Poisson probability distribution with mean rate $f_{in}$, two extreme situations can be considered:

- If none of the neurons are correlated ($r = 0$), the input consists of a single Poisson process of events of height $\Delta V$ and rate $\lambda = Nf_{in}$. The mean interspike interval and output firing rate can then be estimated equation for Poisson inputs and will be denoted by $f_{out,0}$.

- When all ($r = 1$) neurons are perfectly correlated ($T = 0$), the input is equivalent to a single Poisson stream of events of height $N\Delta V$ and rate $\lambda = f_{in}$. Assuming $N > N_t$ (otherwise the neuron will rarely fire), each synchronized event triggers one spike (the refractory period prevents multiple spikes for such

synchronized input currents) and the output frequency is equal to the input frequency $f_{in}$.

The intermediate situation ($rN$ neurons perfectly correlated with $T = 0$, and the rest independent) interpolates between these two limiting cases as shown in Fig. 4.5. Thus increasing the number of perfectly synchronized and correlated neurons is only advantageous if the response in the uncorrelated case is lower than $f_{in}$, that is if $f_{out,0}(N, f_{in}) < f_{in}$. We derive the border between these two domains by finding those values of $N$ and $f_{in}$ where this inequality turns into an equality. As we saw in section 4.2.3, if $\lambda$ is large enough, the value of $T_{spike}$ for Poisson input is well approximated by that of constant input given by case 3 in Table 4.1. Using this latter result as well as $f_{out,0} = 1/(T_{spike} + T_{rp})$ and $\lambda = Nf_{in}$ we arrive at

$$N = \frac{N_t}{\tau_m f_{in}} \times \frac{1}{1 - e^{-(1/f_{in} - T_{rp})/\tau_m}} \tag{4.6}$$

This expression, then, demarcates the two domains. For values of $N$ and $f_{in}$ below and to the left of this border (Fig. 4.5a), increasing the number $rN$ of correlated neurons enhances the output rate while above and to the right of this curve increased synchronization reduces the output rate. The latter effect is due to the fact that at higher $N$ and $f_{in}$, input spikes are rendered ineffective due to the refractory period.

For low values of the input frequency relative to the leak term, i.e., when $f_{in} << 1/\tau_m$, the $f_{in}$ term in the exponent in the right hand of eq. 4.6 side can be neglected, leading to an inverse relationship between $N$ and $f_{in}$ and to a hyperbolic curve for small values of $f_{in}$ in Fig. 4.5a.

What effect does the temporal width of the cross-covariance function $T$ have on postsynaptic firing frequency? We approached this question by numerically evaluating $f_{out}$ for a variety of different settings in the relevant 4-dimensional space spanned by $r, T, N$ and $f_{in}$. In the simulations shown in Fig. 4.5b,c, we compute $f_{out}$ as a function

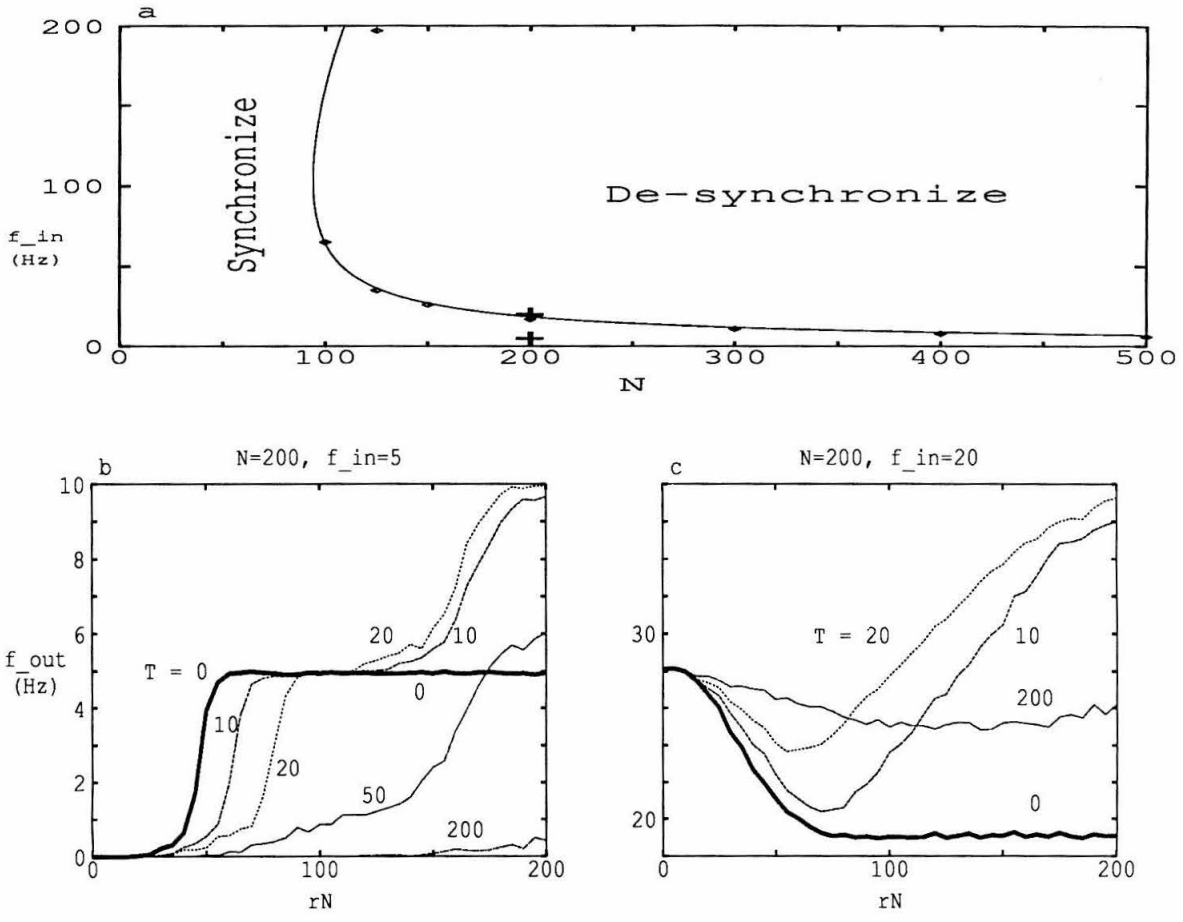


Figure 4.5: Simulation results for the response rate $f_{out}$ of a leaky I&F neuron with current input ($\tau_m = 17\ msec, T_{rp} = 2\ msec$, and $N_t = 60$) to a varying fraction $rN$ of correlated inputs out of a total population of $N = 200$ input neurons. Bold curves in (b) and (c) highlight the response when the correlated neurons are perfectly synchronized ($T = 0$), while thin lines correspond to non-zero values of the desynchronization interval $T$ as indicated. **(a)** Border in the $f_{in} - N$ plane delimiting the parameter range for which perfect synchronization at $T = 0$ reduces the firing rate from the opposing situation (see eq. (5), diamonds represent simulation results). For small values of either $N$ (as long as $N > N_t$) or $f_{in}$, synchronization always increases $f_{out}$. **(b)** For $f_{in} = 5\ Hz$, synchronization (in $r$) always increases the firing frequency. **(c)** For larger values of the input frequency, here $f_{in} = 20\ Hz$, too much or too little temporal synchronization decreases $f_{out}$.

of the number of synchronized inputs using the leaky I&F model with current inputs.

Fig. 4.5b shows the response rate for a population of $N = 200$ input neurons, all firing with a mean input rate $f_{in} = 5\ Hz$. We are here well in the domain (see the lower cross in Fig. 4.5a) where perfect ($T = 0$) synchronization will lead to an increase in the firing rate. If none of the inputs are correlated, we are in the first of the limiting cases discussed at the beginning of the section with $f_{out,0} = 0$. As $rN$ increases, the unit starts to fire. At perfect levels of temporal synchronization, $f_{out}$ steeply rises in the neighborhood of $rN \approx N_t$ and saturates for large values of $rN$ at the firing rate $f_{in}$ (second limiting case discussed above), since all 200 inputs fire at once, causing only a single postsynaptic spike per input volley. For a finite desynchronization interval, here $T = 10$ and $20\ msec$, the steep rise in $f_{out}$ occurs at somewhat larger values of $rN$ than for perfect synchronization. However, as $r$ continues to increase, the firing rate increases to almost twice the frequency compared to perfectly synchronized input ($T = 0$), expressing the fact that two spikes are fired on average per input volley (due to the temporal spread of all 200 inputs over 10 or $20\ msec$). For larger desynchronization intervals (here 50 and $200\ msec$), the leaky membrane limits the response of the I&F unit and the postsynaptic response remains small.

Fig. 4.5c illustrates the reverse case when the input rate is so high (here $f_{in} = 20\ Hz$), that temporal synchronization leads to a reduction in postsynaptic response (see the upper cross in panel a). Here, increasing the fraction of perfectly synchronized neurons $rN$ causes a drop in $f_{out}$, except when a $T = 10\ msec$ desynchronization interval is being used for large values of $rN$. The fact that when all neurons are correlated at the endpoints $rN = 200$ of Fig. 4.5b,c, the optimal desynchronization interval is between $10-20\ msec$ can be understood from our analysis of the single-shot case in section 2.

## 4.5 Discussion

A number of proposals for linking neuronal firing with higher-level "emergent" properties explicitly or implicitly assume that synaptic input synchronization always leads to an increase in postsynaptic firing frequency compared to the desynchronized case (see the Introduction). We investigated this hypothesis in detail. Before we summarize and interpret our results, let us state the principal limitations of our study. We investigated the firing properties of two distinct neuronal models: the analytically treatable integrate-and-fire (I&F) family of integrator models [Knight, 1972] as well as a biophysically detailed compartmental model of an anatomically reconstructed cortical pyramidal cell. This model assumes that no voltage-dependent membrane currents are present in the dendrites (with the exception of the voltage-dependent NMDA synaptic input). We did not consider bursting cells that can generate two or more fast spikes in response to an appropriate synaptic input nor voltage-dependent sodium or calcium currents in the dendritic tree. Both situations render any analysis such as the one carried out here considerably more complex. Sufficiently fast and strong dendritic nonlinearities, such as postulated by Softky [Softky, 1993], can in principle render the cell susceptible to specific temporal arrangements of synaptic input (i.e., specific values of $T$) and would invalidate our analysis. This was beyond the scope of the present study; we provide the baseline against which the performance of more complex neuronal models need to be evaluated.

We assume that synaptic input is either constant or distributed according to a Poisson process. Detailed analysis of the power spectrum, interspike interval distribution and firing variability of non-bursting cortical cells in the awake and behaving monkey firing at high rates supports the Poisson hypothesis [Softky and Koch, 1993, Bair et al., 1993]. Finally, we only consider the effect of excitatory synaptic input, neglecting the effect of synchronization of inhibitory synaptic input. However, in as

far as steady-state conditions are met (i.e., for large enough values of $\lambda$), the current due to the inhibitory synaptic input can be subtracted from the excitatory current, yielding a net effective input current (or input rate) and all of our arguments apply.

Both the I&F models as well as the detailed biophysical model display the same behavior: if the entire excitatory synaptic input is correlated ($r = 1$; single-shot case), temporal synchronization (small values of $T$) only increases the output firing rate if the average number of spikes (as characterized by a Poisson process with rate $\lambda = N/T$) is on the order of the number of inputs $N_t$ needed to reach threshold (Fig. 4.2). For rates significantly larger than $N_t/T$, there will be a non-zero, optimal desynchronization interval. As witnessed in Fig. 4.3, this optimum interval increases linearly with $N/N_t$ and sub-linearly with $\tau_m/T_{rp}$. For desynchronization intervals larger than $T_{opt}$, the response is reduced due to temporal dispersion induced by the membrane leak, while the refractory period limits the usefulness of high synchronization. Any neuronal model with a refractory period will display such a tendency against *overcrowding* of synaptic inputs. It should be noted that such overcrowding can occur at what is believed to be physiological levels of synaptic input. $1,000$ synaptic inputs impinging onto our pyramidal cell within 50 $msec$ give rise to twice the number of spikes than the same number of inputs applied instantaneously ($T = 0$).

Because of the similarity between the I&F and the detailed models, we only use the former when we investigate the more complex situation arising during repetitive input when only a fraction $r$ of the $N$ input synapses are correlated (with the width of the central peak in the cross-covariance function characterized by $T$). This is the situation Murthy and Fetz (1993) studied. Assuming always $T = 0$, they conclude that synchronization is only useful when $N, \Delta V$ or $f_{in}$ are not too large. We quantify (Fig. 4.5a) and extend their results to non-zero desynchronization intervals, explaining the effect in terms of the membrane leak and the refractory period. We explicitly found (Fig. 4.5a) the domain in $N, f_{in}$ space for which correlated inputs enhance the

response. For values of $f_{in}$ and $N$ below the border displayed in Fig. 4.5a, and if the number of correlated inputs $rN < N_t$ ($N_t$ is about 60 as estimated by biophysical parameters from our reconstructed neuron), perfect temporal synchronization (with a zero-width peak) is advantageous (Fig. 4.5a). In this regime, the assumption that high levels of firing synchronization—as expressed by sharp peaks in the cross-covariance function—plays a significant role in various perceptual processes is valid [Milner, 1974, Abeles, 1991, Gray et al., 1989, Crick and Koch, 1990, Kreiter and Singer, 1992]. If $rN > N_t$, perfect synchronization ceases to be optimal due to overcrowding. In this regime, small enough values of the average input frequency $f_{in}$ in combination with small desynchronization intervals ($T \approx 5 - 10\ msec$; Fig. 4.5c) enhances the response rate compared to perfect or no temporal synchronization. Thus, cross-covariance functions with pronounced but wide peaks can indeed be more advantageous than extremely narrow central peaks in the cross-covariance (e.g., cell pairs of the $T$ type in [Nelson et al., 1992]. We conclude that (in the absence of fast and powerful active dendritic conductances) if the synchronization of the firing of cortical cells is indeed a crucial signal underlying higher-level perceptual processes, the brain must take care to assure that only some minimal number of neurons are simultaneously active.

# Chapter 5

# Synaptic Background Activity Controls Spatio-Temporal Integration

## 5.1 Introduction

The standard one-dimensional Rall cable model of nerve cells assumes that their electrotonic structures do not change in response to synaptic input [Rall, 1964, Rall, 1969, Rinzel and Rall, 1974, Rall et al., 1992]. This model is used in a great number of both theoretical and anatomical-physiological structure-function studies. In particular, the membrane time constant, $\tau_m$, and the somatic input resistance, $R_{in}$, are used to characterize single cells and are often thought of as static properties of the neuron. In this chapter we will show that the total synaptic conductance is likely to overshadow the intrinsic conductances, even at rest when only a low spontaneous background firing rate is present. The two key assumptions are that $R_m$ is much higher than previously thought, and that a large number of synapses are modeled as conductance

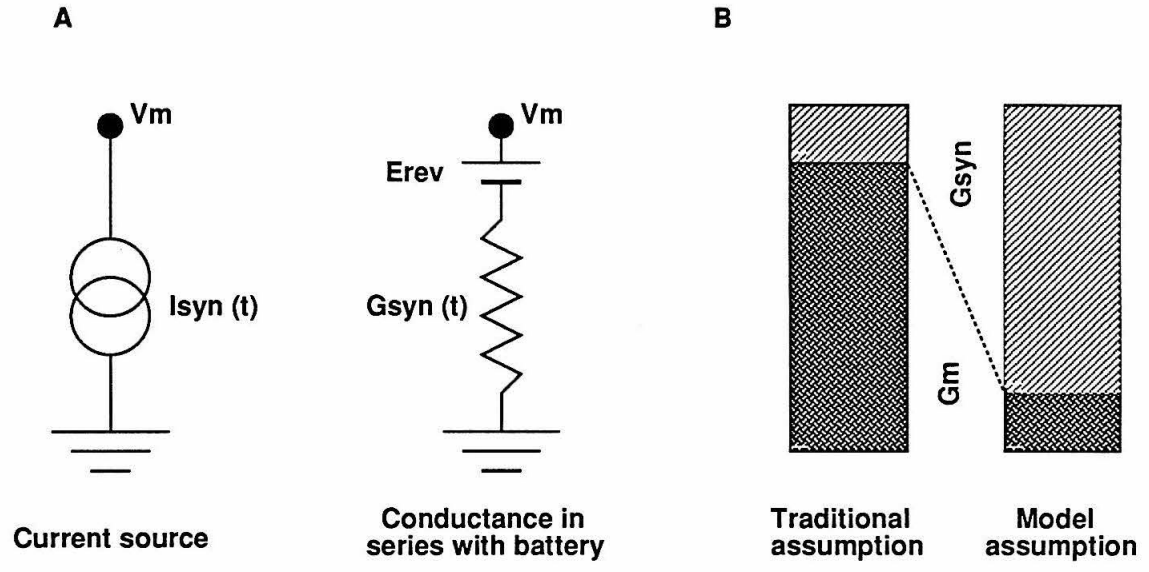


Figure 5.1: Model assumptions. **(a)** Two models of synaptic input. The current source always injects the same current, independent of membrane potential, and is more amenable to analytic treatment. **(b)** Schematic of the relative contributions to the membrane conductance $G_{\mathrm{m,eff}} = G_m + G_{\mathrm{m,syn}}$. Traditionally, the synaptic conductance was assumed small compared to the membrane leak.

changes, not current sources as in most previous analyses [for instance, Rinzel and Rall, 1974]. Significant parts of this work have previously been published elsewhere [Bernander et al., 1991].

As mentioned in chapter 2, it was previously thought that the passive membrane resistance was on the order of 2–20 $k\Omega cm^2$ and values in this range were typically chosen in modeling studies [Koch et al., 1982, Yamada et al., 1989, Koch et al., 1990, Traub et al., 1991, Lytton and Sejnowski, 1991]. Recent patch-clamp recordings and modeling studies have suggested much larger values of 100–600 $k\Omega cm^2$ [Shelton, 1985, Andersen et al., 1990, Major et al., 1990, Spruston and Johnston, 1991, Segev et al., 1992]. This, in conjunction with the fact that neocortical pyramidal cells receive on the order of 5,000–20,000 synapses [Thomas et al., 1980, Larkman, 1991b, Anderson et al., 1993b] forms the basis of our thesis that synaptic background activity will overwhelm the intrinsic conductances. A brief counting example will demonstrate this. The total area of the layer 5 cell is 55,000 $\mu m^2$. Assuming the older estimate of $R_m$=10 $k\Omega cm^2$, the total leak conductance will be $G_{leak,abs} = 55\ nS$. To obtain the same conductance from synaptic input, $G_{syn,abs}$, we need 27,500 inputs per *sec.* Ignoring background activity, this is obtained, for example, by 275 synapses firing at 100 $Hz$. Inputs of this magnitude have rarely been studied in the past and therefore it was logical to model inputs as current sources (see Fig. 5.1(a)). On the other hand, if $R_m$=100 $k\Omega cm^2$, $G_{leak,abs}$ is only 5.5 $nS$ corresponding to only 2,750 inputs per *sec.* If background activity is not ignored, then all 4,000 excitatory inputs need to fire at only 0.69 $Hz$ to match $G_{leak,abs}$. Note that 4,000 is a conservative estimate and that additional inhibitory inputs will add to the background activity. To summarize, the *effective* membrane conductance derives from two components:

$$G_{\mathrm{m,eff}} = \frac{1}{R_{\mathrm{m,eff}}} = G_m + G_{\mathrm{m,syn}};$$

while it was previously assumed that $G_m >> G_{\mathrm{m,syn}}$, we argue in this chapter for the opposite inequality, $G_m << G_{\mathrm{m,syn}}$. Fig. 5.1(b) shows this schematically; in traditional models, a factor 2 change in $G_{\mathrm{m,syn}}$ has a small impact on $G_{\mathrm{m,eff}}$, while in our model it has a large effect.

Previous work along these lines is very recent. Holmes and Woody study the effect of inhomogeneous input distributions, carefully adjusting the input level to yield a constant somatic input resistance and resting potential (except in one case where the input rate is reduced). They do not focus on $f_b$ as the parameter to vary, and changes in electrotonic structure is therefore less compelling. Simultaneously and independently of us, Abbott noted "the synaptic conductance may be comparable to or even larger than the membrane conductance" [Abbott, 1991]. He uses a single cable model to study the *firing rate problem* and notes that electrotonic length $L$ will depend on $G_{\mathrm{m,syn}}$. However, the impact on spatiotemporal integration in terms of $R_{in}$ and $\tau_m$ is not discussed. Finally, Rapp et al. did a simulation study independently of us, using a very similar approach for cerebellar Purkinje cells [Rapp et al., 1992]. They find similar dependencies on $f_b$ for $R_{in}$, $\tau_m$, $V_{rest}$, and $L$.

## 5.2 Methods

### 5.2.1 Measuring input resistance, $R_{in}$

The input resistance, $R_{in}$, can be defined either as an instantaneous resistance, $R_{in,inst}$, or as a steady state resistance, $R_{in,ss}$.

Assume, for a moment, that the cell is highly compact and can be approximated with a single compartment. A voltage clamp is used to make a small voltage step, $\Delta V_m$, and the change in clamp current, $\Delta I$, is measured. Assume further that the voltage clamp is much faster than any of the time constants of the active conduc-

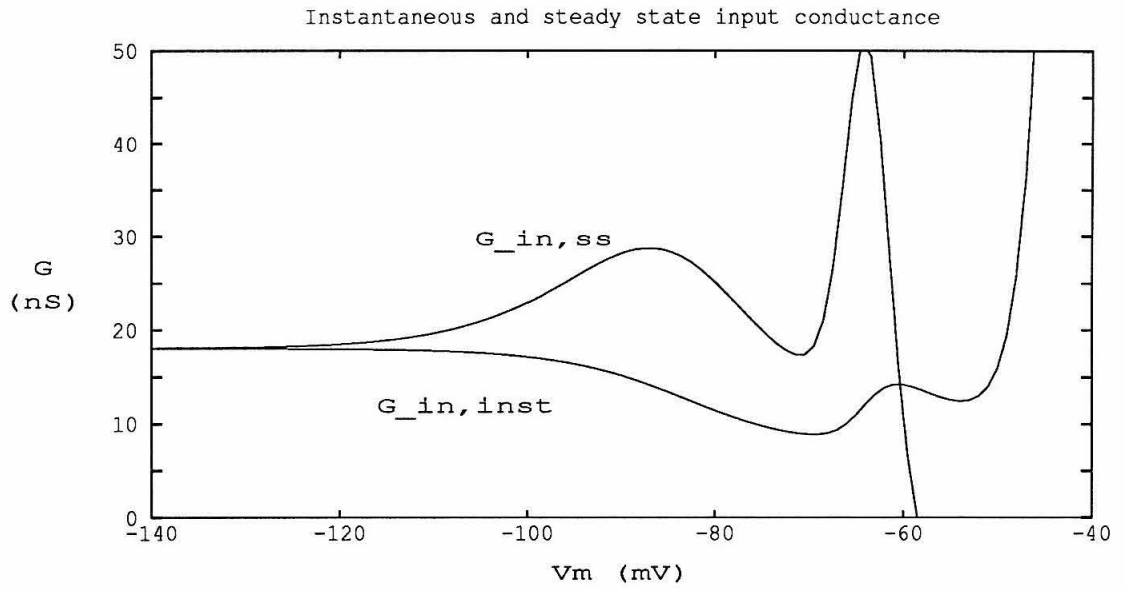


Figure 5.2: Comparison of two definitions of input conductance: instantaneous, $G_{in,inst}$, and steady state, $G_{in,ss}$. See text for definitions and details.

---

tances. $\Delta I$ will initially jump and then slowly change as active conductances relax. $\Delta I_{early}$ and $\Delta I_{late}$ denote the instantaneous (not including the capacitive transient) and steady state changes in clamp current. The *instantaneous input conductance* is then defined as the total parallel conductance:

$$G_{in,inst} = \frac{\Delta I_{early}}{\Delta V_m} = \Sigma_i G_i(V_m),$$

where most of the $G_i(V_m)$ are voltage-dependent, but also include the passive "leak" conductance. However, in an extended, branched cable structure where a high-quality space clamp is impossible, the equalization time constant may be larger than the particle time constants, as is the case in our model. It will then be impossible to measure $\Delta I_{early}$. Instead, the steady state value, $\Delta I_{late}$, can be used to define the *steady state input conductance*:

$$G_{in,ss} = \frac{\Delta I_{late}}{\Delta V_m} \approx \frac{dI_{late}}{dV_m} = \Sigma_i[G_i(V_m) + \frac{dG_i}{dV_m} \cdot (V_m - E_{rev,i})].$$

The apparent conductance for channel type $i$ is thus a sum of the steady state conductance, $G_i(V_m)$, and a correction term, $\frac{dG_i}{dV_m} \cdot (V_m - E_{rev,i})$. The magnitude of the correction term can often be much larger than the steady state conductance and also force it to become negative. If the net sum of all conductances is negative, a regenerative (positive feedback) condition occurs, and the membrane potential runs off.

Fig. 5.2 compares the two definitions of input conductance for a single-compartment version of the standard model. For very hyperpolarized potentials, all active conductances are either turned fully on or off. At this point, the correction term is zero and the two definitions give identical $G_{in}$. For larger values of $V_m$, they differ more, and as threshold for spike generation is approached, the difference is dramatic. Note that while $G_{in,inst}$ is always positive, $G_{in,ss}$ may be either positive or negative.

Throughout this thesis, the steady state conductance, $G_{in,ss}$ is used to compute input resistance $R_{in} = 1/G_{in,ss}$.

### 5.2.2 Measuring the membrane time constant, $\tau_m$

The membrane time constant, $\tau_m$, is a measure of how fast the cell reacts to electrical changes and for how long the cell "remembers" information.

It is straightforward to measure $\tau_m$ in a passive, noise-free cell. Unfortunately, neurons have a limited passive region at best, and the membrane potential as well as the recording equipment are bedeviled with noise that drowns out small exponential transients. Even in simulations, the precision of the arithmetic eventually deteriorates for very small transients.

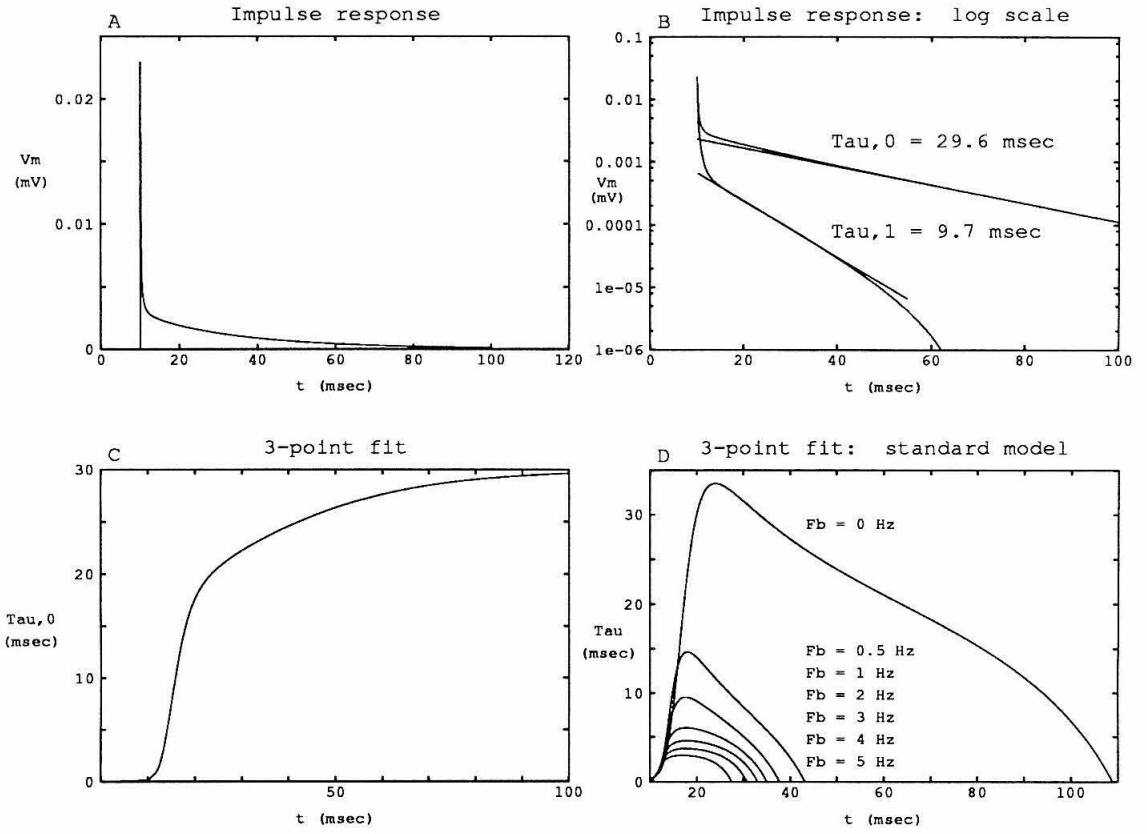


Figure 5.3: Measuring time constants by fitting exponentials to impulse response. **(a)** Impulse response in passive pyramidal cell with uniform $R_m$=30k$\Omega cm^2$. **(b)** Peeling of first two time constants of curve in (a). Note semi-log plot. **(c)** 3-point fit to curve in (a). **(d)** 3-point fits for active pyramidal cell at different levels of synaptic background activation.

### Exponential "peeling"

The impulse or step response can be decomposed into a series of exponentials:

$$V(t) = C_0 e^{-t/\tau_0} + C_1 e^{-t/\tau_1} + ...,$$

where $\tau_0 > \tau_1 > \tau_2 ....$ For a passive neuronal structure with uniform $R_m$, the largest time constant, $\tau_0$, equals the membrane time constant $R_m \cdot C_m$. This expansion forms the basis for the method of "peeling," a method originally used by physicists studying multiple radioactive decay, but also widely used among neurophysiologists after an in-depth treatment by Rall [Rall, 1969]. The peeling method is illustrated in Fig. 5.3. Fig. 5.3(a) shows the voltage transient following a delta current input (a small charge was deposited in the soma at t=10 *msec*). Fig. 5.3(b) shows the same curve in a semi-log plot (top curve). The tail of the curve is linear and thus the decay is at this point dominated by a single exponential. A least-squares fit to this part of the curve yields a time constant of $\tau_0 = 29.6$ *msec*, which is close to the calculated value $R_m \cdot C_m = 30$ *msec*. Next, this exponential is subtracted and the resulting curve is plotted (bottom curve in Fig. 5.3(b)). The slope of the linear tail of this second curve gives a time constant of $\tau_1 = 9.7$ *msec*. Yet higher time constants can theoretically be extracted, but in practice, noise often prohibits this.

For a cylinder with sealed ends, $\tau_0$ and $\tau_1$ can be used to find the electrotonic length of the cylinder[1]:

$$L = \frac{\pi}{\sqrt{\frac{\tau_0}{\tau_1} - 1}}.$$

[1]This expression is easily derived by solving the cable equation, $V''_{XX} = V + V'_T$, using the separation of variables technique. Solutions are of the form $V(X,T) = (A \sin \alpha X + B \cos \alpha X) \cdot e^{-(1+\alpha^2)T}$. The sealed-end boundary condition forces $\alpha$ to take on discrete values $\alpha_n = n\pi/L$, where $n$ is a non-zero integer.

This formula is often used to estimate the compactness of a neuron, even though a dendritic tree can rarely be collapsed to an equivalent cylinder and one end is not sealed but attached to the soma.

There are several practical problems that may arise. First, due to noise, the tail of the impulse response can only be used up to some limited value of t, often in the range of 20–40 *msec* [Laurent, 1990, e.g.]. At this point there might still be contamination from higher time constants. For example, in Fig. 5.3(b), if only the time interval 10–20 *msec* is used to fit $\tau_0$, it is underestimated to be 24.6 *msec*, even though this region appears deceivingly linear in a semilog plot. $\tau_1$, meanwhile, decreases from 9.7 to 2.3 *msec*, changing the estimate of $L$ from 2.2 to 1.0 $\lambda$. While the estimate of $\tau_0$ is still reasonably accurate, the estimates of $\tau_1$ and $L$ change by factors of 4 and 2, respectively. Fig. 5.3(c) shows how 3-point fits[2] will give different values of $\tau_0$ as $t$ increases. Thus, time constants might often be larger than estimated in the literature.

Another problem is posed by the presence of active conductances. Many cell membranes, such as the squid giant axon originally studied by Hodgkin and Huxley [Hodgkin and Huxley, 1952] have a linear region of membrane voltage where a passive analysis is valid. Our model cell does not have such a linear region, except for unphysiological values of $V_m$, such as above -10 $mV$ and below -110 $mV$. Sample step responses are given in Fig. 5.4. At rest (Fig. 5.4(a)), the response overshoots and sags, indicative of a phenomenological inductance. The tail displays "ringing," that is, the response is a damped oscillation that crosses zero repeatedly, and hence cannot be fitted by a single exponential. 3-point fits are shown in Fig. 5.3(d) for different background activations. In these curves, $\tau_m$ never levels out to a constant

[2] A 3-point fit uses only three consecutive data points to fit a line to the semilog plot. While this is straightforward in a noise-free simulation, it will rarely be practical for experimentally recorded traces.

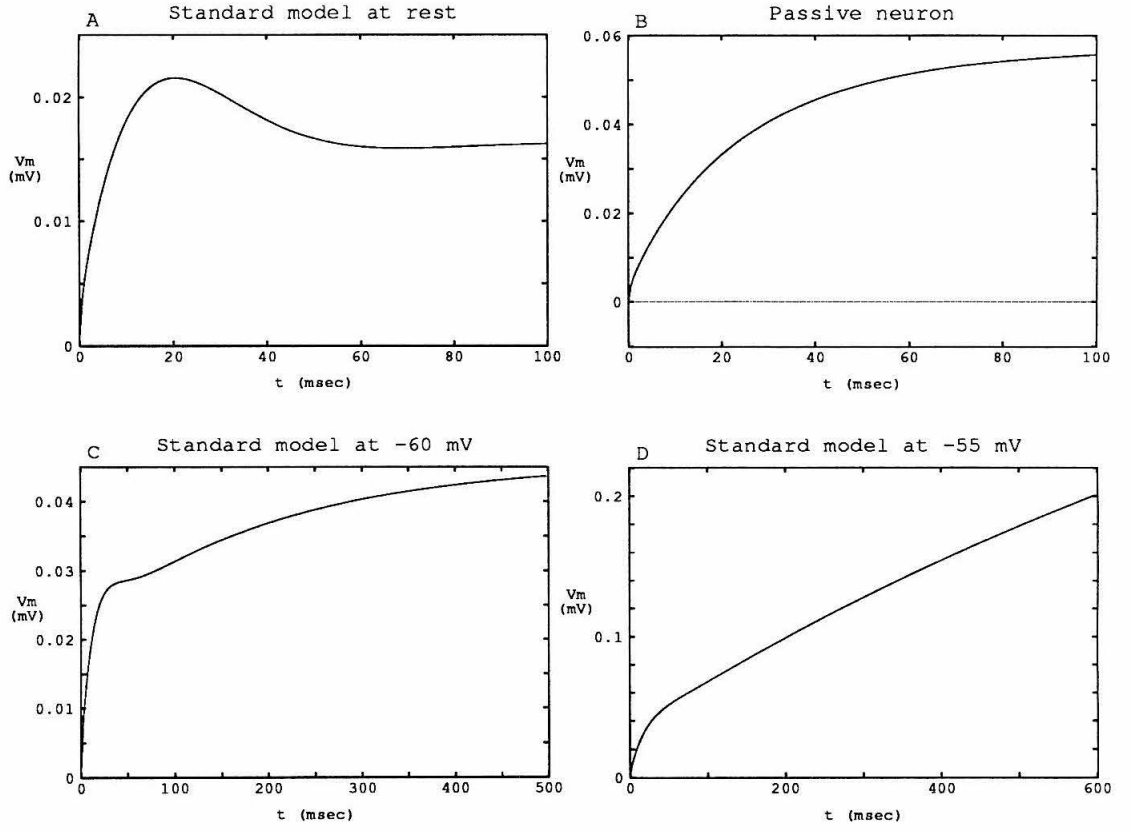


Figure 5.4: Sample current step responses. **(a)** Standard model ($f_b$=0.5 $Hz$). **(b)** Standard model without active conductances. **(c)** Standard model, depolarized to -60 $mV$. **(d)** Standard model, depolarized to -55 $mV$. Note different time scales.

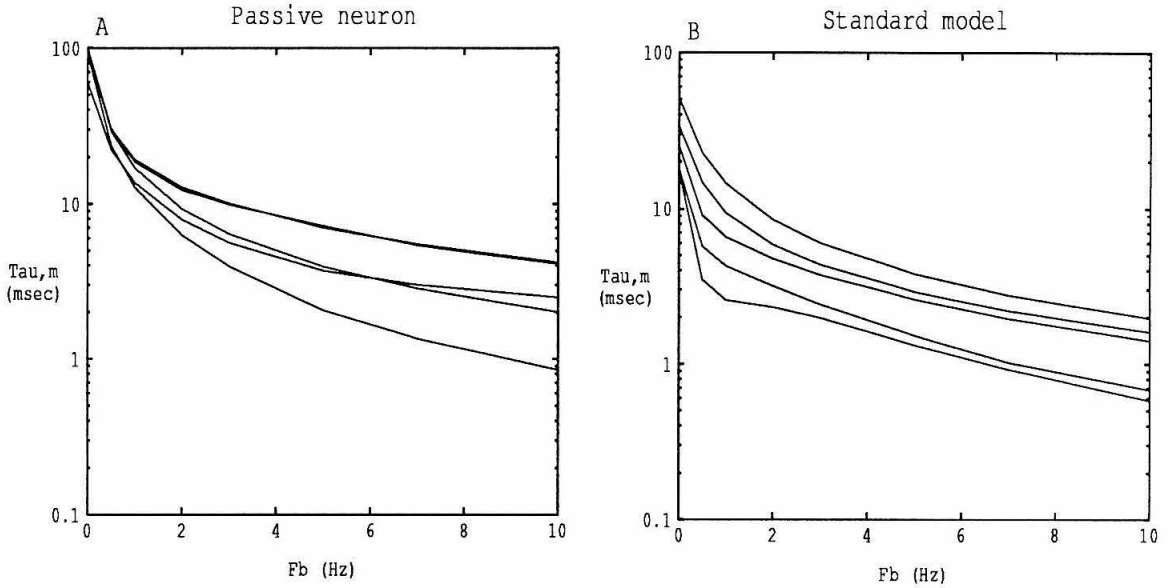


Figure 5.5: Comparison of five $\tau_m$ measures for different levels of background activity. **(a)** Standard model without active conductances. Top to bottom (right end): $\tau_{\delta,late}$ and $\tau_{step}$ (almost identical), $\tau_{\delta,early}$, $\tau_{R_mC_m}$, $\tau_{\frac{1}{e},peak}$ and $\tau_{\frac{1}{e},ss}$ (identical). **(b)** Standard model. Top to bottom: $\tau_{\delta,late}$, $\tau_{step}$, $\tau_{R_mC_m}$, $\tau_{\frac{1}{e},peak}$, $\tau_{\frac{1}{e},ss}$.

---

value, but decreases to zero and goes negative. As an estimate of $\tau_\delta$ (defined below) in this active case, we chose the maximum value for the 3-point fit. As was seen in the passive case, this is likely to be an underestimate, but will have to serve as a working definition. For some depolarized values of $V_m$, the response was non-inductive, as in Fig. 5.4(c,d). The latter part of these curves are fitted by very slow exponentials on the order of 1 *sec.* This effect disappears when the A current, $I_A$, is removed.

### 5 definitions of $\tau_m$

We now proceed to define five different measures of the time constant. For a leaky integrator, that is, a single passive R-C compartment, all measures give the same value, but they will be shown to vary for extended and active structures.

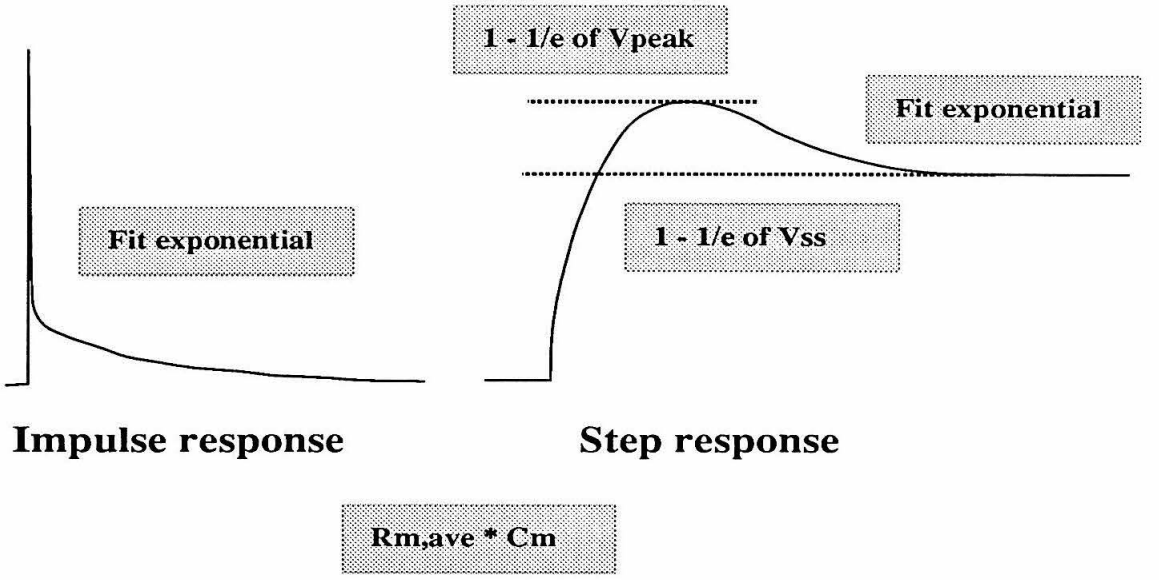


Figure 5.6: Five definitions of $\tau_m$. See text for details.

---

- $\tau_\delta$. Impulse response: fit exponential to tail.
- $\tau_{step}$. Step response: fit exponential to tail.
- $\tau_{\frac{1}{e},peak}$ Step response: time at which $V(t)$ has reached $(1-\frac{1}{e})$ of the *peak* response.
- $\tau_{\frac{1}{e},ss}$. Step response: time at which $V(t)$ has reached $(1-\frac{1}{e})$ of the *steady state* response.
- $\tau_{R_mC_m}$. The average value of the product $R_{\text{m,eff}} \cdot C_m$ throughout the cell, weighted by area. ($R_{\text{m,eff}}$ includes a contribution from the average synaptic activation.)

These measures are all illustrated in Fig. 5.6.

For a passive, lumped cell model both the impulse response and the step response will give a single exponential, which reaches $(1-\frac{1}{e})$ of its final value after one time constant of decay. All five measures will be identical.

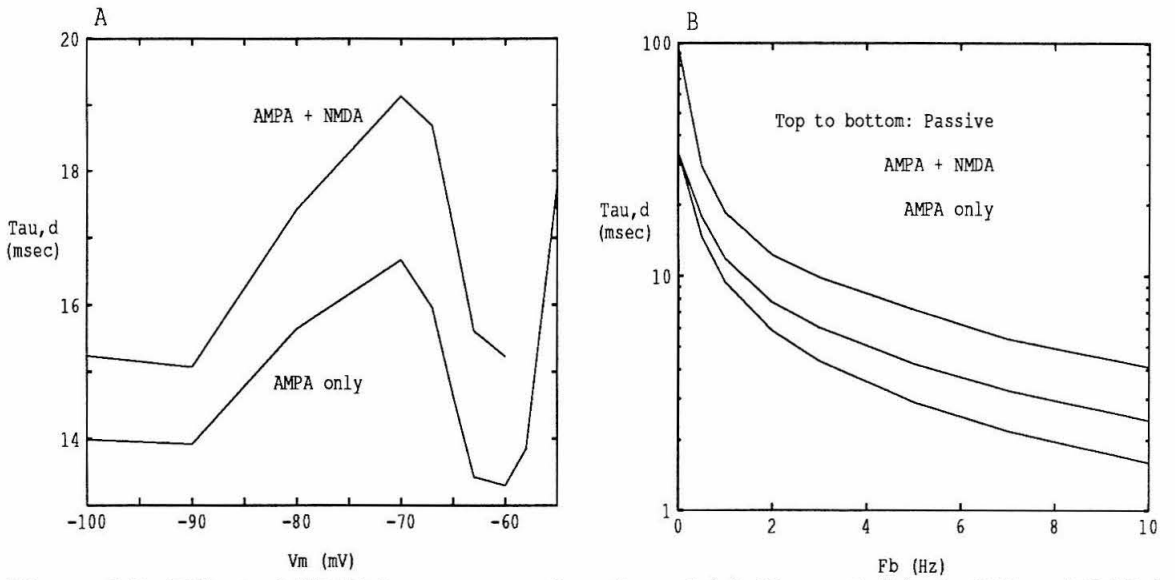


Figure 5.7: Effect of NMDA on $\tau_\delta$ as a function of (a) $V_m$, and (b) $f_b$. When NMDA synapses were used, they were substituted for half of the AMPA synapses.

---

For a passive, extended structure with uniform $R_m$, the initial decay will be faster, involving smaller time constants ($\tau_1$, $\tau_2$, etc.). The tail of the impulse and step responses will still equal $\tau_{R_mC_m}$, but $\tau_{\frac{1}{e},peak}$ and $\tau_{\frac{1}{e},ss}$ will give smaller values, since the $(1-\frac{1}{e})$ point will be approached faster. Further, if $R_{\text{m,eff}}$ is not uniform throughout the cell, $\tau_{R_mC_m}$ may be different from $\tau_\delta$ and $\tau_{step}$.

When active (non-linear) conductances are introduced and linearized, they give rise to phenomenological capacitances and inductances [Mauro et al., 1970, Koch, 1984]. A capacitance will tend to slow down the response of the cell, while an inductance will speed it up and cause an overshoot and sag in the step response. This is commonly seen in neurons [Mason and Larkman, 1990, e.g.]. When the response overshoots, $\tau_{\frac{1}{e},peak}$ and $\tau_{\frac{1}{e},ss}$ will obviously differ, the former always being larger than the latter.

Fig. 5.5(a) compares the different measures of $\tau_m$ for a passive neuron that receives a background synaptic activity that varies from 0 to 10 $Hz$ ($x$ axis). The top two

curves are almost indistinguishable and correspond to $\tau_{step}$ and a fit to the late part of $\tau_\delta$. Below is a fit to the early part of $\tau_\delta$, giving smaller values for the time constant due to contamination of higher time constants, as discussed above. $\tau_{R_mC_m}$ gives smaller values than $\tau_\delta$ and $\tau_{step}$, except for the case $f_b = 0\ Hz$, when $R_{\mathrm{m,eff}} = R_m$ is uniform. For all non-zero values of $f_b$, the effective membrane resistance varies from branch to branch and the average $R_{\mathrm{m,eff}} \cdot C_m$ underestimates $\tau_\delta$. This seems to be true for any non-uniform membrane, whether the proximal membrane has a larger $R_m$ than the distal membrane or vice versa. Finally, $\tau_{\frac{1}{e},peak}$ and $\tau_{\frac{1}{e},ss}$ give smaller values still. This is especially true when the electrotonic length, $L$, increases (large $f_b$), since the amplitude of the second exponential, $C_1$, becomes larger relative to $C_0$ and the $1-1/e$ is approached more rapidly.

Fig. 5.5(b) similarly compares the 5 different measures of $\tau_m$ for the standard model with an active soma. The same ordering is found, except that $\tau_\delta$ is somewhat larger than $\tau_{step}$ and $\tau_{\frac{1}{e},peak}$ is larger than $\tau_{\frac{1}{e},ss}$ due to the inductive overshoot. Also, the ratio of any two measures varies little with $f_b$. For example, the largest measure, $\tau_\delta$, consistently yields an estimate that is approximately 6 times larger than the smallest measure $\tau_{\frac{1}{e},ss}$.

### Dependence of $\tau_m$ on $V_m$ and NMDA

As was shown above, different measures of $\tau_m$ can vary by a factor 6 or more. The two extremes were $\tau_{\frac{1}{e},ss}$, which measures how fast the $(1 - 1/e)$ point of the steady state step response is reached, and $\tau_\delta$, which fits an exponential to the tail of the impulse response. While the former measures the reaction speed to a sudden change, the latter indicates how long information is retained. Since $\tau_\delta$ therefore is a more appropriate measure for studying temporal synaptic integration, it will be the default measure used below.

Fig. 5.7(a) shows the variation of $\tau_m$ (alias $\tau_\delta$) with membrane voltage. The passive

case is not shown, since $\tau_m$ will not depend on voltage. When half of the AMPA synapses are replaced by NMDA synapses, $\tau_m$ is consistently larger. At hyperpolarized potentials, where non-linear effects are small, this is due to the voltage-dependent block of NMDA synapses, effectively reducing $R_{\mathrm{m,eff}} \cdot C_m$. At depolarized potentials, $R_{\mathrm{m,eff}} \cdot C_m$ is approximately equal for the two cases, but $\tau_m$ is still larger due to the non-linear nature of the NMDA conductance. The total variation is small, however, at most 25%.

Fig. 5.7(b) shows the variation of $\tau_m$ with background frequency. For a passive cell the time constant will equal $R_m \cdot C_m = 100\ msec$ at $f_b$=0 $Hz$ ($R_m$ uniform). It drops to 30 $msec$ at $f_b$=0.5 $Hz$ (standard model) and keeps dropping to 4.1 $msec$ at $f_b$=10 $Hz$. For the active cell, $\tau_m$ drops from 33.7 to 14.7 to 1.6 $msec$. Again, the NMDA curve gives values that are up to 50% larger. While the variation with $V_m$ was rather small, the variation with $f_b$ is on the order of 20–25 times over the range studied. In cat visual cortex the spontaneous range is usually smaller, less than 2.5 $Hz$ [Leventhal and Hirsch, 1978], but in other areas, such as motor cortex, spontaneous firing rates of 10 $Hz$ are common [Woody et al., 1984].

To conclude, different definitions of the membrane time constant, $\tau_m$, will give the same value for a compact passive cell, but will differ up to 10-fold when an extended, active cable structure is considered. Throughout the remainder of this thesis, $\tau_\delta$, that is an exponential fit to the impulse response, will be taken as the definition of $\tau_m$. Since the (3-point) fit varies with time, the largest value before the first zero-crossing was used (Fig. 5.3(d)).

## 5.3 Results

### 5.3.1 Basic effect on $R_{in}$, $\tau_m$, $L$, and $V_{rest}$

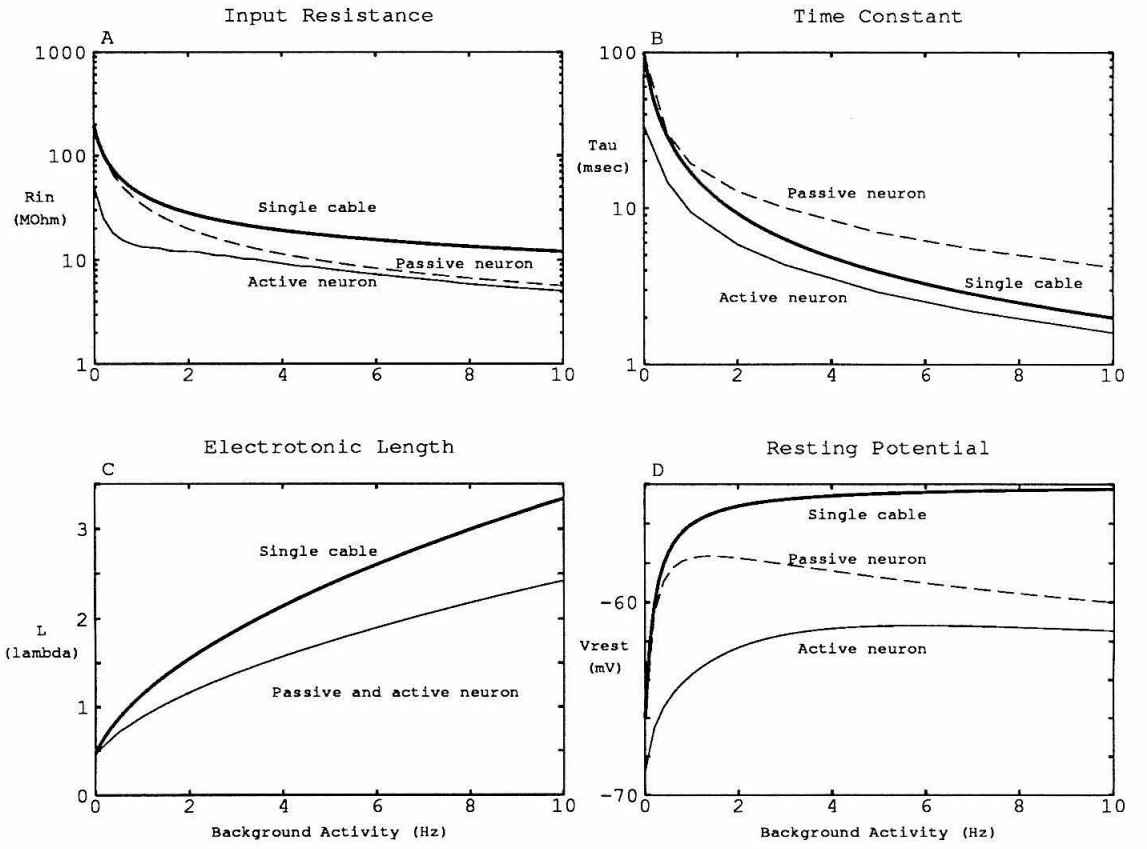


Figure 5.8: Effect of $f_b$ on (**a**) somatic input resistance, (**b**) membrane time constant, (**c**) electrotonic distance from soma to a distal site, and (**d**) somatic resting potential. The single cable approximates the full cell as described in the text. The passive neuron is identical to the active neuron, except that all active conductances have been removed from the soma.

The basic effect of varying background activity can be studied analytically in a very simplified model. The neuron was approximated using a single passive cable with length $l = 3060\ \mu m$ and diameter $d = 5.7852\ \mu m$. These dimensions preserve membrane area and input resistance (for the passive case) in the absence of background activity. The length constant of this cable is $\lambda = \sqrt{\frac{d \cdot R_{\mathrm{m,eff}}}{4 \cdot R_i}}$, where the effective membrane resistance includes a component from the synapses, $1/R_{\mathrm{m,eff}} = 1/R_m + 1/R_{\mathrm{m,syn}}$. The resulting electrotonic length is:

$$L = \frac{l}{\lambda}.$$

According to Rall [Rall, 1989], the input resistance at one end of this cable will be:

$$R_{in} = \frac{R_{\mathrm{m,eff}}}{\pi d \lambda \coth L}.$$

The time constant was calculated as the product of the effective membrane resistance and capacitance:

$$\tau_m = R_{\mathrm{m,eff}} C_m$$

and the resting potential was the weighted average of the reversal potentials of the passive leak and the synapses

$$V_{rest} = \frac{G_m E_{rev} + G_{\mathrm{m,syn}} E_{syn}}{G_m + G_{\mathrm{m,syn}}}.$$

Asymptotic expressions for large $f_b$ are easily obtained by setting $G_m$=0 or, equivalently, setting $R_{\mathrm{m,eff}}$= $R_{\mathrm{m,syn}}$= $1/G_{\mathrm{m,syn}}$.

These four parameters all depend monotonically on the background activity via $G_{\mathrm{m,syn}}$ or $R_{\mathrm{m,eff}}$. The basic results are shown in Fig. 5.8 (bold solid lines marked "single cable"). As the background activity varies from 0 to 10 $Hz$, the input resistance

decreases from 193 to 12.1 MΩ, clearly demonstrating that synaptic conductance tends to dominate for moderate and high background activation rates. Similarly, the time constant decreases from 100 to 2 $msec$. Both $R_{in}$ and $\tau_m$ have asymptotes that depend inversely on $f_b$. The electrotonic length of the cable increases from 0.47 to 3.3 $\lambda$ with an asymptotic square root relationship for large $f_b$. The resting potential at $f_b$=0 $Hz$ is identical to the leak potential, -66 $mV$, and approaches asymptotically the average synaptic potential of -54 $mV$.

This simple cable model captures most of the essential characteristic of the effects of increasing $f_b$. When replacing the cable with the full morphology of a pyramidal cell, and then adding active conductances, the same qualitative behavior is retained for the most part as will be discussed next.

Fig. 5.8 also shows the case of a passive cell with full morphology (thin dashed curves marked "passive neuron"). The cable model was constructed to mimic the passive cell at $f_b$=0 $Hz$ as is evident in the graphs. However, for larger values of $f_b$ the curves deviate. This can largerly be explained by the inhomogeneous distribution of synaptic inputs. Inhibitory synapses are concentrated in proximal regions and therefore the effective membrane resistance, $R_{\mathrm{m,eff}}$, is smaller close to the soma. This causes the somatic input resistance to decrease faster than for the cable model. As for the time constant, it may at first seem logical that the same effect should be noted since $R_{\mathrm{m,eff}}C_m$ is smaller in the vicinity of the soma. However, the opposite effect is seen: the measured time constant is *larger* than for the homogeneous cable model. The best explanation for this phenomenon is that even though distal portions of the membrane are far from the soma, they still make a small contribution to the exponential tail. Since $R_{\mathrm{m,eff}}C_m$ is larger than the average for this distal contribution, a larger time constant is observed. $L$ was calculated by summing up the electrotonic lengths of all cylinder segments between the soma and a location in the apical tuft in layer 1 that had a distance of 0.47 $\lambda$ at $f_b$=0 $Hz$. Because most of these segments

are far from the soma and hence receive a less dense innervation than the average for the cell, $L$ increases more slowly than for the cable. If we had chosen a basal location (none were at a distance of 0.47 $\lambda$), $L$ would have increased faster than for a cable. Finally, the resting potential is more hyperpolarized than a cable for large $f_b$. This is due to the screening effect discussed in chapter 3: inhibitory innervation dominates close to the soma.

The full model with an active soma is shown in thin unbroken lines marked "active neuron." The total contribution of the active somatic conductance is positive and reduces the input resistance most markedly at small $f_b$. The effect on the time constant is likewise to reduce it. Electrotonic distance $L$ is not affected since no conductances were added to the dendritic tree. The resting potential is further hyperpolarized, but does not display a "peak" in this interval, in contrast to the passive case. However, for very large values of $f_b$ the potential declines to an asymptotic value of -70.9 $mV$ (not shown in graph).

### 5.3.2 Control of spatial integration

That background activity can strongly effect spatial integration was pointed out in chapter 3 where efficacy measures were discussed. In the previous section, $R_{in}$ and $L$ were the parameters indicative of spatial integration. Two more examples of how the electrotonic structure changes with $f_b$ are given in Fig. 5.9.

The first illustration uses the morpho-electric transform visualization technique pioneered by Zador et al. [Zador et al., 1991, Zador, 1993]. Each branch is "stretched" or "shrunk" so that its physical length is proportional to its electrotonic length, $L$. The small neuron on the left corresponds to the case when no background activity is present. Note the short length of the dendritic trunk (which has a large diameter) and the relatively long apical dendrites (many of which have diameters of about 0.35 $\mu m$).

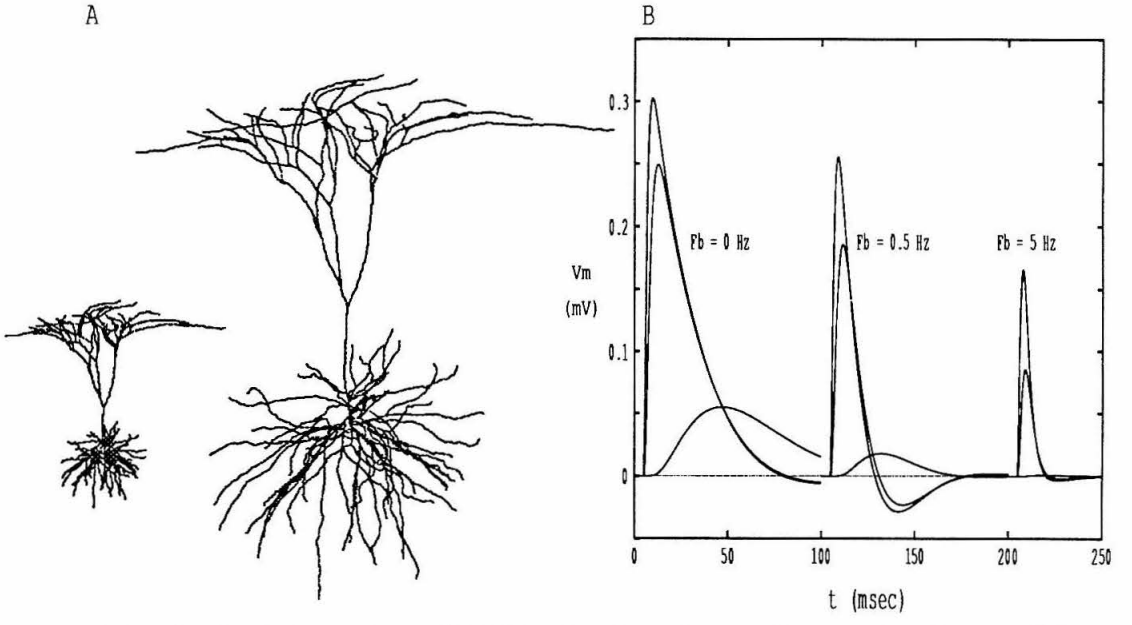


Figure 5.9: Spatial integration. **(a)** Morphoelectric transform at background frequencies $f_b$= 0 (compact cell) and 2 $Hz$ (large cell). **(b)** Attenuation of EPSPs. Synapses were activated at three locations: soma, basal dendrite, and apical dendrite. For each location, there were three different levels of background activity.

The most distal location is about 1.2 $\lambda$ from the soma. As $f_b$ is increased to 2 $Hz$, the cell stretches and becomes much less compact. The most distal location is now 2.6 $\lambda$ from the soma. Note that the basal dendrites tend to stretch more than their apical counterparts due to the more dense innervation in the basal region.

A second illustration is the attenuation of EPSPs with increasing $f_b$(Fig. 5.9(b)). A synapse was activated at three different locations: the soma, a basal dendrite, and an apical dendrite (leftmost three superposed curves) and the potential recorded in the soma. The basal EPSP is only slightly smaller than the somatic one at $f_b$=0 $Hz$, while the apical EPSP is strongly reduced in amplitude, but has a much larger half-width. As $f_b$ increases to 0.5 and 5 $Hz$, the amplitude of somatic and basal EPSPs decrease by a factor 2–3. The amplitude of the distal apical EPSP decreases much more dramatically; for $f_b$=5 $Hz$, almost no deviation from baseline is seen. Also note that the time course is sped up, as witnessed by the smaller half-widths.

### 5.3.3 Control of temporal integration

In section 5.3.1 the membrane time constant, $\tau_m$, was used to demonstrate how temporal integration can be controlled. Chapter 3 also showed how different measures of synaptic delay were affected by background activity. Two more examples are given in this section.

A single burst of excitatory synaptic inputs were activated throughout the cell. The activation was either simultaneous or distributed over a 25 $msec$ time interval, $T$, analogous to the case studied in chapter 4. For each value of $f_b$, the minimum number of cells required to fire one action potential, $N_t$, was found by simulation and graphed in Fig. 5.10(a). For simultaneously activated inputs ($T$ = 0 $Hz$), $N_t$ varies only by about a factor 2 (from 115 to 260) as $f_b$ varies from 0 to 7 $Hz$. For temporally desynchronized inputs, however, $N_t$ varies more than 6-fold (from 145 to 917). The

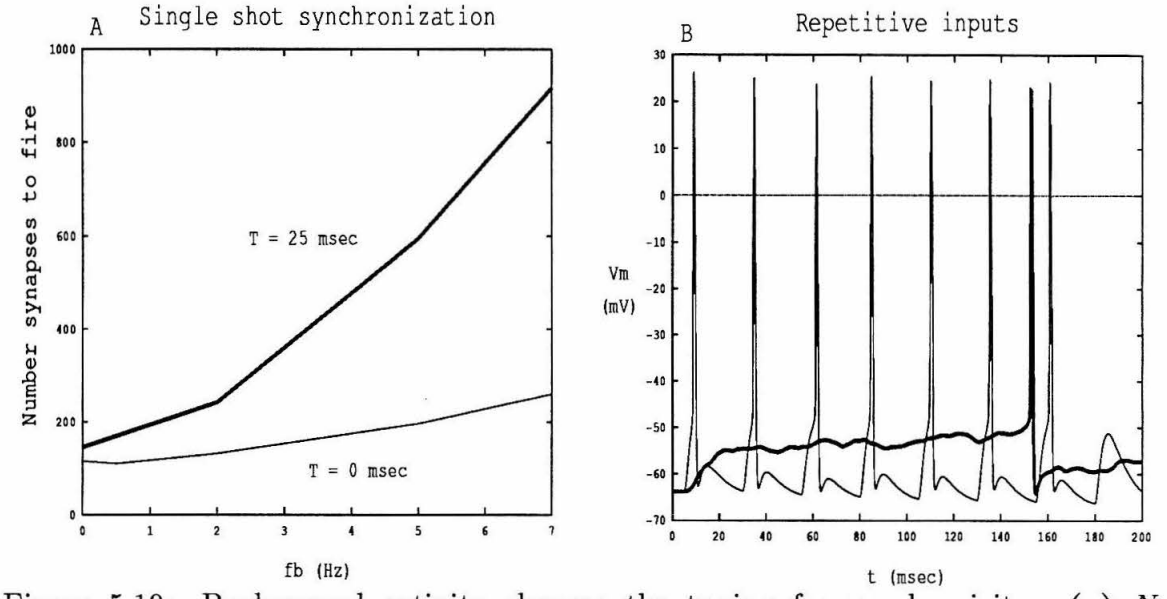


Figure 5.10: Background activity changes the tuning for synchronicity. **(a)** $N$ synapses were activated throughout the cell in addition to a variable background firing rate. The $N$ synapses were either fired simultaneously (thin line) or spread out over a 25 $msec$ interval, $T$ (bold line). The minimum number of synapses needed to fire a single action potential is plotted on the $y$ axis. **(b)** $N = 150$ synapses were activated at 40 $Hz$ for 8 cycles. In one case all synapses were perfectly synchronized (thin line), while in the other case they were distributed over a 25 $msec$ interval (bold line).

neuron therefore changes from being only marginally selective for synchronization for small $f_b$ to being highly selective for large $f_b$. $f_b$ can be viewed as a control signal determining the tuning.

A second example is shown in Fig. 5.10(b). $N$=150 excitatory synapses were activated at 40 $Hz$ for 8 cycles. The inputs were either perfectly correlated ($T = 0$ $msec$) or dispersed throughout a 25 $msec$ interval, resulting in a uniform temporal distribution. In the former case, seven out of eight cycles resulted in an action potential, while in the latter case only one spike was fired towards the end of the eight cycles. If the desynchronization interval was half a period ($T = 12.5$ $msec$), two spikes were generated (not shown).

### 5.3.4 Effect of NMDA on input resistance

In general, if a passive synaptic conductance is opened, such as AMPA or $GABA_A$ or $GABA_B$, the input resistance decreases.[3] However, if the (synaptic) conductance itself is voltage dependent, it may end up *decreasing* the input resistance. This can easily be shown analytically. Consider a simplified version of the case in section 5.2.1 with only one voltage-dependent conductance $G(V)$.

$$I = G(V) \cdot (V - E_{rev})$$

$$G_{in} = \frac{dI}{dV} = G(V) + \frac{dG}{dV} \cdot (V - E_{rev})$$

$G_{in}$ is a sum of the steady state conductance and a correction term. This correction term will be negative if

[3]It is of course possible that the synapses forces the potential into a region where active conductances more than compensate for the increased synaptic conductance.

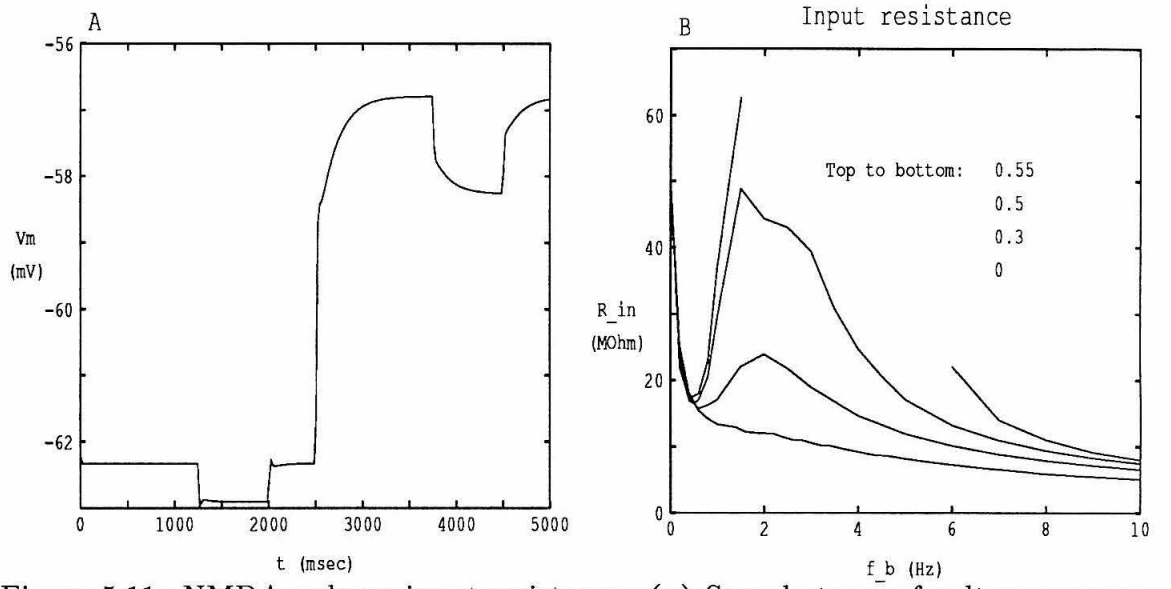


Figure 5.11: NMDA reduces input resistance. **(a)** Sample trace of voltage response to somatically injected current pulse. At $t = 500\ msec$, NMDA synapses were activated in addition to the background activity of AMPA. 0.05 $nA$ current pulses were injected at $t = 250\ msec$ and $t = 750\ msec$. Note that when measuring $R_{in}$, longer current pulses were used to ensure convergence to a steady state asymptote. **(b)** Input resistance as a function of background activity. The standard case (from Fig. 5.8(a)) is shown in bold. The $x$ axis gives the activity of AMPA synapses, as in previous graphs, while the curve labels give the ratio $f_{NMDA}/f_{AMPA}$. There were 4,000 synapses of both the AMPA and NMDA types. For $f_{NMDA}/f_{AMPA} = 0.55$ (top curve, broken) the cell spiked for $2 \leq f_b \leq 5\ Hz$ and the input resistance was not measured for that range.

$$sign(\frac{dG}{dV}) \cdot sign(V - E_{rev})$$

is negative. The correction term will be negative for an *activating* current ($dG/dV > 0$) with a reversal potential above $V_m$, such as a sodium or calcium current, or for an *in*-activating current with a reversal potential below $V_m$, such as certain potassium-dependent anomalous rectifiers. If the correction term is negative and, in addition, of larger magnitude than the steady state term, $G(V)$, the contribution of that conductance to the input conductance will be negative. For NMDA, as modeled in our cell, this occurs at potentials negative to about -27 $mV$.

Fig. 5.11(a) demonstrates how the cell was stimulated with a small (-0.05 $nA$) current pulse (first bump) when $f_b$=2 $Hz$. Next, 4,000 NMDA synapses were added at an input rate of $f_{NMDA}$ = 0.8 $Hz$. When the current step was re-applied, the resulting voltage deflection was approximately twice as large. This was partially due to the negative input resistance of NMDA and partially to the drift in membrane potential, which opens and closes somatic active conductances.

Fig. 5.11(b) repeats the simulation described in the previous paragraph for many values of $f_b$ and $f_{NMDA}$. The bottom curve is for $f_{NMDA}$ = 0 $Hz$ and is identical to the bottom curve in Fig. 5.8(a). As $f_{NMDA}$ is increased, the input resistance is dramatically increased over a large range of background frequencies, often doubling or even tripling.

NMDA can therefore have the paradoxical effect of increasing $R_{in}$, even though, on a biophysical level, more channels have opened.

## 5.4 Discussion

The main contribution of this chapter is to show that the total synaptic conductance of background firing can have a dramatic impact on spatio-temporal integration. The effective membrane conductance has two passive components, $G_{\mathrm{m,eff}} = \frac{1}{R_{\mathrm{m,eff}}} = G_m + G_{\mathrm{m,syn}}$ and the two key assumptions are that $G_m = 1/R_m$ is much smaller than previously thought and that the number of synapses onto a single cell is so large that even at a low spontaneous firing rate, synapses cannot be approximated with current sources. We demonstrated the basic effect of how $R_{in}$ and $\tau_m$ will vary more than 10-fold and $L$ more than 4-fold over a physiologically plausible range of $f_b$= 0–10 $Hz$.

Experimentally recorded values of $f_b$ in primary visual cortex vary between 0.3 and 2.5 $Hz$ [Leventhal and Hirsch, 1978]. There is also a gradient found in that superficial layers displayed lower $f_b$ than middle and deep layers. Larger values of $f_b$, on the order of 5–10 $Hz$ have been measured in extra-striate areas such as cat motor cortex [Woody et al., 1984], rat sensory-motor cortex [Bindman and Prince, 1983], and auditory cortex in cat, rhesus monkey, and baboon [Abeles, 1982]. We found no data that separates the background activity into excitatory and inhibitory components, and so the components were assumed to be equal: $f_{b,e} = f_{b,i} = f_b$.

To our knowledge, no experiment has been made where the background activity is varied as an experimental parameter. However, background activity is typically absent in slice preparations, corresponding to $f_b$= 0 $Hz$. Since the largest effect is seen for $f_b$< 2 $Hz$, it is worthwhile to compare *in vivo* and *in vitro* experiments.

One study directly compares rat sensory-motor cortex *in vivo* and *in vitro* [Bindman et al., 1988]. $R_{in}$ was found to be about twice as large in slice (35.9 *vs.* 18.4 MΩ) while the time constant was 40% larger (9.4 *vs.* 6.8 *msec*). While this supports our results, the difference is not as large as expected. Note however that the investigators used sharp electrodes, which are believed to cause a significant leak due to impale-

ment injury. For example, the perforated patch-clamp introduces a minimal leak and gives values of $R_{in}$ and $\tau_m$ that are 3–10 and 2–4 times larger than other studies [Spruston and Johnston, 1992]. A significant leak will have the effect of reducing the percentage difference between slice and *in vivo*.

The resting potential differs significantly between slice and *in vivo* preparations. In four studies, the reported values of $V_{rest}$ *in vivo* fall in the range -81 – -57 $mV$, with an average of -64.5 $mV$ [Bindman and Prince, 1983, Bindman et al., 1988, Holmes and Woody, 1989, Pockberger, 1991]. Eight studies *in vitro* give a range of -84 – -67 $mV$, with an average of -74 $mV$ [Bindman et al., 1988, Thomson et al., 1988, Mason and Larkman, 1990, Spain et al., 1990, Hirsch and Gilbert, 1991, Mason et al., 1991].

The results are not strongly dependent on the exact details of the model; this is in part evidenced by the fact that the three models (single cable, passive neuron, active neuron) all yield very similar results with only minor variations. Since the time-averaged conductance of a synaptic type is proportional to the product of $G_{max}$, $t_{peak}$, and the number of synapses, an error in the estimation of either of these three parameters will only have the effect of scaling the curves in Fig. 5.8 along the $x$ axis. If the *relative* contributions of excitation *vs.* inhibition varies, the only curve to be seriously affected is $V_{rest}$. When excitation was doubled (by doubling any of the parameters), the cell would spike for $f_b$ in the range 1.1–6 $Hz$. However, for values of $f_b$ outside this range, $V_{rest}$ displayed the same tendency to decrease for very large and very small firing rates.

Examples were given above of potential uses for this dynamic control over integration properties. By changing $L$, distal EPSPs can be differentially more attenuated than proximal ones and the width of a Mexican-hat receptive field can be controlled (chapter 3). By changing $\tau_m$, the sensitivity to synchronization can be varied. It is likely that the tuning of direction- and stereo-selective cells can be changed in a

similar manner, though this has not yet been investigated.

Also note that the change in $R_{in}$ and $\tau_m$ embodies two forms of automatic gain control. First, if a low-contrast stimulus gives a weak input, it is desirable to integrate over a longer time to improve the signal-to-noise ratio (SNR); the model predicts that a weaker input will give rise to a larger time constant. Second, when input rates are high, the noise variance is likely to be high (proportional to the square root of the input rate). By reducing the input resistance, each input will give a smaller contribution and thus reduce the absolute noise variance.

The overall background activity, $f_b$, is a very simple and unsophisticated control signal. While simplicity has many advantages, more complex and selective control signals could implement more sophisticated control mechanisms. A first step would be to differentially control the amount of background excitation and inhibition, which could, for example, keep $V_{rest}$ constant, while varying $R_{in}$ and $\tau_m$ or vice versa. The extreme case of highly selective control would be to gate inputs locally on dendrites, an approach that is likely to allow the neuron to switch between arbitrary response profiles.

In the next chapter we will investigate somewhat more complex control signals that allow for precise control of the gain of apical inputs.

# Chapter 6

# Control of Apical Synaptic Input

## 6.1 Introduction

This chapter deals with the effect exerted on layer V pyramidal neurons by their apical tufts—the distal part of the apical dendrite located in layers I–III. The apical tuft comprises about 25% of the dendritic membrane area in deep-layer neocortical pyramidal cells and receives a correspondingly large number of inputs. Dendrites in these layers are the targets for numerous projections, in particular non-specific projections from the thalamus as well as backward projections from other cortical areas. The latter ones appear to follow principle of reciprocity [Zeki and Shipp, 1988, Felleman and Van Essen, 1991]: if cortical area A sends a projection to cortical area B, another projection originates in B and returns to A. The forward projection terminates most heavily in layer IV (and to some extent layer III), while the backward connections avoid middle layers and terminate most heavily in layer I and II. In the case of the feedback projection from V2 to V1 in monkey, Rockland and Virga [1989] trace single fibers that run horizontally within layer I over 1–4 mm. In the primary somatosensory cortex of rats, Cauller and Connors [1993] find that many of the back-

ward projections course over many millimeters within layer I. Given the importance that feedback projections have in many theoretical models of brain function [see the articles in Koch and Davis, 1994], it is important to study the biophysical properties of superficial input to single pyramidal cells.

From the point of view of electrotonic length, the apical tuft is far removed from the cell body; in the absence of stimulation (slice preparation), the tuft is about 0.5 $\lambda$ from the soma, while for *in vivo* conditions the distance increases to 1–2 $\lambda$ due to the additional synaptic input (see chapter 5). In addition, the axial resistance of the apical trunk severely limits the current that can be delivered to the soma. In our model, in the absence of any voltage-dependent membrane conductances in the apical tree, synapses in all three superficial layers jointly can only deliver $\approx 0.65\ nA$ of current to the soma. Yet Cauller and Connors [1992] showed that synaptic input onto layer I dendrites of layer IV and V pyramidal cells in somatosensory cortical slice can evoke action potentials. Cauller and Connors show that complete depolarization of the distal apical dendrites of a passive compartmental model of such a pyramidal cell will lead to EPSPs no larger than 2 $mV$. On the strength of this discrepancy between experimental evidence for a powerful layer I input yet weak effect in a passive model, they and others [Spencer and Kandel, 1961, Amitai et al., 1993, De Schutter and Bower, 1993] argue for the existence of active currents in the apical tree able to amplify the synaptic input.

The aim of our theoretical investigation is to study at the single neuron, compartmental model level the need for voltage-dependent $K^+$ and $Ca^{2+}$ conductances in the dendrites and their required properties. In particular, we examine the properties of a $K^+$ conductance that linearizes the response to apical input, counteracts saturation, and extends the operating range of the input as well as a $Ca^{2+}$conductance that amplifies dendritic input, in a more graded manner. Our approach allows us to "design" specific conductances in a controlled manner, helping us to understand their function

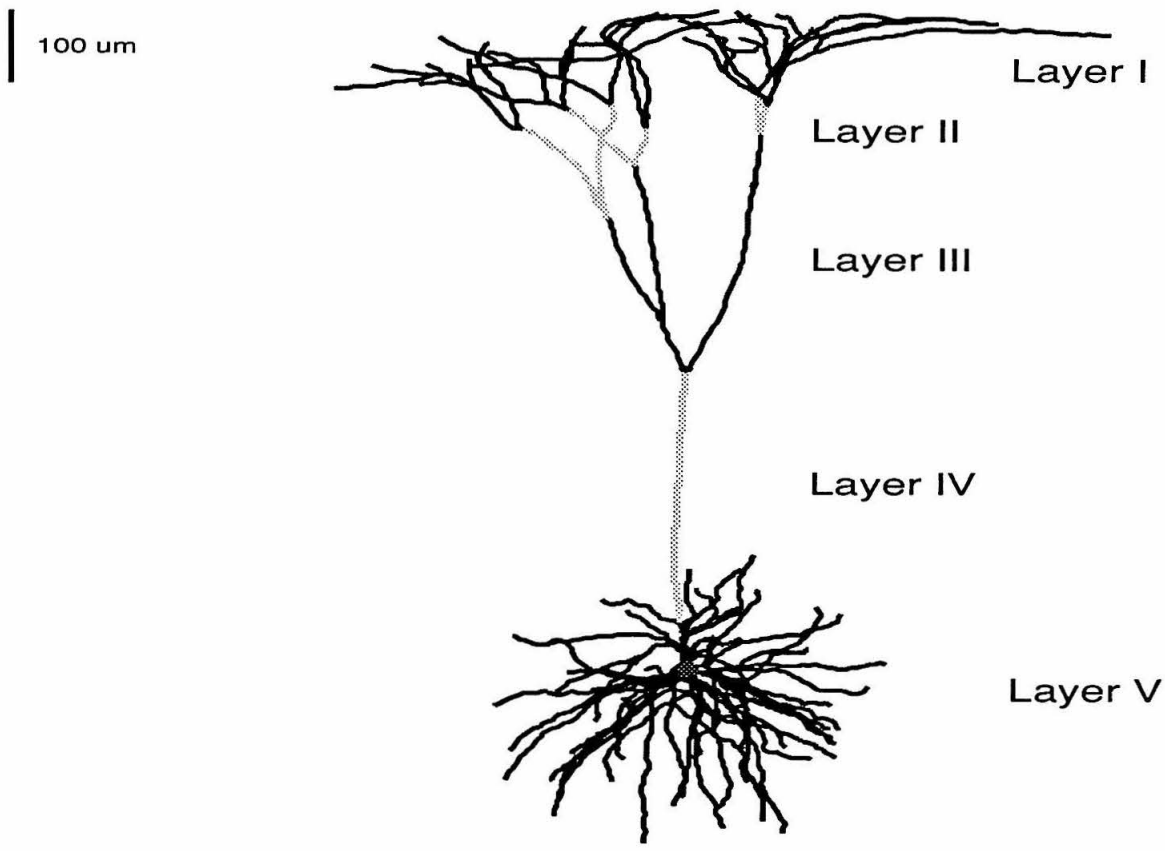


Figure 6.1: **Input regions of layer V cell.** Layers I–V are marked in alternating black and grey. The superficial layers I–III make up 26% of the membrane area, layer IV makes up 10%, and layer V, 62% (see Table 2.1 for morphological data). The boundaries between superficial layers are not exact, but are rough estimates and were chosen at branch points; a few basal dendrites may reach into layer VI. Axon not shown.

within the overall context of dendritic information processing.

We only investigate steady state conditions, including the *dynamic* steady state that occurs when the cell spikes, but the firing rate has adapted. Further, the conductances that we derive have no inactivation kinetics. This is in contrast to the slow spikes that have been observed in intradendritic recordings (see Discussion), but is consistent with the presence of NMDA in the apical trunk, for which there is some evidence [Cauller and Connors, 1993], or the presence of a persistent sodium conductance.

## 6.2 Results

Fig. 6.2A shows the conventional f-I curve for the first eight inter-spike-intervals (ISIs). This is the same set of curves that was shown in chapter 2; it is repeated because many of the results below center around the f-I relationship. A current step of constant amplitude $I$ was injected into the soma and the inverse of the first, second and so on interspike intervals are plotted. Rheobase (the sustained threshold current to initiate spikes) is 0.3 $nA$ and the primary slope of the first ISI, between 0.3 and 0.6 $nA$, is about 50 $Hz/nA$. The shallow slope of this early portion of the curve becomes much steeper if the $A$ current is removed. The f-I curve associated with adapted spike-trains (bold trace) is relative linear, with a slope of 55 $Hz/nA$.

The details of the f–I curve are strongly dependent on the density and kinetics of the spike-generating and adapting currents. For instance, increasing the density of $I_M$ smoothly increases the sustained current necessary to initiate spiking (rheobase), moving the f-I curve to the right, without any change in its slope, while increasing the density of $I_{AHP}$ reduces the slope of the adapted portion of the f-I curve with no effect on the threshold current (see below and figure 6.4B,C).

Fig. 6.2B describes the net effect of all currents involved in expressing and control-

ling somatic spiking. We injected a sustained current of fixed amplitude into the soma and computed the average membrane potential after adaptation was complete. This average includes action potentials, sampled every time step, $dt$. What is remarkable is that once the firing threshold is reached at about 0.3 $nA$, the averaged somatic membrane potential increases by only about 10 $mV$ as the adapted firing frequency increases over its full range from 0 to about 95 $Hz$. The slope of this curve can be interpreted as a "dynamic" input resistance, $R_{in,dyn} = dV/dI$. Near the origin, $R_{in,dyn} \approx 23$ MΩ, which is close to the value of the somatic input resistance, but above firing threshold it decreases by a factor 8 to 3 MΩ over the expected operating range of input currents, $I \leq 3nA$. The inverse of $R_{in,dyn}$ can be considered to be a total conductance that increases with increasing steady-state membrane potential levels. The spike mechanism thus resembles a voltage-gated hyperpolarizing conductance that is able to shunt large input currents and thereby stabilize the somatic voltage, similar to an imperfect voltage clamp.

Due to the low-pass filtering of the dendritic membrane, the high-frequency voltage components associated with the rapid up- and down-stroke of the somatic action potential are prevented from propagating antidromically very far into the dendritic arbor. Therefore, the time-averaged somatic potential shown in Fig. 6.2B is closer to the voltage "seen" at distal sites away from the soma than $V_{soma}(t)$ itself.

### 6.2.1 Passive shunting of apical inputs

We will begin by studying how the already small contribution from apical layers can be shunted by passive conductances. Non-voltage dependent synaptic inputs are conductance changes that will lower the effective $R_m$ and increase the electrotonic length of cable segments and therefore attenuate propagating signals [Abbott, 1991, see also chapters 3 and 5]. This is demonstrated in figure 6.3(a). A brief current pulse

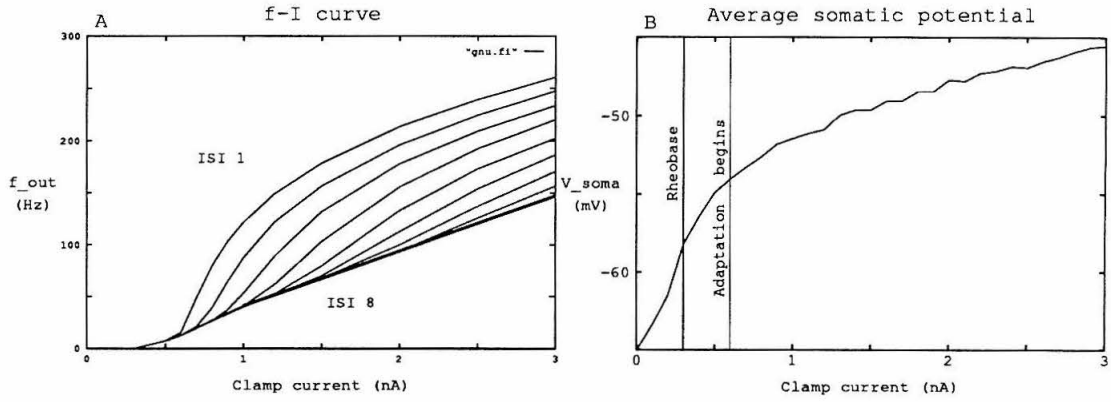


Figure 6.2: **Characteristics of the spike-generating mechanism. A:** $f-I$ curve for the first 8 inter-stimulus intervals (ISIs). Bold line (bottom curve) is the *adapted* f-I curve. **B:** The average somatic potential in response to somatic current injection. The cell spiked for $I_{clamp} > 0.3\ nA$ and the average includes the brief excursions of the potential to above 0 $mV$ during action potentials. Wiggles are due to sampling error.

---

(100 $pA$, 1 $msec$) was injected at the distal end of the apical trunk, the juncture of layers 3 and 4. The resulting EPSC (during voltage clamp) was measured at the soma. When the trunk received no excitatory input, the EPSC peaked at 22 $pA$. As all 463 excitatory synapses on the trunk were activated at 10, 20, 40, and 100 $Hz$, the amplitude decreased to 20, 17, 14, and 8 $pA$. In addition, the width decreased, and so the EPSC area is reduced even more with $f_{trunk}$. A current injection was chosen rather than activation of a synapse in order to avoid the confounding effects of saturation; the injected current and the resulting EPSCs will be independent of the reversal potential of the layer 4 synapses.

Paradoxically, layer 4 input can under certain circumstances *facilitate* apical input. Figure 6.3B shows the output spike rate, $f_{out}$, as a function of the input rate, $f_{apical}$, of 500 synapses in layers 1–3. To simplify the investigation, $I_{Ca}$ was removed and the cell did not adapt but spiked at a constant frequency. The lowest curve represents the

case when the trunk receives no additional input and $f_{out}$ levels out at about 5 $Hz$. The I-f curve in figure 6.2A gives that this corresponds to about 0.45 $nA$. When the trunk receives an input $f_{trunk} = 20\ Hz$ (middle curve), the firing rate varies from 9 to 60 $Hz$, a swing of 51 $Hz$. According to the f-I curve, this is a swing from 0.5 to 0.75 $nA$. Even though the extra current delivered by layers 1–3 is only 0.25 $nA$, about half as much as before, the neuron is now biased to operate on a much steeper part of the f-I curve, where the slope is about 250 $Hz/nA$. If $f_{trunk}$ is further increased to 40 or 100 $Hz$, the swing again decreases since the cell moves to a less steep part of the f-I curve in addition to the attenuation growing stronger.

In order to move the cell response onto the steep part of the f-I curve, the neuron was biased with an excitatory background activation of 1.7 $Hz$. This excitation caused the cell to spike at 11 $Hz$, and the paradoxical facilitation no longer occurred.

The experiment in figure 6.3B was repeated in figure 6.3(C, 4 upper curves) with the addition of the excitatory bias. As layer 4 is stimulated, the cell response increases, but the impact of layers 1–3 decreases, as is witnessed by $f_{out}$ changing less with $f_{in}$. The paradoxical initial increase in apical efficacy is no longer present, due to the bias. Figure 6.3(D, top 2 curves) shows a cut of 6.3C at $f_{apical} = 100\ Hz$, with $f_{trunk}$ on the x axis. For comparison, all 2362 basal synapses were activated at 1.24 $Hz$, resulting in the same $f_{out} = 11\ Hz$ in the absence of layer 4 input. This response is somewhat larger than for apical input, suggesting screening of apical inputs, even though layer 4 excitation dominates.

To remove the confounding effects of excitation, inhibition was added to the apical trunk at approximately twice the excitatory frequency so as to keep the neuron spiking at a biased rate of 11 $Hz$ in the absence of apical input. The combined effect of excitation and inhibition is that of on-the-path shunting inhibition [Koch et al., 1982]. The result is shown in figure 6.3(4 lower curves); the order of the curves (top to bottom) is reversed as compared to case of excitatory input only, and the shunting

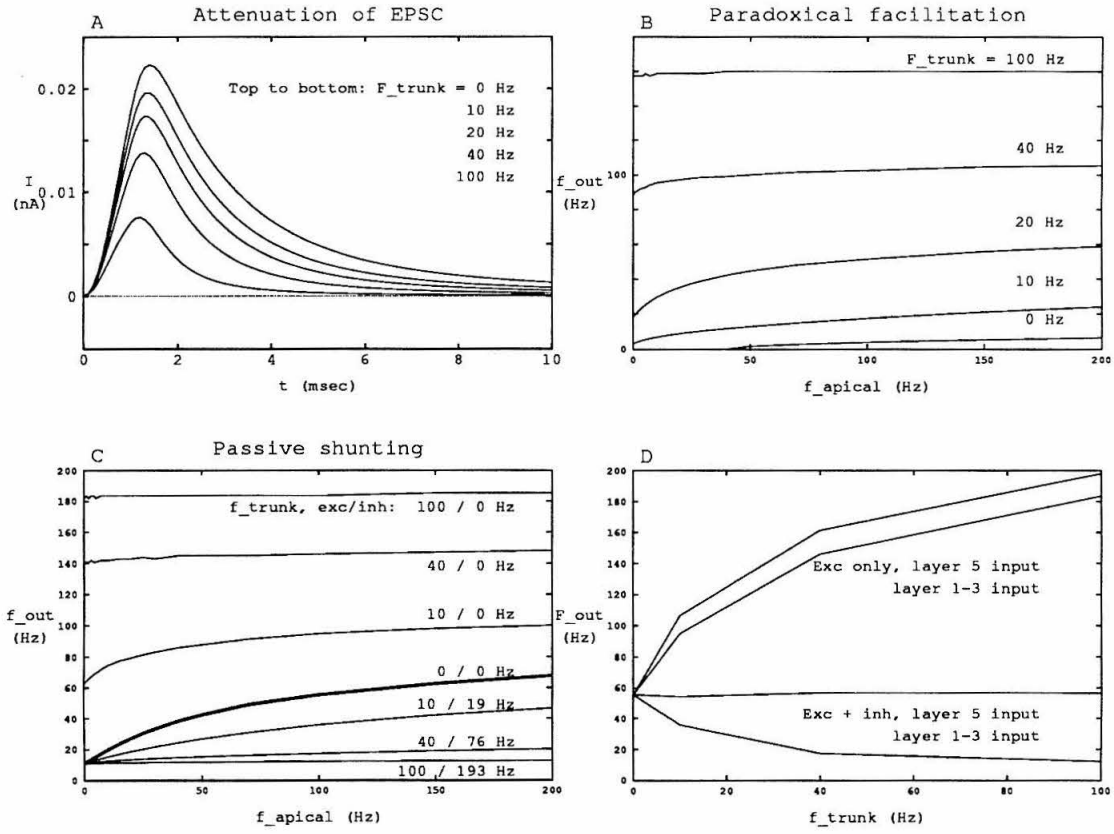


Figure 6.3: **Passive shunting of apical inputs. A:** Somatic EPSCs (during voltage clamp) in response to brief current pulses injected at the distal end of the apical trunk. As 463 excitatory synapses on the trunk are activated, EPSC amplitude and duration are reduced. **B:** $f_{out} = fnc(f_{in})$ for various levels of excitatory input to the apical trunk. Even though $f_{in}$ reduces the current contribution, a paradoxical facilitation is seen, because the layer IV input biases the cell to a steep portion of the f-I curve. **C:** Similar to B, but the cell was biased to spike at 10 Hz by a diffuse excitatory input. This removes paradoxical facilitation. Layer IV received either excitation alone (top four curves) or in combination with inhibition (bottom four curves). **D:** Same as C, except layer IV activity is shown on the ordinate. For comparison, two curves are shown when layer V synapses were stimulated instead of layer I–III synapses. $I_{AHP}$ was removed for all f-I curves in this figure, and so the cell did not adapt.

effect shows up clearly. In figure 6.3(C, lower 2 curves) it is shown that layer 5 input is virtually undisturbed by the layer 4 input while apical input is strongly reduced.

### 6.2.2 A new measure of synaptic efficacy

As will become apparent momentarily, we seek to study the input-output relationship of pyramidal cells, in particular for input to the distal parts of the apical tree. To this purpose, we introduce a new measure of synaptic efficiency that emphasizes the current flow in response to synaptic input and downplays the role of the membrane voltage in controlling the output of the cell.

The key idea is that the contribution by a group of synapses can be best characterized in terms of the current $I_{syn,s}$ that they deliver to the soma rather than by more conventionally defined measures of synaptic efficacy such as electrotonic distance or voltage attenuation all of which have serious drawbacks (see chapter 3). In particular, almost none of these measures take into consideration synaptic conductance changes, voltage saturation, active conductances in the dendrites as well as the spike-generating mechanism at the soma. $I_{syn,s}$ combines the effects of *dendritic* parameters, such as the synaptic conductance change, attenuation, saturation, and active dendritic conductances, into a single measure that directly translates an input firing frequency into a current flowing into the soma. Assuming steady-state conditions, this somatic current in response to synaptic input can then be converted into a firing rate using the measured f-I curve (Fig. 6.4A). The f-I curve is a function of somatic parameters, such as $R_{in}$ and active somatic conductances. In other words, we have

$$f_{out}(f_{in}) = f_{out}(I_{syn,s}(f_{in})). \tag{6.1}$$

We measure the total synaptic current at the soma generated by groups of synapses located in various regions of the dendritic tree. A population of excitatory, AMPA

synapses in, say, layer I, were activated at a particular input rate $f_{in}$ using the time-averaged technique expressed in eq. 2.2. In order to derive a measure of $I_{syn,s}$ independent of spiking activity, the somatic potential was clamped to $-50\ mV$, the average somatic potential for moderate inputs (Figs. 6.2D and 6.4). Clamping the soma to this potential corresponds to a sustained output firing frequency of 55 $Hz$. Two methods were used to measure the somatic current, $I_{syn,s}$. The first method records the current flowing from the apical tree via the axial resistance into the soma. The second method measures the clamp current required to hold the somatic potential at $-50\ mV$ for a fixed synaptic input minus the clamp current needed to hold the soma at $-50\ mV$ in the absence of any synaptic input. The second method has been used to experimentally measure $I_{syn,s}$ in $\alpha$ motoneurons [Powers et al., 1992]. In our simulations, the two methods gave almost identical values for $I_{syn,s}$.

$I_{syn,s}$ as a function of presynaptic firing rates $f_{in}$, evoked by various groups of synapses, is shown in Fig. 6.4B. 500 excitatory synapses, spatially distributed according to eq. 2.1 were activated in one of the following regions: the soma, layer V (excluding the soma, but including apical obliques), layer IV (the apical trunk), and layers I-III. When the entire input was concentrated at the cell body (an unphysiological situation), $I_{syn,s}$ was linear in $f_{in}$ up to very high input rates due to the relative low somatic input resistance. An input rate of 100 $Hz$ delivered an unphysiologically high amount of current ($>$ 5 $nA$). A similar result is obtained when the 500 synapses were distributed throughout layer V, that is, within the basal dendrites. Saturation becomes evident when the synaptic input is distributed along the layer IV portion of the apical tree and becomes severe for inputs in the superficial layers, even when input rates are low. In this case, $I_{syn,s}$ is always less than 0.65 $nA$, even when all 500 synapses are activated every 2 $msec$. This saturation is caused by the high input resistance in the distal dendrite which drives the membrane potential towards the synaptic reversal potential (the most distal unitary EPSPs have local amplitudes

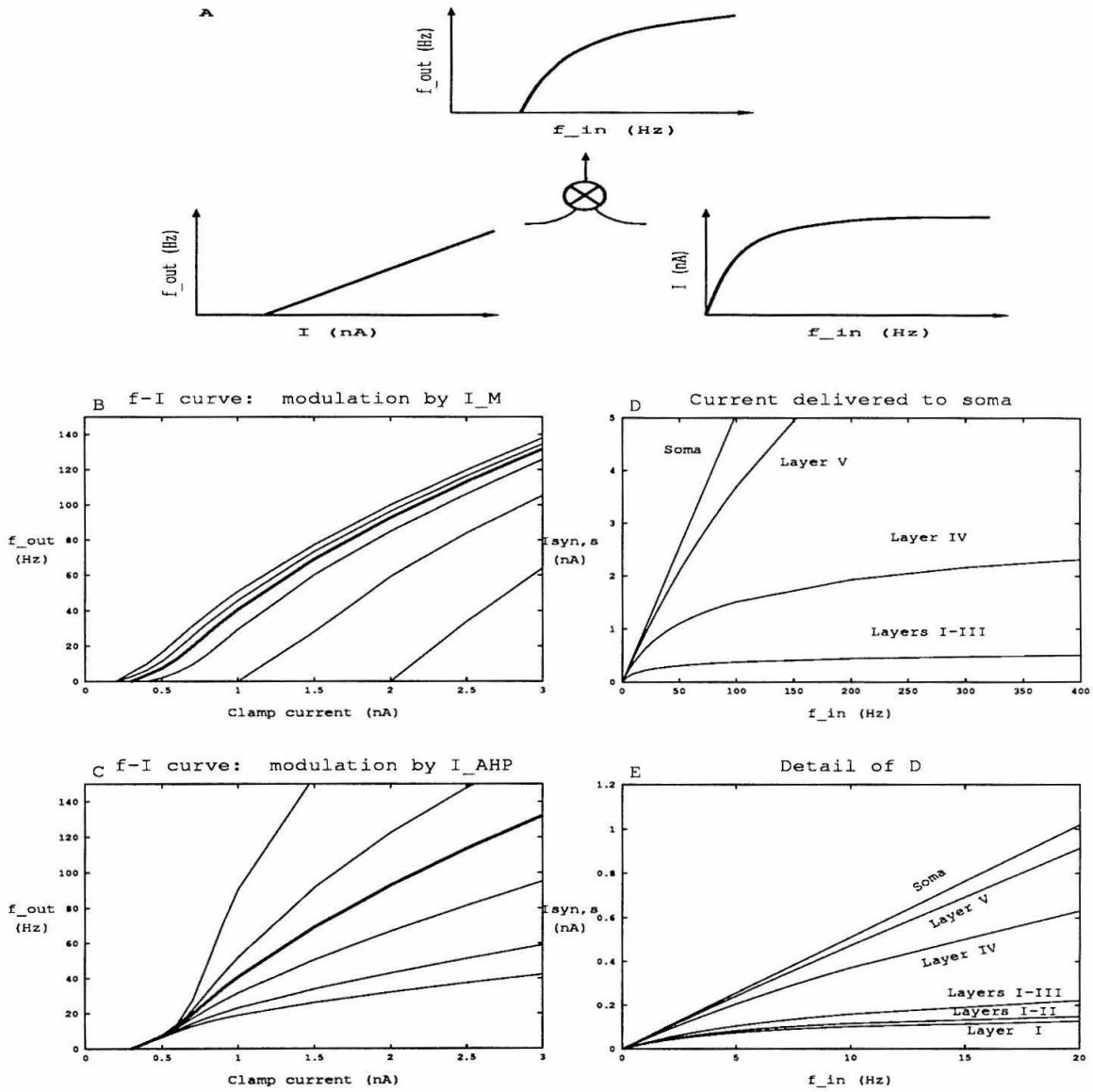


Figure 6.4: **Current delivery as a measure of efficacy. A:** Schematic demonstrating the composite function $f_{out}(f_{in}) = f_{out}(I_{syn,s}(f_{in}))$. The intermediate value is *current* and not *voltage*. The outer function, $f_{out}(I)$, depends mainly on somatic parameters, while the inner function, $I(f_{in})$ is a function of dendritic parameters. **B:** The $M$ current shifts the f-I curve. The (adapted) f-I curve for the standard cell model is plotted in bold. The channel density of $I_M$ was multiplied by (top to bottom) 0, 0.5, 1, 2, 5, and 10. **C:** $I_{AHP}$ determines the slope of the f-I curve. The channel density of $I_{AHP}$ was multiplied by the same values as in B. **D:** Current delivered by 500 synapses stimulated in one of four different regions of the neuron. The soma was clamped to -50 $mV$ and the clamp current current recorded. **E:** Detail of D for small values of $f_{in}$. The "Layers I–III" curve above has been broken down into three curves. The fact that the contribution of synaptic input to the superficial layers saturates at 0.65 $nA$ constitutes the central problem this study addresses.

over 20 $mV$). No amount of additional input can increase the membrane potential beyond $E_{rev,e}$. Even if the membrane leak is removed, i.e., for $R_m \rightarrow \infty$, saturation of the apical tuft ensures that the asymptote of $I_{syn,s}$ is 0.66 $nA$, increasing by only 2% above base level.

It is important to note that if synaptic input behaves as a current source (rather than a conductance input), no saturation would occur. The saturation effect is even stronger when the synaptic input is restricted to layer I and II or layer I only (Fig. 6.4C). In both cases, $I_{syn,s}$ is reduced almost by about a factor 2 and reaches asymptotes of a mere 0.2–0.25 $nA$. This is in stark contrast to experimental evidence showing that layer I synaptic input is sufficient to drive the cell [Cauller and Connors, 1992].

This, then, is the nub of the problem to be addressed in the remainder of this paper—how is it that inputs to the apical tuft can provide a larger functional effect than traditional passive models of the dendrite permit? One possible explanation of the influence of apical inputs is that their effect is modulated by more proximal inputs to the neuron. Fig. 6.2E shows that apical inputs can be conditioned by other sustained inputs. Whereas 0.5 $nA$ of injected current alone causes the cell to fire at a maintained rate of 7.5 $Hz$, if other synaptic inputs delivers 1 $nA$ to the soma thereby causing the cell to fire at 41 $Hz$, the additional 0.5 $nA$ current increases this rate to 68 $Hz$.

To illustrate the composition of $f_{out}$ and $I_{syn,s}$ we activated 500 synapses on the apical trunk in layer IV at $f_{in} = 40$ $Hz$. According to Fig. 6.4D, this results in $I_{syn,s} = 1.01$ $nA$ of current being delivered to the soma. Using the f-I curve (Fig. 6.2E), this should give an output rate $f_{out} = 41.0$ $Hz$. The simulation gives a slightly higher value of 42.6 $Hz$. The discrepancy is small and can be explained in part by the fact that at 1 $nA$ the average somatic potential is -51.4, not -50, increasing the synaptic driving force. Subsequently a 1 $nA$ current clamp was added to the soma, giving a

total of 2.01 $nA$. According to the curves, this should result in $f_{out} = 94.15\ Hz$ and the simulation gives 93.9 $Hz$, again in very close agreement.

In this paper we focus on ways of altering the dendritic function $I_{syn,s}(f_{in})$ and assume that the somatic function, the f-I curve $f_{out}(I_{syn,s})$, is fixed. It is worthwhile to note, however, that the f-I curve can be controlled by modulating active somatic conductances. Fig. 6.4B shows the effect changing the density of the $M$ current from 0 to 10 times its normal value. The result is a shift of the f-I curve with the slope almost intact. In Fig. 6.4C the density of $I_{AHP}$ was varied, which caused a change in slope of the f-I curve, while keeping rheobase constant. A similar shift was obtained by changing the passive membrane leak, while the slope could also be altered by changing the density of $I_{Ca}$ (graphs not shown). The same effect of $I_M$ and $I_{AHP}$ on the f-I curve was found in a very detailed model of bullfrog sympathetic ganglion cells [Yamada et al., 1989].

### 6.2.3 Linearization and amplification of apical inputs

Anatomical and physiological data reviewed above suggests that the apical tuft inputs should have a much greater effect than shown in Fig. 6.4C.

One explanation of this disparity is to appeal to the presence of active conductances in the dendritic tree, as argued by the evidence in the section 6.3. But simple voltage amplification has disadvantages. If the voltage gain is high, the apical dendrite loses its proportional response and becomes more digital in quality. Second, the apical synapses run even more easily into saturation. Therefore, we explore an alternative possibility in which the active membrane conductances both linearize as well as amplify the *current* flowing in response to synaptic input.

In particular, we propose to prevent synaptic saturation by the presence of a $K^+$ conductance, $G_{K,lin}$. As the membrane potential increases and approaches $E_{rev,e}$, the

$K^+$ conductance is activated. The effect of this conductance is to pull the potential to hyperpolarizing levels, close to $E_K$. In a second step, this linearized response is then amplified by the introduction of $Ca^{2+}$ channels into the apical trunk through which the synaptic current must flow prior to reaching the soma. The active $Ca^{2+}$ conductance decreases the effective axial resistance, $R_i$, so that current flows more easily from the apical tuft into the soma.

Rather than using trial-and-error to understand what type of conductances have these two types of effects, we derive the form of their voltage-dependency. That is, given a particular functional relationship between $I_{syn,s}$ and $f_{in}$, we derive the relationship between membrane potential and $G_{K,lin}$ and $G_{Ca,amp}$ that will yield the required $I_{syn,s}$.

### Three Compartment Model

Let us study the principle behind our construction by using a highly simplified three compartment model of a pyramidal cell (Fig. 6.5A): the leftmost node represents the soma and is clamped to $-50\ mV$; the middle node represents the apical trunk with an active $Ca^{2+}$ conductance and the rightmost node represents the apical tuft with a synaptic input in parallel with a $K^+$ conductance. We assume for simplicity that the membrane leak, $R_m$, is infinite. Because we study steady-state behavior, the membrane capacitance can be ignored.

Fig. 6.5B shows the relation between total synaptic conductance applied to the apical tuft and the somatic current that this input evokes. The passive response, in which $G_{K,lin}$ and $G_{Ca,amp}$ are set to zero (dashed thin line), corresponds to Fig. 6.2E. Here $I_{syn,s}$ saturates for a moderate input of about 50 $nS$. Let us linearize this response over the range $g_{syn} = 0$—$200\ nS$ (solid bold line). Since this curve lies below the passive response for the most part, a hyperpolarizing conductance is needed to induce the linearity and a $K^+$ conductance was chosen for this role. The third curve

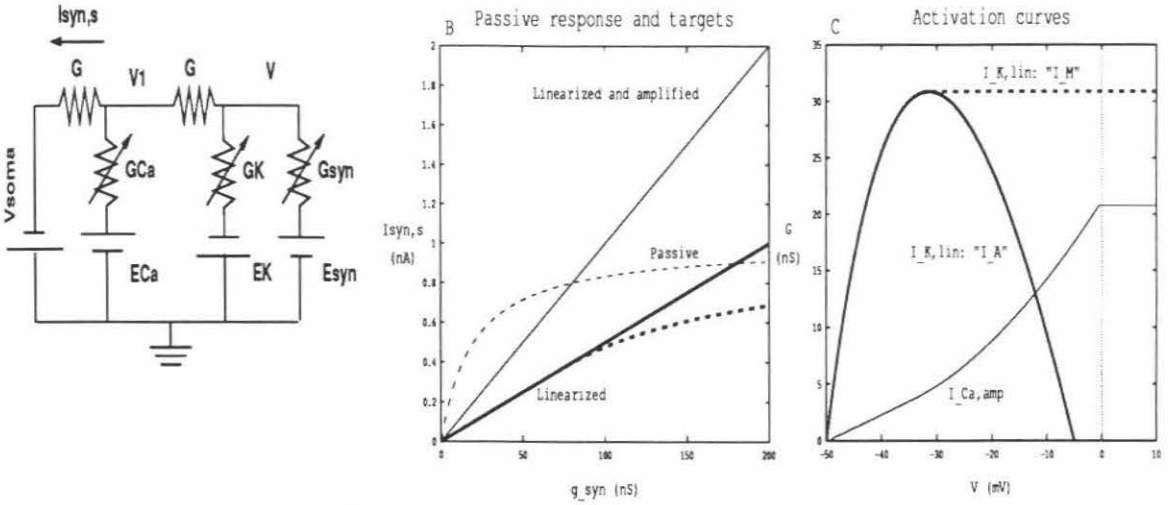


Figure 6.5: **Linearization and amplification in a three-compartment model.** **A:** Circuit diagram. The somatic compartment was clamped to $V_{soma} = -50\ mV$ with $E_{Ca} = 115\ mV$, $E_K = -95\ mV$, $E_{syn} = 0\ mV$, and $G = 40\ nS$. The membrane capacitance was ignored, since only steady state properties were studied, and membrane leak was not included for simplicity. $g_{syn}$ was varied from 0 to 200 $nS$ (independent variable) and $G_{Ca,amp}$ and $G_{K,lin}$ were derived (dependent variables), given the constraint of the target curves shown in B. **B:** Passive response to synaptic input and (active) target curves. The passive response in the absence of $G_{Ca,amp}$ and $G_{K,lin}$ is shown with a thin dashed line. Also shown are the targets for the linearized curve with *constant* $= 5\ mV$ (using $G_{K,lin}$: $I_A$, solid bold line); the amplified curve (gain = 2, using $G_{K,lin}$ and $G_{Ca,amp}$, thin line); and the curve that results when the "monotonized" $G_{K,lin}$ is used ("$I_M$," dashed bold line). **C:** Derived activation curves for $G_{K,lin}$ and $G_{Ca,amp}$ (thin line) using the target curves in B. The version of $G_{K,lin}$ termed $I_A$ (solid bold line) was derived for the linear target curve in A, while the "monotonized" version termed $I_M$ (dashed bold line) was used to further derive $G_{Ca,amp}$.

(solid thin line) represents the linearized response amplified by a factor 2. This amplification requires a depolarizing conductance; either $Na^+$ or $Ca^{2+}$ would suffice. $Ca^{2+}$ was chosen because of the strong evidence for it being present in the apical dendrite.

To obtain the conductances required to achieve the ideal responses indicated in Fig. 6.5B, we derive $G_{K,lin}$ by applying Ohm's law of current conservation to the one node (labeled by voltage $V$ in Fig. 6.5A and setting $G_{Ca,amp}$to zero for now. Adding the desired proportionality between input and current at the soma

$$I_{syn,s} = constant \cdot g_{syn} \tag{6.2}$$

from Fig. 6.5B, the resulting two equations have a unique solution for $G_{K,lin}$ that is a fractional polynomial in $V$:

$$G_{K,lin}(V) = \frac{G}{2 \cdot constant} \frac{(V - V_{soma})(V - E_{syn} + constant)}{E_K - V}. \tag{6.3}$$

Solving for the "dendritic" membrane potential yields

$$V = \frac{2 \cdot constant}{G} g_{syn} + V_{soma}. \tag{6.4}$$

The voltage-dependency for the potassium conductance is graphed in Fig. 6.5C for $constant = 5\ mV$.

At $V = E_{syn} - constant = -5\ mV$, the potassium conductance is zero and the system reverts back to the passive case. This corresponds to the point in Fig. 6.5B where the two $I_{syn,s}$ curves intersect. At more positive membrane potentials, the $K^+$ conductance becomes negative (see Fig. 6.5C). Because this is unphysiological, $G_{K,lin}$ was set to zero for more positive voltages as well as for $V < V_{soma}$ (half-wave

rectification).

The positive part of $G_{K,lin}$ corresponds to $g_{syn}$=0–180 $nS$, which is the range of inputs for which the target curve is *below* the passive curve (Fig. 6.5B); since the potassium conductance is hyperpolarizing, it can never amplify the signal without taking on negative values. The "activation" curve is parabolic, similar to a transient (inactivating) potassium current, and was therefore labeled "$I_A$." The parabolic curve parallels the *difference* between the passive and linearized curves in Fig. 6.5B: $G_{K,lin}$ is switched off for small inputs, but activates rapidly to counteract saturation as the input increases. For large $g_{syn}$, the linearized curve gains on the passive response and hence $G_{K,lin}$ inactivates. Note that the latter part has a negative derivative $dG/dV$, which provides a negative contribution to the local input resistance. This can easily lead to an instability in which the apical potential depolarizes to, and latches up at, the synaptic reversal potential. Such instability would make the dendritic amplification mechanism unreliable. The problem can be cured by "monotonizing" the voltage dependence of $G_{K,lin}$, that is, the activation curve levels out after reaching its peak rather than return to zero. This modification will cause $I_{syn,s}(g_{syn})$ to be slightly sub-linear for large $g_{syn}$, but the benefit is that stability is obtained. Moreover, the amplification mechanism can make up for the sublinearity. In the final analysis, therefore, $G_{K,lin}$ shows no steady-state "inactivation" and is labeled "$I_M$" (Fig. 6.5B, dashed bold line).

Once $G_{K,lin}$ was derived, the circuit equations were again solved, this time for $G_{Ca,amp}$. The $G_{K,lin}$ element was retained in the circuit and the current flowing from the synapse into the "soma" compartment was amplified by a positive gain factor:

$$I_{syn,s} = gain \cdot constant \cdot g_{syn}, \tag{6.5}$$

where *gain* typically was set to 2 or 4. The circuit element $G_{K,lin}$ adds consid-

erable complexity to the equations, especially since it has to be treated piecewise due to monotonization and half-wave rectification. The resulting equation specifying $G_{Ca,amp}$ as a function of $V$ is complex to the point where it provides no further biological insight and so is not shown, but the associated calcium "activation" curve is graphed in Fig. 6.5C. It has the characteristics of a non-activating calcium conductance. Simulations (not shown) verified that the resulting $I_{syn,s}$ attained the target function with high fidelity and stability. The voltage dependency for $G_{Ca,amp}$ is flat for values above 0 $mV$, since we did not attempt to amplify $I_{syn,s}$ beyond the associated conductance input of 200 $nS$.

The circuit equation, eq. 6.5, can, in principle, be solved for any explicit somatic current function, given a single conductance, e.g., $G_{Ca,amp}$, rather than using two distinct conductances (one $Ca^{2+}$ and one $K^{+}$) as we do here. This, however, leads to two problems. First, the conductance would have to take on negative values if it must enhance the response for some values of $g_{syn}$, but suppress it for others. Second, if the local apical response is not linearized, the input voltage to the amplifier will change little over most of the $g_{syn}$ input range. Under these conditions, the amplification mechanism would have to be extremely sensitive to small variations in $V$, and consequently sensitive to noise. Dividing the task between two separate conductances solves both problems.

### Detailed Model

In this and the following sections, we extend the concept of deriving conductances to our model of the layer V pyramidal cell. We assess robustness and control issues, as well as compare the derived conductances to experimentally measured activation curves.

While $G_{K,lin}$ was spread uniformly (per membrane area) throughout layers I–III of the pyramidal cell dendrite, $G_{Ca,amp}$ was placed in at different locations along the

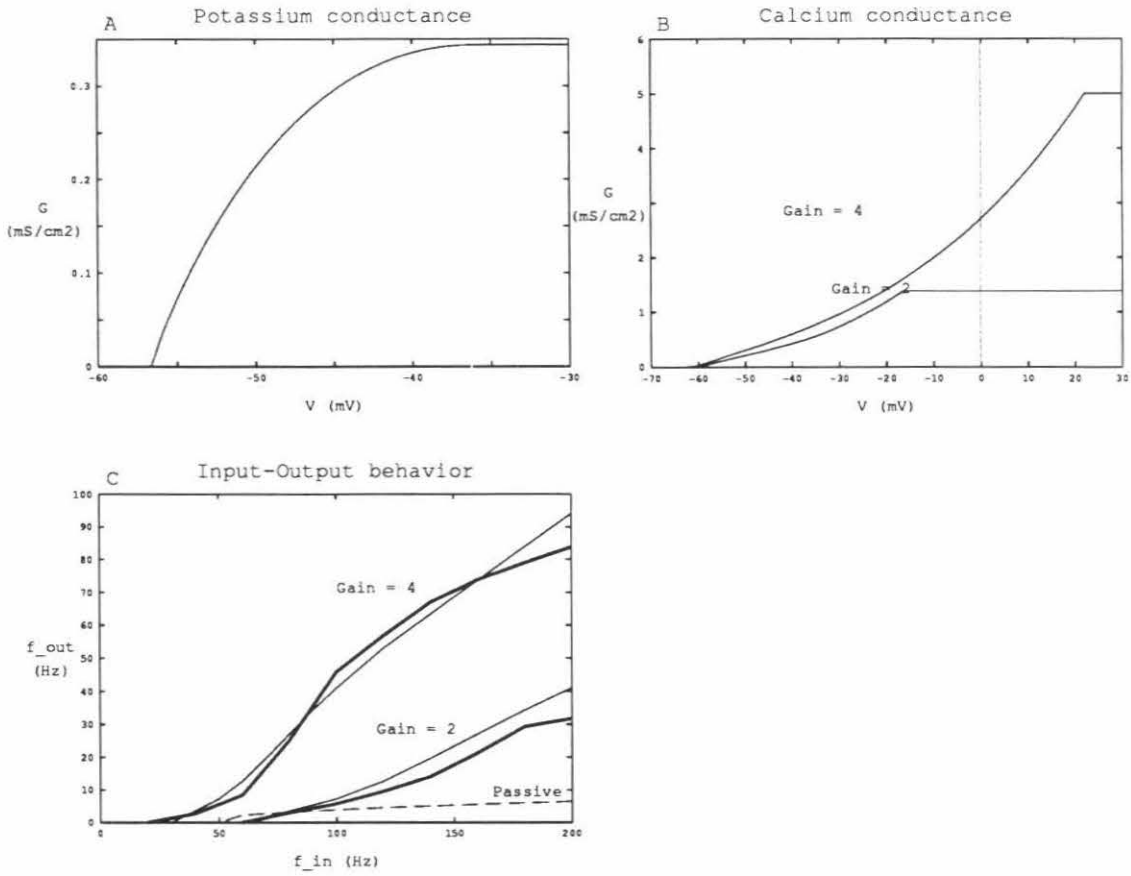


Figure 6.6: **Linearization and amplification in the detailed model. A and B:** Activation curves for numerically derived voltage-dependent conductances. **A:** The potassium conductance, $G_{K,lin}$, is located in superficial layers I–III and linearizes the cell's response to synaptic input. **B:** The calcium conductance, $G_{Ca,amp}$, was located in the center of the apical trunk and amplifies the response. Activation curves are shown for gains of 2 and 4. **C:** Post-synaptic firing rate, $f_{out}$, as a function of the input rate of 500 synapses, $f_{in}$, computed by simulating the cell without voltage clamp (bold) and by evaluating $f_{out}(I_{syn,s})$ for the desired targets (thin). The passive case (dashed) is shown for reference.

apical trunk: in the center or at either end. The default case that is used for most illustration is the first case, in which $G_{Ca,amp}$ was placed in a single compartment at the center of the apical trunk.

Two problems arise when moving from the three compartment model to the full model. First, the circuit is too large and complicated for a purely analytic derivation of the voltage dependencies of $G_{K,lin}$ and $G_{Ca,amp}$ from the shape of the desired $I_{syn,s}(f_{in})$ function. Instead a simulation approach must be used. The second problem arises from the fact that $G_{K,lin}$ and $G_{Ca,amp}$ are distributed over more than one compartment. Since the voltage of each compartment will be different from its neighbors, there will be multiple bids on what the relationship between conductance and voltage should be, over-determining the function. We therefore adopted the following procedure for designing $G_{K,lin}$ and $G_{Ca,amp}$. The independent variable is $f_{in}$, the firing rate of 500 synapses that were located throughout layers I–III, rather than the synaptic conductance, $g_{syn}$. At first, $G_{Ca,amp}$ is set to zero and $G_{K,lin}$ is obtained in the following manner:

1. For a specific value of $f_{in}$ and the associated desired value of the current $I_{syn,s}$, we clamp the soma to the mean somatic potential obtained in response to $I_{syn,s}$. This value can be read off from Fig. 6.2D.

2. A *non-voltage dependent* $G_K$ was inserted uniformly throughout layers I–III.

3. The neuron was simulated until steady state was reached and then $I_{syn,s}$ was measured. $I_{syn,s}$ was taken as the clamp current during synaptic stimulation minus the clamp current in the absence of stimulation. A bisectioning scheme was used to adjust $G_K$ until $I_{syn,s}$ was within 0.01% of the target current.

4. At this point, the *average* $V$ in layers I–III was obtained.

5. The values of $G_K$ and $V_{m,average}$ defined one point on the $G_K(V)$ curve.

6. This entire procedure is repeated for many values of $f_{in}$ and the final function $G_{K,lin}$ obtained by interpolation.

The function $G_{Ca,amp}$ was then obtained in a similar manner in the presence of $G_{K,lin}$. In spite of the above-mentioned problem with non-uniqueness that arises because of the widespread distribution of $G_{K,lin}$, the procedure works remarkably well. Unfortunately, it is time consuming because 20–30 iterations are required to obtain each point on the $G_K(V)$ curve (a typical curve can be computed in about one hour).

The resulting conductances are shown in Fig. 6.6A,B. Increasing the gain had two effects on $G_{Ca,amp}$. First, it took on slightly larger values for $V_m < -20\ mV$. The small difference suggests sensitivity to channel density, as will be discussed below. Second, the activation curve was much more shallow, extending from -60 to about $+20\ mV$.

For verification, simulations were run with $G_{K,lin}$ and $G_{Ca,amp}$ inserted. The resulting curves of $f_{out}$ as a function of $f_{in}$ are displayed in Fig. 6.6C along with the desired target curves. The target curves are reproduced with high fidelity. The passive case in shown for comparison (dashed).

We computed the resulting output rate in response to input rate (Fig. 6.6D). For passive input, superficial input by itself can **at most** drive the cell to fire a few spikes per second (dashed). Furthermore, the response is almost all-or-none. In the presence of the two active currents, superficial input can smoothly vary the output rate in a linear manner over at least 50 $Hz$. $f_{out}$ was computed in two ways, by applying the f-I curve (Fig. 6.2E) to the desired target current (thin lines), and by simulations incorporating the derived activation curves (bold lines).

It is instructive to study the distribution of voltage in the apical tree during the linearization and amplification process. The schematic in Fig. 6.7A shows five

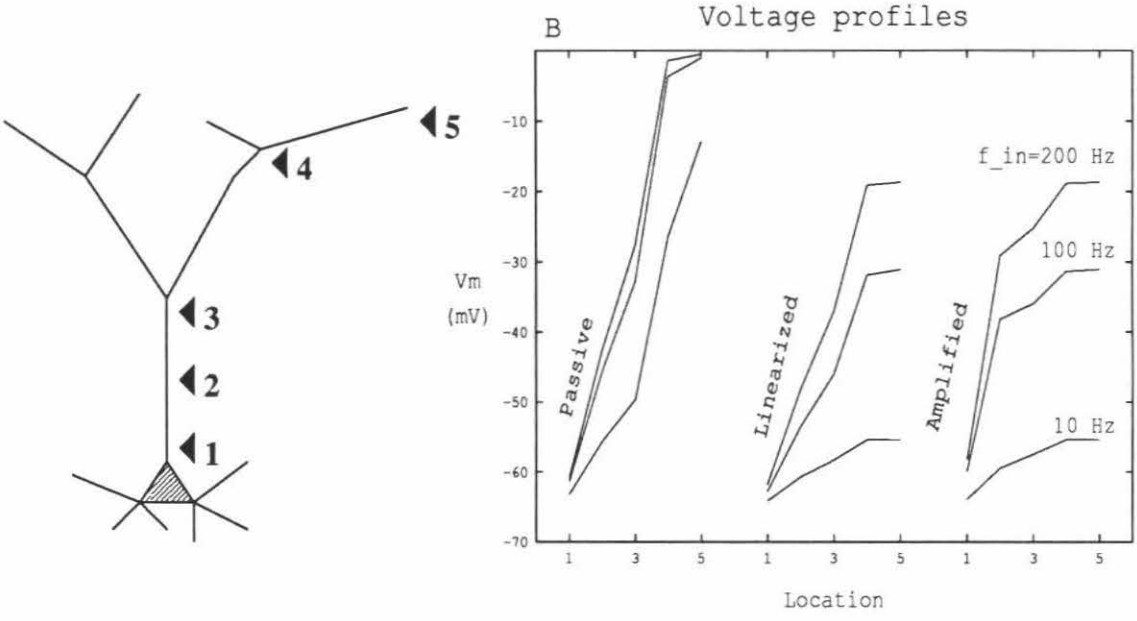


Figure 6.7: **Voltage profiles A:** Schematic of the detailed model, showing three locations (1–3) along the apical trunk, one in the middle of layer I (location 4) and one at a distal tip (location 5). **B:** Voltage distribution along the five locations. The three groups of curves correspond to (left to right): passive dendrite, $G_{K,lin}$ present, both $G_{K,lin}$ and $G_{Ca,amp}$ present. The three curves within each group correspond to (top to bottom): $f_{in} = 200$, 100, and 10 $Hz$, respectively.

locations at which the voltage was tapped. Locations 1–3 are situated along the apical trunk, and locations 4 and 5 are in layer I. Layers 1–3 were stimulated at $f_{in} = 10$, 100, and 200 $Hz$. The three leftmost curves in Fig. 6.7B is for a passive dendrite. The voltage drop across the apical trunk is almost linear and saturation is evident from the close spacing of the curves. When $G_{K,lin}$ is inserted in the tuft (middle three curves), the voltage drop is still linear, but saturation is strongly reduced. The main effect of adding $G_{Ca,amp}$ to location 2 (center of trunk) is to cause the trunk voltage to follow the tuft voltage; while layer I is hardly affected, the depolarization of the tuft spreads far into the trunk. The voltage gradient between locations 1 and 2 increases and a larger axial current is the result.

### Robustness and Gain Control

Since the exact channel density is difficult to measure in a real cell, it is important to know how sensitive the model is to variations in $\overline{G}$. Therefore, simulations were run where the density of $G_{K,lin}$ was varied by a factor 2 and $G_{Ca,amp}$ by 10%. Fig. 6.8A shows the resulting change in $f_{out}$. Two points are worth noticing. First, the curve changes in a well-behaved way, staying fairly linear, while only varying the slope and the point of saturation. Thus, by modulating the channel density, the slope can be set arbitrarily. Second, the cell is much more sensitive to changes in $G_{Ca,amp}$ than in $G_{K,lin}$. This sensitivity is due to the positive-feedback nature of the $Ca^{2+}$ current. This suggests that the $K^+$ channels should be modulated to achieve a *graded* control of the amplification gain, while the $Ca^{2+}$ channels provide a mechanism for possibly switching the contribution made by the apical tuft *on* or *off*.

Fig. 6.8B shows the sensitivity to the exact location of $G_{Ca,amp}$. The activation curve for a location at the center of the trunk was used and $f_{out}$ was computed (curve labeled "Control"). Subsequently the same activation curve was used, but the location was moved by 40 $\mu m$ (10% of the length of the apical trunk). As $G_{Ca,amp}$ was

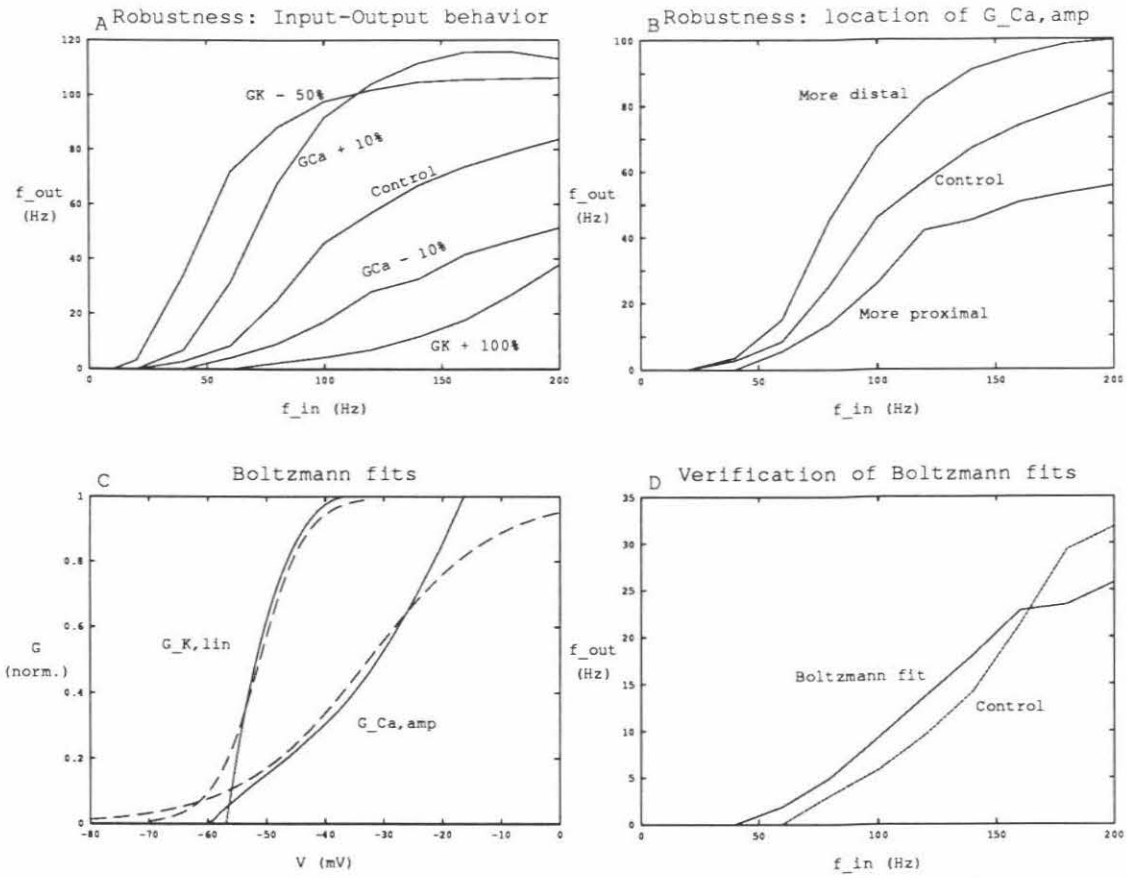


Figure 6.8: **Robustness to variations in $G_{K,lin}$ and $G_{Ca,amp}$.** **A:** The density of channels ($G_K$ and $G_{Ca}$) was varied 10–100% and the resulting $f_{out}$ was graphed for $gain = 4$. **B:** The location of $G_{Ca,amp}$ was moved more proximal or more distal by 40 $\mu m$ (10% of the length of the apical trunk). The activation curve was derived for a central location and $gain = 4$. **C:** A straight line was fit to the central portion (10–90%) using the root-mean-square fit. The resulting slope, $1/K$, and midpoint, $V_{half}$, were used to define a Boltzmann sigmoid: $1/(1 + e^{(V_{half}-V)/K})$. Solid curves: derived activation curves; dashed curves: Boltzmann fits. **D:** Simulation results using the Boltzmann fits in (C). Maximum deviation was $< 6$ $Hz$; average deviation was 3.6 $Hz$.

moved closer to the soma, $f_{out}$ *decreased.* This may seem paradoxical at first since the more proximal location ensures less attenuation. However, the distance to the tuft has increased and so $G_{Ca,amp}$ senses a lower membrane potential and becomes less activated.

Both $G_{K,lin}$ and $G_{Ca,amp}$ are sigmoidal in shape (monotonically increasing with $V$, but bound by two asymptotes), but their derived shapes are different from the Boltzmann sigmoidal relationship often used to fit activation curves: $1/(1 + e^{(V_{half}-V)/K})$ [Hille, 1992]. The Boltzmann formalism can be justified biophysically and is convenient to use because only two parameters determine the shape of the activation curve: the inverse slope $K$ and the midpoint $V_{half}$. Therefore, we chose to fit $G_{K,lin}$ and $G_{Ca,amp}$ with Boltzmann sigmoids. A root-mean-square fit was performed on the central portion (10–90% of $\overline{G}$) and the resulting slope and midpoint were used. Fig. 6.8C shows the two derived conductance functions for a gain of 2 and their Boltzmann fits. The performance of the pyramidal cell was then simulated using the Boltzmann fits rather than the derived original functions. The resulting $f_{out}$ differed little from the target and was off by less than 5 $Hz$ for $G_{Ca,amp}$ and 1 $Hz$ for $G_{K,lin}$.

Background synaptic activity was modeled using the steady state approximation described in chapter 2. This approximation may not be valid along the trunk where $G_{Ca,amp}$ will amplify any changes in membrane potential. To test this, we ran several simulations comparing Poisson synapses with the steady state approximation (fig. 6.10B). The top trace in each pair shows the spike times for the Poisson case, while the bottom trace shows the steady state approximation. For three different input rates (top three pairs), a small amount of noise was added in the Poisson case, but the average $f_{out}$ changed by less than 1%. For the bottom trace pair, $G_{K,lin}$ was removed. The cell did not spike in the absence of stimulation in either case, but for very small input rates (1 $Hz$ in the figure), the spike mechanism was triggered and spiked at the same $f_{out}$ in both cases.

### Selectivity of amplification

If the amplification mechanism ($G_{Ca,amp}$) were located in the soma, all inputs would be expected to be amplified by the same amount, independent of location. Since one aim of this study was to explore ways in which apical inputs can be amplified *specifically*, $G_{Ca,amp}$ was placed in the apical trunk. While this ensures that apical inputs are selected for over basal inputs, it is important to assess how strong this selectivity is.

To explore this, the relative amplification of apical *vs.* basal inputs was compared. First, $G_{K,lin}$ and $G_{Ca,amp}$ were removed; synapses were activated either in the apical tuft or in the basal dendrites (layer 5) at different $f_{in}$ so as to produce an output firing rate ($f_{passive}$) in the range 0–6 $Hz$. Next, $G_{K,lin}$ and $G_{Ca,amp}$ were re-inserted and the same inputs applied. The new firing rate, $f_{active}$, was higher because of the amplification. Fig. 6.10A is a parametric plot of $f_{active}$ ($y$ coordinate) *vs.* $f_{passive}$ ($x$ coordinate); the independent variable was $f_{in}$ (not shown).

We computed $f_{out}$ for two different calcium conductances. One version of $G_{Ca,amp}$ was derived when the calcium channels were placed in the middle of the apical trunk (bold curves) while a second version, with a different voltage-dependency, was derived when the $Ca^{2+}$ channels were located at the distal end of the apical trunk (thin curves). We then either activated apical synaptic input (continuous lines) or basal, layer V, synaptic input (dashed lines). As expected, the response to apical input depends little on whether $G_{Ca,amp}$ is located in the middle of the trunk or at the distal end of the trunk, since the exact form of $G_{Ca,amp}$ was derived to deliver the same current to the soma. The amplification of basal inputs, however, depends strongly on the position of $G_{Ca,amp}$. When $G_{Ca,amp}$ was placed in the center of the trunk (bold dashed curve), the response was significantly elevated by approximately 3 $Hz$ above the Identity curve for a passive dendritic tree. When $G_{Ca,amp}$ was placed at the end

of the trunk (thin dashed curve), however, $f_{out}$ was practically identical to $f_{in}$. In other words, the more distal the location of apical calcium channels, the more specific the amplification.

## 6.3 Discussion

We have demonstrated that the presence of two types of voltage-dependent conductances in the apical dendritic tuft and trunk can serve to linearize and amplify the cell's response to apical input. This mechanism is robust to variations in the potassium conductance, but is sensitive to variations in the calcium conductance. This difference provides a mechanism for controlling the level of amplification of apical input simply by modulating channel densities. Modulation of potassium channels achieves a graded control of amplification gain, whereas the calcium channels provide a mechanism for switching the amplifier on or of.

For simplicity, the concept of deriving optimal conductances was proven on a minimal three-compartment model. Then the same strategy was successfully applied to a physiologically detailed and biologically realistic cell model. However, several assumptions were made in the realistic case. One principal assumption was that the dendrites contain no active conductances other than the two that were specifically derived, $G_{K,lin}$ and $G_{Ca,amp}$. In this study we have explored the derivation of conventional voltage-gated channels only. However, in principle, it is possible to derive a synaptic conductance such as the NMDA conductance. Background activation of NMDA synapses can be time-averaged just like the AMPA conductance in eqs. 2.2 and 2.3, and will yield a voltage-dependent conductance.

The presence of more than two active conductances is not expected to alter the results, since the objective of the algorithm is to derive optimal conductances for a given target function, *regardless of the morphology and electronic structure* of the cell.

However, if other dendritic conductances are strongly non-linear and present in high enough concentrations, stability may be affected. We tested the effect of additional conductances by incorporating a generic conductance, $G_{test}$ to the apical trunk, co-localized with $G_{Ca,amp}$. The conductance had a single activation ($m$) particle with $V_{half} = -30\ mV$ and $K = 7\ mV$, ensuring a significant non-linearity in the critical range of membrane voltage. $G_{max}$ was set to 1/3 of that of $G_{Ca,amp}$ in the absence of the test conductance, the reversal potential was set to either 50 $mV$ (sodium) or -95 $mV$ (potassium), and the particle time constant was arbitrarily set to either 5 or 50 $msec$ (which made little difference). The re-derived $G_{Ca,amp}$ deviated only little from the original (graphs not shown) and the resulting $I_{syn,s} = fnc(f_{in})$ did not change at all and showed no instability. When the soma was un-clamped and left to spike, however, the resulting output firing rate, $f_{out}$, demonstrated a larger change. When $G_{test}$ was a potassium conductances, the cell became somewhat less excitable and the $f_{out}$ curve shifted by about 10 $Hz$. When $G_{test}$ was a sodium conductance, $f_{out}$ approached its maximum value much more rapidly, for $f_{in} = 80\ Hz$ rather than 200 $Hz$. Note, however, that $G_{Ca,amp}$ was derived according to a given target function for $I_{syn,s}$. If the target function instead was given for $f_{out}$ (which is computationally much more expensive), $f_{out}$ is expected to show as little variation as $I_{syn,s}$ in the example described above.

A further assumption is that we have only considered sustained (steady state) inputs. This is a reasonable simplification since stimuli used in physiological experiments typically last for several hundred $msec$ or even seconds, which is longer than the time constants of most conductances as well as the membrane time constant, $\tau_m$. The N- and L-type $Ca^{2+}$ channels, which most resemble $G_{Ca,amp}$, show either no inactivation, very slow inactivation (up to many seconds) or variable and partial inactivation [Fisher et al., 1990, Sayer et al., 1990]. This is consistent with our model, as long as there is some residual $Ca^{2+}$ current. Only the T-type $Ca^{2+}$ channel

consistently shows rapid and complete inactivation.

### 6.3.1 Experimental evidence for active dendrites

Experimental data suggests that not only do the soma and axon hillock harbor active, voltage-dependent conductances, but that dendrites do so as well [for reviews see Llinas, 1988 and Mel, 1993]. These experiments have demonstrated the existence and the ionic selectivity of these conductances, but little is known about their kinetics and densities. The evidence for such dendritic excitability in cortical pyramidal cells comes from three different sources: indirect inferences from EPSP amplitude and time course, direct recordings from dendrites, and imaging of internal ionic concentrations.

Early evidence for active dendrites were found in intracellular recordings from motoneurons and hippocampal cells [Eccles et al., 1958, Spencer and Kandel, 1961]. Millisecond time scale depolarizations, termed "fast prepotentials," were seen usually at the beginning of the action potential, but sometimes in isolation. These prepotentials were thought to reflected the electrotonic propagation of dendritic spikes. More recently, Williams and Johnston [1991] compared EPSPs to somatically injected currents shaped like alpha functions in hippocampus. The EPSPs decayed slowly (79–135 $msec$) and showed a strong voltage dependence, while the alpha currents showed faster decay (32–37 $msec$) and little voltage dependence. Since the membrane time constant was $\approx$ 30 $msec$, the dendritic synapses apparently activated a local conductance that could not be reached by the somatically injected current. In these experiments, potassium currents were blocked by intracellular cesium, and the NMDA antagonist APV had little effect, suggesting that the putative conductances were calcium or sodium dependent. Similar discrepancies between the decays of EPSPs and current injections have been found in rat neocortical slices [Thomson et al., 1988].

Recently, further evidence for active dendrites have been obtained from somatic

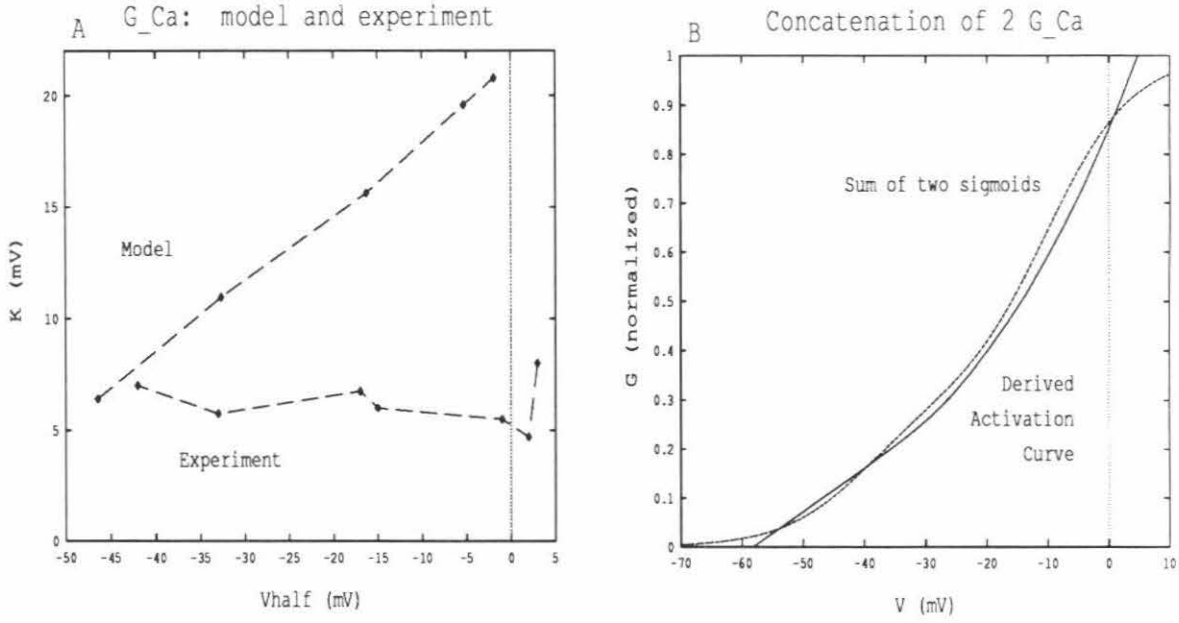


Figure 6.9: **Comparison of $G_{Ca,amp}$ to experimental data.** The Boltzmann sigmoid, $1/(1+e^{(V_{half}-v)/K})$, uses only two parameters to specify an activation curve: $K$ and $V_{half}$. **A:** Loci of seven experimentally determined calcium conductances and five model values of $G_{Ca,amp}$. Data points are marked with diamonds; dashed lines are only used to group data points into two groups: model (top) and experimental (bottom). The locations of $G_{Ca,amp}$ along the trunk was (left to right): proximal end, center, distal end, center, and distal end; the gain was 2 for the three points on the left and 4 for the two points on the right. **B:** The (normalized) activation curve for $G_{Ca,amp}$ at the distal end of the trunk and $gain = 2$, has $V_{half} = -27.7\ mV$ and $K = 14.7\ mV$. The algebraic sum of two sigmoids, both with $K = 7$, provides a close fit. The amplitudes of the two sigmoids were 0.3 and 0.7, respectively; $V_{half}$ = -40 and -10 $mV$, respectively.

recordings in the presence of TTX and TEA which block the action potential mechanism and so enhance the visibility of underlying active processes [Reuveni et al., 1993]. The multiple plateau potentials that are seen under these conditions are best explained by $Ca^{2+}$ channels of the same type spatially segregated throughout the distal parts of the dendritic tree, rather than somatic $Ca^{2+}$channels of different types.

Several reports describe intradendritic recordings from dendrites of hippocampal neurons [Wong et al., 1979, Benardo et al., 1982, Masukawa and Prince, 1984, Poolos and Kocsis, 1990, Wong and Stewart, 1992]. In some of those experiments, the soma had been cut off from the apical dendritic tree (isolated preparation). Both fast and slow spikes were seen. The slow spikes were insensitive to TTX, and so likely to be mediated by a $Ca^{2+}$ conductance. In neocortex, cell-attached patch clamp recordings revealed comparable densities of $Na^{+}$ current at the soma and on the dendrites [Huguenard et al., 1989]. However, the cells were immature with dendrites being shorter than 100 $\mu m$ and thus still quite close to the soma. Somatic recordings in the presence of TTX and TEA, which blocked fast spikes and $K^{+}$ channels, reveal Ca-dependent spikes [Franz et al., 1986]. Direct recordings from histologically confirmed apical dendrites reveal both fast and slow spikes [Pockberger, 1991, Amitai et al., 1993]. Slow spikes were not observed in somatic recordings, are insensitive to TTX and resemble $Ca^{2+}$ spikes in hippocampus and cerebellum.

Calcium imaging of hippocampal pyramids reveal high $[Ca^{2+}]_i$ concentrations in the proximal half of the apical dendrite, with very low concentrations in the distal half and at the soma [Regehr et al., 1989] in response to synaptic activation. $Ca^{2+}$ is likely to enter the dendritic trunk through voltage-gated calcium channels, rather than through synaptic NMDA channels, since AP5 had only a minimal effect on the evoked $Ca^{2+}$. Another study has found somewhat higher concentrations in distal dendrites, though still considerably lower than proximal dendrites, with similar results for $[Na^{+}]$ [Jaffe et al., 1992].

In summary, there is strong evidence that $Ca^{2+}$ channels are present in dendrites and able to generate spikes. Unfortunately, details about kinetics and densities are lacking. There is less evidence for the presence of dendritic $Na^+$ and $K^+$ channels, and the question of regenerative $Na^+$ spikes is still open.

### 6.3.2 Comparison with known activation curves

How well does $G_{Ca,amp}$ compare to activation curves measured in real cells? Once again, it is convenient to use the Boltzmann parameters $K$ and $V_{half}$ to characterize the conductances. Figure 6.9A shows the loci in $K$–$V_{half}$ space for $G_{Ca}(v)$ for five different locations of the conductances as described in section 6.2.3 as well as in the figure legend. This is compared to the activation curves of seven channels described for chick dorsal root ganglion cells [Fox et al., 1987], bullfrog sympathetic ganglion cells [Yamada et al., 1989], and guinea-pig hippocampus [Fisher et al., 1990]. While the midpoints are roughly in the right range, the slopes $1/K$ are up to a factor 3 too shallow. $K$ factors of more than 10 have rarely been described in any preparation. A possible solution to this problem is to use two different $Ca^{2+}$ conductances in parallel with different activation thresholds and, in a sense, "concatenate" their activation curves. Such multiple $Ca^{2+}$ conductances have been described in several cell types [Fox et al., 1987, Fisher et al., 1990, Sayer et al., 1990]. Figure 6.9B shows the sum of two activation curves, both with $K = 7$, but with different midpoints and amplitudes (see figure legend). This concatenated activation curve provides a better fit than the single Boltzmann sigmoid used in Fig. 6.8C. A third $Ca^{2+}$ conductance with a yet higher threshold, can be added to obtain even more shallow curves. It is interesting to note that the activation curves become much more shallow for larger gains, extending into more positive potentials. If calcium channel types are differentially modulated, reducing the higher-threshold type, $f_{out}$ will saturate at different values, keeping the

slope of $f_{out}(f_{in})$ constant.

A Boltzmann fit to $G_{K,lin}$ has a midpoint $V_{half} = -51\ mV$ and a slope factor $K = 3.9\ mV$. Little data exists on the activation curve for $I_M$. In bullfrog sympathetic ganglion cells, $V_{half}$ is $\approx -35\ mV$ [Yamada et al., 1989], the same as a very slowly inactivating ($> 10sec$) $K^+$ current in neocortex [Spain et al., 1991, Fig. 4D], while $K$ was $\approx 10\ mV$. The delayed rectifier described by Frankenhaeuser and Huxley [1964] has a $V_half$ of -40 $mV$ and $K = 8.7\ mV$. While both these examples of $K^+$ currents are less steep than $G_{K,lin}$, other channel types have been described with $K$ of about 4 [Fisher et al., 1990].

### 6.3.3 Variations of the amplification mechanism

It was shown in the previous section that the parameters of $G_{Ca,amp}$ vary with the location at which the channels are inserted as well as with the gain of amplification (fig .6.9A). As the location of $G_{Ca,amp}$ is moved further distally, a larger depolarization is needed to deliver the same current, and so the activation curve reaches into higher voltages. Similarly, as the gain is increased, more current is needed.

$G_{Ca,amp}$ was derived for other conditions as well. The first case involved reducing the cross-sectional area of the apical trunk by a factor 2. This would correspond to the smaller values reported for trunk diameters in rat [Larkman, 1991a]. The slimmer trunk will have a larger axial resistance, and, again, a larger depolarization is needed to deliver the same current (Fig. 6.10C).

Throughout this chapter, the amplification mechanism has been a calcium conductance with a reversal potential of 115 $mV$. Other ionic selectivities can be specified simply by changing the reversal potential to 50 $mV$ (sodium) or 0 $mV$ (NMDA). Fig. 6.10D compares the activation curves for reversal potentials of 0 and 115 $mV$. The curves span the same domain of membrane potentials, but the "NMDA" conduc-

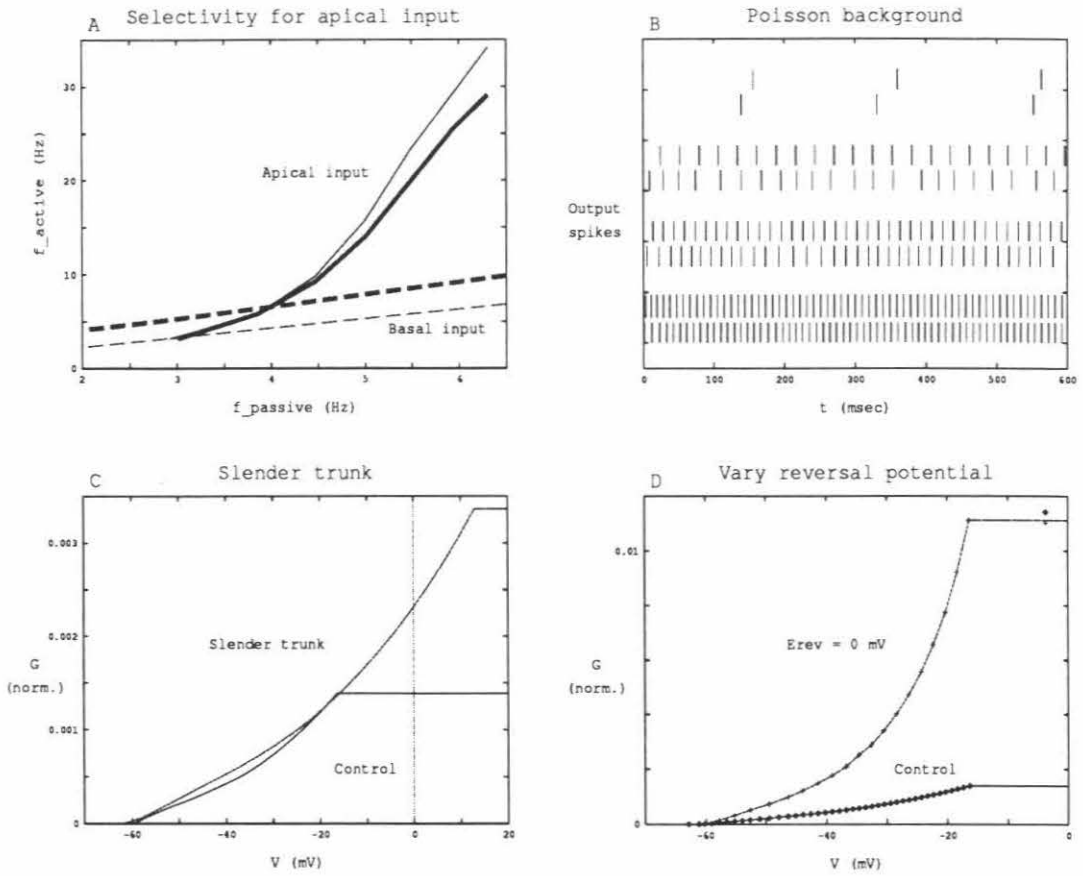


Figure 6.10: **A:** Selectivity of amplification. The output frequency was plotted parametrically in the absence of $G_{K,lin}$ and $G_{Ca,amp}$ ($x$ coordinate) as well as in their presence ($y$ coordinate). This was repeated for apical (solid) and basal (dashed) input as well as for two locations of $G_{Ca,amp}$: center of trunk (bold) and distal end of trunk (thin). For the apical input, both locations of $G_{Ca,amp}$ result in approximately the same output firing frequency. The output rate for basal input is almost identical to the rate for a purely passive membrane (the associated Identity curve coincides and so is not shown) for a distal placement of $G_{Ca,amp}$ and elevated by about 3 $Hz$ for the more proximal one. $gain = 2$. **B:** Poisson background activity. Background synapses were either replaced with their average steady state activation (top trace in each pair) or were explicitly modeled (bottom trace in each pair) and the time of output spikes were marked with horizontal lines. Top three trace pairs: $gain = 4$ and (top to bottom) $f_{in} = 50$, 100, and 150 $Hz$. Bottom trace pair: $G_{K,lin}$ was removed and $f_{in} = 1$ $Hz$ (no spikes occurred for $f_{in} = 0$ $Hz$). **C:** The diameter of the apical trunk was reduced by a factor 1.414 and $G_{Ca,amp}$ was rederived. **D:** The reversal potential of the amplification mechanism was set to 0 $mV$ (NMDA) rather than 115 $mV$ and $G_{Ca,amp}$ was rederived.

tance has a higher density, since the driving force, $E_{rev}$-$V_m$, is smaller. A persistent sodium conductance has been observed in neocortical cells [Stafstrom et al., 1985] though its distribution is unknown, and there is evidence for NMDA being present in the apical dendrite [Cauller and Connors, 1993].

The work presented in this chapter has assumed (dynamic) steady-state conditions and the derived conductances do not inactivate. This would fit well with the amplification mechanism being either a persistent sodium conductance or NMDA. It would also be consistent with calcium channels of the N- and L-types, which show either partial or no inactivation, as discussed above. However, intradendritic recordings have revealed the presence of a spike mechanism in some cells [Pockberger, 1991, Amitai et al., 1993]. It is beyond the scope of this chapter to model the effects of such a spike mechanism, but an interesting avenue for future research is suggested. The f-I curve of this spike mechanism is likely to be crucial for the results presented here. If the f-I curve is similar to the one described for squid axon [Hodgkin and Huxley, 1952] in that it displays a discontinuity and a very limited range of frequencies, then amplification will take on an all-or-none character, rather than a graded one. On the other hand, if the f-I curve resembles the almost linear somatic spike mechanism modeled here, then it would still be possible to achieve a graded response to apical inputs. As far as we know, there is no description of an f-I curve for dendritic calcium spikes. However, the procedure for deriving $G_{Ca,amp}$ could be modified to generate an f-I curve rather than a single activation curve.

### 6.3.4 Modulation of active conductances

Our results suggest a simple mechanism for controlling the gain of apical inputs: partially inactivate either the layer IV calcium conductance or the layer I–III potassium conductance. The apical tuft can be viewed as a separate integrative region, and the

impact of this region on cell output behavior can be controlled.

Calcium channels that activate upon depolarization give a negative contribution to the input conductance and provide positive feedback for changes in membrane potential. They are therefore relatively sensitive to channel density. Consequently, $Ca^{2+}$ channels in the apical trunk provide a possible mechanism for connecting or disconnecting more distal input in an all-or-none fashion. This gating may be graded as well, but there would be relatively high demands on the precision of the neuromodulatory control of these channels.

Block and modulation of $Ca^{2+}$ currents by various transmitters is well established in sensory and sympathetic neurons [Plummer et al., 1991, Swandulla et al., 1991, Cox and Dunlap, 1992] as well as in central neurons [Sayer et al., 1992]. In hippocampus, adrenergic and muscarinic agonists cause changes in L channel activity by as much as 8-fold [Fisher et al., 1990].

Two crucial aspects of our model conductance, $G_{Ca,amp}$, are thus consistent with experimental evidence: $Ca^{2+}$ conductances are indeed present in the apical trunk and $Ca^{2+}$ channels can be modulated by specific inputs.

Potassium channels that activate upon depolarization have positive input conductance and are negative feedback in nature. This is often expressed electrophysiologically as a phenomenological inductance or "sag" in response to current steps. The effect of $K^+$ channels is therefore less sensitive to channel density and a more graded control can be exerted by putative modulators with less demand for high precision. Their location in the model is in conjunction with the apical inputs themselves, in layers I–III.

The $M$ current, $I_M$, has been named for its sensitivity to muscarine, and is an obvious candidate for $G_{K,lin}$. In human neocortex, it is reduced by activation of muscarinic receptors by either acetylcholine (ACh) or serotonin [McCormick and Williamson, 1989]. While little is known about the spatial distribution of $K^+$ channels, labeling

studies of muscarinic fibers have demonstrated particularly dense innervation of layer I [Bear et al., 1985, De Lima and Singer, 1986], an area that contains few somata; confirmed extrinsic sources are nuclei in the basal forebrain, intralaminar and midline nuclei of the thalamus, including the LGN, as well as the striatum and reticular formation [Bear et al., 1985, De Lima and Singer, 1986].

# Chapter 7

# Conclusions

*Of making many books there is no end, and much study is a weariness of the flesh.* – Ecclesiastes 12:11

## 7.1 Why simulations?

This thesis studies the input/output relationship of neocortical pyramidal cells and how this relationship can be controlled in various ways. A simulation approach is used. Consequently, the longest chapter in the thesis (chapter 2) is devoted to the development of a very detailed and biologically plausible cell model. This model is subsequently used to investigate four different problem domains. Note that very simplified models are introduced to demonstrate proof of concept and allow for an analytic treatment (chapters 4, 5, 6). The detailed model is then applied to show that the simplification was valid and to point out complications arising from the dendritic morphology and the presence of active or non-uniformly distributed conductances.

The model was tuned by replicating certain current clamp experiments from the literature (see chapter 2). The model thus demonstrates realistic spikes and f-I curves,

including spike adaptation and a primary slope, as well as overshoot, sag, and proper input resistance and time constant. The most important electrophysiological piece of evidence, that has not been incorporated into the standard model, is the demonstration of calcium spikes either as inferred by somatic recordings [Franz et al., 1986] or intradendritic recordings [Pockberger, 1991, Amitai et al., 1993]. It is the premise of this thesis, however, that an understanding of passive dendritic trees is a necessary stepping stone to investigating active dendritic trees. In addition, exploratory studies of the possible effects of active dendrites were often undertaken by adding NMDA, or were the main subject as in chaper 6.

There are many obvious advantages of using simulations over real experiments. Parameters can be exactly controlled; noise can be eliminated or added at will; the specific effect of various conductances can be investigated; the sensitivity to parameter variations can be assessed; simulations can be reproduced with identical conditions, varying only a single parameter; etc.

There are also serious disadvantages with a simulation approach. The most critical one is the lack of hard data for model parameters, especially the exact kinetics of channels and their distributions. Further, the nature and sequence of inputs in behaving animals is not well known, making it difficult to ask the right questions.

The lack of hard data was addressed in several ways. Many of these were discussed in conjunction with model development (chapter 2), such as the sensitivity to channel densities or errors in the measurement of morphological data. Further, a given phenomenon was investigated under different conditions, such as different background activity (slice, "standard," and intense activity), in a different and smaller cell (layer II/III pyramid), or in the presence of NMDA input. Errors in synaptic parameters ($G_{syn}$, $t_{peak}$, total number of synapses) are all lumped together since the time-averaged background activity involves the product of these parameters; the investigation in chapter 5 is therefore qualitative and any error would result in a scaling along the $x$

axis ($f_b$). In chapter 6, where activation curves were derived, the sensitivity of firing rate to the density and shape of these currents was assessed by bracketing. This not only served to study the robustness of the *model* but also indicated a mechanism for *controlling* the cell's sensitivity to apical input.

## 7.2 What have we learned?

We used a detailed compartmental model to investigate synaptic integration of single excitatory inputs. Nine measure of efficacy and four measures of delay were defined. Using these measures, the range of efficacies and delays throughout two model cells were histogramed. A careful comparison of these measures showed that they will assign dramatically different values to distal synapses. Current-related measures of efficacy, such as EPSP area, charge attenuation, and differential change in output spike rate, were found to be useful measures, while voltage-related measures, with the exception of EPSP amplitude, were of little value.

Integration of large numbers of synapses were investigated in the context of synchronization. It was found that for moderate number of inputs, more output spikes were produced when the inputs were temporally synchronized. For large number of inputs, however, it was advantageous to *de*-synchronize the inputs. This observation is of great consequence for many higher-level models that depend on detecting synchronized input activity. An important caveat, however, is that our model only used a passive dendritic tree; the presence of active dendritic conductances may change the results.

The main thrust of this thesis is to consider the neuron not as an inflexible, static device with a fixed input-output relationship, but as a flexible unit with a dynamic transfer function that can be changed according to various control signals. These control signals are rather crude, either encompassing the whole cell (background

activity) or restricting themselves to one or more layers. The signals take the form of synaptic conductance changes or a modulation of the density of active conductances.

We made two major departures from classical cable theory. The first is that we treat synapses as conductance changes and not current sources. The total passive membrane resistance in the absence of synaptic input, is only on the order of 5 $nS$, while the peak conductance of a single excitatory AMPA synapse is 0.5 $nS$. This is why large numbers of inputs will directly and dramatically affect the electrotonic structure of the cell. The membrane time constant, $\tau_m$, which is a measure of temporal integration, varied by more than an order of magnitude as the background activity ranged from 0 to 10 $Hz$. Similarly, $R_{in}$ and $L$, which are indicative of spatial integration, varied by factors of more than 10 and 4, respectively. This control over $R_{in}$, $L$, and $\tau_m$ provides a means for modulating receptive field profiles and tuning curves.

A second departure from classical cable theory is to de-emphasize voltage as the important parameter, and focus on current. In chapter 6, the current delivered to the soma by a group of synapses, $I_{syn,s}$, is taken as a measure of their efficacy. $I_{syn,s}$ is then translated into an output firing rate by the spike-generating mechanism. It is thus possible to go from an input rate to an output rate via *current* as an intermediate variable, without dealing with voltage. To use mathematical formalism, $f_{out}$ is the *composition* of two functions:

$$f_{out}(f_{in}) = f_{out} \otimes I_{syn,s}(f_{in}) = f_{out}(I_{syn,s}(f_{in}))$$

The outer function, $f_{out}(I_{syn,s})$, describes the spike generation mechanism and is mainly a function of somatic parameters. By modulating channel densities of *somatic* conductances, this function can be changed: increasing the density of $I_M$ shifts the function to the right, while increasing $I_{AHP}$ or $I_{Ca}$ reduces the slope. The inner function, $I_{syn,s}(f_{in})$, measures the efficacy of a group of synapses. This measure takes

into account features of the dendrites, such as saturation, attenuation, and active conductances, and the morphology of the dendrites. By varying dendritic parameters, especially the densities of active dendritic conductances, $I_{syn,s}(f_{in})$ can be changed selectively for one group of synapses. Chapter 6 showed specifically how $I_{syn,s}$ for layer I–III inputs could be linearized and amplified, with only a moderate influence on $I_{syn,s}$ for layer V inputs.

The brain remains one of the most intriguing unsolved mysteries facing man. It has tickled the intellectual curiosity of vast numbers of researchers for more than a century and has been the subject of both philosophical treatises and works of fiction [for instance, Bernander, 1991b]. To understand how information is processed in our brains, to know the neural correlates of love and hate, to understand why one pattern of neuronal firing is music to our ears while another makes us remember a dear friend—those are the ultimate goals of neuroscience. The work presented in this thesis aspires to be one small step on the long path that lies ahead.

# References

[Abbott, 1991] Abbott, L. (1991). Realistic synaptic inputs for model neuronal networks. *Network*, 2:245–258.

[Abeles, 1982] Abeles, M. (1982). Role of the cortical neuron: integrator or coincidence detector? *Israel J. Medical Sciences*, 18:83–92.

[Abeles, 1991] Abeles, M. (1991). *Corticonics – Neural circuits of the cerebral cortex.* Cambridge University Press.

[Aertsen et al., 1989] Aertsen, A., Gerstein, G., Habib, M., and Palm, G. (1989). Dynamics of neuronal firing correlation: modulation of effective connectivity. *J. Neurophysiology*, 61(5):900–917.

[Agmon-Snir and Segev, 1992] Agmon-Snir, H. and Segev, I. (1992). Signal delay and propagation velocity in passive dendritic structures. *Submitted to J. Neurophysiology.*

[Allman et al., 1985] Allman, J., Miezin, F., and McGuinnes, E. (1985). Direction- and velocity-specific responses from beyond the classical receptive field in the middle temporal visual area (mt). *Perception*, 14:105–126.

[Amitai et al., 1993] Amitai, Y., Friedman, A., Connors, B., and Gutnick, M. (1993). Regenerative activity in apical dendrites of pyramidal cells in neocortex. *Cerebral Cortex*, 3:26–38.

[Andersen et al., 1990] Andersen, P., Raastad, M., and Storm, J. F. (1990). Excitatory synaptic integration in hippocampal pyramids and dentate granule cells. *Symp. Quant. Biol.*, 55:81–96.

[Anderson et al., 1993a] Anderson, Douglas, R., and Martin, K. (1993a). Unpublished observations.

[Anderson et al., 1993b] Anderson, Douglas, R., Martin, K., and Nelson (1993b). In preparation.

[Bair et al., 1993] Bair, W., Koch, C., Newsome, W., and Britten, K. (1993). Power spectrum analysis of MT neurons in the awake monkey. In Eeckman, F., editor, *Computation and Neural Systems 92*. Kluwer Academic Publishers. In Press.

[Barrett and Crill, 1974] Barrett, J. and Crill, W. (1974). Specific membrane properties of cat motoneurones. *J. Physiology*, 2:301–324.

[Baxter and Byrne, 1991] Baxter, D. and Byrne, J. (1991). Ionic conductance mechanisms contributing to the electrophysiological properties of neurons. *Current Opinion in Neurobiology*, 1:105–112.

[Bear et al., 1985] Bear, M., Carnes, K., and Ebner, F. (1985). An investigation of cholinergic circuitry in cat striate cortex using acetylcholinesterase histochemistry. *J. Comparative Neurology*, 234:411–430.

[Bekkers and Stevens, 1989] Bekkers, J. and Stevens, C. (1989). NMDA and non-NMDA receptors are co-localized at individual excitatory synapses in cultured rat hippocampus. *Nature*, 341:230–233.

[Benardo et al., 1982] Benardo, L., Masukawa, L., and Prince, D. (1982). Electrophysiology of isolated hippocampal pyramidal dendrites. *J. Neuroscience*, 2(11):1614–1622.

[Bernander, 1991] Bernander, Ö. (1991). A plea for mercy. In Budrys, A., editor, *Writers of the future, Vol. 7*. Bridge Publications.

[Bernander et al., 1992] Bernander, Ö., Douglas, R., and Koch, C. (1992). A model of cortical pyramidal neurons. CNS memo 16, California Institute of Technology, Pasadena, CA, 91125.

[Bernander et al., 1993a] Bernander, Ö., Douglas, R., and Koch, C. (1993a). Control of efficacy of apical inputs to neocortical pyramidal cells. In preparation.

[Bernander et al., 1993b] Bernander, Ö., Douglas, R., and Koch, C. (1993b). Synaptic inputs to neocortical pyramidal cells: Efficacy, delay, and integration. CNS memo 21, California Institute of Technology, Pasadena, CA, 91125.

[Bernander et al., 1991] Bernander, Ö., Douglas, R., Martin, K., and Koch, C. (1991). Synaptic background activity influences spatiotemporal integration in single pyramidal cells. *Proc. Natl. Acad. Sci. USA*, 88:11569–11573.

[Bernander et al., 1993c] Bernander, Ö., Koch, C., and Usher, M. (1993c). The effect of synchronized inputs at the single neuron level. Submitted to Neural Computation.

[Bhalla and Bower, 1993] Bhalla, U. and Bower, J. (1993). Exploring parameter space in detailed single neuron models: Simulations of the mitral and granule cells of the olfactory bulb. *In Preparation.*

[Bhide and Bedi, 1984] Bhide, P. and Bedi, K. (1984). The effects of a lengthy period of environmental diversity on well-fed and previously undernourished rats II. synapse-to-neuron ratios. *J. Comp. Neurol.*, 227:305–310.

[Bindman et al., 1988] Bindman, L., Meyer, T., and Prince, C. (1988). Comparison of the electrical properties of neocortical neurones in slices in vitro and in the anaesthetized rat. *Brain Research*, 68:489–496.

[Bindman and Prince, 1983] Bindman, L. and Prince, C. (1983). Intracellular recording from neurones in the cerebral cortex of the anaesthetized rat. *J. Physiology (London)*, 341:7–8P.

[Borg-Graham, 1987] Borg-Graham, L. (1987). Modeling the somatic electrical response of hippocampal pyramidal neurons. Master's thesis, MIT.

[Borg-Graham and Grzywacz, 1992] Borg-Graham, L. and Grzywacz, N. (1992). A model of the directional selectivity circuit in retina: Transformations by neurons singly and in concert. In McKenna, T., Javis, J., and Zarnetzer, S., editors, *Single Neuron Computation*, chapter 13, pages 347–375. Academic Press, Boston, Massachusetts.

[Brown and Griffith, 1983] Brown, D. and Griffith, W. (1983). Persistent slow inward calcium current in voltage-clamped hippocampal neurones of the guinea-pig. *J. Physiology*, 337:303–320.

[Busch and Sakmann, 1990] Busch, C. and Sakmann, B. (1990). Synaptic transmission in hippocampal neurons: Numerical reconstruction of quantal IPSCs. *Cold Spring Harbor symposia on quantitative biology*, LV:69–80.

[Bush, 1989] Bush, P. (1989). A theoretical and experimental investigation of the ionic conductances that govern the repetitive firing of neocortical neurons. Thesis, Oxford, 1989.

[Bush and Sejnowski, 1992] Bush, P. and Sejnowski, T. (1992). Dendritic saturation and effects of inhibition in simulated neocortical pyramidal cells. Submitted to J. Neurophysiology.

[Carpenter et al., 1971] Carpenter, D., Hovey, M., and Bak, A. (1971). Intracellular conductance of Aplysia neurons and squid axon as determined by a new technique. *Int. J. Neuroscience*, 2:35–48.

[Cauller and Connors, 1992] Cauller, L. and Connors, B. (1992). Functions of very distal dendrites: experimental and computational studies of layer I synapses on neocortical pyramidal cells. In McKenna, T., Javis, J., and Zarnetzer, S., editors, *Single Neuron Computation*, chapter 8, pages 199–229. Academic Press, Boston, Massachusetts.

[Cauller and Connors, 1993] Cauller, L. and Connors, B. (1993). Cortical origins of long horizontal axons in layer I of primary somatosensory cortex in rats. Submitted.

[Cole and Nicoll, 1984] Cole, A. and Nicoll, R. (1984). Characterization of a slow cholinergic post-synaptic potential recorded in vitro from rat hippocampal pyramidal cells. *J Physiology (London)*, 352:173–188.

[Connor and Stevens, 1971] Connor, J. and Stevens, C. (1971). Inward and delayed outward membrane currents in isolated neural somata under voltage clamp. *J. Physiology*, 213:31–53.

[Connors and Gutnick, 1990] Connors, B. and Gutnick, M. (1990). Intrinsic firing patterns of diverse neocortical neurons. *Trends Neurosci.*, 13(3):99–104.

[Connors et al., 1988] Connors, B., Malenka, R., and Silva, L. (1988). Two inhibitory postsynaptic potentials, and GABAa, and GABAb receptor-mediated responses in neocortex of rat and cat. *J. Physiology*, 406:443–468.

[Coss, 1985] Coss, R. (1985). The function of dendritic spines: A review of theoretical issues. *Behavioral and neural biology*, 44:151–185.

[Cox and Dunlap, 1992] Cox, D. and Dunlap, K. (1992). Pharmacological discrimination of N-type from L-type calcium current and its selective modulation by transmitters. *J. Neuroscience*, 12(3):906–914.

[Crick and Koch, 1990] Crick, F. and Koch, C. (1990). Towards a neurobiological theory of consciousness. *Seminars Neuroscience*, 2:263–275.

[Crick and Koch, 1992] Crick, F. and Koch, C. (1992). The problem of consciousness. *Sci. Am.*, 267(3):152–159.

[De Lima and Singer, 1986] De Lima, A. and Singer, W. (1986). Cholinergic innervation of the cat striate cortex: A choline acetyltransferase immunocytochemical analysis. *J Comparative Neurology*, 250:324–338.

[De Schutter and Bower, 1993] De Schutter, E. and Bower, J. (1993). An active membrane model of the cerebellar purkinje cell: I. Simulation of current clamps in slice. In preparation.

[Desmond and Levy, 1982] Desmond, N. and Levy, W. (1982). A quantitative anatomical study of the granule cell dendritic fields of the rat dentate gyrus using a novel probabilistic method. *J. Comp. Neurol.*, 212:131–145.

[DiFrancesco, 1987] DiFrancesco, D. (1987). A new interpretation of the pace-maker current in calf purkinje fibers. *J. Physiology*, 314:359–376.

[Douglas and Martin, 1990] Douglas, R. and Martin, K. (1990). Neocortex. In Shepherd, G., editor, *The synaptic organization of the brain, 2nd edition*, chapter 12, pages 389–438. Oxford University Press, Oxford.

[Douglas and Martin, 1991] Douglas, R. and Martin, K. (1991). A functional microcircuit for cat visual cortex. *J. Physiology*, 440:735–769.

[Douglas et al., 1991] Douglas, R., Martin, K., and Whitteridge, D. (1991). An intracellular analysis of the visual responses of neurones in cat visual cortex. *J. Physiology*, 440:659–696.

[Eccles et al., 1958] Eccles, J., Libet, B., and Young, R. (1958). The behavior of chromatolysed motoneurones studied by intracellular recording. *J. Physiology*, 143:11–40.

[Edwards et al., 1990] Edwards, F., Konnerth, A., and Sakmann, B. (1990). Quantal analysis of inhibitory synaptic transmission in the dentate gyrus of rat hippocampal slices: A patch-clamp study. *J. Physiology*, 430:213–249.

[Ehrenstein et al., 1970] Ehrenstein, G., Lecar, H., and Nossal, R. (1970). The nature of the negative resistance in bimolecular lipid membranes containing excitability-inducing material. *J. Gen. Physiology*, 55:119–133.

[Engel et al., 1992] Engel, A., König, P., Kreiter, A., and Schillen, T. (1992). Temporal coding in the visual cortex - new vistas on integration in the nervous system. *Trends in the Neurosciences*, 15(6):218–226.

[Felleman and Van Essen, 1991] Felleman, D. and Van Essen, D. (1991). Distributed hierarchical processing in the primate cerebral cortex. *Cerebral Cortex*, 1:123–200.

[Ferster and Jagadeesh, 1992] Ferster, D. and Jagadeesh, B. (1992). EPSP-IPSP interactions in cat visual cortex studied with in vivo whole-cell patch recording. *J. Neuroscience*, 12(4):1262–1274.

[Finkel and Redman, 1983] Finkel, A. and Redman, S. (1983). The synaptic current evoked in cat spinal motoneurones by impulses in single group 1a axons. *J. Physiology*, 342:615–632.

[Fisher et al., 1990] Fisher, R., Gray, R., and Johnston, D. (1990). Properties and distribution of single voltage-gated calcium channels in adult hippocampal neurons. *J. Neurophysiology*, 62(1):91–104.

[Fox et al., 1987] Fox, A., Nowycky, M., and Tsien, R. (1987). Single-channel recordings of three types of calcium channels in chick sensory neurons. *J. Physiology*, 394:173–200.

[Frankenhaeuser and Huxley, 1964] Frankenhaeuser, B. and Huxley, A. (1964). Action potential in myelinated nerve fibre of Xenopus laevis as computed on the basis of voltage clamp data. *J. Physiology*, 171:302–315.

[Franz et al., 1986] Franz, P., Galvan, M., and Constanti, A. (1986). Calcium-dependent action potentials and associated inward currents in guinea-pig neocortical neurons in vitro. *Brain Research*, 366:262–271.

[French et al., 1990] French, C., Sah, P., Buckett, K., and Gage, P. (1990). A voltage-dependent persistent sodium current in mammalian hippocampal neurons. *J. Gen. Physiology*, 95:1139–1157.

[Gray et al., 1989] Gray, C., König, P., Engel, A., and Singer, W. (1989). Oscillatory responses in cat visual cortex exhibit inter-columnar synchronization which reflects global stimulus properties. *Nature*, 338:334–337.

[Gulyas et al., 1987] Gulyas, B., Orban, G., Duysens, J., and Maes, H. (1987). The suppressive influence of moving textured backgrounds on responses of cat striate neurons to moving bars. *J. Physiology*, 57:1767–1791.

[Hagiwara et al., 1961] Hagiwara, S., Kusano, K., and Saito, N. (1961). Membrane changes of onchidium nerve cell in potassium-rich media. *J. Physiology*, 155:470–489.

[Hille, 1984] Hille, B. (1984). *Ionic Channels of Excitable Membranes*. Sinauer Associates, Inc. Publishers, Sunderland, Massachusetts, first edition.

[Hines, 1989] Hines, M. (1989). A program for simulation of nerve equations with branching geometries. *Int. J. Biomed. Comput.*, 24:55–68.

[Hirsch and Gilbert, 1991] Hirsch, J. and Gilbert, C. (1991). Synaptic physiology of horizontal connections in the cat's visual cortex. *J. Neuroscience*, 11(6):1800–1809.

[Hodgkin and Huxley, 1952] Hodgkin, A. and Huxley, A. (1952). A quantitative description of membrane current and its application to conduction and excitation in nerve. *J. Physiology*, 117:500–544.

[Holmes and Woody, 1989] Holmes, W. and Woody, C. (1989). Effects of uniform and non-uniform synaptic activation-distributions on the cable properties of modeled cortical pyramidal neurons. *Brain Research*, 505:12–22.

[Hopfield, 1982] Hopfield, J. (1982). Neural networks and physical systems with emergent collective computational abilities. *Proc. Natl. Acad. Sci. USA*, 79:2554–2558.

[Hopfield, 1984] Hopfield, J. (1984). Neurons with graded response have collective computational properties like those of two-state neurons. *Proc. Natl. Acad. Sci. USA*, 81:3088–3092.

[Huguenard et al., 1989] Huguenard, J., Hamill, O., and Prince, D. (1989). Sodium channels in dendrites of rat cortical pyramidal neurons. *Proc. Natl. Acad. Sci. USA*, 86:2473–2477.

[Jack et al., 1975] Jack, J., Noble, D., and Tsien, R. (1975). *Electric current flow in excitable cells.* Oxford University Press, Oxford.

[Jaffe et al., 1992] Jaffe, D., Johnston, D., Lasser-Ross, N., Lisman, J., Miyakawa, J., and Ross, W. (1992). The spread of Na+ spikes determines the pattern of dendritic Ca++ entry into hippocampal neurons. *Nature*, 357:244–246.

[Jahr and Stevens, 1987] Jahr, C. and Stevens, C. (1987). Glutamate activates multiple single channel conductances in hippocampal neurons. *Nature*, 325:665–688.

[Jahr and Stevens, 1990] Jahr, C. and Stevens, C. (1990). A quantitative description of NMDA receptor-channel kinetic behavior. *J. Neuroscience*, 10(6):1830–1837.

[Johnston et al., 1980] Johnston, D., Hablitz, J., and Wilson, W. (1980). Voltage clamp discloses slow inward current in hippocampal burst-firing neurones. *Nature*, 286:391–393.

[Jones, 1989] Jones, S. (1989). On the resting potential of isolated frog sympathetic neurons. *Neuron*, 3:153–161.

[Kandel and Schwartz, 1985] Kandel, E. and Schwartz, J. (1985). *Principles of Neural Science.* Elsevier Science Publishing Co., Inc., New York, New York, 2 edition.

[Kauer et al., 1988] Kauer, J., Malenka, R., and Nicoll, R. (1988). A persistent postsynaptic modification mediates long-term potentiation in the hippocampus. *Neuron*, 1:911–917.

[Knight, 1972] Knight, B. (1972). Dynamics of encoding in a population of neurons. *J. Gen. Phys.*, 59:734–766.

[Koch, 1984] Koch, C. (1984). Cable theory in neurons with active, linearized membranes. *Biol. Cybern.*, 50:15–33.

[Koch and Davis *(Editors)*, 1994] Koch, C. and Davis *(Editors)*, J. (1994). *Large scale neuronal theories of the brain.* MIT Press (In Press).

[Koch et al., 1990] Koch, C., Douglas, R., and Wehmeier, U. (1990). Visibility of synaptically induced conductance changes: Theory and simulations of anatomically characterized cortical pyramidal cells. *J. Neuroscience*, 10(6):1728–1744.

[Koch et al., 1982] Koch, C., Poggio, T., and Torre, V. (1982). Retinal ganglion cells: a functional interpretation of dendritic morphology. *Phil. Trans. R. Soc. Lond.*, B 298:227–264.

[Koch et al., 1992] Koch, C., Zador, A., and Brown, T. (1992). Dendritic spines: Convergence of theory and experiment. *Science*, 156:973–974.

[Kreiter and Singer, 1992] Kreiter, A. and Singer, W. (1992). Oscillatory neuronal responses in the visual cortex of the awake macaque monkey. *European J. Neuroscience*, 4:369–375.

[Kriegstein and LoTorco, 1990] Kriegstein, A. and LoTorco, J. (1990). Gabaergic synaptic currents in slices of neocortex analyzed with whole-cell and cell-detached patch-clamp techniques. In *Neuroscience Abstr. 16*, page 30.9.

[Kuffler et al., 1984] Kuffler, S., Nicholls, J., and Martin, A. (1984). *From Neuron to Brain.* Sinauer Associates, Inc. Publishers, Sunderland, Massachusetts, 2 edition.

[LaCaille, 1991] LaCaille, J.-C. (1991). Postsynaptic potentials mediated by excitatory and inhibitory amino acids in interneurons of stratum pyramidale of the CA1 region of rat hippocampal slices in vitro. *J. Neurophysiology*, 66(5):1441–1454.

[Lancaster et al., 1991] Lancaster, B., Nicoll, R., and Perkel, D. (1991). Calcium activates two types of potassium channels in rat hippocampal neurons in culture. *J. Neuroscience*, 11(1):23–30.

[Larkman, 1991a] Larkman, A. (1991a). Dendritic morphology of pyramidal neurones of the visual cortex of the rat: I. branching patterns. *J. Comp. Neurol.*, 306:307–319.

[Larkman, 1991b] Larkman, A. (1991b). Dendritic morphology of pyramidal neurones of the visual cortex of the rat: III. spine distributions. *J. Comp. Neurology*, 306:332–343.

[Larkman et al., 1990] Larkman, A., Stratford, K., and Jack, J. (1990). Quantal analysis of excitatory synaptic transmission in the CA1 subfield of rat hippocampus in vitro. In *Oxford Meeting*, page 61P.

[Laurent, 1990] Laurent, G. (1990). Voltage-dependent nonlinearities in the membrane of locust nonspiking local interneurons, and their significance for synaptic integration. *J. Neuroscience*, 10(7):2268–2280.

[Leventhal and Hirsch, 1978] Leventhal, A. and Hirsch, H. (1978). Receptive-field properties of neurons in different laminae of visual cortex of the cat. *J. Neurophysiology*, 41(4):948–962.

[Llinás, 1988] Llinás, R. (1988). The intrinsic electrophysiological properties of mammalian neurons: Insights into central nervous system function. *Science*, 242:1654–1664.

[Llinás and Sugimori, 1980b] Llinás, R. and Sugimori, M. (1980b). Electrophysiological properties of in vitro Purkinje cell dendrites in mammalian cerebellar slices. *J. Physiology (London)*, 305:197–213.

[Llinás and Sugimori, 1980a] Llinás, R. and Sugimori, M. (1980a). Electrophysiological properties of in vitro Purkinje cell somata in mammalian cerebellar slices. *J. Physiology (London)*, 305:171–195.

[Lytton and Sejnowski, 1991] Lytton, W. and Sejnowski, T. (1991). Simulations of cortical pyramidal neurons synchronized by inhibitory interneurons. *J. Neurophysiology*, 66(3):1059–1079.

[Madison et al., 1987] Madison, D., Lancaster, V., and Nicoll, R. (1987). Voltage clamp analysis of cholinergic action in the hippocampus. *J. Neuroscience*, 7:733–741.

[Major et al., 1990] Major, G., Larkman, A., and Jack, J. (1990). Constraining non-uniqueness in passive electrical models of cortical pyramidal neurones. *J. Physiology*, 430:13P.

[Mason and Larkman, 1990] Mason, A. and Larkman, A. (1990). Correlations between morphology and electrophysiology of pyramidal neurons in slices of rat visual cortex. II. Electrophysiology. *J. Neuroscience*, 10(5):1415–1428.

[Mason et al., 1991] Mason, A., Nicoll, A., and Stratford, K. (1991). Synaptic transmission between individual pyramidal neurons of the rat visual cortex in vitro. *J. Neuroscience*, 11(1):72–84.

[Masukawa and Prince, 1984] Masukawa, L. and Prince, D. (1984). Synaptic control of excitability in isolated dendrites of hippocampal neurons. *J. Neuroscience*, 4(1):217–227.

[Mauro et al., 1970] Mauro, A., Conti, F., Dodge, F., and Schor, R. (1970). Subthreshold behavior and phenomenological impedance of the squid giant axon. *J. Gen. Phys.*, 55:497–523.

[Mayer and Westbrook, 1987] Mayer, M. and Westbrook, G. (1987). The physiology of excitatory amino acids in the vertebrate central nervous system. *Progress in Neurobiology*, 28:197–276.

[McCormick, 1990] McCormick, D. (1990). Membrane properties and neurotransmitter actions. In Shepherd, G., editor, *The synaptic organization of the brain, 2nd edition*, chapter 2, pages 32–66. Oxford University Press, Oxford.

[McCormick, 1992] McCormick, D. (1992). Neurotransmitter actions in the thalamus and cerebral cortex and their role in neuromodulation of thalamocortical activity. *Progress in Neurobiology*, 39:337–388.

[McCormick et al., 1985] McCormick, D., Connors, B., Lighthall, J., and Prince, D. (1985). Comparative electrophysiology of pyramidal and sparsely spiny stellate neurons of the neocortex. *J. Neurophysiology.*, 54(4):782–806.

[McCormick et al., 1992] McCormick, D., Huguenard, J., and Strowbridge, B. (1992). Determination of state dependent processing in thalamus by single neuron properties and neuromodulators. In McKenna, T., Javis, J., and Zarnetzer, S., editors, *Single Neuron Computation*, chapter 10, pages 259–290. Academic Press, Boston, Massachusetts.

[McCormick and Williamson, 1989] McCormick, D. and Williamson, A. (1989). Convergence and divergence of neurotransmitter action in human cerebral cortex. *Proc. Natl. Acad. Sci. USA*, 86:8098–8102.

[McCullough and Pitts, 1943] McCullough, W. and Pitts, W. (1943). A logical calculus of the ideas immanent in nervous activity. *Bull. Math. Biophys.*, 5:115–133.

[Mel, 1992] Mel, B. (1992). NMDA-based pattern discrimination in a modeled cortical neuron. Submitted.

[Mel, 1993] Mel, B. (1993). Information processing in dendritic trees. Submitted.

[Miles and Wong, 1984] Miles, R. and Wong, R. (1984). Unitary inhibitory synaptic potentials in the guinea-pig hippocampus in vitro. *J. Physiology*, 356:97–113.

[Milner, 1974] Milner, P. (1974). A model for visual shape recognition. *Psychol. Review*, 81:521–535.

[Murthy and Fetz, 1993] Murthy, V. and Fetz, E. (1993). Effects of input synchrony on the response of a model neuron. In Eeckman, F., editor, *Computation and Neural Systems 92*. Kluwer Academic Publishers. In Press.

[Nelson and Frost, 1985] Nelson, J. and Frost, B. (1985). Intracortical facilitation among co-oriented, co-axially aligned simple cells in cat striate cortex. *Exp. Brain Research*, 61:54–61.

[Nelson et al., 1992] Nelson, J., Salin, P., Munk, M.-J., Arzi, M., and Bullier, J. (1992). Spatial and temporal coherence in cortico-cortical connections: A cross-correlation study in areas 17 and 18 in the cat. *Visual Neuroscience*, 9:21–37.

[O'Leary, 1941] O'Leary, J. (1941). Structure of the area striata of the cat. *J. Comp. Neurol.*, 75:131–164.

[Olshausen et al., 1992] Olshausen, B., Anderson, C., and Van Essen, D. (1992). A neural model of visual attention and invariant pattern recognition. CNS memo 18, California Institute of Technology, Pasadena, CA, 91125.

[Olshausen et al., 1993] Olshausen, B., Anderson, C., and Van Essen, D. (1993). A neurobiological model of visual attention and invariant pattern recognition based on dynamic routing of information. *In preparation*, 255.

[Peters, 1987] Peters, A. (1987). Number of neurons and synapses in primary visual cortex. In Peters, A. and Jones, E., editors, *Cerebral Cortex Vol. 6: Further Aspects of Cortical Function, Including Hippocampus*, pages 267–294. Plenum, New York.

[Pettet and Gilbert, 1992] Pettet, M. and Gilbert, C. (1992). Dynamic changes in receptive-field size in cat primary visual cortex. *Proc. Natl. Acad. Sci. USA*, 89:8366–8370.

[Plummer et al., 1991] Plummer, M., Rittenhouse, A., Kanevsky, M., and Hess, P. (1991). Neurotransmitter modulation of calcium channels in rat sympathetic neurons. *J. Neuroscience*, 11:2339–2348.

[Pockberger, 1991] Pockberger, H. (1991). Electrophysiological and morphological properties of rat motor cortex neurons in vivo. *Brain Research*, 539:181–190.

[Poolos and Kocsis, 1990] Poolos, N. and Kocsis, J. (1990). Dendritic action potentials activated by NMDA receptor-mediated EPSPs in CA1 hippocampal pyramidal cells. *Brain Research*, 524:342–346.

[Powers et al., 1992] Powers, P., Tobinson, R., and Konodi, M. (1992). Effective synaptic current can be estimated from measurements of neuronal discharge. *J. Neurophysiology*, 68(3):964–968.

[Purpura et al., 1968] Purpura, D., Prelevic, S., and Santini, M. (1968). Hyperpolarizing increase in membrane conductance in hippocampal neurons. *Brain Research*, 7:310–312.

[Rall, 1964] Rall, W. (1964). Theoretical significance of dendritic trees for neuronal input-output relations. In Reiss, R., editor, *Neural Theory and Modeling*, pages 73–97. Stanford University Press, Stanford.

[Rall, 1969] Rall, W. (1969). Time constants and electrotonic length of membrane cylinders and neurons. *Biophysics J.*, 9:1483–1508.

[Rall, 1989] Rall, W. (1989). Cable theory for dendritic neurons. In Koch, C. and Segev, I., editors, *Methods in Neuronal Modeling*, chapter 2. MIT Press, Cambridge, Massachusetts.

[Rall et al., 1992] Rall, W., Burke, R., Holmes, W., Jack, J., Redman, S., and Segev, I. (1992). Matching dendritic neuron models to experimental data. *Physiological reviews*, 72(4):S159–S186.

[Rall and Segev, 1985] Rall, W. and Segev, I. (1985). Space-clamp problems when voltage clamping branched neurons with intracellular microelectrodes. In Smith, T. J., Lecar, H., Redman, S., and Gage, P., editors, *Voltage and Patch Clamping With Microelectrodes*, chapter 9. Academic Press, Bethesda, Maryland.

[Ramon ỳ Cajal, 1909] Ramon ỳ Cajal, S. (1909). Histologie du système nerveux de l'homme et des vertébrés. *translated by L. Azoulay.* Malaine, Paris.

[Rapp et al., 1992] Rapp, M., Yarom, Y., and Segev, I. (1992). The impact of parallel fiber background activity on the cable properties of cerebellar purkinje cells. *Neural Computation*, 4:518–533.

[Rasmussen, 1986] Rasmussen, H. (1986). The calcium messenger system I. *N. Engl. J. Med.*, 314:1094–1101.

[Regehr et al., 1989] Regehr, W., Connor, J., and Tank, D. (1989). Optical imaging of calcium accumulation in hippocampal pyramidal cells during synaptic activation. *Nature*, 341:533–536.

[Reuveni et al., 1993] Reuveni, I., Friedman, A., Amitai, Y., and Gutnick, M. (1993). Stepwise repolarization from Ca2+ plateaus in neocortical pyramidal cells: Evidence for non-homogeneous distribution of HVA Ca2+ channels in dendrites. *Submitted to J. Neuroscience.*

[Rinzel and Rall, 1974] Rinzel, J. and Rall, W. (1974). Transient response in a dendritic neuron model for current injected at one branch. *Biophysics J.*, 14:759–789.

[Rockland and Virga, 1989] Rockland, K. and Virga, A. (1989). Terminal arbors of individual "feedback" axons projecting from area V2 to V1 in the macaque monkey: a study using immunohistochemistry of anterogradely transported phaseoulus vulgaris-leucoagglutinin. *J. Comp. Neurol.*, 285:54–72.

[Rumelhart and McClelland, 1986] Rumelhart, D. and McClelland, J. (1986). *Parallel distributed processing.* MIT Press, Cambridge, Massachusetts.

[Sayer et al., 1990] Sayer, R., Schwindt, P., and Crill, W. (1990). High- and low-threshold calcium currents in neurons acutely isolated from rat sensorimotor cortex. *Neuroscience Letters*, 120:175–178.

[Sayer et al., 1992] Sayer, R., Schwindt, P., and Crill, W. (1992). Metabotropic glutamate receptor-mediated suppression of L-type calcium current in acutely isolated neocortical neurons. *J. Neurophysiology*, 68(3):833–842.

[Schwindt et al., 1992a] Schwindt, P., Spain, W., and Crill, W. (1992a). Calcium-dependent potassium currents in neurons from cat sensorimotor cortex. *J. Neurophysiology*, 67(1):216–226.

[Schwindt et al., 1992b] Schwindt, P., Spain, W., and Crill, W. (1992b). Effect of intracellular calcium chelation on voltage-dependent and calcium-dependent currents in cat neocortical neurons. *Neuroscience*, 47(3):571–578.

[Schwindt et al., 1988] Schwindt, P., Spain, W., Foehring, R., Stafstrom, C., Chubb, M., and Crill, W. (1988). Multiple potassium conductances and their functions in neurons from cat sensorimotor cortex in vitro. *J. Neurophysiology*, 59(2):424–449.

[Segal and Barker, 1984] Segal, M. and Barker, J. (1984). Rat hippocampal neurons in culture: Potassium conductances. *J. Neurophysiology*, 51:1409–1433.

[Segal et al., 1984] Segal, M., Rogawski, M., and Barker, J. (1984). A transient potassium conductance regulates the excitability of cultured hippocampal and spinal neurons. *J. Neuroscience*, 4(2):604–609.

[Segev et al., 1989] Segev, I., Fleshman, J., and Burke, R. (1989). Compartmental models of complex neurons. In Koch, C. and Segev, I., editors, *Methods in Neuronal Modeling*, chapter 3. MIT Press, Cambridge, Massachusetts.

[Segev et al., 1992] Segev, I., Rapp, M., Manor, Y., and Yarom, Y. (1992). Analog and digital processing in single nerve cells: dendritic integration and axonal propagation. In McKenna, T., Javis, J., and Zarnetzer, S., editors, *Single Neuron Computation*, chapter 7, pages 173–198. Academic Press, Boston, Massachusetts.

[Shelton, 1985] Shelton, D. (1985). Membrane resistivity estimated for the purkinje neuron by means of a passive computer model. *J. Neuroscience*, 14(1):111–131.

[Smith and Augustine, 1988] Smith, S. and Augustine, G. (1988). Calcium ions, active zones and synaptic transmitter release. *Trends Neurosci.*, 11:458–464.

[Softky, 1993] Softky, W. (1993). Sub-millisecond coincidence detection in active dendritic trees. Submitted to J. Neuroscience.

[Softky and Koch, 1992] Softky, W. and Koch, C. (1992). Cortical cells should fire regularly, but do not. *Neural Computation*, 4(5):643–646.

[Softky and Koch, 1993] Softky, W. and Koch, C. (1993). The highly irregular firing of cortical cells is inconsistent with temporal integration of random EPSP's. *J. Neuroscience*, 13(1):334–350.

[Spain et al., 1987] Spain, W., Schwindt, P., and Crill, W. (1987). Anomalous rectification in neurons from cat sensorimotor cortex in vitro. *J. Neurophysiology*, 57(5):1555–1576.

[Spain et al., 1990] Spain, W., Schwindt, P., and Crill, W. (1990). Post-inhibitory excitation and inhibition in layer V pyramidal neurons from cat sensorimotor cortex. *J. Physiology*, 434:609–626.

[Spain et al., 1991] Spain, W., Schwindt, P., and Crill, W. (1991). Two transient potassium currents in layer V pyramidal neurones from cat sensorimotor cortex. *J. Physiology*, 4347:591–607.

[Spencer and Kandel, 1961] Spencer, W. and Kandel, E. (1961). Electrophysiology of hippocampal neurons. IV fast prepotentials. *J. Neurophysiology*, 24:272–285.

[Spruston and Johnston, 1992] Spruston, N. and Johnston, D. (1992). Perforated patch-clamp analysis of the passive membrane properties of three classes of hippocampal neurons. *J. Neurophys*, 67(3):508–529.

[Stafstrom et al., 1985] Stafstrom, C., Schwindt, P., Chubb, M., and Crill, W. (1985). Properties of persistent sodium conductance and calcium conductance of layer V neurons from cat sensorimotor cortex in vitro. *J. Neurophysiology*, 53(1):153–170.

[Stafstrom et al., 1984] Stafstrom, C., Schwindt, P., and Crill, W. (1984). Repetitive firing in layer V neurons from cat neocortex in vitro. *J. Neurophysiology*, 52(2):264–277.

[Stratford et al., 1989] Stratford, K., Mason, A., Larkman, A., Major, G., and Jack, J. (1989). The modelling of pyramidal neurones in the visual cortex. In Durbin, R., Miall, C., and Mitchison, G., editors, *The Computing Neuron*. Addison-Wessley, London.

[Swandulla et al., 1991] Swandulla, D., Carbone, E., and Lux, H. (1991). Do calcium channel classifications account for neuronal calcium channel diversity? *Trends Neurosci.*, 14(2):46–51.

[Thomas et al., 1980] Thomas, Y., Peeling, A., Bedi, K., Davies, C., and Dobbing, J. (1980). Deficits in synapse-to-neuron ratio due to early undernutrition show evidence of catch-up in later life. *Experiencia*, 36:556–557.

[Thomson et al., 1988] Thomson, A., Girdlestone, D., and West, D. (1988). Voltage-dependent currents prolong single-axon postsynaptic potentials in layer III pyramidal neurons in rat neocortical slices. *J. Neurophysiology*, 60:1896–1907.

[Traub et al., 1985] Traub, R., Dudek, F., Taylor, C., and Knowles, W. (1985). Simulation of hippocampal afterdischarges synchronized by electrical interactions. *J. Neuroscience*, 4:1033–1038.

[Traub et al., 1991] Traub, R., Wong, R., Miles, R., and Michelson, H. (1991). A model of a CA3 hippocampal pyramidal neuron incorporating voltage-clamp data on intrinsic conductances. *J. Neurophysiology*, 66(2):635–650.

[Ts'o et al., 1986] Ts'o, D., Gilbert, C., and Wiesel, T. (1986). Relationships between horizontal interactions and functional architecture in cat striate cortex as revealed by cross-correlation analysis. *J. Neuroscience*, 6(4):1160–1170.

[Turner and Greenough, 1985] Turner, A. and Greenough, W. (1985). Differential rearing effects on rat visual cortical synapses I. Synaptic and neuronal density and synapses per neuron. *Brain Research*, 329:195–203.

[Turner et al., 1982] Turner, R., Baimbridge, K., and Miller, J. (1982). Calcium-induced long-term potentiation in the hippocampus. *Neuroscience*, 7:1411–1416.

[von der Malsburg and Schneider, 1986] von der Malsburg, C. and Schneider, W. (1986). A neural cocktail-party processor. *Biol. Cybern.*, 54:29–40.

[Warren and Bedi, 1982] Warren, M. and Bedi, K. (1982). Synapse-to-neuron ratios in the visual cortex of adult rats undernourished from about birth until 100 days of age. *J. Comp. Neurol.*, 210:59–64.

[Warren and K.S., 1984] Warren, M. and K.S., B. (1984). A quantitative assessment of the development of synapses and neurons in the visual cortex of control and undernourished rats. *J. Comp. Neurol.*, 227:104–108.

[White, 1989] White, E. (1989). *Cortical Circuits.* Birkhaeuser, Boston.

[Williams and Johnston, 1991] Williams, S. and Johnston, D. (1991). Kinetic properties of two anatomically distinct excitatory synapses in hippocampal CA3 neurons. *J. Neurophysiology*, 66(3):1010–1020.

[Wilson, 1992] Wilson, C. (1992). Dendritic morphology, inward rectification and the functional properties of neostriatal neurons. In McKenna, T., Javis, J., and Zarnetzer, S., editors, *Single Neuron Computation*, chapter 6, pages 141–171. Academic Press, Boston, Massachusetts.

[Wilson and Bower, 1989] Wilson, M. and Bower, J. (1989). The simulation of large-scale neural networks. In Koch, C. and Segev, I., editors, *Methods in Neuronal Modeling*, chapter 9. MIT Press, Cambridge, Massachusetts.

[Wong et al., 1979] Wong, R., Prince, D., and Basbaum, A. (1979). Intradendritic recording from hippocampal neurons. *Proc. Natl. Acad. Sci. USA*, 76:986–990.

[Wong and Stewart, 1992] Wong, R. and Stewart, M. (1992). Different firing patterns generated in dendrites and somata of CA1 pyramidal neurones in guinea-pig hippocampus. *J Physiology*, 467:675–687.

[Woody et al., 1984] Woody, C., Gruen, E., and McCarley, K. (1984). Intradendritic recordings from neurons of the motor cortex of cats. *J. Neurophysiology*, 51:925–938.

[Woody et al., 1988] Woody, C., Gruen, E., and McCarley, K. (1988). Intradendritic recordings from neurons of motor cortex of cats. *J. Neurophysiology*, 51(5):925–938.

[Woolf et al., 1991] Woolf, T., Shepherd, G., and Greer, C. (1991). Local information processing in dendritic trees: subsets of spines in granule cells of the mammalian olfactory bulb. *J. Neuroscience*, 11(6):1837–1854.

[Yakel et al., 1988] Yakel, J., Trussell, L., and Jackson, M. (1988). Three serotonin responses in cultured mouse hippocampal and striatal neurons. *J. Neuroscience*, 8:1273–1285.

[Yamada et al., 1989] Yamada, W., Koch, C., and Adams, P. (1989). Multiple channels and calcium dynamics. In Koch, C. and Segev, I., editors, *Methods in Neuronal Modeling*, chapter 4. MIT Press, Cambridge, Massachusetts.

[Zador, 1993] Zador, A. (1993). Biophysics of computation in single hippocampal neurons. Ph.D. Thesis, Yale University, 1993.

[Zador et al., 1991] Zador, A., Claiborne, B., and Brown, T. (1991). Attenuation transforms of hippocampal neurons. In *Neuroscience Abstr. 17*, page 605.6.

[Zador et al., 1992] Zador, A., Claiborne, B., and Brown, T. (1992). Nonlinear pattern separation in single hippocampal neurons with active dendritic membrane. In Lippman, R., Moody, J., and Touretzky, D., editors, *Neural information processing systems 4*, pages 51–58, 2929 Campus Drive #260, San Mateo, CA 94403. Morgan Kaufmann.

[Zador et al., 1990] Zador, A., Koch, C., and Brown, T. (1990). Biophysical model of a hebbian synapse. *Proc. Natl. Acad. Sci. USA*, 87:6718–6722.

[Zeki and Shipp, 1988] Zeki, S. and Shipp, S. (1988). The functional logic of cortical connections. *Nature*, 355:311–317.